Numerical Investigation of Novel Rotorcraft Propulsion Systems

Geng Qiao

Submitted in partial fulfillment of the requirements for the
Degree of Doctor of Philosophy

School of Engineering
University of Glasgow

March 2025

Abstract

In recent years, an upsurge in advanced air mobility (AAM) aircraft can be noticed worldwide, e.g. , Rolls Royce, Airbus, NASA, DARPA, Advanced Aircraft Company, Bell Helicopter, Aurora, Honeywell, and others. Future AAM will operate near the ground in the urban area, and thus it should be environmentally and community-friendly while maintaining excellent aerodynamic performance. As is known, a high-intensity of sound is emitted by the VTOL aircraft, but noise emission is crucial in the VTOL aircraft certification process and urban operation. It is clear that the propulsors are generating most of the noise from the whole aircraft. Therefore, there is a growing demand for low-noise emission propulsors, reduced wake interference, and improved aerodynamic performance. Previous works show that distributed and wingtip-mounted propulsion systems are promising candidates as a novel compact propulsor with excellent performance. However, the combination of multiple sources of lift and thrust brings significant challenges in terms of aerodynamic interactions, noise emissions, vibration, instability, control, trim difficulties, power allocation, and others. Nevertheless, AAM research is emerging mainly in Europe, the USA, and Asia, as the appeal for better civil rotorcraft is growing. Several demonstrators, e.g. the US DARPA XV-24A, Joby S4, and the VX4 from Vertical Aerospace, have been delivered, illustrating the superior performance of AAM aircraft. Ahead of routine deployment of AAM aircraft, there is still significant aerodynamic/aeroacoustic research and development to be carried out.

This thesis aims to investigate novel propulsion concepts, including tip-mounted propellers and distributed propulsion systems, through CFD verification, optimisation, and aerodynamic performance evaluation. The first part of the study validates the employed multi-fidelity simulation methods using experimental data from the NASA Workshop for Integrated Propeller Prediction (WIPP) and the Folding Conformal High Lift Propeller (HLP) project for isolated and installed cases under various conditions. Additionally, aerodynamic and aeroacoustic validation via the hybrid methods for rotor-rotor interactions was also conducted using the GARTEUR Action Group 26 measurements.

Applying the same methods and simulation strategies used in the validation, the thesis further examines a series of installed propeller configurations with actuator disks to identify performance differences based on their position relative to a lifting wing. The reduced-order method was cost-effective and suggested the approximate optimal position of the distributed propellers. The actuator disk method has successfully captured the leading-edge suction induced by inflow. In addition, the performance of the propulsion system changes due to different installation effects. Furthermore, additional surfaces from nacelle and pylon structures will also have an impact on the propulsion system. Therefore, additional verification cases utilising high-fidelity methods were carried out, and the investigation of the conventional tractor and the optimal over-the-wing (OTW) configurations was conducted for different numbers of propellers and conditions.

Wingtip-mounted propellers are known to be a promising configuration for reducing induced drag through favourable wake interactions. This thesis presents, for the first time, the integration of wingtip-mounted propellers with an OTW distributed propulsion (DP) system, in-

vestigated using high-fidelity, fully resolved simulations. To investigate this novel tip-mounted propeller–distributed propulsion (TMP-DP) configuration, equivalent-performance propulsion systems were proposed based on realistic aircraft operational conditions. The study examines complex interactional flow phenomena inherent to such systems, including propeller–wing, propeller–propeller, propeller–slipstream, and propeller–wake interactions. Given the intricacy of the distributed propulsion setup, key aerodynamic and propulsive parameters, such as thrust and power distribution, wing lift, drag, lift-to-drag ratio (L/D), and pitching moments, are thoroughly analysed and reported.

To harness the benefits of multirotors in a distributed propulsion system, synchrophasing has been implemented as a means of reducing noise. Tandem rotors, with and without vertical offset, are investigated using fully resolved simulations under both hover and edgewise flight conditions. A comprehensive synchrophasing study reveals varying levels of cumulative rarefaction and compression effects in the resulting acoustic waves. To better account for the relative loudness as perceived by the human ear, A-weighting and one-third-octave band analysis have been employed. These approaches help to identify how different frequency components contribute to the overall acoustic signature and can inform targeted noise control and mitigation strategies. Finally, this study quantifies noise reductions across the frequency spectrum for each synchrophasing case and identifies the most effective phase angles. These optimal phase configurations can be tuned to achieve maximum noise reduction at specific observer locations.

Publications

Journal Papers

- **Geng Qiao**, George Barakos. "Aerodynamic Study of Wingtip-mounted Propeller and Distributed Propulsion System." *The Aeronautical Journal*, (2025) doi: 10.1017/aer.2025.36 The authors contributed to the work as follows: [George Barakos] conceived the research idea and supervised the project. [Geng Qiao] performed the simulations, analysed the data, and drafted the manuscript. All authors contributed to discussions throughout the study, reviewed the manuscript critically for intellectual content, and approved the final version for submission.

- **Geng Qiao**, Tao Zhang, George Barakos. "Numerical Simulation of Distributed Propulsion Systems Using CFD" *Aerospace Science and Technology*, (2024) doi: 2024.109011 The authors contributed to the work as follows: [George Barakos] conceived the research idea and supervised the project. [Geng Qiao] performed the simulations, analysed the data, and drafted the manuscript. [Tao Zhang] contributed to the reduced-order (AD) simulations and analysed their data. [Geng Qiao] and [George Barakos] contributed to discussions throughout the study, reviewed the manuscript critically for intellectual content, and approved the final version for submission.

- **Geng Qiao**, Emma San Martin, George Barakos. "Assessment of Synchrophasing for a Pair of Rotors in Close Proximity" *Aerospace Science and Technology*, (2024) doi:2024.109808. [George Barakos] conceived the research idea and supervised the project. [Geng Qiao] performed the simulations, analysed the data, and drafted the manuscript. [Emma San Martin] contributed to the simulations and analysed their data. [Geng Qiao] and [George Barakos] contributed to discussions throughout the study, reviewed the manuscript critically for intellectual content, and approved the final version for submission.

- J. Yin, F. De Gregorio, K.-S. Rossignol, L. Rottmann1, G. Ceglia, G. Reboul, G. Barakos, **Geng Qiao**, M. Muth, M. KesslerA. Visingardi, M. Barbarino, F. Petrosino, A. Zanotti, N. Oberti,L. Galimberti, G. Bernardini, C. Poggi, L. Abergo, F. Caccia,A. Guardone, C. Testa, S. Zaghi "Acostic and Aerodynamic Evaluation of DLR Small-scale Rotor Configurations Within GARTEUR AG26" *CEAS Aeronautical Journal*, (2024) doi: 10.1007/s13272-024-00790-2. [George Barakos] supervised the project. [Geng Qiao] performed the simulations, analysed the data, and drafted the manuscript. [Geng Qiao] and [George Barakos] contributed to discussions throughout the study, reviewed the manuscript critically for intellectual content, and approved the final version for submission.

Papers in Conference Proceedings

- **Geng Qiao** and George Barakos. "Aerodynamic Study of Wingtip-mounted Propeller and Distributed Propulsion System." In *Proceedings of the 50th European Rotorcraft Forum (ERF)*, Marseille, France, September 10–12, 2024.

- Antonio Visingardi et al. **Geng Qiao** and George Barakos. "Analysis of the Aeroacoustic Performance of Twin Propellers in Hover by Using the CIRA-Cusano Test Rig." In *Proceedings of the 50th European Rotorcraft Forum (ERF)*, Marseille, France, September 10–12, 2024. (Contribution: The far-field acoustic prediction method and coupling code have been employed and validated for the first time for the twin-propeller and synchrophasing cases.)

- **Geng Qiao** and George Barakos. "CFD Validation for eVTOL Propeller Performance and Acoustics." In *Proceedings of the 49th European Rotorcraft Forum (ERF)*, Bückeburg, Germany, September 5–7, 2023.

- J. Yin, F. De Gregorio, K.-S. Rossignol, L. Rottmann1, G. Ceglia, G. Reboul, G. Barakos, **Geng Qiao**, M. Muth, M. KesslerA. Visingardi, M. Barbarino, F. Petrosino, A. Zanotti, N. Oberti,L. Galimberti, G. Bernardini, C. Poggi, L. Abergo, F. Caccia,A. Guardone, C. Testa, S. Zaghi "Acostic and Aerodynamic Evaluation of DLR Small-scale Rotor Configurations Within GARTEUR AG26" In *Proceedings of the 49th European Rotorcraft Forum (ERF)*, Bückeburg, Germany, September 5–7, 2023. (Contribution: The near-field prediction method and coupling code have been employed and validated for the first time for the isolated and twin-propeller cases.)

- **Geng Qiao** and George Barakos. "Verification and Optimisation of Distributed Propulsion Using High-Fidelity CFD Method." In *Proceedings of the 79th American Helicopter Society Annual Forum (AHS)*, West Palm Beach, Florida, USA, May 16–18, 2023.

- **Geng Qiao**, Ross J Higgins, Tao Zhang and George Barakos. "CFD Study of eVTOL Distributed Propulsors." In *Proceedings of the RAeS Applied Aerodynamics Conference*, London, UK, 13-15 September 2022. doi: 280193.

- Tao Zhang, Ross J Higgins, **Geng Qiao** and George Barakos. "Optimisation of Distributed Propulsion Using CFD." In *Proceedings of the Aviation and Aeronautics Forum (AIAA)*, Chicago, USA, 27 June - 1 July 2022. doi: 10.2514/6.2022-3299.

Papers In conference without Proceedings

- **Geng Qiao** and George Barakos. "Aerodynamic and Aeroacoustic Study of Wingtip-mounted Propeller and Distributed Propulsion System." In *the 9th UK Vertical Lift Network Annual Technical Workshop*, Shrigley Hall, Manchester, UK, 21-23 May 2024.

- **Geng Qiao** and George Barakos. "Near-field acoustics and aerodynamics validation using experiments of the AG26 GARTEUR Group" In *the 8th UK Vertical Lift Network Annual Technical Workshop*, Shrigley Hall, Manchester, UK, 21-23 May 2023.

- **Geng Qiao**, Ross J Higgins, Tao Zhang and George Barakos. "Fluid Interaction of the Wing Tip Mounted Propeller, Distributed Propulsion Systems and the Integration Optimisation." In *the 7th UK Vertical Lift Network Annual Technical Workshop*, Shrigley Hall, Manchester, UK, 21-23 May 2022.

- **Geng Qiao**, Tao Zhang and George Barakos. "Parametric Study of Aerodynamic Performance of Equivalent Ducted/un-ducted Rotors." In *the 6th UK Vertical Lift Network Annual Technical Workshop*, Shrigley Hall, Manchester, UK, 17-19 April 2021.

Tecnical Reports

- **Geng Qiao** and George Barakos. "GARTEUR AG26 - Glasgow contribution 2022-2025" In *GARTEUR AG26 6th Technical Meeting*, DLR and online, Germany, 25 Feb 2025.
- **Geng Qiao** and George Barakos. "CIRA-Cusano configurations" In *GARTEUR AG26 4th Technical Meeting*, Politecnico di Milano and online, Italy, 14-15 March 2024.
- **Geng Qiao** and George Barakos. "High-Fidelity CFD Assessment of Synchrophasing for eVTOL Compound Rotor Acoustics and Performance" In *GARTEUR AG26 3rd Technical Meeting*, Italian Air Force Academy and online, Italy, 4th October 2023.
- **Geng Qiao** and George Barakos. "Aerodynamic and acoutic validation of DLR ACCID 13x7 rotor using different simulation strategies" In *GARTEUR AG26 2nd Technical Meeting*, University of Glasgow, Scotland, UK, 15-16 February 2023.
- **Geng Qiao** and George Barakos. "Aerodynamic and acoutic validation of DLR ACCID 13x7 rotor using steady simulations" In *GARTEUR AG26 1st Technical Meeting*, University of Glasgow, Scotland, UK, 16-20 September 2022.

Tecnical Notes

- **Geng Qiao** "Helicopter Rotor BELL412 Project" *TN24*
- **Geng Qiao** "Towards the investigation of the synchrophasing mechanism of the multi-rotor system via multi-fidelity methods." *TN25*
- **Geng Qiao** "Numerical study of multiple propellers-wing installed configuration within the GAAPS." *TN26*

Contents

List of Figures

List of Tables

Acknowledgements

Time flies, and in the blink of an eye, my three-year doctoral journey is coming to an end. Looking back, I feel incredibly fortunate to have had the opportunity to step into this field, explore cutting-edge knowledge, and conduct meaningful research. Throughout this period, I have received invaluable guidance, encouragement, and support, for which I am deeply grateful.

First and foremost, I would like to express my heartfelt gratitude to my supervisor, Prof. George N. Barakos. He introduced me to the fascinating world of CFD, expertly guided me in formulating my research plans, and provided rigorous scientific training throughout my journey. His meticulous attention to detail and unwavering dedication to research have made a profound impact on me. In our work on helicopter rotors, especially in studying ground effects, he offered invaluable insights and consistently delved deeply into every facet of the problem. His academic rigor and passion have been a constant source of inspiration. Our collaboration was never merely about sharing responsibilities, like 50% and 50%, but was instead characterized by a wholehearted commitment, 100% effort from both of us. I am deeply grateful for his guidance, which has shaped not only my research but also my personal and professional growth.

I would also like to sincerely acknowledge Dr. Nicholas Bojdo (University of Manchester) and Dr. Albert S.J. van Heerden (University of Glasgow), who served as the external and internal examiners of my viva. Their thoughtful discussions and constructive feedback greatly enriched the quality of this thesis. My gratitude also extends to Dr. Jagan Selvaraj for his kind assistance in arranging the viva and ensuring the process ran smoothly.

I am also immensely grateful to my friends and colleagues in the laboratory: Tao Zhang, Ye Yuan, Ross John Higgins, Thomas A. Fitzgibbon, Federico Rovere, Mark A. Woodgate, Andrea Petrocchi, Clément H. Civrais, Murray McKechnie, Rinaldo Steininger, Emma San Martin, Oyedoyin S. Dada, James Nelson, Daniele Zagaglia, Alexander D. Croke, and Gaargi Jain. The camaraderie, collaboration, and shared passion for science within our lab have been among the most rewarding parts of my doctoral journey. Your support has made my research more fulfilling and my life richer and more vibrant. The laughter we shared and the challenges we faced together will remain cherished memories for a lifetime. I also extend my heartfelt thanks to everyone who has cared for me along the way, wishing you all health, happiness, and continued success.

Finally, my deepest and most heartfelt gratitude goes to my parents. It is your endless love, unwavering belief in me, and constant support, both emotionally and financially, that have made it possible for me to pursue and complete my undergraduate, postgraduate, and doctoral studies. You are my greatest blessing and my strongest foundation. I love you more than words can express, and I will always strive to give back everything you have given me and more.

Declaration

I certify that the thesis presented here for examination for a Doctor of Philosophy degree of the University of Glasgow is solely my own work other than where I have clearly indicated that it is the work of others (in which case the extent of any work carried out jointly by me and any other person is clearly identified in it) and that the thesis has not been edited by a third party beyond what is permitted by the University's PGR Code of Practice.

I declare that the thesis does not include work forming part of a thesis presented successfully for another degree.

I declare that this thesis has been produced in accordance with the University of Glasgow's Code of Good Practice in Research.

I acknowledge that if any issues are raised regarding good research practice based on review of the thesis, the examination may be postponed pending the outcome of any investigation of the issues.

March 2025

.....
Geng Qiao

Nomenclature

Latin Symbols

F Flux vector in x direction

G Flux vector in y direction

H Flux vector in z direction

n Unit normal vector

R Flow residual vector

S Source term vector

v Arbitrary vector

W Vector of conserved variables

M_∞ Mach number

Re Reynolds number, $Re = \dfrac{U_{(ref)} c_{(ref)}}{\nu}$

A Area $\left[m^2\right]$

a Lift curve slope or speed of sound

AoA Angle of attack $[deg]$

c Chord $[m]$

C_D Drag coefficient, $\frac{D}{\frac{1}{2}\rho U_\infty^2 S}$

C_{F_x} Longitudinal force coefficient

C_L Lift coefficient, $\frac{L}{\frac{1}{2}\rho U_\infty^2 S}$

C_{M_x} Non-dimensional rotor rolling moment coefficient(US), $\frac{M_x}{\rho_{(ref)} U_{(inf)}^2 \pi (AR)^(3)}$

C_{M_y} Non-dimensional rotor pitching moment coefficient(US), $\frac{M_y}{\rho_{(ref)} U_{(inf)}^2 \pi (AR)^(3)}$

C_{M_z} Non-dimensional rotor torque (US), $\frac{M_z}{\rho_{(ref)} U_{(inf)}^2 \pi (AR)^(3)}$

C_M Pitching moment coefficient, $\frac{M}{\frac{1}{2}\rho U_\infty^2 c S}$

C_N Section normal force coefficient

C_{P_z} Non-dimensional rotor thrust coefficient, $\frac{P_z}{\rho_{(ref)} U^2_{(inf)} \pi (AR)(2)}$

C_P Pressure coefficient, $\frac{p-p_\infty}{\frac{1}{2}\rho(\Omega r)^2}$

C_{Qprop} Torque coefficient (propeller), $\frac{T}{\rho n^2 D^5}$

C_Q Torque coefficient (rotor), $\frac{Q}{\rho(\Omega R)^2 \pi R^3}$

C_q Blade section torque coefficient (US), $\frac{\frac{dQ}{dr}}{\frac{1}{2}\rho c_{(ref)} R(\Omega r)^3}$

C_{Tprop} Thrust coefficient (propeller), $\frac{T}{\rho n^2 D^4}$

C_T Thrust coefficient (rotor), $\frac{T}{\rho(\Omega R)^2 \pi R^2}$

C_t Blade section thrust coefficient, $\frac{\frac{dT}{dr}}{\frac{1}{2}\rho c_{(ref)} (\Omega r)^2}$

D Drag force $[N]$ or Fourier collocation derivative operator

d Distance $[m]$

E Energy per unit mass, $\left[m^2/s^2\right]$ or harmonic balance transformation matrix or Young's modulus $\left[kg/(ms^2)\right]$

f Frequency $[1/s]$

FoM Figure of merit, $\frac{C_T^{3/2}}{\sqrt{2}C_Q}$

G Shear modulus $\left[kg/(ms^2)\right]$

H_{out} Source-sink model distance of outflow region from rotor disk plane

J Jacobian matrix, $\frac{\partial R}{\partial W}$ or torsion constant

k Turbulent kinetic energy per unit mass $\left[m^2/s^2\right]$ or reduced frequency of oscillation, $\frac{f_c}{2U_\infty}$ or number of restarted Krylov eigenvectors in GMRESDR method

k_h Heat transfer coefficient

L Lift,$[N]$

L/D Lift to drag ratio

m Flow equation pseudo-time step level or number of inequality constants or number of Krylov vectors in the GMRES method

M^2C_d Blade section drag coefficient(rotor disk in-plane force), $\frac{D}{\frac{1}{2}\rho a^2 c}$

M^2C_l Blade section lift coefficient(rotor disk normal force), $\frac{L}{\frac{1}{2}\rho a^2 c}$

M^2C_m Blade section pitching moment coefficient, $\frac{M_y}{\frac{1}{2}\rho a^2 c^2}$

N Mesh metrics vector

n Rotational speed, $[Hz]$

N_b Number of blades

P Preconditioner or rotor power $\left[kgm^2/s^3\right]$, ΩQ

p Pressure pressure $\left[kg/(ms^2)\right]$ or number of equality constraints

Q Rotor torque $\left[kgm^2/s^2\right]$ or Q-criterion

q Heat flux vector

r Radial position along blade span $[m]$

R_{et} Turbulent eddy viscosity ratio, $\frac{\mu_t}{\mu}$

R_{sp} Specific gas constant $\left[m^2/(s^2K)\right]$

S_{ij} Strain rate tensor

T Rotor thrust $[N]$ or time $[s]$ or oscillation period, $\frac{2\pi}{\omega}$

t Time $[s]$

t^* Non-dimensional time

T^s Sutherland Temperature $[K]$

$T_{install}$ Installed propulsive thrust, $[N]$

$U = (u,v,w)^T$ Cartesian velocity vector [m/s]

U_∞ Free-stream velocity $[m/s]$

V Velocity $[m/s[$ or cell volume $\left[m^3\right]$

v_i Induced velocity far down stream $[m/s]$

W Non-dimensional rotor downwash velocity

W_{in} Source-sink model inflow velocity

W_{out} Source-sink model inflow velocity

x,y,z Spacial coordinates in Cartesian system $[m]$

$x = (x,y,z)^T$ Fluid position vector $[m]$

X_S Surface mesh

X_V Volume mesh

y Chordwise position $[m]$

y^+ Non-dimensional wall distance, $\frac{yu_\tau}{\nu}$

Greek Symbols

α Angle of acctack

α Angle of incidence $[deg]$ or adjoint design variable vector

β Angle of sideslip

β_0 Rotor coning angle $[deg]$

δ_{ij} Kronecker delta

$\eta^{overall}_{propulsive}$ Overall propulsive efficiency, $\eta^{overall}_{propulsive} = \frac{T_{install} \times U_\infty}{P_{shaft}}$

η_{Prop} Propeller Froude efficiency, $\eta_{Prop} = \frac{T_{propeller} \times U_\infty}{P_{shaft}}$

γ Shear rate $[1/s]$ or turbulence intermittency factor or specific heat ratio or rotor Lock number

μ Dynamic Viscosity $[kg/(ms)]$, $\frac{\tau}{\dot{\gamma}}$ or rotor advance ratio, $\frac{M_\infty}{M_{tip}}$

μ_t Turbulent eddy viscosity $[kg/(ms)]$

Ω Rotor rotational speed $[rad/s]$

ω Specific dissipation rate of turbulent kinetic energy $[1/s]$ or Specific dissipation frequency of turbulence $[1/s]$

ψ Azimuthal position $[deg]$

ρ Density $\left[kg/m^3\right]$

σ, σ_N Nominal rotor solidity, $\sigma_N = N_b / \left(\pi \mid R/c_{ref}\right)$

σ_G Geometric rotor solidity, $\sigma_G = \int_0^1 \sigma(r) dr$

σ_T Thrust-weighted rotor solidity, $\sigma_T = 3\int_0^1 \sigma(r) r^2 dr$

τ Shear stress $\left[kg/(ms^2)\right]$

τ_{ij} Viscous shear stress tensor

τ^R_{ij} Reynolds shear stress Tensor

τ_w Wall shear stress $\left[kg/(ms^2)\right]$

ε Turbulent energy dissipation rate

v Kinematic viscosity $\left[m^2/s\right]$

v_t Turbulent kinematic viscosity $\left[m^2/s\right]$

Subscripts

∞ Free-stream value

i, j, k Indices

p Pressure term

ref Reference value

rms Root mean square

tip Blade tip value

v Viscous term

Superscripts

i Inviscid

v Viscous

Acronyms

AAC Advanced Aircraft Company

ABASPL A-weighted Band Averaged Sound Pressure Level

AG Action Group

AIAA American Institute of Aeronautics and Astronautics

ARC Aerospace Research Central

ASPL A-weighted Sound Pressure Level

BL Boundary Layer

BPF Blade Passing Frequency

BVI Blade-Vortex Interaction

CFD Computational Fluid Dynamics

CIRA Italian Aerospace Research Centre

DARPA Defense Advanced Research Projects Agency

dB Decibel

DLR German Aerospace Center

DP Distributed Propulsion

EU European Union

eVTOL Electric Vertical Takeoff and Landing

FVM Finite Volume Method

GARTEUR Group for Aeronautical Research and Technology in Europe

HLP High Lift Propeller

HMB3 Helicopter Multi-block Solver

MUSCL Monotonic Upwind Scheme for Conservation Laws

NASA National Aeronautics and Space Administration

NTRS NASA Technical Reports Server

OSPL Overall Sound Pressure Level

OTW Over-The-Wing

PIV Particle Image Velocimetry

RANS Reynolds-Averaged Navier–Stokes Equations

RB Resolved Blades

RPM Revolutions Per Minute

RRF Rotating Reference Frame

SAS Scale Adaptive Simulation

SCEPTOR Scalable Convergent Electric Propulsion Technology Operations Research

SPL Sound Pressure Level

SST Shear Stress Transport

TMP Tip-Mounted Propeller

TMS Time-Marching Simulation

UAV Unmanned Aerial Vehicle

US United States

VTOF Vertical Take-Off and Landing

WIPP Wingtip-mounted Propeller Workshop

Chapter 1

Introduction

1.1 Motivation

A new era of aerial transportation is rapidly emerging under concepts such as On-Demand Mobility (ODM), Urban Air Mobility (UAM), Air Taxi Operations, and Advanced Air Mobility (AAM). While helicopters were the first practical aircraft capable of vertical takeoff and landing, with complex rotor systems and control mechanisms, the focus of modern aerial mobility has evolved. Over recent decades, attention has shifted toward enhancing cruise efficiency, increasing flight speed, reducing noise and vibration, and improving overall safety and sustainability [1, 2]. Among the most promising technological advancements enabling these goals is the development of novel configurations based on distributed propulsion (DP). These configurations offer significant potential to optimise aerodynamic performance, enable better load distribution, improve redundancy and control, and enhance overall propulsive efficiency. As future air mobility systems move beyond conventional VTOL paradigms, the integration of distributed propulsion architectures is poised to play a central role in achieving quieter, more efficient, and scalable next-generation aircraft. In addition to performance considerations, future platforms must also address key challenges related to noise, safety, automation, energy storage and utilization, manufacturing, and system integration.

In recent years, many projects have been proposed and conducted in AAM aircraft and operations. [3] The NASA Revolutionary Vertical Lift Technology (RVLT) project is investigating

UAM VTOL aircraft operations [2], designs [4, 5], investigating approach [6], associated technology development [7], baseline assumptions [8], noise [9], the tiltwing concept [10], and practical quiet conceptual design [11] that can guide the VTOL aircraft development for the emerging aviation markets. Different reduced-emission rotorcraft concepts were proposed, implementing advanced drive system materials and approaches. [5] Vehicle classes are defined where different configurations are adopted based on the requirements of payload, range, rotor radius, disk loading, power, etc., and each class of design promises a different level of emission reduction. There is a 30% emissions reduction achieved using the coaxial rotors for the relatively low payload requirement concepts. [3] Furthermore, implementing advanced turboshaft engines and multiple rotors achieved 65% reduction of emissions. [3] These proposed vehicles incorporate novel features such as advanced propulsion architectures, including distributed and tip-mounted propulsion, and more efficient, quieter rotors. Therefore, it is essential to investigate these innovative designs, which serves as a primary motivation for this work.

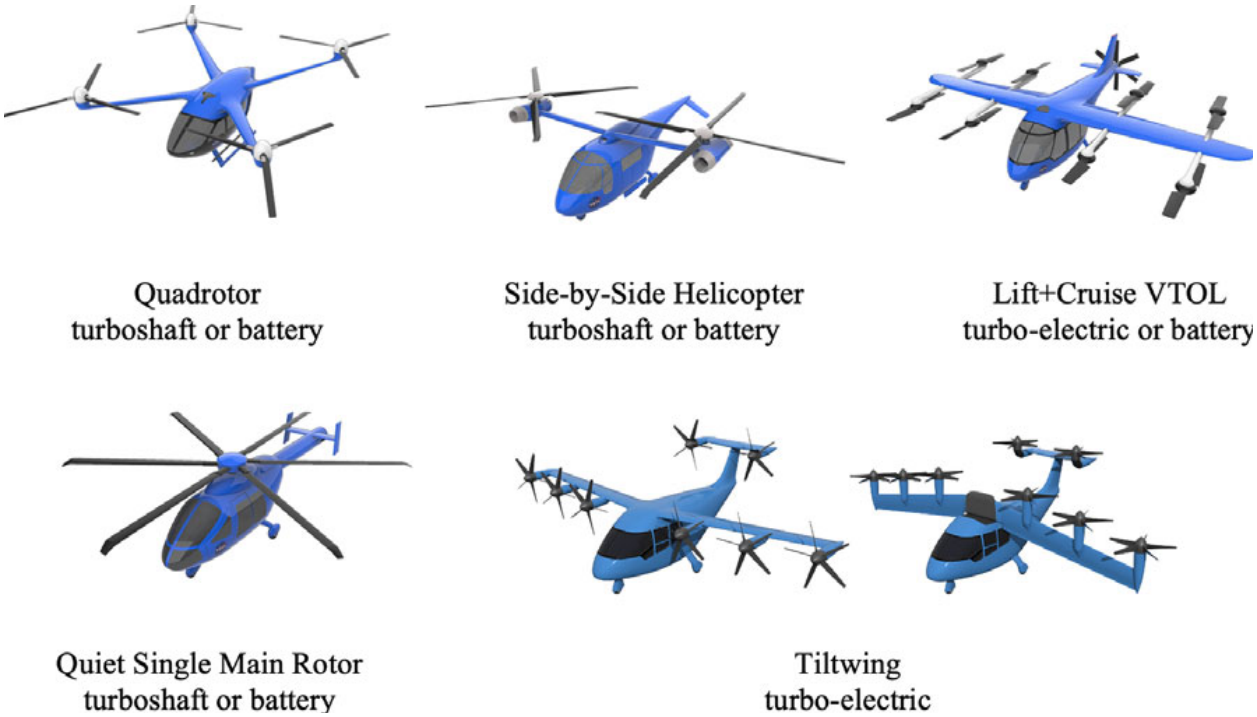

Figure 1.1: UAM aircraft designs: six occupants (1,200lb), 75nm range [7, 9, 10].

Proposed configurations include quadrotor aircraft [7], side-by-side aircraft [7], lift+cruise aircraft [7], a quiet single-main rotor helicopter [9], and a tiltwing aircraft [10] are shown in Fig-

ure 1.1. Their designs implemented turbo-electric propulsion and can perform different missions. Furthermore, those designs are generic and intentionally have a different appearance and design detail from prominent industry arrangements. The aim of these concepts is to provide common configurations and communication of the AAM research for examining the designs, analysis tool development, technology trade studies, performance, noise emissions, and modelling of operations. The common configurations with proposed advanced technologies can be used for studies in propulsion efficiency, aerodynamic interactions, acoustics, flight dynamics, propulsion safety, reliability, crashworthiness, and more disciplines. The concepts are also widely shared and documented and aim for realistic performance. There are computational tools available for rotorcraft analysis and design from NASA [3]. These tools are also capable of noise prediction; however, they are primarily suited for preliminary studies due to limitations in required input data, computational expense, fidelity, and the overall research effort involved. This highlights the necessity for accurate noise prediction, which forms one of the central motivations of this work.

The NASA X-57 Maxwell aircraft is shown in Figure 1.2 [13] [14] and incorporates 12 small electrically driven propellers distributed along the wing in front of the leading edge, along with 2 large propellers mounted at the wingtips, compared to the traditional configuration of the Tecnam P2006T with isolated propellers installed in each semi-wing. The design featured in X-57 reduced the original wing area, drag, and wingtip vortex at cruise, and a significant improvement of lift at low speeds. However, the interactional aerodynamic effects have not been quantitatively assessed in the public literature, and it is crucial to investigate both the aerodynamic performance and noise reduction potential of distributed propulsion systems. This forms another key motivation for the present work.

Previous investigations in distributed propulsion systems transitioned from conventional tractor propulsion systems to over-the-wing distributed propulsion (OTWDP) systems, gradually increasing the fidelity from low-order models to steady-state actuator disk simulations, and experimental methods. However, it is rare to find studies examining conventional and OTW propulsion systems, with equivalent performance at high load conditions. The benefits of the OTW configuration and OTWDP system, when directly compared to equivalent conventional tractor configura-

(a) Tecnam P2006T [12]

(b) X-57 Maxwell [13, 14]

Figure 1.2: The traditional Tecnam P2006T rotorcraft and the new X-57 Maxwell design.

tions, remain unexplored and not quantified. Furthermore, the impact of pylon structures in OTW configurations has been overlooked in previous studies, both with low-order simulations, and experiments. Pylon structures not only create a blockage effect for the propeller but also add more surface area, increasing the drag of the entire propulsion system. Additionally, these designs were not studied as part of a distributed propulsion system, either via experiments or simulations. As a result, future distributed propulsion designs may need further research. This thesis aims to provide computation and assessment of tractor, OTWDP and tip-mounted propeller (TMP) systems at high-performance conditions.

1.2 Background and Literature Survey

A literature survey was conducted to identify AAM/eVTOL designs with different propulsion systems installed. Different propulsion designs, and their aerodynamic and aeroacoustic performance are with the aims and objectives of the present research. The survey involved four databases: Scopus, Web of Science, Aerospace Research Central-American Institute of Aeronautics and Astronautics (ARC-AIAA), and the National Aeronautics and Space Administration Technical Reports Server (NASA-TRS). In addition, conference proceedings of the Vertical Flight Society (VFS) and European Rotorcraft Forum (ERF) were also reviewed. Various sets of keywords were used for the searches, and are presented in Table 1.1. Ducted propulsors and their thrust vectoring, other flow control methods and acoustic control methods such as acoustic liners, and different propulsion configurations were also reviewed to have a better understanding of the background of rotorcraft propulsion systems. The present research is then focused on the different propulsion systems based on the findings of the survey, such as the Wingtip Mounted Propeller (WIPP), distributed propulsion systems, and the noise reduction from such multirotor systems.

1.2.1 Recent Rotorcraft Propulsion System Development

Over the last few years, VTOL aircraft developed rapidly from abstract concepts to emerging operational vehicles. However, many challenging aspects of these novel designs have been identified

Table 1.1: Literature survey keywords and findings from five databases. A total of **143** articles and conferences in proceedings were collected.

Keywords	Scopus	Web of Science	AIAA	NTRS	Total
Acoustic FWH Method	9	1	9	6	25
Adjoint Optimisation Noise	6	3	20	6	35
Vibration Noise	3	1	3	7	14
Noise Prediction Validation Reudction	2	3	3	3	11
VTOL Duct Propulsion	7	10	3	8	28
Review Noise Aeroacoustic	5	1	3	20	29
Boundary Layer Ingestion Inlet (active flow control)			4	2	6
Helmholz Resonator	1	2	2		5
Thrust Vecotring	1	2	2	4	9
Wingtip Mounted Propeller (WIPP)			11		11
Distributed Propulsion System (DPS)			8	1	9
Airframe Integration	1				1
Acoustic Liners Modelling	1		4		5
Inlet flow control for VTOL		1	2	1	4
Circulation Control				1	1

by designers and government agencies through their development. According to the report "Urban Air Mobility Noise: Current Practice, Gaps, and Recommendations" published in 2020 [15], a demand for experimental data for isolated, installed, and multirotor configurations was suggested to improve the validation of predictive models and to better understand scattering of noise. Unlike traditional rotorcraft and propellers, current VTOL designs involve multiple open and ducted propellers with lower loading, tip Mach numbers (M_{tip}), and acoustic shielding. Due to these changes, there are different aerodynamic interactions, and the complex broadband noise sources are now the primary emphasis instead of the tonal and impulsive noise sources that predominate the acoustic spectra of conventional rotorcraft [15].

Ducted propellers show promising performance and acoustic benefits, and have been used as novel propulsors, e.g., the Airbus E-Fan, CityAirbus, and Bell Nexus eVTOL. Extensive experimental tests on ducted propellers were conducted by NASA [16] [17] [18], and started with the development of the Bell X22 and the Doak VZ4D aircraft. Recently, Zhang and Barakos conducted comprehensive computational works [19] [20] [21], further showing that the ducted propeller is a promising candidate for eVTOL propulsors at low advance ratios. However, the ducted propeller becomes less efficient than the open propeller at the aircraft speeds due to the drag of the

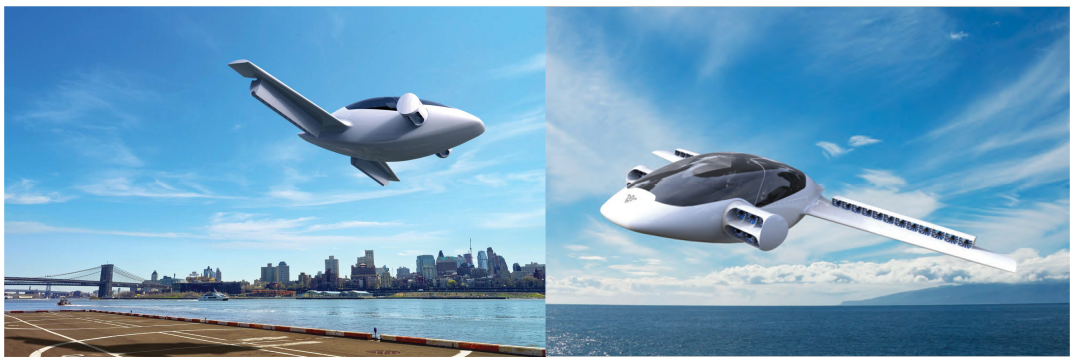

(a) Lilium Jet at hover flight

(b) Lilium Jet at cruise flight

(c) US DARPA XV-24

Figure 1.3: Various AAM designs with distributed propulsion systems, ducted on shown examples.

duct. A much higher nose-up pitching moment was also observed, compared to the open propellers at crosswinds [20]. In terms of the acoustic benefit, their work reported 5 to 10 dB reduction by ducting, in the near and far field noise.

Some other early conceptual studies on novel propulsion systems suggest that DP systems appear to be an attractive and realistic solution for a wide range of aircraft configurations offering different operational possibilities while addressing environmental and energy concerns. Several distributed electric ducted propulsion designs have been proposed, including the Lilium Jet and XV-24, as shown in Figure 1.3, utilises multiple electric ducted fans [22]. In addition, various AAM concepts with open propellers/rotors have been proposed and developed by companies like Joby Aviation in California, US (S4 aircraft) and Vertical Aerospace in Bristol, UK (VX4) as shown in Figure 1.4. Most recently, the S2 aircraft of Joby Aviation has been delivered to the U.S. Air Force and conducted multiple flight tests [23].

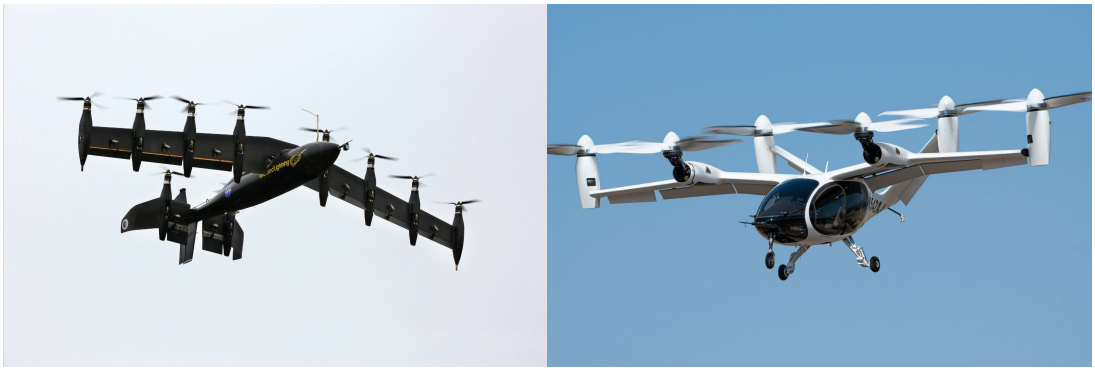

(a) AAC hercules UAS (b) Joby aviation hexa tiltrotor S4

(c) Volocopter VC200 (d) Vertical aerospace VX-4

Figure 1.4: Various eVTOL employ open rotors.

1.2.2 Distributed Propulsion System

Since the last decade, several studies have shown that hybrid-electric, distributed propulsion (DP) can reduce the impact on pollution [24, 25]. However, such complex configurations bring more complex flow phenomena and aerodynamic interactions.

One of the early studies on DP was conducted in 2003 by Ko et al. [26], who assessed the potential advantages of the DP concept. The central idea behind improving the propulsive efficiency involves accelerated air from the trailing edge of the upper surface covering part or the entire span of the wing due to the installed propulsive units. Their study quantified the influence of DP in a blended-wing-body (BWB) multidisciplinary optimisation exercise. Minimising the takeoff gross weight and comparing it to a conventional BWB aircraft, the newly designed aircraft was found to be 4.4% lighter and required 2.7% less fuel. Additionally, they state that the DP eliminated the need for traditional control surfaces and offered a reduction in perceived noise.

In a subsequent study in 2010, Kim [27] discussed various DP systems for subsonic and supersonic vehicle configurations, including the NASA N3-X, Empirical Systems Aerospace ECO-150/250, MIT H3.1, and GIT [28]. These conceptual studies identified several benefits of DP systems, such as reduced fuel consumption by ingesting the thick boundary layer flow and filling in the wake generated by the airframe with the distributed thrust stream, achieving high span-wise lift, by distributing propulsors. Additional benefits were reduced noise through airframe shielding and structural integration, eliminating control surfaces through thrust vectoring, allowing for high production rates, and easy maintenance of small and lightweight propulsors.

1.2.2.1 Early computational works

In 2015, Wick et al. [29] of the Air Force Research Laboratory (AFRL) and Lockheed Martin investigated the integration and benefits of distributed propulsion systems for future commercial and military vehicles. In addition to the power benefits of DP systems [30], their study also showed the integration benefits of the DP systems. An early configuration optimisation study, as in Figure 1.5, showed that the over-wing nacelle propulsion airframe integrations could potentially improve aerodynamic efficiency by 5% compared to conventional under-wing nacelle configurations at transonic cruise. They used the USM3D [31] flow solver and performed RANS simulations with the one-equation Spalart-Allmaras turbulence model [32]. Their solver could generate prismatic viscous layers near the walls combined with an inviscid outer volume mesh. The resulting mesh was smooth with full anisotropic stretching on the surface, layer, and volume. In addition, local refinement was applied to specific regions.

In 2-D, the aerodynamic efficiency of engine placement, size, propulsive area, and thickness was investigated. [29]. More than 2000 N-S CFD solutions were performed, and three 2-D distributed propulsion concepts were then selected for further investigation, which were the Lower trailing-edge (TE), Upper TE, and embedded configurations. For the Lower TE concept, an inlet at cruise could slow the air down when the capture ratio (mass flow rate divided by the freestream flow through the equivalent area) was less than one, which in turn, created high pressure and generated additional lift. It can be used as a flap-like shape in 3-D to control thrust angle and create

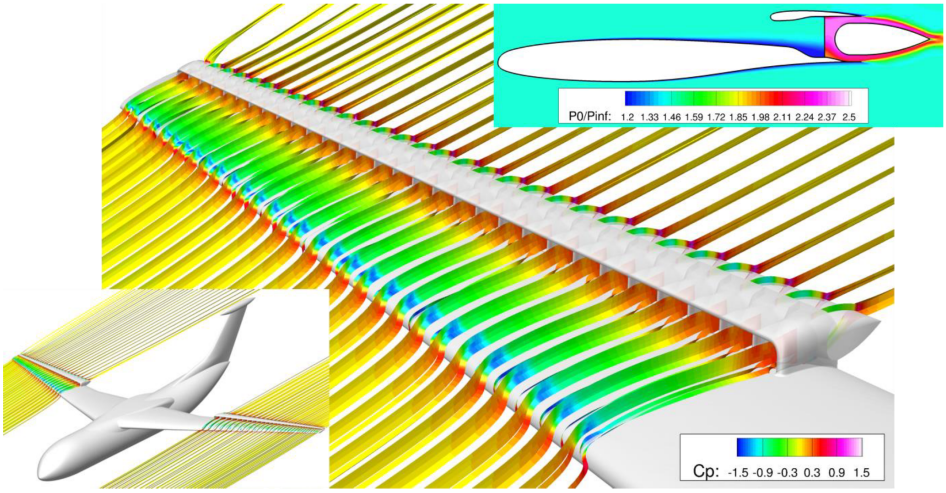

Figure 1.5: Integrated distributed propulsion study of the Lockheed Martin company, and the Air Force Research Laboratory. [29]

additional lift at low speeds. The concept of Upper TE is mounting the propulsor on the upper side of the wing at the trailing edge to help accelerate the flow over the upper surface of the wing, and expand suction regions. The final concept presented in the study was an embedded concept; the leading edge of the aerofoil was converted into an inlet. This design enhances propulsion efficiency by enlarging the effective propulsive area through an expanded high-pressure region. Moreover, it combines two high-pressure regions into one, and further reduces the wetted area.

These early conceptual studies on novel propulsion systems suggest that DP systems appear to be an attractive and realistic solution for a wide range of aircraft configurations, offering different operational possibilities, while addressing environmental and energy concerns in the context of the growing demands of aviation.

1.2.2.2 Recent prototypes and experimental works

Given the promising advantages of distributed propulsion systems, a range of innovative designs have emerged in recent years to further explore and optimise their performance. For instance, the NASA X-57 Maxwell aircraft, developed by ESAero, incorporates 12 small electrically driven propellers distributed along the wing in front of the leading edge, and 2 large propellers mounted at the wingtips. [13] [14]. The Aurora XV-24 utilises multiple electric fans for VTOL capability

and for achieving high cruise speeds [22]. With the emergence of the ”air taxi” market, and the potential advantages of DP systems, various VTOL aircraft concepts have been proposed, or are under development by companies like Joby Aviation[33] in California, US (S2 aircraft), Lilium Jet[34] in Munich, Germany, and Vertical Aerospace [35] in Bristol, UK (VX4). Most recently, the S2 aircraft of Joby Aviation [33] has been delivered to the U.S. Air Force and is currently undergoing assessment.

Transition from vertical to horizontal flight and back is known as flying through the transition corridor. The NASA Langley Research Centre [36] have conducted flight tests for a variety of VTOL configurations with distributed electric propulsion, in wind tunnel to better understand transition, and help improve aircraft safety in the complex transition corridors. The Langley Aerodrome 8 (LA-8) is shown in Figure 1.6, and features a high-risk/high-reward tandem tilt-wing, and partially deflected slipstream. After wind tunnel tests, all aerodynamic data was documented, including the longitudinal, lateral, and directional force and moment aerodynamic coefficients, at different phases of flight. The first major finding was that longitudinal and directional stability were significantly influenced by the blown wing and led to the vehicle becoming unstable in the longitudinal (pitch) and directional (yaw) axes at cruise conditions. Another major finding was that, with constant-pitch propellers, a trade-off emerges between achieving static stability and attaining a favourable trim point without the use of control surface deflections. For lift, it can be created from propellers, wings, and lift from wing sections blown by propellers. Suggesting the contribution from each component was different and needed to be determined at different flight configurations for the future work.

1.2.2.3 Single propeller system

The aforementioned work also suggests that understanding the propeller performance envelope beforehand is crucial for the vehicle-level installed investigation. Litherland et al. [37] reported the design and investigation of a high-lift propeller for the NASA X-57 ”Maxwell” distributed electric aircraft. In the X57, twelve fixed-pitch, high-lift propellers were mounted on the wing’s leading edge to increase lift at low speeds. They were folded at high speeds to reduce drag. The blade has

Figure 1.6: LA-8 UAS in the 12-foot low-speed tunnel. [36]

chord, twist, skew, and rake distributions in the radial direction that produce constant induced velocity at the downstream of the propeller. Predictions of thrust, moments, power consumption, and model accuracy were conducted to determine the aircraft performance and the flight envelope. In addition, these performance prediction models were validated by a series of full-scale wind tunnel tests, conducted at the NASA Langley Research Centre Low-Speed Aeroacoustic Wind Tunnel. Apart from the validation, the experiments also included the adverse operating conditions and the accuracy of the experimental setup. There were two sets of the same propellers that were manufactured and named as right- and left-hand propellers for the wind tunnel tests. The results indicated that the right-hand propeller had lower torque and thrust than the left-hand propeller, at a given speed. Furthermore, a higher tonal noise was measured from the left-hand propeller. The authors claimed that different material properties during propeller production caused the tonal noise difference between right- and left-hand propellers. High-speed images showed no blade oscillations or instabilities from the operated propeller at any tested conditions. Based on validation and per-

formance comparisons, this study aimed to improve the X-57 high-lift propeller prediction models and obtain the propeller's acoustics. Two potentially adverse low rotational speed conditions were then identified from the dynamic events and thus suggested as ones that should be avoided during the aircraft operation.

1.2.2.4 Multirotor system

The multirotor system was also seen as a key feature of these novel full vehicle designs. Previous studies investigated tandem rotors at hover (zero forward velocity) or near-zero forward flight conditions. The performance of the rotors was affected when placed close together, without overlap, and the thrust droped by 2% - 8%[38] [39]. In addition, the interaction leads to unexpected unsteady loading on the propeller blades[38, 40]. It has also been reported that the sideslip was increased when the propeller was in forward flight conditions[41]. Apart from the edgewise effect, multi-rotors also have streamwise development and change the aerodynamic loads on downstream surfaces such as flow control devices, wings, or fuselage. In addition, it was noticed that the interaction between vortical structures in the slipstream leads to the blade wake and tip vortices breaking down earlier than usual[38]. The third effect of the rotor-rotor interaction was a different noise generation mechanism. Placing the two rotors within a short separation distance increased the noise level compared to the isolated rotors [40] [42]. The noise directivity pattern of the system was also changed[43], but this could be manipulated by regulating the blade phase angles, which was termed the synchrophasing technique[44]. However, the syschrophasing technique remains challenging if the rotational speed and blade phase angles of the propellers are not properly controlled[45, 46]. The development of phase detection and control using encoders makes the synchrophasing technique possible[47, 48].

1.2.2.5 Tractor propeller installation

Considering there is also significant aerodynamic interaction between propellers in the distributed propulsion system, de Vries [49] investigated a three-propeller configuration as shown in Figure 1.7. The study included the performance, flow-field characteristics, and noise emissions. Their

experimental results showed that in a three-propeller configuration, there was a 1.5% decrease in performance observed at the middle propeller. This penalty was found to be insensitive to the rotation direction and to the relative blade phase angle. Additionally, the slipstream from adjacent propellers induced local loading variations on the propeller disk, ranging from 5% to 10% of the average disk loading.

In addition, noise measurements [49] presented in Figure 1.8 indicated that interactions in distributed propellers altered the tonal and broadband noise waveforms compared to a single installed propeller. Distributed propellers have a higher Sound Pressure Level (SPL) in the spectrum apart from the 5th Blade Passing Frequency (BPF). Reducing the propeller separation distance significantly increased tonal noise at odd numbers of BPFs. Furthermore, the study explored an active control method, changing the relative blade phase angles between propellers, to effectively modify the noise directivity pattern of the DP system. A clear noise reduction, represented by ΔSPL at the region beneath the propulsion system, was seen in Figure 1.9, especially at the relative blade phase angle difference $\Delta\theta = 40^o$ and $\Delta\theta = 50^o$. The study, further calculated the mean phase-averaged SPL_{mean} from the experiments that involved the distributed propellers in different rotation directions, separation distances, and relative phase angle differences, as shown in Figure 1.10. It was shown that the larger propeller separation distance ended up resulting in the lowest SPL_{mean}. Regarding the rotation direction, co-rotating propellers were quieter than the counter-rotating propellers. Considering the overall effect from the investigated configuration, it was concluded that the quietest configuration was the distributed propulsion system with a 1.0 d/R propeller separation distance, co-rotating, and a 30^o relative blade phase difference. Most importantly, this work concluded that the noise from the propellers in close proximity was higher than three times the isolated propeller noise levels on the wind tunnel floor, but when the propellers were placed far from each other (d/R = 1.0), the noise was comparable to the summation of three individual propellers.

In the most recent work, De Vries et al.[50] expanded the OTW DP system from component to aircraft level to assess its continued applicability. Preliminary sizing was conducted based on a partial turboelectric regional passenger aircraft and compared its performance with a conventional

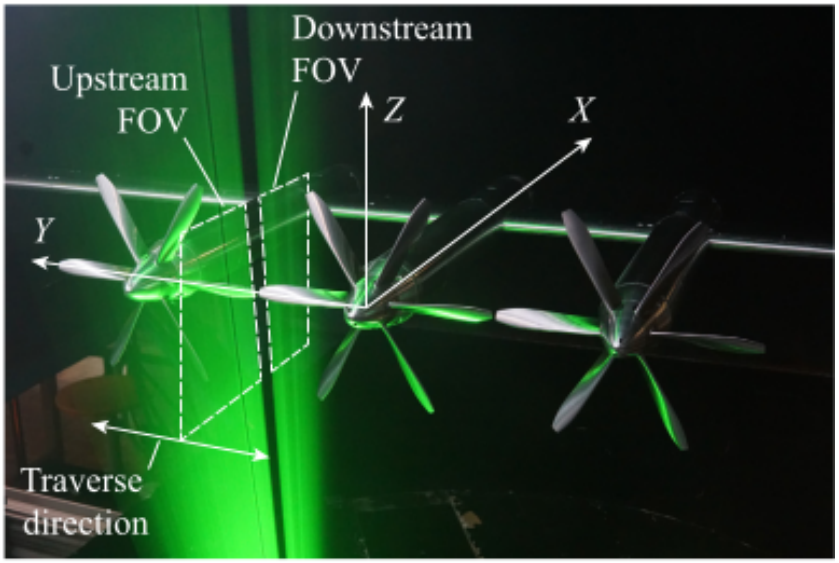

(a) Position of the fields of view (FOV) in the PIV setup

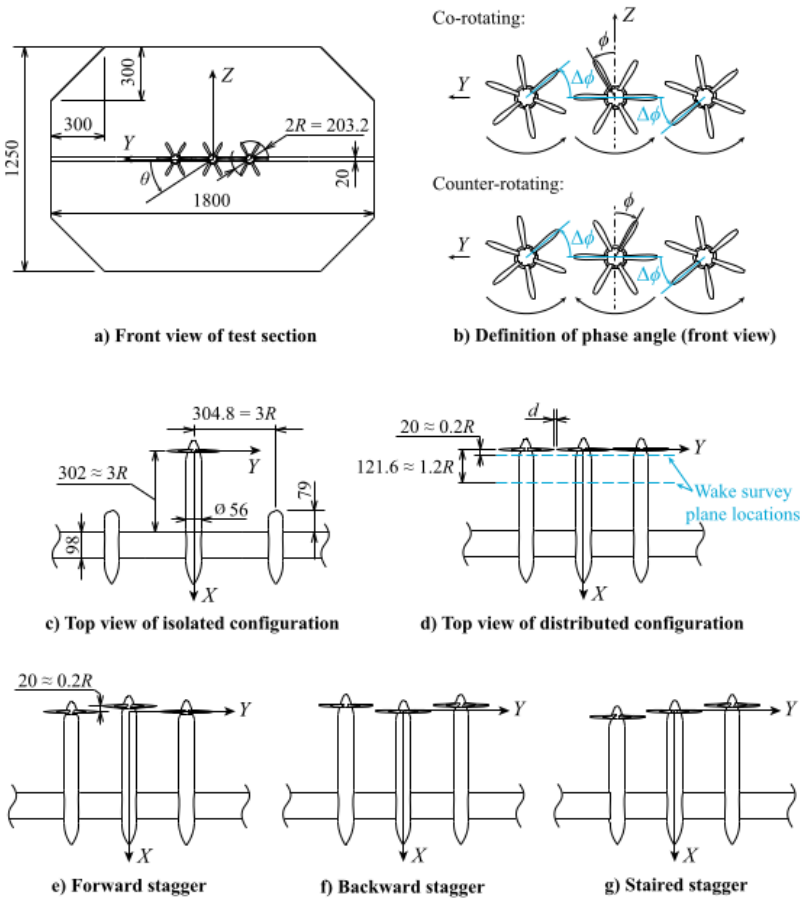

(b) Overview of test setup, indicating main dimensions, reference systems, and configurations. Dimensions in mm.

Figure 1.7: Visualisation of experiment setup and test matrix setups [49]

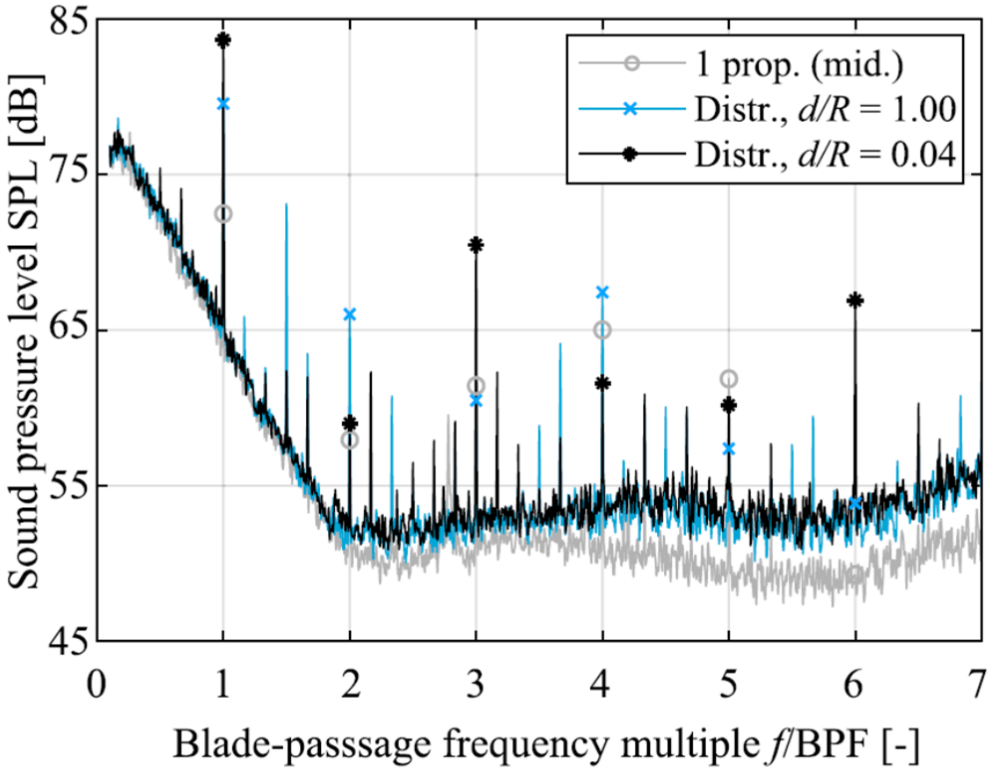

Figure 1.8: Pressure spectra recorded on the wind-tunnel floor beneath the propellers (X/R = 0,Y/R = 0). Co-rotating, BPF = 1107 Hz, J=0.8, $\Delta\theta = 0^o$. [49]

twin-turboprop aircraft. Experimental data was used to validate a low-order computational method to study an unducted OTW DP system. At cruise, for an aircraft with 53% of its wingspan covered by the OTW DP system, the numerical method suggested a 45% improvement in local lift-to-drag ratio at a cost of a 12% reduction in propeller efficiency. The coupling between the aerodynamic performance of the propeller wing and the aircraft system level was found to increase the propulsive efficiency of the aircraft by 9% over a 1500 nautical mile mission. Additionally, this work considered the increase in takeoff mass due to the electrical drivetrain and the reduction in fuel weight due to the OTWDP system, resulting in a 5% reduction in the overall energy consumption.

1.2.2.6 Propeller installation location

Another important question is which configuration needs to be adopted by novel rotorcraft. Müller et al. [51] investigated three different configurations with the propeller installed in tractor, over the wing, and channel wing configurations as shown in Figure 1.11. The study of these three designs

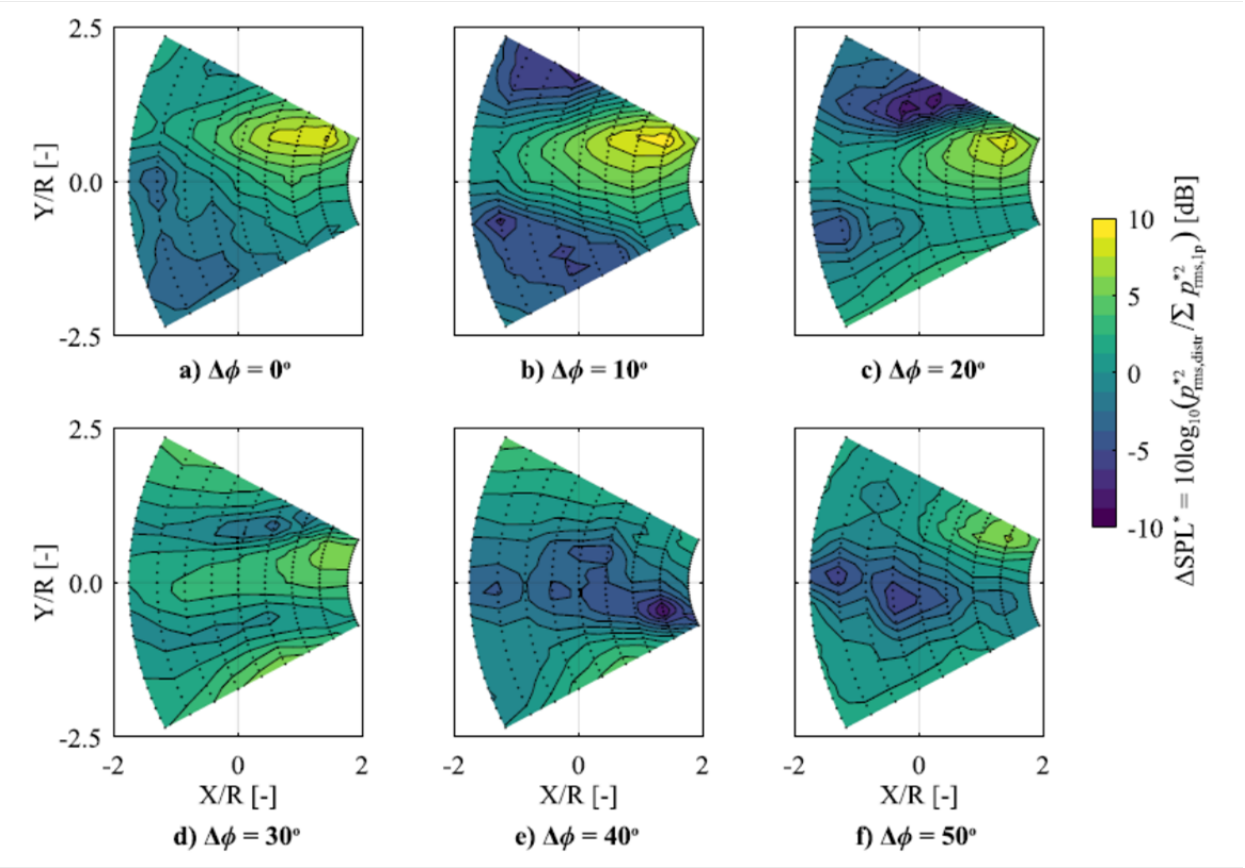

Figure 1.9: Change in SPL distribution on the wind tunnel floor (Z/R=-6.15) relative to the summation of three (incoherent) individual propellers. Dots indicate measurement locations. Co-rotating, d/R=0.04, J=0.8. [49]

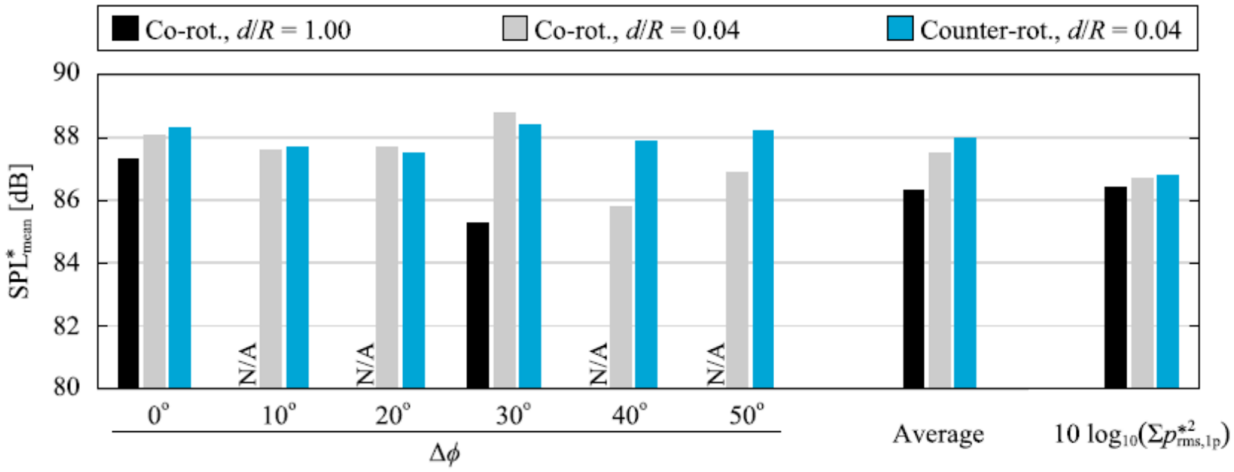

Figure 1.10: Mean phase-averaged sound-pressure level, SPL mean [dB], for different configurations and relative phase angles. "N/A" indicates the corresponding phase angle was not measured. [49]

assessed their climb performance using actuator disk models and steady RANS simulations. Given the interaction between the blown flap from the high lift configuration and the propeller, the conventional tractor propeller resulted in significant increments in lift and drag due to the slipstream. For the over-the-wing design, lift and drag of the wing were reduced compared to the tractor configuration, but the lift-to-drag ratio and propulsive efficiency were further improved. Although the channel wing configuration (see Figure 1.11(c)) provided moderate lift gains, a lower nosedown pitching moment was noticed due to the location of the thrust vector closer to the centre of gravity. Apart from the over-the-wing configuration gains, mostly in lift-to-drag ratio, inhomogeneous inflow at higher velocity was observed, resulting in oscillating blade loads and reduced propeller efficiency.

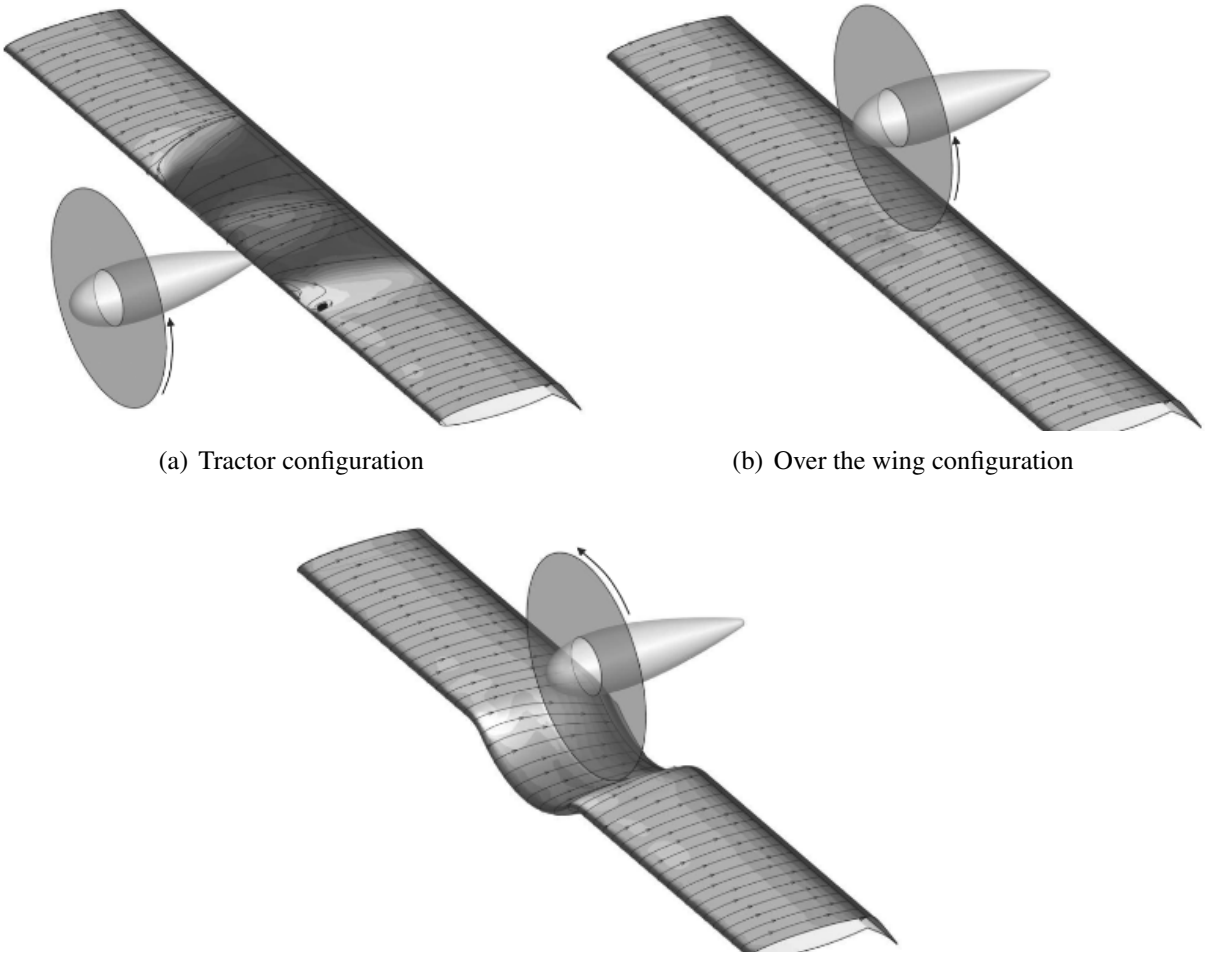

(a) Tractor configuration

(b) Over the wing configuration

(c) Channel wing configuration

Figure 1.11: Propeller installed in tractor, over the wing, and channel wing configurations. [51]

1.2.2.7 Over-the-wing propeller installation

Later, motivated by the performance improvement from the OTW design, Marcus [52] extends the OTW study into the DP systems, employing a combination of experiments and low-fidelity numerical tools. The low-fidelity numerical tools encompassed non-uniform inflow and blade-element models for the propeller, a panel method for the wing, and a vortex lattice model for the propeller slipstream. After validating the numerical tool using wind tunnel data, the effects of the axial position and diameter of the propeller were investigated. The results revealed that the optimal axial propeller position was near the trailing edge of the wing. In that location, the lift produced by the wing was increased by 8% in cruise, and 3% in high-lift configurations. Additionally, reducing the propeller diameter while maintaining a constant thrust coefficient at the same location also yielded performance benefits.

Studies have shown the performance benefit in the OTW design, but the associated flow physics have not yet been understood. De Vries et al. [53] then conducted a comprehensive wind tunnel investigation into the OTW propeller and its interaction with the wing boundary layer. Their experiments involved placing the OTW propeller above the hinge line of the wing. The experimental setups and their geometry, flat-wall and flapped configurations, are shown in Figure 1.12. Measurements were carried out with and without axial pressure gradients. In addition, time-averaged and unsteady interaction effects were quantified by using phase-averaged velocity, vorticity pressure coefficient, and unsteady pressure coefficient root-mean-square contours. Their experiments involved placing the OTW propeller above the hinge line of the wing. Measurements were taken with and without axial pressure gradients, encompassing time-averaged and unsteady interactional effects. Their work revealed that positioning the propeller over the wing surface induced flow separation, where the propeller slipstream did not follow the flap surface shown in Figure 1.13, and an adverse pressure gradient on the wing as shown in 1.14, which was linearly proportional to the thrust.

The authors attributed this to the contraction of the slipstream leading to a deceleration of the flow near the surface of the wing. Additionally, the propeller-induced fluctuations in the surface pres-

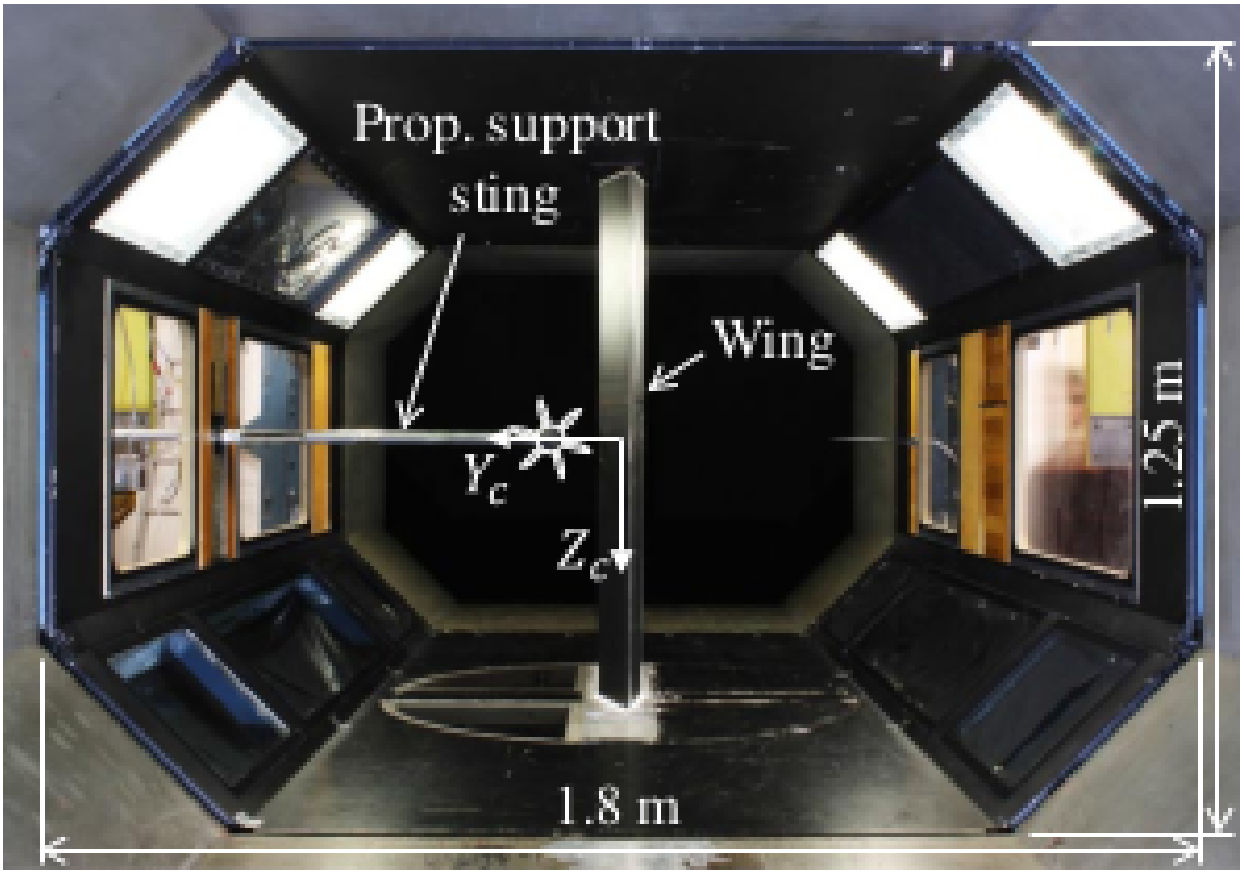

(a) Test section (viewed from behind)

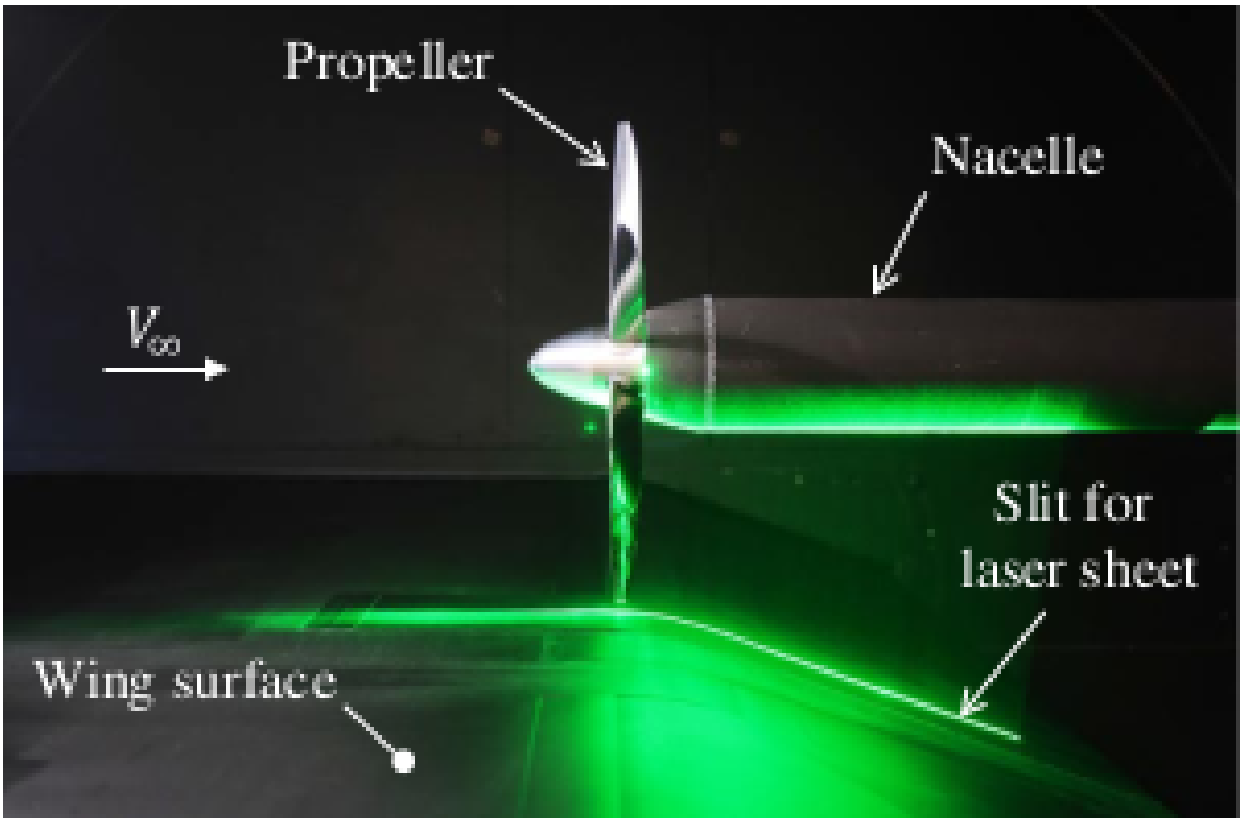

(b) Close-up of propeller (viewed from below)

Figure 1.12: Experimental setups for the OTW configuration in the wind tunnel [53].

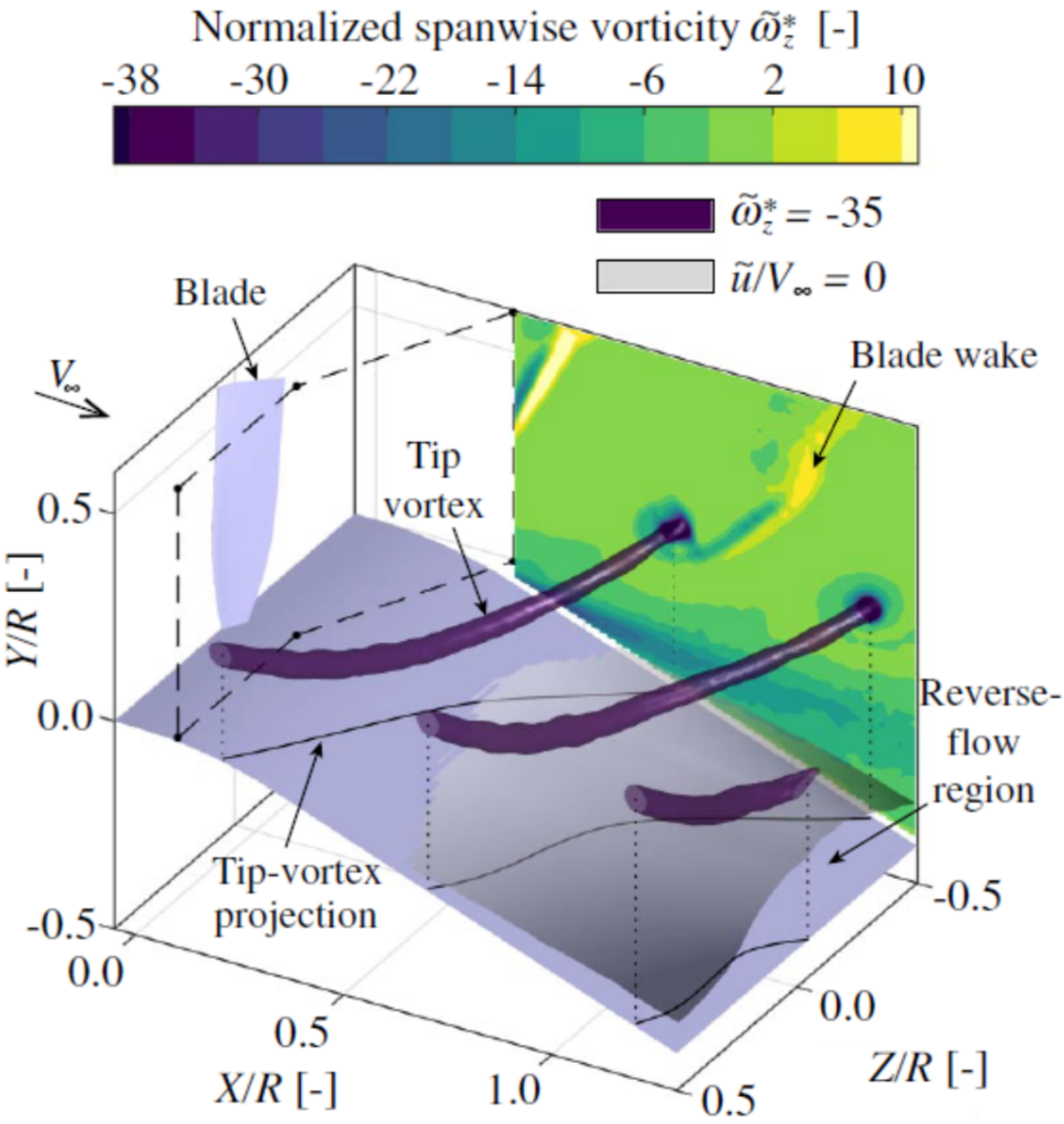

Figure 1.13: Phase-averaged vorticity distribution downstream of propeller with flap deflected, including an axial-velocity isosurface that delimits the region of reverse flow [53]

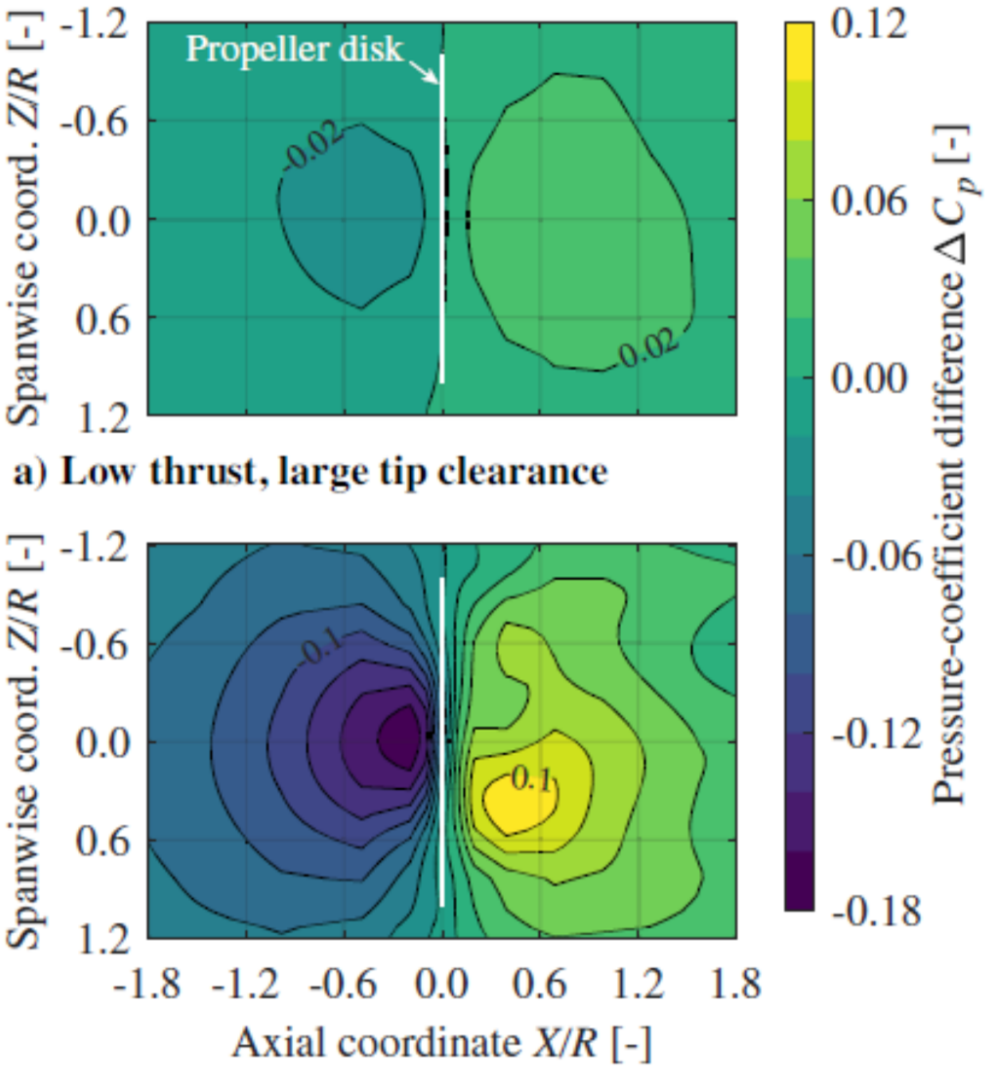

Figure 1.14: Pressure distribution induced by the propeller on the wing surface in flat-wall configuration. Measurements performed at a) V_∞ = 40m/s, C_T=-0.2, and ε/R = 0.14; b) V_∞ = 20m/s, C_T=0.35, and ε/R = 0.037 [53].

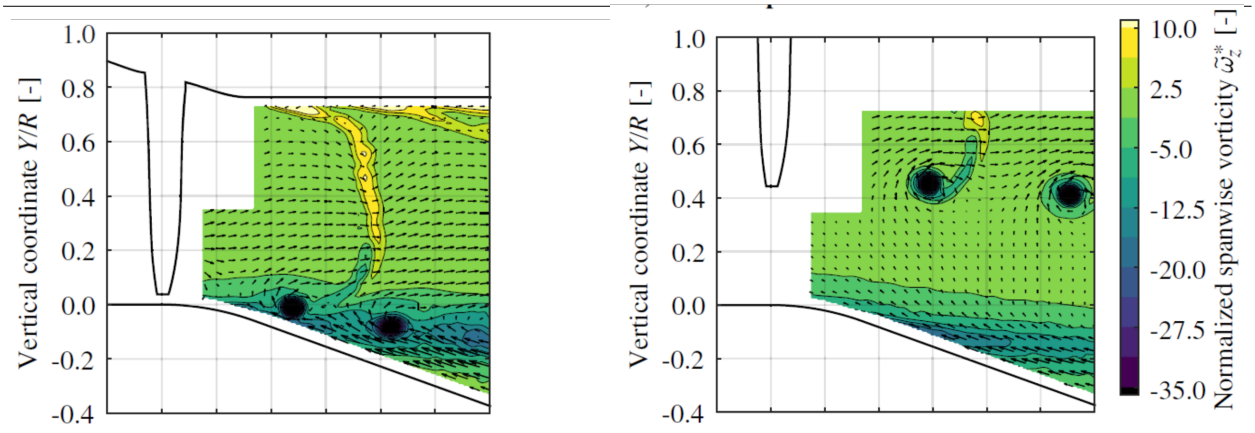

(a) Baseline position

(b) Increased tip clearence (Tip clearence/Propeller radius=0.044)

Figure 1.15: Phase-averaged spanwise vorticity distribution, and in-plane propeller-induced velocity vectors, at three propeller positions. [53]

sure, and contributed to an increase in time-averaged pressure due to outflow deceleration. Also, they explored different propeller locations as shown in Figure 1.15 and concluded that increasing the tip clearance did not effectively alleviate flow separation. Conversely, positioning the propeller half a radius upstream of the hinge line, generated a Coanda effect, which caused the flow to attach to the flap surface. This effect led to a noticeable increase in lift for the entire configuration.

1.2.2.8 System-level investigation

In more recent studies in the literature, it is rare to see the investigation of the distributed propulsion system work at the aircraft system level, but it is crucial for the future works. To this end, De Vries et al. [54] proposed a preliminary sizing method for hybrid-electric DP aircraft. Their work takes into account the powertrain architecture and the associated effects of integrating propulsion systems with the airframe, making it suitable for the conceptual design process of hybrid-electric aircraft. By comparing three powertrain architectures, it was observed that while the energy consumption increased by 3% when implementing the DP system, there was a significant increase in wing loading, and a 6% improvement in lift-to-drag ratio at cruise.

1.2.3 Wingtip Mounted Propeller

Propellers are more efficient than other propulsion techniques at subsonic speeds [55]. However, the installation of propellers on the airframe can significantly influence the overall aircraft performance. Notably, wingtip-mounted propellers are a promising configuration for reducing induced drag through favourable wake interactions. This is particularly true when the propeller rotation is opposite to that of the wingtip vortex in a tractor configuration, as this setup can mitigate the induced drag [56, 57, 58]. In a pusher layout, where the propeller counter-rotates relative to the wingtip vortex, the swirling flow induced by the wingtip can lead to reduced shaft power [58, 59, 60]. However, the tip-mounted propeller configuration also has drawbacks, including the adverse effects of a highly loaded wingtip, the significant weight of the engine, inertia loads, and a large yawing moment arm during one-engine-out scenarios.

Given the potential of the wingtip-mounted propulsion system for delivering increased aerodynamic efficiency, the workshop for integrated propeller prediction (WIPP) was established. Helden Aerospace Corporation, Empirical Systems Aerospace, and NASA together conducted wingtip-mounted propellers to investigate the propeller-wing interactions in the NASA Lockheed Martin Low-Speed Wind Tunnel (LSWT). Their work collected a wide range of data under different conditions and attracted great interest in validating computational fluid dynamics (CFD) codes. Two primary objectives were achieved through experiments. The first was to produce an open-powered database for CFD validation of propeller effects in a wingtip-mounted configuration. The second was to study the tip-mounted propeller efficiency due to induced drag reductions by rotating the propeller opposite the wingtip vortex direction. The distributed report among the project partners documented the overall effort, wind tunnel model design, the test matrix, and their data.

Motivated by the WIPP and their available test database, Baruzzi et al. [62] examined the same configuration using four different numerical models with progressively increasing fidelity and compared their cost and accuracy. The study first compared the FENSAP Actuator Disc Model (ADM) and the Virtual Blade Model (VBM). FENSAP ADM used the Spalart-Allmaras turbulence model, and Fluent VBM used the $k-\omega$ SST turbulence model with an intermittency transition.

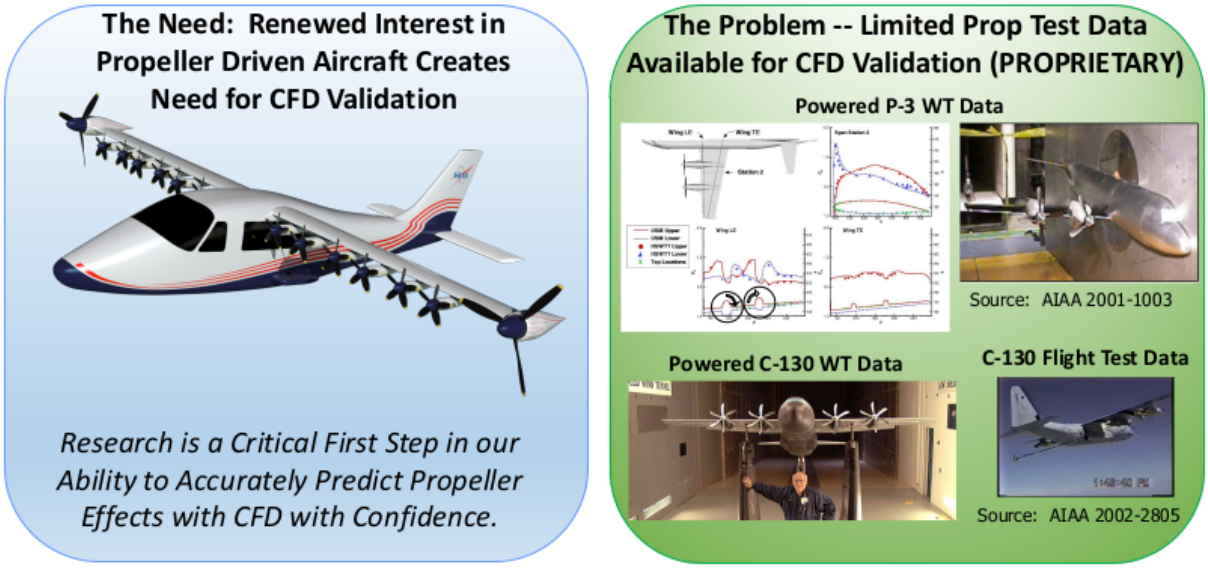

Figure 1.16: The status of the propeller-driven aircraft [61].

Figure 1.17: Model-scale tip mounted propeller mounted in the lockheed martin low speed wind tunnel (LM LSWT) [61].

In the region away from the propeller-wing interactions, both methods resulted in good agreement with the experiment at thrust, torque, and pressure coefficients at $AoA = 0°$ when mounted with-/without a propeller. However, due to the propeller slipstream, both methods lost accuracy close to the interaction regions. At $AoA = 15°$, the ADM agreed reasonably well with the experimental data. It was noted that the slipstream of the propeller at high AoA prevented the flow separation

Figure 1.18: 10%-scale C-130 4-blade Propeller [61].

from the wing by locally accelerating the flow. Furthermore, the multi-reference frame (MRF) with the frozen rotor model (FRM) method has been applied to this study, and it was found out that the MRF-FRM performed less accurately than ADM and VBM except for the section close to the interaction region at the $AoA = 0^{\circ}$ case. The sliding mesh model (SMM) [62] had better accuracy when compared to the ADM and VBM methods. However, in these cases, the results for the section near the interaction region at $AoA = 15^{\circ}$ were not measured in the experiment. Overall, these experiments and simulations investigated the complex flow induced from the wingtip-mounted propeller with different methods, suggesting a high-accuracy method is required for this type of configuration.

Aref [63] applied different grids to this case. The first grid had a single component, including wind tunnel walls, and the second used overset levels, and an adaptive Cartesian method for the near-body grid and wind tunnel walls. KCFD, the Kestrel CFD solver, used a second-order accurate cell-centred finite volume discretisation that discretises the Reynolds averaged Navier-Stokes equa-

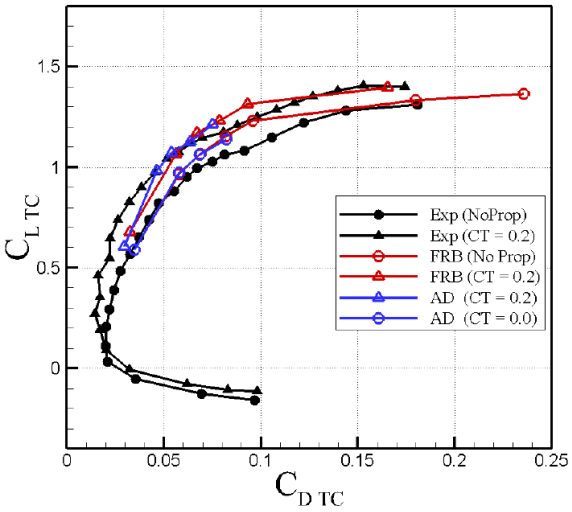

(a) Drag polar; CT=0.2

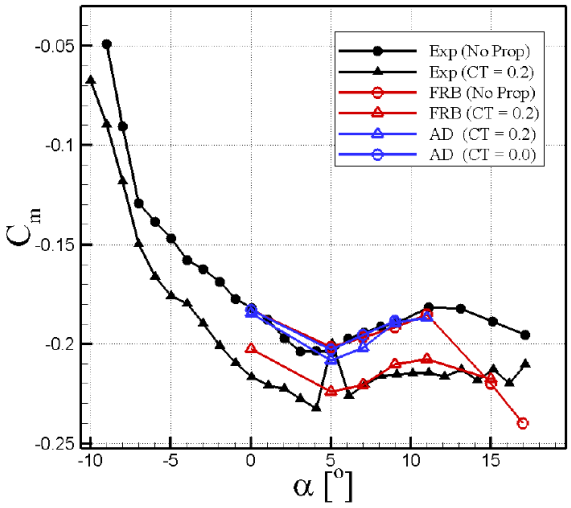

(b) Pitch moment; CT=0.2

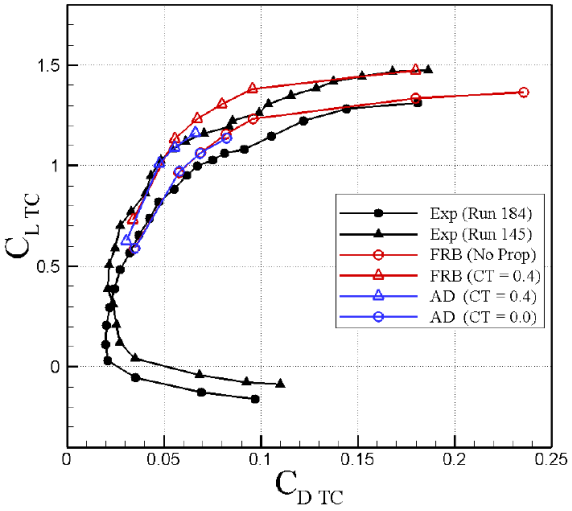

(c) Drag polar; CT=0.4

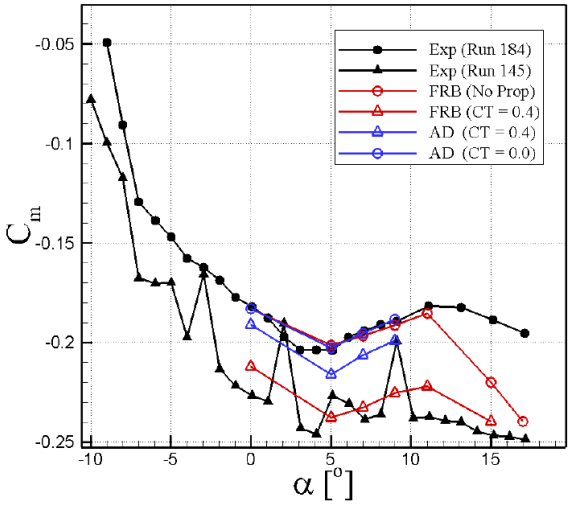

(d) Pitch moment; CT=0.4

Figure 1.19: Drag polar and pitch moment plots for isolated wing and the wing-propeller at $CT = 0.4$ and $CT = 0.2$ and $\alpha = 0°$ using actuator disk and fully-resolved blade models. [63]

tions (RANS) into a second-order cell-centred finite volume form, and this approach was applied to the single unstructured grid simulation. The second approach used the SAMAir solver, which is a fifth-order volume code employing Cartesian meshes. Adaptive mesh refinement (AMR) was used between the near-body and off-body Cartesian grids to increase the resolution where needed. Their study investigated an isolated wing, a wing with a powered-off propeller, and a propeller at different thrust coefficients. The RANS results from SAMAir are shown in Figures 1.191.20,

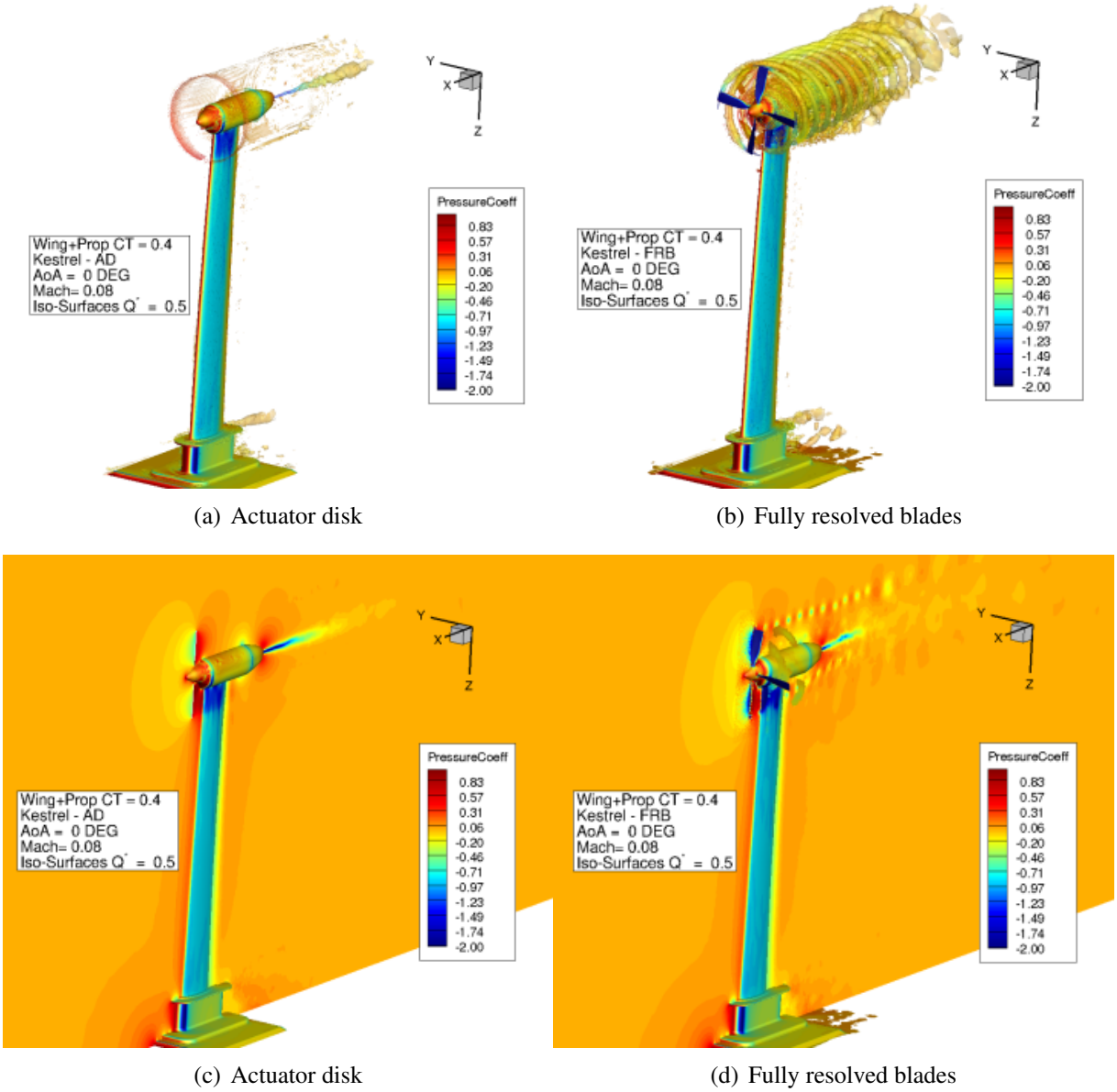

(a) Actuator disk

(b) Fully resolved blades

(c) Actuator disk

(d) Fully resolved blades

Figure 1.20: Flow solutions of the wing-propeller at $C_T = 0.4$ and $C_T = 0.2$ and $\alpha = 0°$ using actuator disk and fully-resolved blade models. [63]

and were in good agreement with experiments, especially at low incidence. Better wing aerodynamic performance in powered-on propellers, indicating a performance enhancement in wingtip-mounted propeller configuration. The benefit of the wingtip-mounted propeller system was also evidenced by Taniguchi and Oyama [64] in the study of the propeller mounting position effect on aerodynamic propeller/wing interaction. Their study assessed the middle-mounted propeller and wingtip-mounted propeller configurations using unsteady Reynolds-Averaged Navier-Stokes sim-

ulation. They concluded that the wingtip-mounted propeller offers a significant increment in lift coefficient due to the wingtip vortex effect.

Reveles et al. [65] also conducted the effects of model fidelity effects on propeller-wing interactions. Models used from NASA Langley FUN3D include a uniform actuator disk with/without accounting for the swirl effects, and discrete moving overset blades. The study compared wake velocities obtained from these numerical models with available experimental data, and analysed the pressure coefficient distribution along the wing, as well as the integrated forces. They concluded that swirl effects are critical to the rotor and wing interaction studies. However, the influence of swirl on sectional wing pressure is reduced due to the increased wing sectional lift. In addition, the actuator disk was promising in reducing computational costs, but it compromised in underpredicting the overall drag forces.

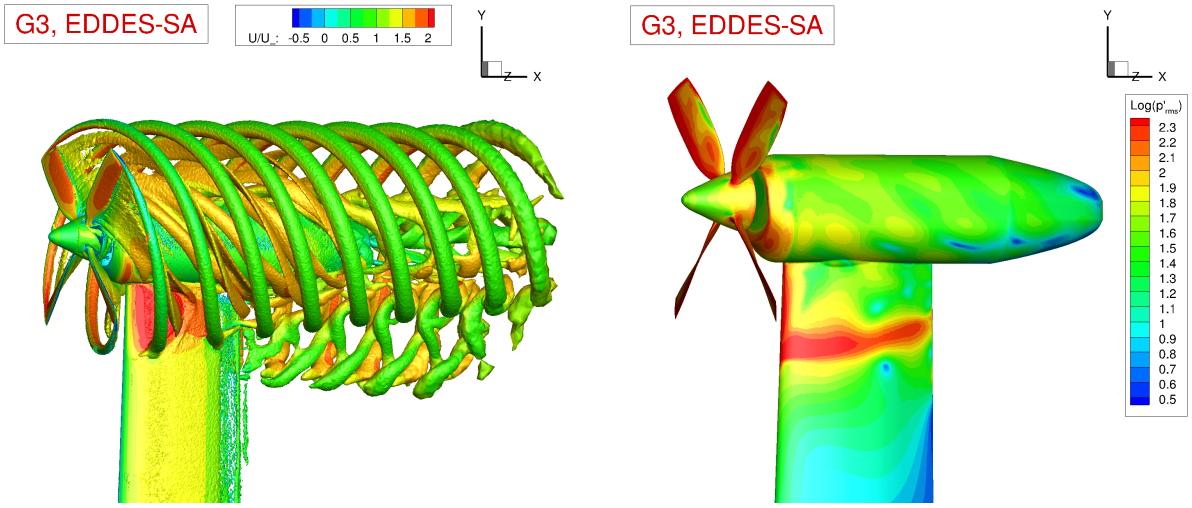

(a) Q-criterion isosurface coloured by the dimensionless streamwise velocity

(b) The log of root-mean-square of pressure fluctuation

Figure 1.21: Results computed by EDDES-SA on fine grid, $M = 0.11$, $C_T = 0.40$, $AoA = 0_\circ$ [66]

Early work has shown that fully resolved simulations with high-order schemes are critical for the accurate prediction of the flow with strong aerodynamic interactions. Zhou et al. [66] performed simulations and sensitivity analyses for the wingtip-mounted propeller configuration using unsteady Reynolds-averaged Navier-Stokes to resolve the turbulent flow. Also, enhanced delayed detached eddy simulations with the Spalart-Allmaras turbulence model were employed

to predict separated flows. The flight condition at Mach 0.11 with $Re = 0.66 \times 10^6$ was selected to meet the thrust requirement $C_T = 0.4$, and three blade pitch angles were investigated. Time-averaged pressure coefficients along the wing surface, and the propeller slipstream were extracted from simulations and compared with experiments, showing good agreement. The results suggested that finer grids captured better the wake profiles. However, the peak values were under-predicted, except for the swirl velocity. Simulation and experiment results of the WIPP found that the wake did not extend beyond the propeller tip. Acoustic characteristics were also investigated from the simulations. Two noise sources were identified from the aeroacoustic analysis and visualised in Figure 1.21 to trace the noise footprints on this integrated configuration, which includes turbulent wake and blade tip vortex impinging upon the wing and nacelle surfaces. It was evident that the leading edge of the wing, and the location below the nacelle were dominant noise sources due to the impingement of propeller tip vortices. Finally, the sensitivity analysis was conducted using an unsteady, discrete adjoint, approach to evaluate the surface sensitivity concerning the mean thrust coefficient design objective. In conclusion, authors claimed that improving the mesh resolution in the propeller wake region can reduce the time step to 0.25 degree of revolution per time step, thus having a higher resolution of the flow field to advantage aeroacoustic analysis. This study also suggested that the two adjoint-based shape optimisations can be subjected to maximising the aerodynamic efficiency and minimising the far-field noise.

Zhou et al. [67] also investigated the turbulent flow fields and aeroacoustics of WIPP. Using the same modelling strategy in the turbulent wake and blade tip regions. Noise computations of the propeller rotation plane and the flyover plane evidenced that the blade tip vortices impinged on the wing and nacelle surfaces were the most dominant noise sources.

In addition to the wingtip-mounted propeller configuration, integrated wingtip-mounted propellers with a distributed propulsion system were included in the X-57 Maxwell aircraft [68] and the Scalable Convergent Electric Propulsion Technology and Operations Research (SCEPTOR) concept [14]. These concepts attracted significant attention from industry, academia, and government.

1.2.4 Noise Reduction in the multirotor system

Helicopter and electric VTOL operations are, to an increasing extent, limited by noise, which is becoming an obstacle to their public acceptance [69]. Studies in aerodynamics and aeroacoustics of multirotor configurations are therefore appearing in the literature. Greenwood *et al.*[70] conducted a review, presenting the challenges and opportunities associated with low-noise electric aircraft. The review highlighted the importance of low rotor tip speeds, and the complexities due to the varied configurations of electric aircraft.

Designing multirotor aircraft necessitates a thorough understanding of the physics and noise sources associated with the multiple flow interactions, and their subsequent sound propagation. While the noise sources and scattering effects in conventional rotorcraft, such as helicopters, have been extensively studied, these differ significantly for multirotor vehicles. Helicopters typically operate at Reynolds numbers around 10^6 which are determined by chord length at 75% station of the tip radius and the speed of the blade tip, whereas multirotor eVTOLs, which utilise multiple smaller blades, operate at lower Reynolds numbers in the range of 10^4-10^5. In terms of noise sources, blade vortex interaction (BVI) is a critical factor during descent in traditional rotorcraft [71]. Greenwood *et al.*[70] reported that with a reduced tip Mach number, the tonal noise (thickness and loading) was diminished due to lower thrust generation and reduced flow acceleration. However, in a multirotor system, the increased number of blades lead to more interactions, between rotor blades and the turbulent flow, which contributes to the dominance of the broadband noise. Nevertheless, the overall sound pressure level (OSPL) resulting from BVI in urban air mobility (UAM) vehicles remains lower than conventional helicopters, mainly due to the smaller rotor sizes used in UAM designs [72].

Regarding the multirotor system in the UK, several universities (University of Glasgow and University of Manchester) and industries (Defence Science & Tech Lab DSTL and Rolls-Royce Plc) started a project on Greener Aviation with Advanced Propulsion Systems (GAAPS). Rotorcraft, particularly those equipped with electric or hybrid-electric propulsion systems, demonstrate significantly higher efficiency than conventional gas turbines under low-speed, low-altitude flight

conditions typically required for urban air mobility and short-range missions. This efficiency advantage stems from their ability to generate lift through large-diameter rotors at lower disc loading, resulting in reduced power consumption and improved overall aerodynamic performance However, new vehicles are facing issues of scaling from sub-scale (unmanned) to full-scale (manned transport). The conventional propellers used in aviation operate at constant RPM and are fully reversible, but the new propellers addressed in the project are to operate over a wide range of RPM and are mostly non-reversible (fixed-pitch). The goal of the project was to build understanding of these new propeller systems, and to generate experimental data that can be used for further eVTOL developments in the industry. The mix of design, simulation models and strategies, advanced manufacturing, wind tunnel testing, and open-air flight testing was combined within the project.

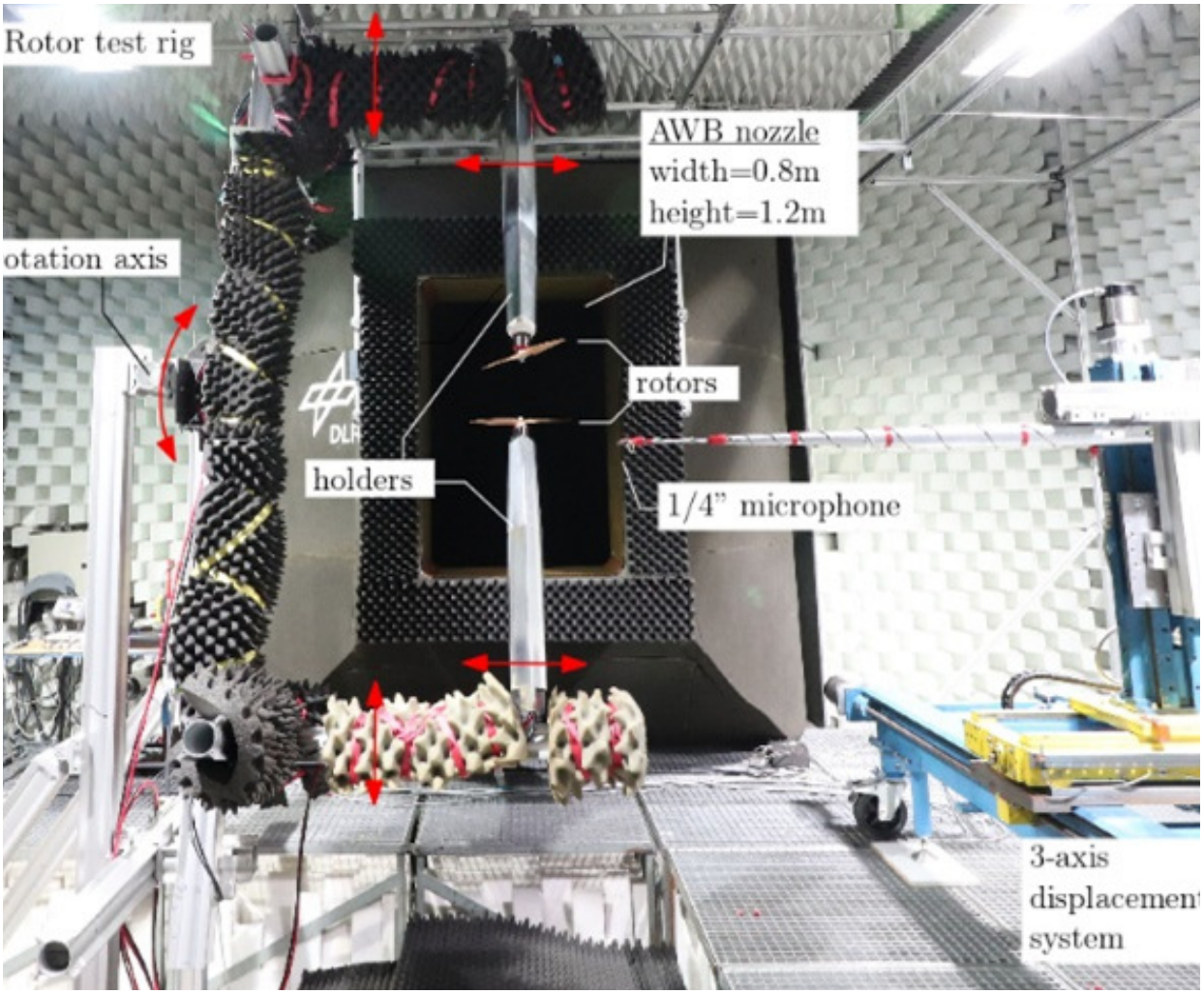

Figure 1.22: Full test rig and microphone setup installed in the AWB's section [73, 74].

Zhou *et al.*[75] investigated rotor-to-rotor interactions on small UAVs. Their findings indicated that the separation distance between rotors had minimal impact on thrust performance; however, reducing the separation distance increased thrust fluctuations and noise levels. Similarly, Shukla and Komerath [76] found that the close proximity of adjacent rotors adversely affected rotor performance due to intensified blade-vortex interactions. These effects were particularly pronounced at low Reynolds numbers in hover conditions. Celik *et al.*[77] studied cruise conditions, reporting a strong impact on noise at the first blade passage frequency (BPF) due to the presence of upstream rotors.

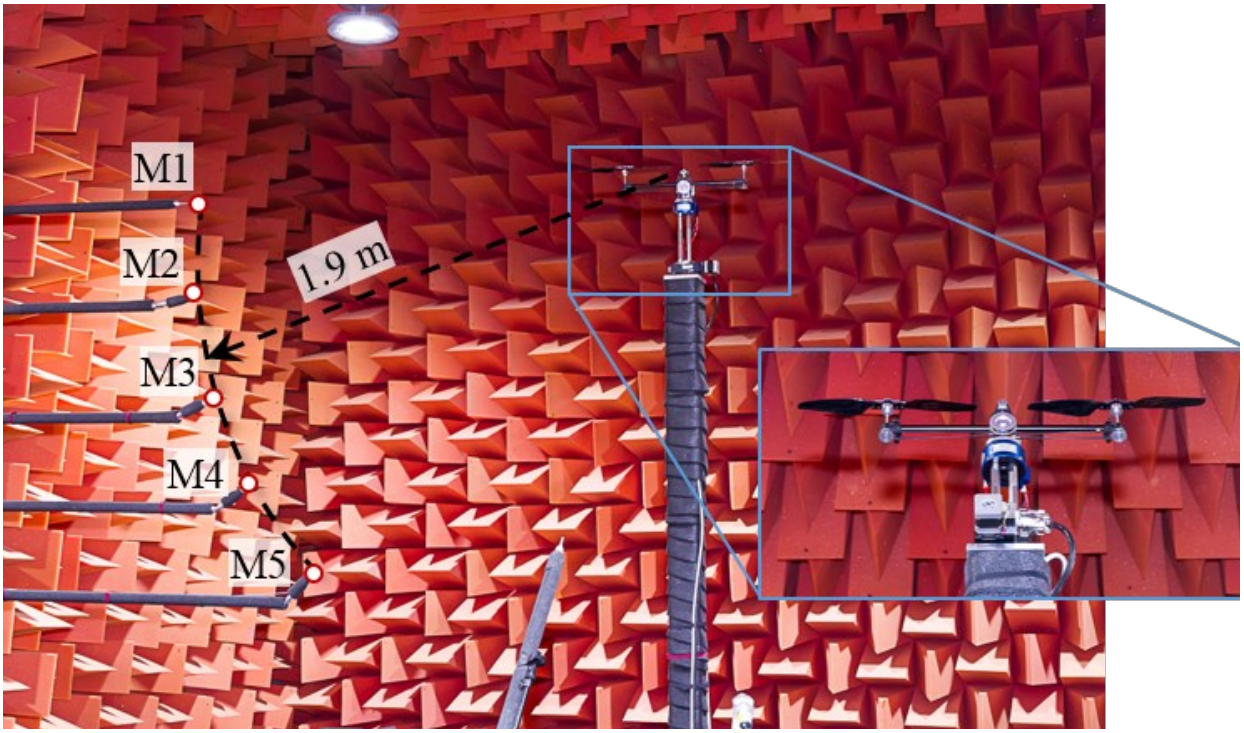

Figure 1.23: Test setup in the NASA Langley Structural Acoustic Loads and Transmission (SALT) anechoic chamber [78].

The aforementioned studies highlight increased noise levels resulting from flow interactions in multirotor systems and suggest that effective noise attenuation strategies are needed. For tandem rotors, Alvarez *et al.*[40] investigated rotor-rotor aeroacoustic interactions in hover, demonstrating that reducing the tip-to-tip distance, and the downstream spacing between two rotors could lead to a 10 dB increase in noise, with A-weighted sound pressure level, as measured directly beneath the rotors. Interestingly, these interactions had minimal impact on blade loading. The study also found

that introducing a vertical offset between side-by-side rotors, reduced noise with the A-weighted sound pressure level going down by 4 dB without compromising aerodynamic performance. Phase synchronisation is also a promising approach for tonal noise reduction, particularly in notional octocopters [78], installed propellers [79, 80], and distributed propulsion systems [43, 44].

Phase synchronisation in multirotor systems has been studied by Shao *et al.*[81] and Guan *et al.*[82]. Their research shows reduced noise in the low-frequency band, and at multiple harmonic frequencies at specific locations, achieving a maximum noise reduction of 5 dB with counter-rotating dual rotors and 11 dB with co-rotating dual rotors. On the downside, co-rotating rotor pairs generated a significant net vehicle torque. [83].

NASA also conducted extensive measurements for dual rotor systems by applying synchrophasing, and the test setup is shown in Figure 1.23. The measured and predicted source directivity at the BPF are shown in Figure 1.24. Table 1.2 compares the measurements and predictions of the normalised sound power [78]. It was found that the counter-rotating rotors have approximately the same noise level as the baseline case, which is two times that of the single rotor, regardless of the relative phase angle. An increase of 2 dB was suggested by both prediction and measurements for the co-rotating rotors. However, the increase of sound power was reduced to the baseline level with a 45° phase offset, and reached a 5-6 dB reduction in radiated power at a 90° phase offset.

Table 1.2: Radiated power, at the blade passage frequency, relative to 2x the power of a single rotor δ PWL [78]. Measurements were acquired on a portion of the lower hemisphere spanning elevation angles from 0° to -45°. Here, co denotes co-rotating, cntr denotes counter-rotating, and Ψ represents the phase delay angle between the rotors.

Configuration	Measured, hemisphere* (dB)	Predicted, hemisphere (dB)	Predicted, sphere (dB)
Single	-3.0	-3.0	-3.0
cntr, $\Psi = 0°$	0.4	0.2	-0.1
cntr, $\Psi = 90°$	-0.3	-0.1	0.1
co, $\Psi = 0°$	2.5	2.3	2.3
co, $\Psi = 45°$	-0.2	-0.1	0.0
co, $\Psi = 45°$	-5.8	-5.2	-5.3

Recently, the GARTEUR Action Group HC/AG-26 was established and coordinated by DLR

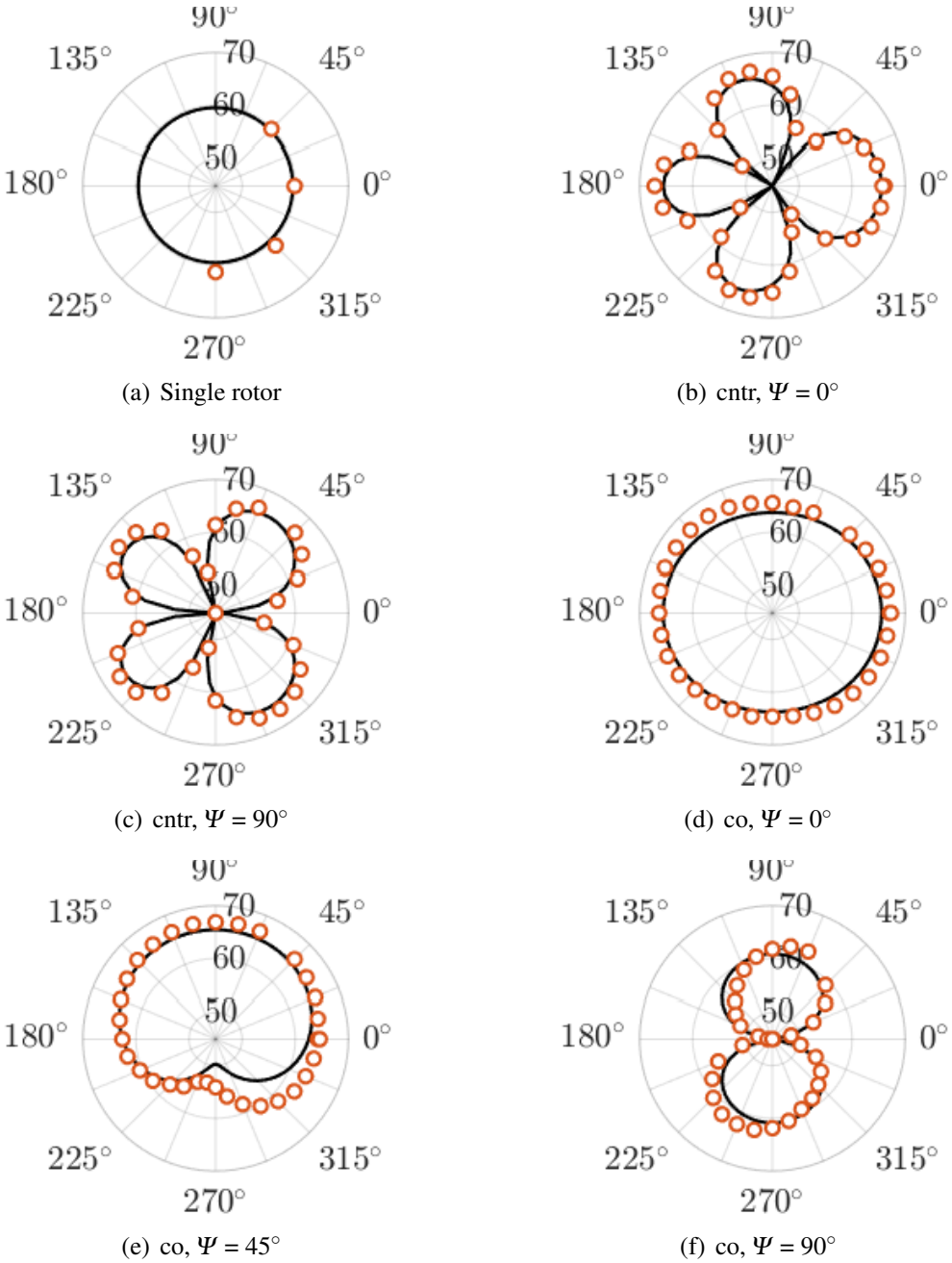

(a) Single rotor

(b) cntr, $\Psi = 0°$

(c) cntr, $\Psi = 90°$

(d) co, $\Psi = 0°$

(e) co, $\Psi = 45°$

(f) co, $\Psi = 90°$

Figure 1.24: Comparison of the predicted (solid black lines) and measured (red circles) sound pressure level in dB at the blade passage frequency at an elevation angle of 0°. [78]

with the aim of advancing the fundamental understanding of multirotor systems and developing solutions for urban air mobility (UAM). This group includes fourteen partners from research and industry. One of the key objectives of GARTEUR AG26 is to gain insights into noise generation and propagation in multirotor systems, including the effects of various installations. Tests conducted by CIRA/DLR [84] involved Particle Image Velocimetry (PIV) measurements on small rotor configurations as shown in Figure 1.22. These tests also included wind tunnel experiments that assessed the aerodynamic performance and acoustics of isolated, coaxial, and tandem rotor configurations [74, 85, 86]. Aerodynamic simulations for acoustic predictions were performed by AG26 partners using a range of methods, from lifting line techniques to advanced Computational Fluid Dynamics (CFD). Results across most cases showed satisfactory agreement between experiments and numerical predictions, regardless of the employed methods [87]. Researchers at the CFD Lab from the University of Glasgow (UoG) used the high-fidelity solver HMB3 to capture rotor performance, flow phenomena, and acoustic emissions with strong rotor-rotor interactions for the small isolated and tandem rotors of AG26 [87, 88, 89].

Aligned with the objectives, this study aims to conduct high-fidelity CFD simulations to analyse the unsteady flow around a pair of tandem, counter-rotating 13x7 rotors in edge-wise forward flight. The simulations will look at coplanar rotors and rotors with a vertical offset. Rotor synchrophasing will also be studied. The findings are expected to advance the current understanding of the sensitivity of angular phase offsets in different tandem rotor configurations.

1.2.5 Summary and Research Challenges

Regarding the propulsion system design, previous investigations transitioned from conventional tractor propulsion systems to over-the-wing (OTW) systems, gradually increasing the fidelity from low-order models, steady-state actuator disk simulations, and experimental methods. However, it is rare to find studies examining both conventional and OTW propulsion systems, with equivalent performance at high load conditions. The benefits of the OTW and OTWDP systems, when directly compared to equivalent conventional tractor configurations, remain unexplored and not quantified.

Furthermore, the impact of the pylon structure in the OTW configuration has been overlooked in previous studies, with low-order simulations and experiments. The pylon structure not only creates a blockage effect for the propeller but also adds more surface area, may increasing drag on the entire propulsion system. Additionally, neither configuration, when integrated with a distributed propulsion system, has been properly compared or thoroughly investigated using experiments or fully resolved simulations. As a result, future distributed propulsion designs may lack certainty regarding which configuration to adopt. To address these critical gaps in the research, the future work aims to provide comprehensive insights and quantitative assessments of tractor and OTW DP systems at high performance conditions.

The literature survey concluded that superior aerodynamic performance can be obtained from tip-mounted propellers, but research combining tip-mounted propellers with distributed propulsion systems using high-fidelity simulation is currently rare since it requires complex simulation strategies. As a result, the performance and flow characteristics resulting from increased propeller-wing, and propeller-propeller interactions remain largely unexplored. Therefore, a generic configuration design with the integrated distributed propulsion system, and wingtip-mounted propellers should be investigated using the fully resolved simulations to study the interactional aerodynamics, associated flow, and their performance.

There are obstacles to leveraging the knowledge we had in the conventional rotorcraft to the AAM. For example, isolated rotors from helicopters have been widely investigated in terms of thrust, drag, efficiency, and Reynolds number effects. [90] [91]. These studies are generally helpful for rotors in forward flight, but the full transition flight is also crucial for AAM. Most of the proposed eVTOLs have edgewise flight with a small angle between the freestream flow and the rotor disk. It needs to be better studied, as the helicopter rotor normally operates at hover and low advance ratio conditions. At these conditions, forces across the rotor disk can be treated as uniform due to the slight loading variation between the advancing and retreating sides of the rotor plane. At low-tip speeds, VTOL rotors in edgewise flight, show a higher difference in dynamic pressure between advancing and retreating sides at higher advance ratio conditions, generating higher thrust [92]. It also leads to a strong tip vortex generation, thus changing the flow around the rotor disk

and the lift distribution along the rotor blade [93, 94]. In addition, the flow and sectional lift change will alter the thrust and acoustics of the rotor in comparison to conventional helicopter rotors. These changes, particularly in low-speed rotors, are pronounced, highlighting the importance of conducting detailed studies on rotor performance in VTOL aircraft.

Another obstacle is that the installation of propellers on the airframe and pylon can significantly influence the overall aircraft performance. Notably, wingtip-mounted propellers are a promising configuration for reducing induced drag through favourable wake interactions. This is particularly true when the propeller rotation is opposite to that of the wingtip vortex in a tractor configuration, as this setup can help mitigate the induced drag [56, 57, 58]. In a pusher layout, where the propeller counter-rotates relative to the wingtip vortex, the swirling flow induced by the wingtip can lead to reduced shaft power [58, 59, 60]. However, the tip-mounted propeller configuration also has drawbacks, including adverse effects on highly loaded wingtips, engine weight, inertia loads, and a large yawing moment arm during one-engine-out scenarios.

Another obstacle is that the installation of propellers on the airframe and pylon can significantly change the aerodynamic interactions, which may influence the overall aircraft performance. Nevertheless, wingtip-mounted propellers are a promising configuration for reducing induced drag through favourable wake interactions. This is particularly true when the propeller rotation is opposite to that of the wingtip vortex in a tractor configuration, as this setup can help mitigate the induced drag [56, 57, 58]. In a pusher layout, where the propeller counter-rotates relative to the wingtip vortex, the swirling flow induced by the wingtip can lead to reduced shaft power [58, 59, 60]. However, the tip-mounted propeller configuration also has drawbacks, including the adverse effects of a highly loaded wingtip, the significant weight of the engine, inertia loads, and a large yawing moment arm during one-engine-out scenarios.

1.3 Thesis Objectives and Organisation

This thesis is structured to provide a comprehensive literature review and investigation into advanced rotorcraft propulsion systems, with a particular focus on distributed and multirotor con-

figurations. The main motivation for this research stems from the increasing demand for high-performance, quieter, and safer aircraft in the context of Advanced Air Mobility (AAM). As environmental concerns become more prominent, addressing propulsion efficiency and noise emissions is critical, particularly those arising from installation effects, multirotor interactions, and aero-propulsive coupling.

Given the lack of consensus on optimal configurations for AAM platforms, current research reveals considerable variability in predicted performance and noise characteristics, often due to differences in simulation fidelity, trimming strategies, and modelling assumptions. Low- and mid-fidelity methods, although widely used, often lack the resolution needed for robust design decisions. Consequently, this work presents a systematic and high-fidelity investigation into the modelling, trimming, and analysis strategies for novel propulsion concepts in rotorcraft applications.

Propulsors are recognised as a major source of noise in aircraft systems; hence, their design plays a central role in achieving noise mitigation and performance optimisation goals. It is essential to investigate various multirotor and propeller configurations to better understand the complex flow physics, aerodynamic interactions, performance characteristics, and associated noise emissions.

In particular, the objectives of this thesis are:

1. To assesses multiple design parameters, including a range of propeller installation locations, the number of propellers, and advance ratios, using various computational methods. An optimal trade-off between accuracy and computational cost is achieved by strategically integrating different methods at appropriate stages of the investigation.

2. To establish computational criteria, strategies, and codes for aerodynamic and acoustic analysis across various installed propulsion systems, considering variable RPM and diverse flight conditions.

3. To evaluate noise control strategies that minimise adverse impacts on aerodynamic performance and propulsion system configurations, using measured data from acoustic anechoic chamber experiments as benchmarks.

To address those uncertainties, the work based on the objectives in 1.3 is brought forward and documented as follows.

- Chapter 1 presents the literature survey, the survey mechanism, and keywords associated with the theme of the current work, such as DP, TMP, and the rotor synchronisation commonly used for noise reduction. The work is then motivated after the extensive critical literature review.

- Chapter 2 describes the HMB3 solver and methods applied in the current work. The chapter contains the CFD solver formulation, turbulence modelling, actuator disk modelling, kriging surrogate model, simulation strategies and techniques, including hover formulation, the overset grid method, and the visulization method, and the method used for the acoustic predictions/analysis in the results chapters.

- Chapter 3 presents the validation and assessment of isolated conformal folding high lift propellers (HLP), tip-mounted propellers (WIPP), and multirotor systems (GARTEUR AG26), along with a time-step and mesh refinement study to evaluate the capabilities of different simulation strategies and methods for modelling the installed multirotor propulsion systems.

- Chapter 4 presents the investigation of distributed propulsion using validated geometries and methods. Multi-levels of fidelities are used at different stages of the investigations to maintain the accuracy and the resonable cost. The fully resolved investigations were based on constrained analysis using either lift or thrust trimming strategies. A novel distributed configuration has been proposed with superior overall performance.

- Chapter 5 introduces the main configuration used in this work. It combines the TMP and DP systems to have the wing-blowing effects to improve lift generation and drag reduction. Together with improved propeller efficiency, resulting in improved overall propeller efficiency. The use of blade-resolved simulation captured the interactional flows to aid a

deeper understanding of interactional aerodynamics in various advanced propulsion technologies. Most importantly, the performance trimming is considered and detailed to pave the way for practical applications.

- Chapter 6 examines the noise reduction technique using high-fidelity simulations by introducing phase synchronization. A complete set of test cases is conducted with different phase-delays between two rotors from different tandem configurations. Their effects are analysed in aerodynamics and acoustics, accounting for human perception to shape the understanding of the effectiveness of sychrophasing in noise control at different configurations and conditions. An equivalent configuration was also investigated to quantify the benefit of tandem rotors.

- Chapter 7 summarises the findings of the current work and offers suggestions for future work.

Chapter 2

HMB3 Solver and Other Methods

The in-house Helicopter Multi-Block (HMB3) CFD solver is employed in this study. HMB3 can predict the aerodynamic performance and acoustics of propulsion systems, as shown in previous studies [95, 96]. HMB3 has been widely used in the investigation of rotorcraft flows [97, 98, 99, 100], helicopter rotor aeroelasticity [101], propeller aeroacoustics [102], flight mechanics [103], and missile trajectory prediction [104]. Moreover, good agreement when compared to experimental results in aerodynamics, acoustics, and aeroelasticity of propellers has been reported in previous studies [105, 106, 107, 108]. Most recently, its ability to capture the interactions of multi-rotor flows and estimate the performance of ducted propellers was also documented [109, 21, 110].

HMB3 solves the Unsteady Reynolds Averaged Navier-Stokes (URANS) equation in integral form using the Arbitrary Lagrangian-Eulerian formulation for time-dependent domains, including moving boundary layers. HMB3 uses a cell-centered finite volume approach to discretise the Navier-Stokes equations on multi-block, structured grids. The 3^{rd} order MUSCL (Monotone Upstream-centered Schemes for Conservation Laws) approach is applied to provide high-order accuracy in space. In the present work, simulations are performed with the $k-\omega$ shear stress transport (SST) [111] turbulence model.

For an isolated rotor in axial flight, the azimuthal symmetry of the configuration can be exploited, whereby only a fraction of the grid needs to be generated. The Rotating Reference Frame (RRF) method is implemented in HMB3 [112] for simulations with rotational periodicity.

The governing flow equations are solved in a non-inertial rotating reference frame, effectively transforming the inherently unsteady rotor problem into a steady-state formulation. In practice, this is implemented by applying periodic boundary conditions to capture the rotational symmetry of the problem. Conceptually, this approach is analogous to shifting perspective: in the inertial frame, we observe the rotor from a stationary point on the ground as it spins; in the non-inertial (rotating) frame, it's as if we are seated on the rotor, rotating along with it, thereby rendering the flow field steady relative to the rotating observer. For unsteady simulations, the entire grid is required. However, this can be obtained by copying and rotating the grids of the steady simulations using the HMB3 tools. Additionally, unsteady calculations are possible using the implicit, dual-time stepping approach. Chimera overset grids [113] are employed to capture the high-pressure gradient region, such as propeller-wing/propeller-propeller aerodynamic interactions and wakes, by including high-resolution Chimera blocks and have been carefully designed for efficient load balancing. In addition, the overset grid method allows for overlapping and non-matching grids to be used, where flow variables are interpolated from the components based on a predefined hierarchy.

This chapter introduces the details of the HMB3 flow solver, including the discretisation method, turbulence modelling, the Chimera method, simulation strategies and techniques, and acoustic analysis. Moreover, the hover formulation, as well as the visualisation techniques, are also presented. Finally, the mid-fidelity methods and the meta model are described in this chapter and applied in this study to compare with the validation results and improve the work efficiency, respectively.

2.1 Navier-Stokes Equations

All simulations performed in this work were conducted with the Helicopter Multi-Block 3 (HMB3) solver [95] [114]. The solver was initially designed for solving rotorcraft problems on structured grids using a control volume-based approach. Over years of development, HMB3 has been extended to handle overset grids, sliding planes, and unstructured meshes. It has been validated for

a wide range of flows. The HMB3 solves the compressible Navier-Stokes equations in the 3D Cartesian frame of reference (with space transformation of curvilinear grids). The Navier-Stokes equations are Partial Differential Equations stemming out of the conservation laws.

- **Conservation of mass (Continuity equation)**
- **Conservation of Momentum (Newton's 2nd Law)**
- **Conservation of energy (1st Law of Thermodynamics)**

The continuity equation describes the principle of mass conservation in a fluid flow and, when expressed in Cartesian coordinates, ensures that the rate at which mass enters a control volume equals the rate at which it leaves. In mathematical terms, it states that the divergence of the velocity field is zero for incompressible flow, or that changes in density are accounted for in compressible flow. This equation is fundamental in fluid dynamics as it guarantees that mass is neither created nor destroyed within the flow field. The continuity equation describes the mass conservation in Cartesian coordinates, x_i , as follows:

$$\frac{\partial \rho}{\partial t} + \frac{\partial (\rho u_i)}{\partial x_i} = 0 \tag{2.1}$$

Newton's 2^{nd} Law describes that linear momentum conservation, this is written as follows:

$$\frac{\partial (\rho u_i)}{\partial t} + \frac{\partial (\rho u_i u_j)}{\partial x_j} = \rho f_i - \frac{\partial p}{\partial x_i} + \frac{\partial \tau_{ij}}{\partial x_j}. \tag{2.2}$$

Here f_i are any acting body forces, and τ_{ij} is the viscous stress tensor, defined as:

$$\tau_{ij} = \mu \left[\left(\frac{\partial u_i}{\partial x_j} + \frac{\partial u_j}{\partial x_i} \right) - \frac{2}{3} \delta_{ij} \frac{\partial u_k}{\partial x_k} \right], \tag{2.3}$$

Here, μ is the molecular viscosity and δ is the Kronecker delta, which is defined as follows:

$$\delta_{ij} = \begin{cases} 1, & \text{if } i = j, \\ 0, & \text{if } i \neq j. \end{cases} \tag{2.4}$$

In terms of viscosity, Sutherland's law is applied:

$$\mu = \mu_0 \left(\frac{T}{T_{ref}} \right)^{\frac{3}{2}} \left(\frac{T_{ref} + T_S}{T + T_S} \right), \tag{2.5}$$

where T is the temperature of fluid condition, T_{ref} is a reference temperature (T_{ref} = 273.15 K), μ_0 is the viscosity at that reference temperature ($\mu_{ref} = 1.716 \times 10^{-5}$ kg/ms) and T_S is the Sutherland temperature (T_S = 110.4 K).

The 1^{st} Law of Thermodynamics states that total energy is constant within an isolated system. This can be expressed as follows:

$$\frac{\partial \rho E}{\partial t} + \frac{\partial}{\partial x_j} \left[u_j (\rho E + p) \right] - \frac{\partial}{\partial x_j} \left(u_i \tau_{ij} - q_{ij} \right) = 0. \tag{2.6}$$

Here, E is the total energy of the fluid per unit mass, e is the internal energy per unit mass and q is the vector of heat flux. The total energy per unit mass is defined as:

$$E = \left[e + \frac{1}{2} u_i u_i \right], \tag{2.7}$$

where $\frac{1}{2} u_i u_i$ express the kinetic energy per unit mass. The heat flux vector is calculated by using Fourier's Law:

$$q_i = -k_h \frac{\partial T}{\partial x_i}, \tag{2.8}$$

where k_h is the heat transfer coefficient. The assumption of ideal gas approximation is applied to relate pressure and density. Dry air is considered as default, with a specific gas constant, R_{sp}, of 287.058 J/KgK,

$$p = \rho R_{sp} T \tag{2.9}$$

The HMB3 solver uses a dimensionless form based on four reference variables: length L_{ref}, a density ρ_{ref}, a velocity U_{ref} and a temperature T_{ref}. The values of the reference variables are

arbitrary and typically chosen depending on the nature of the problem. The following dimensional-to-nondimensional rescaling is applied:

$$\begin{gathered} x = \frac{x^*}{L^*}, \quad y = \frac{y^*}{L^*}, \quad t = \frac{t^*}{L^*/V_\infty^*} \\ u = \frac{u^*}{V_\infty^*}, \quad v = \frac{v^*}{V_\infty^*}, \quad \mu = \frac{\mu^*}{\mu_\infty^*} \\ \rho = \frac{\rho^*}{\rho_\infty^*}, \quad p = \frac{p^*}{\rho_\infty^* V_\infty^{*2}}, \quad T = \frac{T^*}{T_\infty^*}, \quad E = \frac{e^*}{V_\infty^{*2}} \end{gathered} \tag{2.10}$$

2.1.1 Vector Form of Governing Equations

In the conservative form of the governing equations, the combination of continuity, energy, and momentum equations can be expressed in the same generic equation. This will ease the implementation of a computer program. The vector of conserved variables $\mathbf{W}$ is expressed as follows:

$$\mathbf{W} = \begin{bmatrix} \rho \\ \rho u \\ \rho v \\ \rho w \\ \rho E \end{bmatrix} \tag{2.11}$$

and together with the conserved variables of the Navier-Stokes equations written in the previous section. The vector form of the conservation laws in Cartesian coordinates reads:

$$\frac{\partial \mathbf{W}}{\partial t} + \frac{\partial \left(\mathbf{F}^i + \mathbf{F}^v\right)}{\partial x} + \frac{\partial \left(\mathbf{G}^i + \mathbf{G}^v\right)}{\partial y} + \frac{\partial \left(\mathbf{H}^i + \mathbf{H}^v\right)}{\partial z} = \mathbf{S} \tag{2.12}$$

In the equation above, superscripts i and v express the inviscid and viscous components. The superscripts i and v are used to present the inviscid and viscous components of the flux vectors $\mathbf{F}$, $\mathbf{G}$ and $\mathbf{H}$, in the three directions (x,y,z).

The inviscid flux vectors of $\mathbf{F}^i$, $\mathbf{G}^i$, $\mathbf{H}^i$ are given by the following:

$$\mathbf{F}^i = \begin{bmatrix} \rho u \\ \rho u^2 + p \\ \rho uv \\ \rho uw \\ \rho uH \end{bmatrix} \mathbf{G}^i = \begin{bmatrix} \rho v \\ \rho vu \\ \rho v^2 + p \\ \rho vw \\ \rho vH \end{bmatrix} \mathbf{H}^i = \begin{bmatrix} \rho w \\ \rho wu \\ \rho wv \\ \rho w^2 + p \\ \rho wH \end{bmatrix} \tag{2.13}$$

where $H = E + p/\rho$ is the total enthalpy.

In terms of the viscous flux vectors, $\mathbf{F}^v$, $\mathbf{G}^v$, $\mathbf{H}^v$, contain terms for the heat flux and viscous forces exerted on the body as follows:

$$\mathbf{F}^v = \frac{1}{\mathrm{Re}} \begin{bmatrix} 0 \\ \tau_{xx} \\ \tau_{xy} \\ \tau_{xz} \\ u\tau_{xx} + v\tau_{xy} + w\tau_{xz} + q_x \end{bmatrix}$$

$$\mathbf{G}^v = \frac{1}{\mathrm{Re}} \begin{bmatrix} 0 \\ \tau_{xy} \\ \tau_{yy} \\ \tau_{yz} \\ u\tau_{xy} + v\tau_{yy} + w\tau_{yz} + q_y \end{bmatrix} \tag{2.14}$$

$$\mathbf{H}^v = \frac{1}{\mathrm{Re}} \begin{bmatrix} 0 \\ \tau_{xz} \\ \tau_{yz} \\ \tau_{zz} \\ u\tau_{xz} + v\tau_{yz} + w\tau_{zz} + q_z \end{bmatrix}$$

In the above equations, where the Re = $\rho_{ref} U_{ref} L_{ref}$ / μ_{ref}. The term τ_{ij} describes the viscous stress tensor and q_i is the heat flux vector. In equation 2.12, **S** is the source term, which is set to 0 in most calculations. On the other hand, for rotors in hover and axial flight conditions, a non-

inertial reference frame is normally used, and a source term will be added. The Hover formulation is presented in section 2.4.1.

2.1.2 Spatial Discretisation

The Helicopter Multi-Block solver has adopted Navier-Stokes equations, which are presented by the differential form of equation2.12, and can also be written in the Arbitrary Lagrangian-Eulerian (ALE) formulation for time-dependent domains with moving boundaries:

$$\frac{d}{dt}\int_{V(t)} \mathbf{W}dV + \int_{\partial V(t)} \left(\mathbf{F^i} - \mathbf{F^v}, \mathbf{G^i} - \mathbf{G^v}, \mathbf{H^i} - \mathbf{H^v}\right) \cdot \mathbf{n}dS = \int_{V(t)} \mathbf{S}dV, \tag{2.15}$$

The above equations describe a system of conservation laws for any time-dependent control volume V(t) with its boundary $\partial V(t)$ and **n** is outward normal to the volume boundary. $\mathbf{F}^i$ and $\mathbf{F}^v$ are the inviscid and viscous fluxes, respectively. The fluxes include the mesh velocity formulation or deformation. The source term $S = 0$ in the absence of volume forces and for inertial frames of reference. For the rotors in hovering conditions, a non-inertial frame of reference is used for which $S \neq 0$.

On structured multi-block grids, the Navier-Stokes equations 2.12 are discretised using a cell-centred finite volume method. The spatial discretisation introduces a set of time-dependent ordinary differential equations,

$$\frac{d}{dt}\left(\mathbf{W}_{i,j,k}V_{i,j,k}\right) = -\mathbf{R}_{i,j,k}(\mathbf{W}_{i,j,k}), \tag{2.16}$$

Where **W** and **R** are the vectors of cell conserved variables and residuals, respectively. The convective terms are discretised using Osher's upwind scheme [115] in consideration of robustness, accuracy, and stability characteristics. Additionally, the Monotone Upstream-centred Scheme for Conservation Laws (MUSCL) variable extrapolation[116] and the Van Albada limiter [117] are applied to provide second-order accuracy, and to prevent spurious oscillations around shock waves, respectively. The viscous terms are discretised using central differencing. The ghost cells are applied for boundary conditions from each block.

2.1.3 Steady State Solver

For steady-state issues, the time derivative component in equation 2.16 is set to zero. The pseudo-time stepping method is adopted in HMB3 to reach a steady-state from the system of equations expressed in Equation2.16 using an implicit time-marching scheme:

$$\frac{\mathbf{W}_{i,j,k}^{n+1} - \mathbf{W}_{i,j,k}^{n}}{\Delta t} = -\frac{1}{V_{i,j,k}} \mathbf{R}_{\mathbf{i,j,k}} \left(\mathbf{W}_{i,j,k}^{n+1} \right). \tag{2.17}$$

where n+1 defines the time $(n+1) * \Delta t$. To simplify the solution procedure, a system of non-linear algebraic equations 2.17 is applied, the flux residual $\mathbf{R}_{\mathbf{i,j,k}} \left(\mathbf{W}_{\mathbf{i,j,k}}^{n+1} \right)$ is linearised in time as follows:

$$\begin{aligned} \mathbf{R}_{\mathbf{i,j,k}} \left(\mathbf{W}^{n+1} \right) &= \mathbf{R}_{\mathbf{i,jk}} \left(\mathbf{W}^{n} \right) + \frac{\partial \mathbf{R}_{\mathbf{i,jk}}}{\partial t} \Delta t + O\left(\Delta t^2 \right) \\ &\approx \mathbf{R}_{\mathbf{i,j,k}}^{n} \left(\mathbf{W}^{n} \right) + \frac{\partial \mathbf{R}_{\mathbf{i,j,k}}}{\partial \mathbf{W}_{\mathbf{i,j,k}}} \frac{\partial \mathbf{W}_{\mathbf{i,j,k}}}{\partial t} \Delta t \\ &\approx \mathbf{R}_{\mathbf{i,j,k}}^{n} \left(\mathbf{W}^{n} \right) + \frac{\partial \mathbf{R}_{\mathbf{i,j,k}}}{\partial \mathbf{W}_{\mathbf{i,j,k}}} \Delta \mathbf{W}_{\mathbf{i,j,k}} \end{aligned} \tag{2.18}$$

where $\Delta \mathbf{W}_{\mathbf{i,j,k}} = \mathbf{W}_{\mathbf{i,j,k}}^{n+1} - \mathbf{W}_{\mathbf{i,j,k}}^{n}$. Equation 2.17 can be derived in linear system form:

$$\left[\frac{V_{i,j,k}}{\Delta t} \mathbf{I} + \frac{\partial \mathbf{R}_{\mathbf{i,j,k}}}{\partial \mathbf{W}_{\mathbf{i,j,k}}} \right] \Delta \mathbf{W}_{\mathbf{i,j,k}} = -\mathbf{R}_{i,j,k}^{n} \left(\mathbf{W}^{\mathbf{n}} \right). \tag{2.19}$$

It is prohibitive as the number of equations increases, to solve this linear system of equations using direct methods. The iterative Generalised Conjugate Residual (GCR) method is adopted to solve large systems of equations efficiently in both time and memory requirements. In addition, the GCR method is applied in conjunction with a Block Incomplete Lower Upper (BILU) factorisation method [118] adopted as a pre-conditioner for the system of equations. Several explicit iterations are done in the early stages of the solution to smooth out the initial flow. The use of an estimated flux Jacobian (first-order discretisation) requires less CPU time and memory for better storage and computational efficiency [119], through a smaller linear system and a more diagonally dominant Jacobian. Finally, to improve the parallel efficiency by reducing the parallel communication overhead, the BILU pre-conditioner is used decoupled between grid blocks.

2.1.4 Unsteady State Solver

For unsteady problems using the time-accurate simulations, the flow is calculated using the implicit dual-time stepping method of Jameson [120]. The implicit equations at each real-time step are solved using the implicit method through inner pseudo-time, therefore like for the steady solver. Expanding from that, the residual used for the steady-state solver is re-defined to obtain a steady-state equation using acceleration techniques. The re-defined residual is discretised into three levels (n-1, n, n+1) by using the conserved variables as presented as follows:

$$\mathbf{R}^* = V\frac{3\mathbf{W}^{n+1} - 4\mathbf{W}^n + \mathbf{W}^{n-1}}{2\Delta t} + \mathbf{R}(\mathbf{W}^{n+1}). \tag{2.20}$$

With the introduction of the pseudo time τ, the equations can be rewritten as similar ones that are used for the steady-state solver:

$$\frac{\mathbf{W}^{n+1,m+1} - \mathbf{W}^{n+1,m}}{\Delta\tau} = -\frac{1}{V}\mathbf{R}^*(\mathbf{W}^{n+1,m+1}), \tag{2.21}$$

Then the non-linear system is solved using the steady-state method by using pseudo-time, where m denotes the m-th inner iteration of the implicit integration within the pseudo-time.

2.2 Turbulence Modelling

Applying direct numerical simulation of all flow scales is too costly for the flows considered in this thesis. Large length scale approaches an order of rotor radii in the rotor wake from rotary-wing flows, whereas the turbulent length scale in the rotor boundary layer, which is dominated by viscous dissipation, has very short length scales approaching the Kolmogorov scale [121]. An imbalance between the turbulence production and dissipation terms in the rotor wake was also present. The use of the Reynolds number is as the ratio between the inertial and viscous forces, where the ratio between the smallest and largest length scales that exist in the flowfield is $Re^{3/4}$. This means that the greater the Reynolds number, the greater the ratio of the minimum length scale to the maximum length scale. This restricts DNS simulation to low Reynolds numbers with an order of $Re^{9/4}$ grid

points required based on computational resources today. Due to its cost-effectiveness, prior studies showing the importance and most common modelling approach today are the Reynolds Averaged Navier-Stokes (RANS) equations. The RANS equations based on a statistical description of all the turbulent scales are described in the following subsection.

In contrast to low computational cost, the RANS method has limitations in high numerical diffusion and the need for empirical relationships to model turbulence. The gap between LES and RANS simulations is filled by using Detached Eddy Simulation (DES), which is seen as one of the hybrid turbulence models, and it has been applied in some rotary-wing flows successfully [121]. The DES model works as the RANS method used in the near-body region and the LES method in the rotor wake region, based on a grid length scale. The present study will be constrained to the RANS modelling approach. DES, LES approaches are available within the HMB3 solver, but these are not used here.

2.2.1 The $k-\omega$ SST Turbulence Model

It is known that the biggest challenge in turbulence modelling is to estimate the Reynolds stress tensor. This work applied the Menter SST model since it combined the benefit of k - ω model for the flow near the wall and the k - ε for the flow far from the wall and leads to better accuracy for adverse pressure gradient flows [111]. In addition, most proposed models are based on the Boussinesq assumption, resulting in the similar Reynolds stress tensor τ_{ij}^R and the viscous one τ:

$$\tau_{ij} = 2\mu S_{ij} - \frac{2}{3}\mu\frac{\partial u_k}{\partial x_k}\delta_{ij}, \quad \tau_{ij}^R = 2\mu_t S_{ij} - \frac{2}{3}k\delta_{ij}, \tag{2.22}$$

where S_{ij} is the traceless mean strain rate, k is the turbulent kinetic energy, and μ_t is the turbulent viscosity (or *eddy viscosity*), giving the additional contribution of turbulence to dissipation. In the SST model, the eddy viscosity can be computed by the following:

$$\mu_t = \rho\frac{k}{\omega}, \tag{2.23}$$

where ω is the turbulent specific dissipation. In the SST model, two governing transport equations for k and ω are solved as:

$$\frac{\partial \rho k}{\partial t} + \frac{\partial \rho U_j k}{\partial x_j} = \underbrace{\tau_{ij}\frac{\partial U_i}{\partial x_j}}_{\text{production}} - \underbrace{\beta^* \rho \omega k}_{\text{destruction}} + \underbrace{\frac{\partial}{\partial x_j}\left[(\mu + \mu_t \sigma_k)\frac{\partial k}{\partial x_j}\right]}_{\text{diffusion}}, \tag{2.24}$$

$$\frac{\partial \rho \omega}{\partial t} + \frac{\partial \rho U_j \omega}{\partial x_j} = \underbrace{\frac{\gamma}{\nu_t}\tau_{ij}\frac{\partial U_i}{\partial x_j}}_{\text{production}} - \underbrace{\beta \rho \omega^2}_{\text{destruction}} + \underbrace{\frac{\partial}{\partial x_j}\left[(\mu + \mu_t \sigma_\omega)\frac{\partial \omega}{\partial x_j}\right]}_{\text{diffusion}} + \underbrace{2(1-F_1)\frac{\rho \sigma_{\omega 2}}{\omega}\frac{\partial k}{\partial x_j}\frac{\partial \omega}{\partial x_j}}_{\text{cross-diffusion}}. \tag{2.25}$$

In the above equations, F_1 is a blending function for calculating the model closure coefficients γ, σ_k, σ_ω, and β. The k-ω is on in the near-wall region, and the k-ε is on in the wake and free shear layer to obtain the advantages of each model in different flow regions. The blended model feature with the k-ω has no dependency on the free-stream value of the turbulent specific dissipation compared to the initial version [111], where the blending function F_1 is:

$$\phi = F_1 \phi_1 + (1 - F_1)\phi_2. \tag{2.26}$$

In the above equation, the blended closure coefficient ϕ is determined by each closure coefficient of ϕ_1 and ϕ_2 from k-ω and k-ε models. The relation of turbulent quantities applied in the derivation is $\omega = \varepsilon/(C_\mu k)$. The coefficients used in the Wilcox k-ω model [122] are:

$$\sigma_{k1} = 0.5, \quad \sigma_{\omega 1} = 0.5, \quad \beta_1 = 0.075, \quad \gamma_1 = \frac{\beta_1/\beta^* - \sigma_{\omega 1}\kappa^2}{\sqrt{\beta^*}}. \tag{2.27}$$

and the coefficients used for the k-ε model are:

$$\sigma_{k2} = 1.0, \quad \sigma_{\omega 2} = 0.856, \quad \beta_2 = 0.0828, \quad \gamma_2 = \frac{\beta_2/\beta^* - \sigma_{\omega 2}\kappa^2}{\sqrt{\beta^*}}. \tag{2.28}$$

In both scenarios, $\beta^* = 0.09$ and $\kappa = 0.41$, and the F_1 blending function is defined as:

$$F_1 = \tanh(arg_1^4), \tag{2.29}$$

$$arg_1 = \min\left[\max\left(\frac{\sqrt{k}}{0.09 d_w \omega}, \frac{500\nu}{d_w^2 \omega}\right), \frac{4\sigma_{\omega 2} k}{CD_{k0} d_w^2 \omega}\right], \tag{2.30}$$

$$CD_{k0} = \max\left(2\rho\sigma_{\omega 2}\frac{1}{\omega}\frac{\partial k}{\partial x_j}\frac{\partial \omega}{\partial x_j}, 10^{-20}\right). \tag{2.31}$$

Further improvements based on the Bradshaw assumption were applied to modify the eddy viscosity, resulting in the turbulent shear stress in the boundary layer being proportional to the turbulent kinetic energy as $-\rho\overline{u'v'} = \rho a_1 k$. With the introduction of the function F_2, the eddy viscosity is defined to satisfy the Bradshaw relationship in the boundary layer and without modifying the rest of the formulations. As a result, the function F_2 drops to zero in the free shear layers. The modified eddy viscosity is:

$$\mu_t = \frac{a_1 k}{\max(a_1\omega; \Omega F_2)}, \tag{2.32}$$

$$\Omega = \sqrt{2\Omega_{ij}\Omega_{ij}}, \tag{2.33}$$

$$\Omega_{ij} = \frac{1}{2}\left(\frac{\partial U_i}{\partial x_j} - \frac{\partial U_j}{\partial x_i}\right). \tag{2.34}$$

where Ω is the absolute value of the mean vorticity vector. This modification avoids the over-prediction of the turbulent shear stress in the boundary layer, where $\Omega > a_1\omega$. The function F_2 is:

$$F_2 = \tanh(arg_2^2), \tag{2.35}$$

$$arg_2 = \max\left(\frac{\sqrt{k}}{0.09 d_w \omega}, \frac{500\nu}{d_w^2 \omega}\right). \tag{2.36}$$

Finally, eddy viscosity is corrected with an additional function, F2, and the resulting model is called SST.

2.3 Actuator Disk Models

The current study used the actuator disk representation of rotors for modelling interactional aerodynamics. The actuator disk is an efficient modelling approach offering reduced computational cost but has low fidelity. It has been widely used for rotors [123, 124] and propellers [125]. Here, the actuator disk model is implemented as equivalent momentum and energy sources injected into the flow field, with an illustration of the method presented in Figure 2.1.

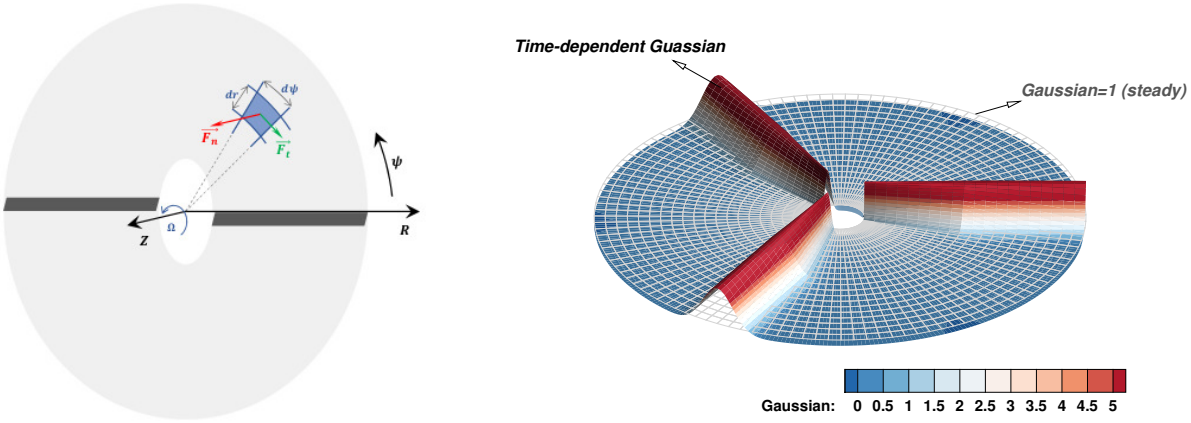

(a) Rotor disk and local forces in a space cylindrical coordinate system.

(b) Time-dependent Gaussian representing a three-bladed rotor.

Figure 2.1: Illustration of the actuator disk modelling of rotors.

Dividing a rotor disk into segments, in a polar coordinate system, centred at the rotor hub, as shown in Figure 2.1(b), the local force vector for a specific cell is correlated with a pressure jump using:

$$T = a_x \int_0^{2\pi} \int_{R_{rt}}^{R_{tp}} \Delta P(r,\psi) g(r,\psi,t) \sigma(x,y,z) dr d\psi, \tag{2.37}$$

$$Q = a_t \int_0^{2\pi} \int_{R_{rt}}^{R_{tp}} \Delta P_t(r,\psi) g(r,\psi,t) \sigma(x,y,z) r^2 dr d\psi, \tag{2.38}$$

where (r,ψ) are the local polar coordinates on the disk, with the subscripts rt, tp denoting the root and tip values, respectively. Here, a_x and a_t are scaling factors ensuring that the total thrust or torque imposed on the flow field equals specified amounts, and $\sigma(x,y,z)$ is a distribution function

introduced to adjust the strength of the disk in space as read as:

$$\sigma = \sigma_r \cdot \sigma_{ax}, \tag{2.39}$$

where σ_r is the radial distribution, and representing that the jumps at the root and the tip were replaced by smooth sine functions.

$$\sigma_r = \begin{cases} 0.5\sin\left(\frac{r-r_0}{2\delta}\pi\right)+0.5, & r_0-\delta < r < r_0+\delta; \\ 1, & r_0+\delta \leq r \leq r_1-\delta; \\ 0.5\sin\left(\frac{r_1-r}{2\delta}\pi\right)+0.5, & r_1-\delta < r < r_1+\delta; \\ 0, & \text{otherwise.} \end{cases} \tag{2.40}$$

where r is the radial distance from a cell centre to the disk centre, r_0 and r_1 are the root and tip radial coordinates, respectively. δ is a tolerance factor that can be used to adjust the size of the smoothing region.

In the axial direction, the Gaussian function or a cosine square function σ_{ax} was used to represent the jump, which reads as.

$$\sigma_{ax} = \begin{cases} \cos^2\left(\frac{\delta Z\pi}{2\varepsilon}\right), & -\varepsilon < \delta Z < \varepsilon; \\ 0, & \text{otherwise.} \end{cases} \tag{2.41}$$

where δ_Z is the normal distance from a cell centre to the disk plane. Tolerance value ε used to adjust the size of the smooth region, which is normally set as 1 or 2 times the local mesh cell size in the norm direction. The jump ratio can also be controlled by adjusting the power, and the Gaussian function used was tended to have a smoother transition to zero.

The function $g(r,\psi,t)$ in Equations 2.37 and 2.38 is a time-dependent Gaussian to redistribute the initial pressure jump in space to resemble discrete blades [126], as shown in Figure 2.1(b). This is to model the time-resolved blade motions, thereby allowing for more similar tip/root vortex systems and the induced flow features. Since it distributes the momentum sources into the blade shapes, this model is also called the Actuator Line (AL) method. In steady simulations, $g(r,\psi,t)$ is set to a constant value of 1. The function $g(r,\psi,t)$ is read as:

$$g = \frac{\sqrt{\pi}(r - r_{rt})}{0.75 N_b c} \sum_{k=1}^{N_b} e^{\left(-\frac{L_k^2}{\varepsilon_k^2}\right)}, \tag{2.42}$$

where N_b is the number of blades, and c is the nominal blade chord length. r and rt are the local radial positions of the nominal blade tip and root cutout. The azimuth distance L_k between the local cell centre and the k^{th} blade is read as

$$L_k = \pi \cos^{-1}(\cos(\Delta\psi)), \tag{2.43}$$

where $\Delta\psi$ is the azimuthal difference between the local point and the k^{th} blade. The spatial distribution ε_k is defined as:

$$\varepsilon_k = \begin{cases} c\frac{2r}{R}, & 0 < r \leq 0.5R, \\ c, & 0.5R < r \leq R, \end{cases} \tag{2.44}$$

where R is the nominal blade radius. Similar to the actual blade loading distribution, the Gaussian distribution concentrates the majority of the loads to the blade tip region. A sample Gaussian distribution for a three-bladed rotor is shown in Figure 2.1(a) to show the discrete blades.

The pressure distributions ΔP and ΔP_t are critical for the actuator disk modelling. A non-uniform disk model is normally applied at edgewise forward flight. In the present work, we used a uniform disk model for the axial flight propeller. The uniform disk model assumes a constant pressure jump ΔP across the disk for each discrete blade. By solving the integration in Equation 2.37, the pressure jump ΔP in the disk normal direction is read as:

$$\Delta P = \frac{T}{\pi\left(r^2 - r_{rt}^2\right)} = \frac{C_{T_{UK}} 0.5 \rho_\infty V_{tip}^2 \pi R^2}{\pi\left(r^2 - r_{rt}^2\right)} = \frac{C_{T_{UK}} 0.5 \rho_\infty V_{tip}^2}{1 - \left(\frac{r_{rt}}{r}\right)^2}, \tag{2.45}$$

In the HMB3 solver, the dimensionless ΔP is calculated using reference pressure $\rho_{ref} V_{ref}^2$ as follows:

$$\Delta \bar{P} = \frac{\Delta P}{\rho_{ref} V_{ref}^2} = \frac{C_{T_{UK}} 0.5 \bar{\rho}_\infty \bar{V}_{tip}^2}{1 - \left(\frac{\bar{r}_{rt}}{\bar{r}}\right)^2}, \tag{2.46}$$

where all barred values are made dimensionless using corresponding reference values. For example, reference length used for the simulation are used here to calculate the dimensionless blade radius and root cutout. For ρ_{ref}, ρ_∞ was chosen, indicating $\bar{\rho}_\infty = 1$. For the reference speed V_{ref}, the free-stream velocity is commonly used. However, the freestream speed is unfavourably small at hover or high-performance conditions, this work applied blade tip speed instead.

The tangential momentum ΔP_t is also a constant in Equation 2.38, which was calculated as:

$$\Delta P_t = \frac{3Q}{2\pi\left(r^3 - r_{rt}^3\right)} = \frac{3C_{Q_{UK}} 0.5\rho_\infty V_{tip}^2 \pi r^3}{2\pi\left(r^3 - r_{rt}^3\right)} = \frac{3C_{Q_{UK}}\rho_\infty V_{tip}^2}{4\left(1 - \frac{r_{rt}^3}{r^3}\right)}. \tag{2.47}$$

The dimensionless ΔP_t was then derived using $\rho_{ref} V_{ref}^2$, which reads as:

$$\Delta \bar{P}_t = \frac{3C_{Q_{UK}}\bar{\rho}_\infty \bar{V}_{tip}^2}{4\left(1 - \frac{\bar{r}_{rt}^3}{r^3}\right)}. \tag{2.48}$$

Finally, Equations 2.37 and 2.38 are evaluated at each computational cell, and the thrust value is converted to its corresponding momentum and energy sources and passed into the discretised governing flow equations of the HMB3 solver. The actuator disk models resolve less geometry, motion, and boundary layer details compared to fully blade-resolved simulations, but the computational cost is significantly reduced due to fewer computational cells and faster convergence. Suggesting that the actuator disk models are promising potential tools for preliminary studies of interactional aerodynamics with the feature of cost efficiency and reasonable simplification.

2.3.1 Kriging Surrogate Model

The Kriging surrogate model [127] is an interpolation method based on Gaussian regression, and is used here to search for optimal configurations of propellers. Kriging, estimates the value of an unobserved evaluation point using a predictor function plus a small, stochastic variance as follows:

$$Z(\mathbf{x}) = Z_0 + \varepsilon(\mathbf{x}), \tag{2.49}$$

where $Z(\mathbf{x})$ is the prediction at the unknown location $\mathbf{x}$, and Z_0 is the mean value of the data set. $\varepsilon(\mathbf{x})$ is a random variable depending on the distance between the unknown point, and the sampling points, and has a mean value of zero. In most cases, it is common that values at the interpolation points are very similar to their immediate known neighbours, and have weaker correlations with sampling points that are far away. The Kriging model uses prescribed variograms to describe the correlation between the sampling and predicted points, thereby solving for the term $\varepsilon(\mathbf{x})$ for the interpolation [127]. Kriging models can be categorised into different types, depending on the function types of Z_0 and $\varepsilon(\mathbf{x})$ used. The current work adopts the Ordinary Kriging with Z_0 denoted by a constant, and $\varepsilon(\mathbf{x})$ a normal distribution [127]. More details can be found in Saves *et al.*[128].

Compared to deterministic interpolation methods e.g. radial-base functions or polynomial approximations, the benefit of Kriging is that it provides not only predictions of function values at unobserved points, but also the uncertainty of the predictions. Kriging has hence been widely used in various applications, including shape optimisation studies. The drawbacks are the slightly larger computational cost for solving linear systems (which scales with the number of sampling points) assumptions on the data set, in terms of stationarity and compliance with normal distributions. Nonetheless, these disadvantages are not critical, as the demanded computational cost is much smaller than the CFD simulations, and the assumptions can be examined by verifying and assessing the interpolation results.

2.4 Simulation strategies and techniques

2.4.1 Hover Formulation

The computational expense can be reduced by using periodicity of flow in the azimuthal direction, i.e. for a rotor with N blade/blades, 1/N of the complete domain with pre-set periodic boundary conditions can be simulated [95]. A non-inertial reference frame has employed to account for rotor rotation since it allows the flow field around the rotating blades to be treated as steady relative to the rotating system. In an inertial (stationary) frame, the rotor motion introduces time-dependent

boundary conditions, making the problem inherently unsteady and computationally expensive to resolve. By switching to a rotating (non-inertial) reference frame that moves with the rotor, the blades appear stationary relative to the observer, simplifying the governing equations and enabling the use of steady-state solvers. This significantly reduces computational cost while still capturing the essential aerodynamic characteristics of the rotating system. To present the centripetal and Coriolis accelerations, a combination of mesh velocity in the ALE formulation of the Navier-Stokes equations and source terms for the momentum equations. The mesh rotation in the direction of the rotor is presented by mesh velocity, thus a formulation with reference velocity $u_{\overrightarrow{ref}} = \omega \times \vec{r}$ is created. *vecr* is the position vector of a mesh cell. The source term for the momentum equations can also be formulated in the following form:

$$S = [0, -\rho\,\omega \times \overrightarrow{u_h}, 0]^T \tag{2.50}$$

where $\overrightarrow{u_h}$ presents the velocity field.

In hover, a source-sink model was used to provide far-field boundary conditions. This model estimates the rotor field using a three-dimensional source-sink singularity with a strength defined by the rotor thrust. The singularity is placed on the rotor disc plane and on the rotor axis of rotation.

The sink draws flow from the surrounding area into the computational domain, resulting in a velocity as follows:

$$W_{in} = -\frac{1}{8}\sqrt{C_{T_{UK}}}\left(\frac{R}{d}\right)^2 \tag{2.51}$$

The distance (d) of an arbitrary point (x_p, y_p, z_p) from the rotational axis of the rotor set at the origin of the coordinate system is $d^2 = x_p^2 + y_p^2 + z_p^2$. The rotor tip speed M_{tip} is used to normalise the magnitude of the total incoming velocity M_{in}. The velocity is assumed uniform at the far-field exit. The 1-D momentum theory is applied to calculate the magnitude of the outflow using rotor thrust coefficient,$C_{T_{UK}}$ and the following formulation:

$$W_{out} = -\sqrt{\frac{C_{T_{UK}}}{4}} \Big/ \left(\frac{R_{out}}{R}\right)^2, \tag{2.52}$$

where R_{out} indicates the radius of the outflow region. An empirical equation implemented in HMB3 is used for R_{out}:

$$R_{\text{out}} = R\left(0.78 + 0.22e^{H_{\text{out}}/R}\right) \tag{2.53}$$

In the above equation, H_{out} is the distance between the outflow boundary and the rotor plane. By establishing a target thrust coefficient, $C_{T_{UK}}$, based on experimental data or user estimation, the strength of the sink is selected to balance the mass flow into and out of the computational domain.

2.4.2 Overset Grid Method

In HMB3, the grid is built based on the overset grid method [129], including splitting the computation domain into independently generated sub-domains, overlapping, non-matching sub-domains. These sub-domains are sorted with different levels, thus presenting calculation priority. The interpolation method is applied following the level hierarchy to exchange data between the sub-domain levels. Generally, for rotor computations, a foreground near-body grid overlaps the background far-field domain. Overset grids have various advantages for rotorcraft, including simplicity of grid generation and lower cell counts. The concept of the overset grid for a 2D aerofoil example is shown in Figure 2.2, where a lower grid level (level=0) is shown in black, as the background grid, and a higher grid level (level=1), is shown in red as the foreground aerofoil grid.

In the overset grid scheme, inter-grid communication and high-order interpolation techniques are necessary. To deal with these problems, the block and solid minimum volume bounding boxes (MVBB) are identified using a localisation technique based on the second moment of the area matrix. The cells inside the MVBBs are then identified using an Overset Mesh Search (OMS) with a range-tree method. An Exact Arithmetics Library (EAL) is utilised to verify that every point can only be placed in the correct cell. This step ensures the determination of the node quantities following the grid priority identified during the cell flagging procedure. The cells shown in Figure 2.2 can be classified into three main categories, i.e. holes, interpolations cells and normal/computational cells. The details have been described as the following:

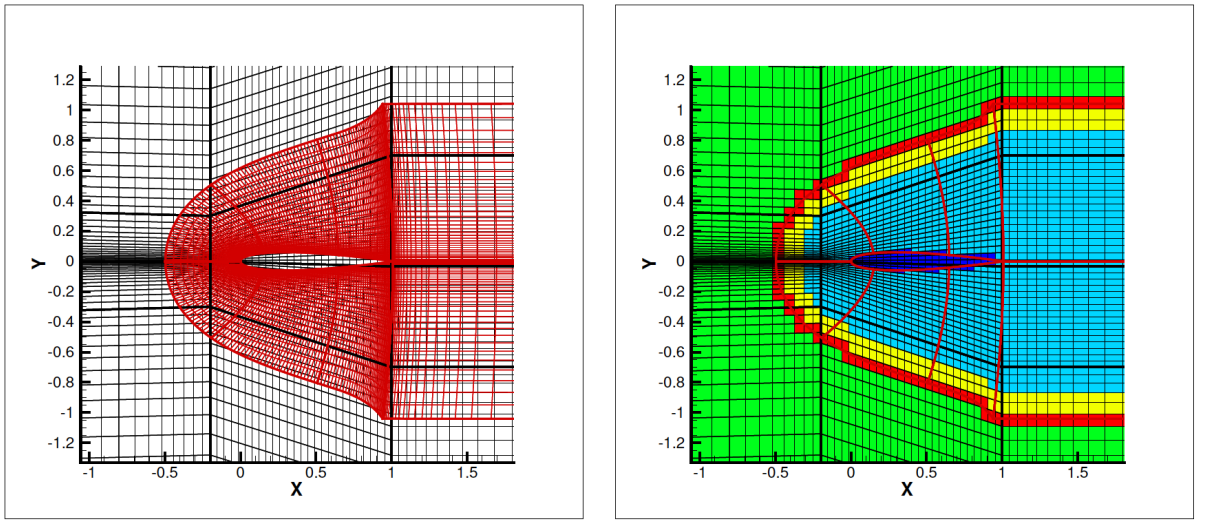

(a) Overset grids for a 2D aerofoil (background->black, foreground->red)

(b) Cell flags on background grid after hole cutting procedure

Figure 2.2: Example overset grid setup for a 2D aerofoil including background and foreground grid layouts with grid cell flags[130]

Normal cell, where equations are solved

Fringe cell, corresponds to the last layer of computational cell

Interpolation cell

Hole cell, non computational cell due to the overlapping of a higher level grid

Solid hole cell, where cell is not computational as it is inside a solid

enoindent Figure 2.2 shows the grid localisations and cell flags. It should be noted that the interpolation cells obtain information from the foreground grid, where the foreground grid is also updated information from the background grid. The information from cells is then applied to calculate flux on the overset mesh boundary of foreground grid cells. Additional information on the overset grid method and its implementation in HMB3 are presented in reference[113].

2.4.3 Visualisation of Vortical Structures

To visualise the wake, isosurfaces of Q-criteria are adopted. In this method, vortices are defined as regions with a positive second invariant of the velocity gradient tensor,∇u [131]. The quantity can be derived as follows:

$$Q = \frac{1}{2}\left(\hat{\Omega_{ij}}\hat{\Omega_{ij}} - \hat{S_{ij}}\hat{S_{ij}}\right) \tag{2.54}$$

where the antisymmetric $\Omega_{ij}$and symmetric $\hat{S_{ij}}$ parts of the velocity gradient tensor can be expressed as follows:

$$\hat{\Omega}_{ij} = \frac{1}{2}\left(\frac{\partial \hat{u}_i}{\partial x_j} - \frac{\partial \hat{u}_j}{\partial x_i}\right), \quad \hat{S_{ij}} = \frac{1}{2}\left(\frac{\partial \hat{u}_i}{\partial x_j} + \frac{\partial \hat{u}_j}{\partial x_i}\right) \tag{2.55}$$

This criterion describes the local balance between vortex rotation and vortex stretching into vorticity magnitude and strain rate, respectively. In hover, this value is also utilised to calculate the locations of the rotor blade tip vortices vs azimuth. Finally, the non-dimensionalisation of the Q-criterion value utilised in HMB3 is as follows:

$$\widetilde{Q} = Q\left(\frac{L_{ref}}{V_{ref}}\right)^2 \tag{2.56}$$

2.5 Performance Analysis

2.5.1 Propeller Theory and Definitions

This section describes the propeller performance coefficients and the advance ratio [132].

Advance Ratio (J):

$$J = \frac{V}{nD} \tag{2.57}$$

where:

- V is the freestream velocity (m/s),
- n is the propeller rotational speed (revolutions per second),

- D is the propeller diameter (m).

Thrust Coefficient (C_T):

$$C_T = \frac{T}{\rho n^2 D^4} \tag{2.58}$$

where:

- T is the thrust produced by the propeller (N),
- ρ is the air density (kg/m^3).

Power Coefficient (C_P):

$$C_P = \frac{P}{\rho n^3 D^5} \tag{2.59}$$

where:

- P is the power absorbed by the propeller (W).

As the advance ratio J increases:

Thrust Coefficient (C_T): Initially increases, reaches a maximum, and then decreases. This behavior is due to the changing angle of attack experienced by the propeller blades as the aircraft's forward speed increases relative to the rotational speed of the propeller.

Power Coefficient (C_P): Generally decreases with increasing J. As the propeller operates more efficiently at higher advance ratios, less power is required to produce the same amount of thrust, leading to a decrease in C_P.

Propeller efficiency typically increases with J up to a certain point, after which it decreases. The peak efficiency occurs at an optimal advance ratio, which depends on the propeller design and operating conditions. Understanding these relationships is crucial for optimising propeller design and performance across different flight regimes, and designing advanced propulsion systems.

2.5.2 System Performance Analysis

Furthermore, to assess the interference between propellers and lifting surfaces, it is evident that both components of each configuration cannot be independently evaluated. Thus, an integration

of relevant forces (Thrust T, drag D) should be employed to comprehensively compare the overall performance of different configurations.

In Equation (2.60), the overall installed thrust (T_{install}) is calculated by subtracting the drag ($D_{\text{lifting surfaces}}$) of the lifting surface and the pylon from the total thrust ($T_{\text{propellers}}$) generated by the propellers.

$$T_{install} = T_{propellers} - D_{lifting\,surface} \tag{2.60}$$

Subsequently, the overall propulsive efficiency can be simplified, This can be seen in Equation (2.61). Here, V_∞ represents the free-stream velocity, and P_{shaft} denotes the power required by the propellers.

$$\eta^{overall}_{propulsive} = \frac{T_{install} \times V_\infty}{P_{shaft}} \tag{2.61}$$

Finally, this study will apply the aforementioned equations to evaluate the overall propulsive efficiency of different configurations, ensuring that the lifting surface is trimmed to produce a higher or the same amount of lift.

2.6 Acoustic Methods

2.6.1 Near-field Acoustics

The present work estimate the tonal acoustics from the resolved pressure fields, computed with the high-fidelity HMB3 tool. Then, the sound pressure signal is obtained by subtracting the time-averaged pressure field solution. All CFD grids were made to have at least 20 cells in the near-field region to capture the target wavelength, which is calculated based on 20 times the BPF ($400Hz$ at 12,000 RPM for two bladed rotor). Moreover, the equivalent of 20 revolutions, and proper time steps were chosen based on time refinement study. This approach has also been applied to previous work by Chirico *et al.* [133, 134], Zhang, and Barakos [135].

2.6.2 Far-field Acoustics

Directly resolving the far-field acoustics by using the same approach as near-field acoustics is costly due to the large computational domain, and the fine mesh needed to resolve the adequate acoustic wave at far-field. This is unaffordable for the present simulations. The Ffowcs Williams-Hawkings (FW-H) equation [136] therefore should be used to evaluate the far-field acoustics with significant reduced computational cost but with resonable accuracy.

The coupling of HMB3-HFWH tools was applied with the input of surface pressure fields computed by HMB3 to efficiently calculate the far-field acoustics. The current work focusses on the non-porous formulation obtained from Farassat Formulation 1A [137] with a completely anechoic condition, by introducing the concept of the retarded time, it solves the thickness noise and the loading noise in the time domain. Two linear equations are formulated as shown in Equation 2.62 for thickness noise and Equation 2.63 for loading noise.

$$4\pi r p'_T(\mathbf{x},t) = \int_{f_i=0} \left(\frac{\rho_0 \hat{v_n}}{r(1-M_r)^2} + \frac{\rho_0 v_n \hat{r_i} \dot{M_i}}{r(1-M_r)^3} + \frac{\rho_0 v_n c(M_r - M_i^2)}{r^2(1-M_r)^3} \right)_{\text{ret}} dS, \tag{2.62}$$

$$4\pi r p'_L(\mathbf{x},t) = \int_{f_i=0} \left(\frac{l_i \hat{r_i}}{cr(1-M_r)^2} + \frac{(l_i \hat{r_i})\dot{M_i}}{cr(1-M_r)^3} + \frac{l_i \hat{r_i} - M_i l_i}{r^2(1-M_r)^2} + \frac{l_i \hat{r_i}(M_r - M_i^2)}{r^2(1-M_r)^3} \right)_{\text{ret}} dS. \tag{2.63}$$

More definitions of the variables used in Equations 2.62 and 2.63 are presented in 2.1.

The current non-porous formulation assumed infinite impedance of solid surfaces and avoided the integration to ignore the quadrupole sources, thus reducing the computational cost and making it more efficient, but still maintaining adequate accuracy due to the nature of subsonice flow. The far-field acoustic prediction method and coupling code have been employed and validated for the first time for the twin-propeller and synchrophasing cases, as shown in Section 3 and in the joint publication [88].

Symbol	Variable
c	Sound speed (assumed constant at low flow speeds)
$f_i = 0$	The wall surface
p'_T	Thickness noise received at $(\mathbf{x}, t)$
p'_L	Loading noise received at $(\mathbf{x}, t)$
ρ_0	Free-stream density
$l_i = (p - p_0)n_i$	Loading vector, p is the local surface pressure and p_0 is the free-stream pressure
$M_i = \frac{v_i}{c}$	Mach number vector
$M_r = M_i \hat{r}_i$	Projected Mach number vector in the radiation direction
$r_i = x_i - y_i$	Space vector between receiver and source positions
$\hat{r}_i = \frac{r_i}{r}$	Normalized directivity vector
t	The receiver time $t = \tau + \frac{\lvert\mathbf{x}-\mathbf{y}(\tau)\rvert}{c}$
$\mathbf{x}$	Receiver position
$\mathbf{y}$	Emission point on the wall surface at emission time τ
v_n	Surface normal velocity in tensor form
$\dot{v}_n$	Temporal derivative of the surface normal velocity
$\dot{M}_i$	Temporal derivative of the Mach number vector
$\dot{l}_i$	Temporal derivative of the loading vector
$()_{\text{ret}}$	The formulation is calculated at emission time τ

Table 2.1: Symbols and their corresponding descriptions

2.6.3 Acoustic Analysis

The motivation for this study was to investigate the acoustic impact of distributed propulsion systems, particularly in the context of eVTOL and future advanced aerial vehicles. These systems, designed to enhance aerodynamic efficiency, reduce environmental footprint, and more sustainable flight, but introduce complex flow interactions that significantly influence noise generation and propagation. Understanding their acoustic signature is critical to ensuring public acceptance, meeting regulatory noise limits, and guiding the design of quieter, more sustainable next-generation aircraft. By examining how multiple, spatially distributed rotors affect acoustic signatures, including directivity and perceived loudness, results were interpreted accordingly, with specific attention to the unique noise characteristics introduced by distributed propulsion configurations. The A-weighted SPL [138] standards is used in an effort to account for the relative loudness perceived by the human ear, as the ear is less sensitive to low audio frequencies. In general, the human auditory system perceives sound differently across various frequency bands. Therefore, by averaging ASPL

within audible frequency bands, the analysis better correlates with how humans perceive sound, providing a more accurate representation of the overall perceived loudness. To this end, ASPL are averaged across each of twenty bands, identified by one-third-octaves as listed in Table 2.2 and evaluated with identified specific frequency bands with familiar names. The use of one-third-octaves to understand how different frequency components contribute to the overall sound can also aid in targeted noise control and mitigation efforts, leading to more effective noise reduction strategies.

Table 2.2: 1/3 octave bands and frequencies.

Name	**Band#**	**Central Frequency (Hz)**	**Range (Hz)**
Sub-Bass:	1	50	44.7-56.2
Bass:	2	63	56.2-70.8
	3	80	70.8-89.1
	4	100	89.1-112
	5	125	112-141
	6	160	141-178
	7	200	178-224
Low Midrange:	8	250	224-282
	9	315	282-355
	10	400	355-447
Midrange:	11	500	447-562
	12	630	562-708
	13	800	708-891
	14	1000	891-1120
	15	1250	1120-1410
	16	1600	1410-1780
Upper Midrange:	17	2000	1780-2240
	18	2500	2240-2820
	19	3150	2820-3550
Presence:	20	4000	3550-4470

In the acoustic analyses, the OSPL and SPL as functions of the sound frequency, f, are given in equations (2.64) and (2.65). Here p_{ref}, is the acoustic reference pressure, equal to $2 \cdot 10^{-5}$ Pa. Human perception is considered by applying the A-weighting filter for the estimation of sound pressure, as the loudness-corrected weighting Effective Perceived Noise Level (EPNL) [139] is required. According to acoustic standards [140, 141], the A-weighted SPL (ASPL) is determined

using equation (2.66), where $G_A(f)$ is the frequency-dependent filter gain defined in equation 2.67.

$$OSPL(f) = 20 \cdot \log_{10}\left(\frac{p'_{\text{rms}}}{p_{\text{ref}}}\right) dB, \tag{2.64}$$

$$SPL(f) = 20 \cdot \log_{10}\left(\frac{\text{PSD}\left(p'\right)}{p_{\text{ref}}}\right) dB, \tag{2.65}$$

$$ASPL = SPL(f) + 20 \cdot \log_{10}(G_A(f)) + 2dB_A, \tag{2.66}$$

$$G_A(f) = \frac{12200^2 \cdot f^4}{(f^2+20.6^2)\sqrt{(f^2+107.7^2)(f^2+737.9^2)}(f^2+12200^2)} dB, \tag{2.67}$$

Chapter 3

CFD Validation and Assessment

This chapter has been published as: J. Yin, et al., "Acostic and Aerodynamic Evaluation of DLR Small-scale Rotor Configurations Within GARTEUR AG26," CEAS Aeronautical Journal, (2024) doi: 10.1007/s13272-024-00790-2.

Before carring out the investigation of the distributed rotorcraft propulsion system, it is essential to verify the accuracy of methods and strategies used to resolve the aerodynamics and acoustics in the isolated, multirotor and installaed propeller/rotor propulsion systems. This chapter focuses on validating the employed simulation methods, using experimental data from the Folding Conformal High Lift Propeller (HLP) and the NASA Workshop for Integrated Propeller Prediction (WIPP) projects, for isolated and installed cases. Additionally, validation for rotor-rotor interactions, following time-step and grid refinement studies was conducted using the GARTEUR Action Group 26 measurements, to confirm the accuracy of the applied solver in predicting interactional aerodynamics and acoustics. An assessment of simulation methods, propeller/rotor performance, and acoustics is also detailed.

3.1 High Lift Propeller (HLP)

3.1.1 Test Cases Description

In a DP system, it is possible to use smaller propellers compared to those used in a tip-mounted configuration [142]. Litherland et al. [37] conducted wind tunnel tests on a conformal high-lift propeller (HLP), which was designed for use with the DP system of the X-57 "Maxwell" electric aircraft. The X-57 utilises twelve fixed-pitch, conformal, high-lift propellers mounted on the wing leading edge to increase lift at low speeds. The conformal design enables the blades to fold into the nacelles at cruise, reducing drag and performance losses. The experiments recorded the performance of conformal high-lift propellers at various advance ratios and compared it with low and high order prediction models [61] [143].

This section presents the validation of the conformal/non-conformal HLP. The HLP has five blades with a radius of 0.288 m, and a pitch angle of 24.1 degrees at 75% of the blade radius. Advance ratios J from 0.65 to 1.17 were tested with varying RPMs from 4200 to 4800, and flight velocities from 30 m/s to 54 m/s. The blade was of a constant MH114 aerofoil profile, which was modified to include a 5.08 $\times 10^{-4}$ m (0.02 inch) thick trailing edge for easier manufacturing. The modification was achieved by relofting the blade's upper surface and rotating it back to prevent changes in the aerofoil chord line. The non-conformal propeller blades were given rake and skew parameters to become foldable.

The blade geometry was then generated using OpenVSP [144] of NASA using twist, chord, skew and rake distribution, and its details can be obtained from [37]. In addition to the blade design function, OpenVSP also provides aerodynamic analyses using low-order methods, including actuator disk models, and vortex lattice methods. In this work, the OpenVSP [37] were used to support the CFD mesh generation.

The $1/N_b$ computational domains presented in Figure 3.1 were used for the validation of the folding conformal HLP. The computational resources were reduced due to the rotating reference frame, and the periodic domain. Froude conditions were also used by defining a target thrust

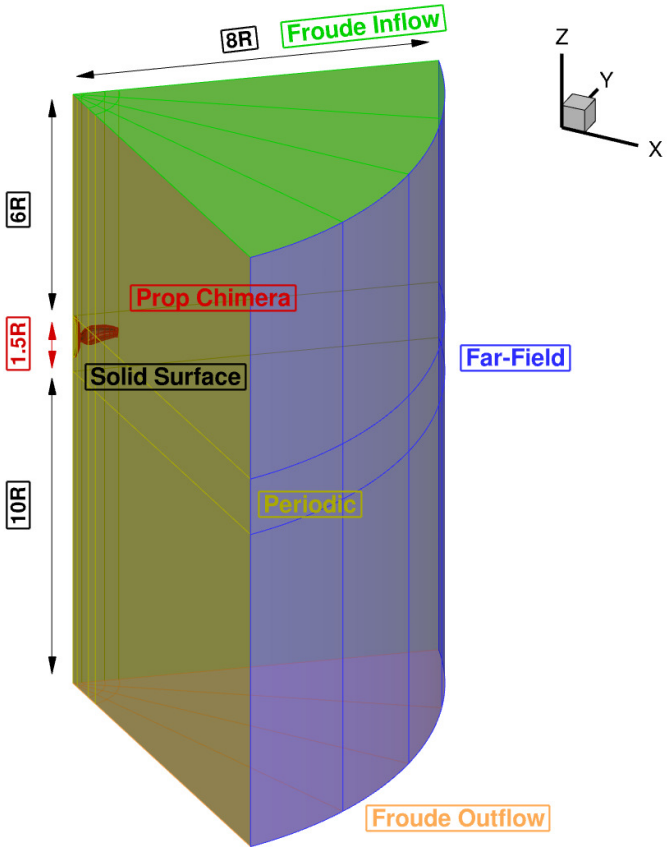

(a) Computation domain.

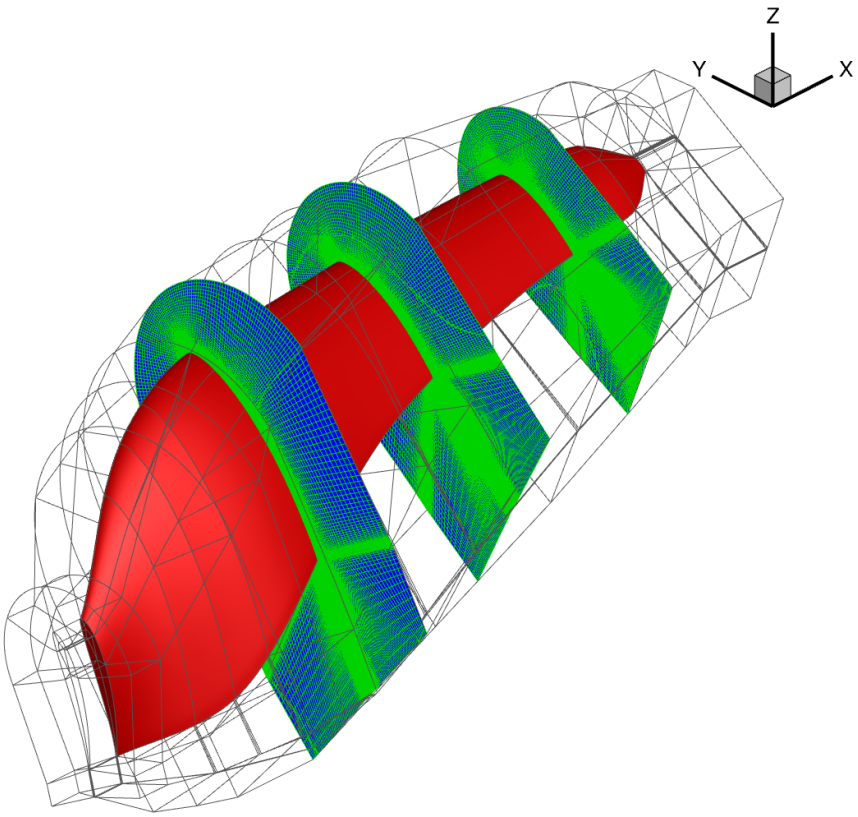

(b) Blade mesh.

Figure 3.1: Conformal HLP mesh details.

coefficient, and a source-sink model placed in the centre of the rotor to accelerate the convergence of simulations.

Table 3.1: Summary of the propeller design and test conditions for the non-conformal HLP [143].

Design parameters:	
Radius (m)	0.288
Pitch angle at $0.75R$ (degrees)	27.4
Number of Blades (-)	5
Design condition:	
Rotational velocity (RPM)	4549
Flight velocity (m/s) (Sea Level)	29.84
Design performance:	
Thrust (N)	222
Torque (Nm)	21.62
Power (kW)	10.3

3.1.2 Comparison with Numerical and Experimental Data

After preparing the propeller geometry and the CFD grids, the test condition were used defined by Litherland et al. [37] and are shown in Table 3.1. High performance conditions were selected, comparisons between different solvers and propeller designs are shown in Table 3.2. Good correlations can be found for different propeller designs and numerical methods.

Table 3.2: Comparisons of predicted propeller performance for the non-folding and folding designs [142] using the Overflow [145] and HMB3 [146] CFD solvers.

Propeller Design	Overflow	HMB3	Δ
Thrust (N)			
Non-conformal	222.0	222.2	0.1%
Conformal	217.0	217.6	0.3%
Torque (N.m)			
Non-conformal	21.50	22.42	4.2%
Conformal	20.80	21.97	5.6%

In addition to the comparison of the results between different solvers, the validation was also carried out with the recent folding conformal HLP experimental results [37]. High performance take-off and landing conditions are presented in Table 3.3, and used for CFD calculations.

Furthermore, the HLP was also investigated with a sweep of advance ratios to understand the performance at different flight conditions.

Table 3.3: Summary of the propeller design and take-off conditions for conformal HLP [37].

Design parameters:	
Radius (m)	0.288
Pitch angle at $0.75R$ ($^\circ$)	24.1
Number of Blades (-)	5
Blade tip Reynolds number (-)	0.07×10^6
Design condition:	
Blade tip Mach number (-)	0.421
Rotational velocity (RPM)	4800
Flight velocity (m/s) (Sea Level)	29.84
Design performance:	
Propeller thrust coefficient (-)	0.238

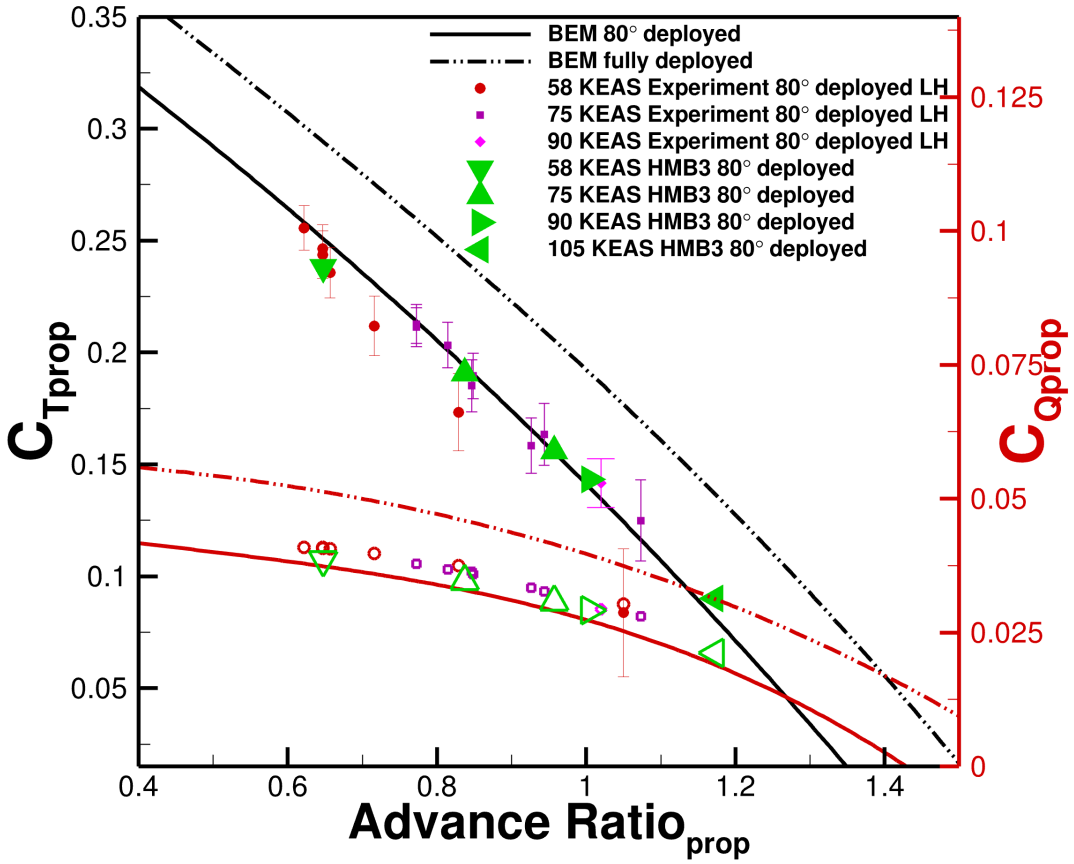

Figure 3.2: Validation of HMB3 solver for the conformal HLP. Empty symbols represent the respective torque coefficients. (Blade Element Momentum (BEM) and experimental data are from Litherland et al. [37].)

The HMB3 CFD solver was used to predict performance, as shown in Figure 3.2. Aerodynamic coefficients were compared against the experiments with various advance ratios. Good agreement can be observed between the HMB3 and experimental results. [37]

3.2 Workshop for Integrated Propeller Prediction (WIPP)

3.2.1 Test Cases Description

In an effort to bridge the knowledge gap in propeller/wing interactions, the wingtip-mounted propeller (WIPP) tests in the Lockheed Martin low-speed wind tunnel (LSWT) were conducted [61]. The test model of the WIPP featured a semi-span wing measuring 1.7 meters (67 inches), and a wingtip-mounted C-130 propeller scaled at 10% of the actual size. Detailed measurements of forces and moments were collected at various angles of attack and thrust settings.

Table 3.4: Summary of the grid sizes used for the WIPP cases.

Grid Component	**Volume Cells (Million)**
Background	1.17
Local refinement	5.29
Wing	30.75
Tip propeller	30.32
Total	67.50

To this end, before studying the propeller wing interaction for DP systems, the WIPP case was compared to verify that HMB3 has the ability to predict associated flows. The geometry and the computational domain for the WIPP cases [147] is shown in Figure 3.3. In addition, the mesh size and the employed computational setup are shown in Tables 3.4 and 3.5. Using the tip-mounted propeller geometry of the WIPP project for the current study, the CFD method was validated against experimental data [147]. The selected test cases were referenced as Cases 79, and 180 in the experimental report [147], and their conditions are presented in Table 3.5.

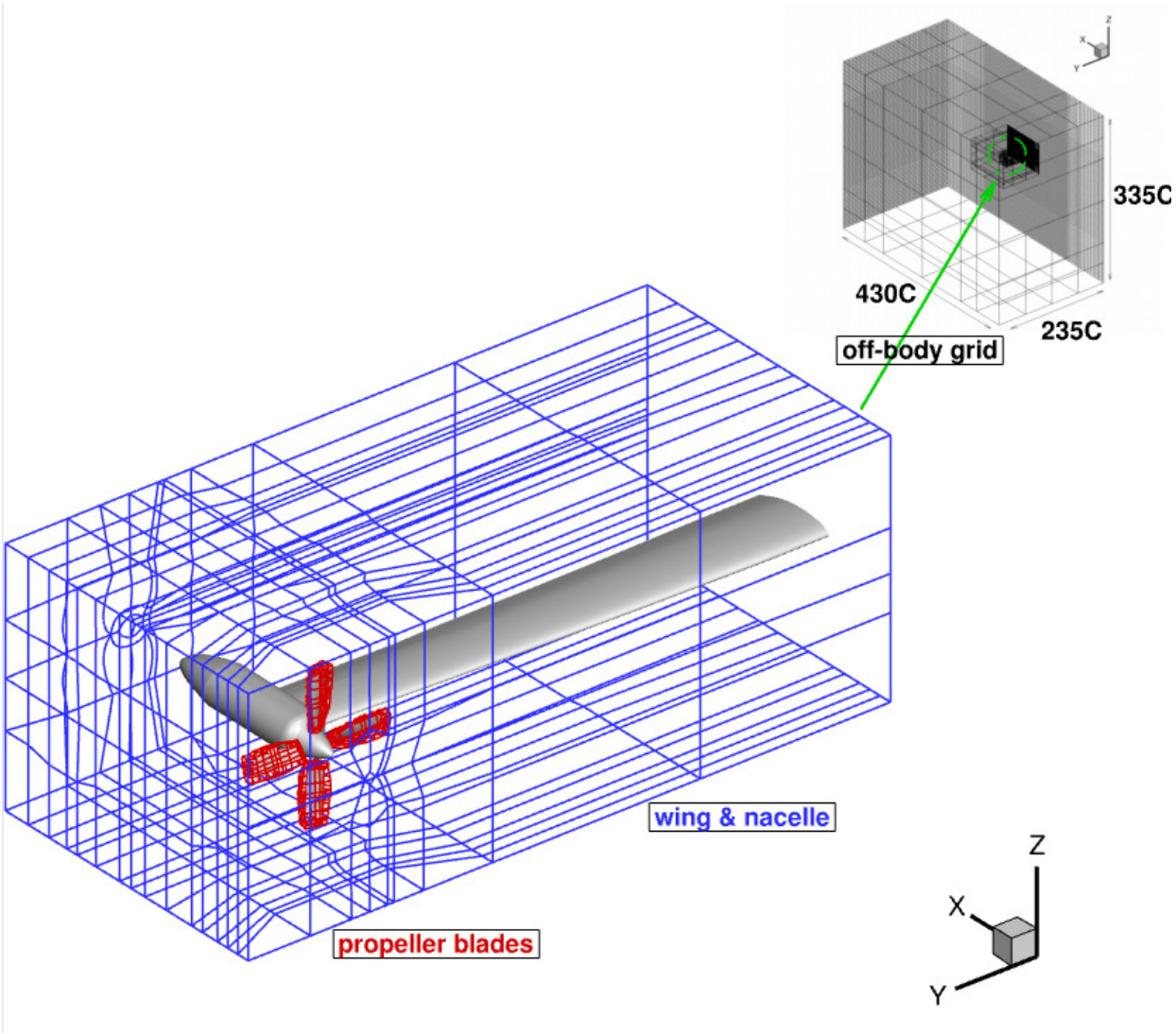

Figure 3.3: Grid topologies employed for the WIPP cases.

Table 3.5: Summary of conditions for Case 180 of WIPP.

Wingtip-mounted propeller:	
Pitch angle at $0.7R$ (degrees)	19.5
Test conditions:	
Free-stream Reynolds number (-)	0.08×10^6
Free-stream Mach number (-)	0.08
Rotational velocity (RPM)	8060
Target performance:	
Thrust coefficient (-)	0.4

3.2.2 Comparison with Experimental Data

The surface pressure coefficients at 2 degrees of wing angle of attack, the surface pressure data from various extracted locations at BL 60.75 and BL 57 are presented and compared in Figure 3.4. These locations were chosen, because the BL 60.75 strip is nearest to the impinging propeller tip vortex, and BL 57 is outside the propeller slipstream. From the sliced surface pressure coefficients, it can be seen, that the most interesting station is BL 60.75 of Figure 3.4(a), that is directly influenced by the propeller tip vortex. In comparison to BL 57, a significant increase in the suction peak and stagnation pressure was observed due to the propeller wake.

The difference between the SAS method and the URANS model in capturing pressure near the trailing edge arises from their respective treatments of turbulence and unsteadiness. In the present study, the URANS simulations may not resolve the pressure accurately near the trailing edge, likely due to insufficient mesh resolution or inadequate temporal resolution. Nevertheless, the URANS method remains accurate and efficient for capturing the average effects of turbulence in the context of interactional aerodynamics. More analyses involved extracting wing loading, surface pressure and wake profile data at the highest selected thrust and Mach number conditions. Using resolved blades, the wake profiles at 0 degrees of wing angle of attack, are compared at two distances in Figure 3.5. The propeller wakes at distances of +19.95 and +16.45 inches ahead of the trailing edge of the nacelle are in good agreement with the experimental data. Due to the unsteadiness of the wake, time averaged CFD results were provided and compared with test data. The validation studies presented in this section demonstrated that the propeller wake and wing interaction were accurately predicted, and resolved. More specifically, the AD method accurately captures the suction on the upper surface and the pressure on the lower surface of the wing, indicating that this reduced-order approach, with significantly lower computational cost, is promising for wing performance optimisation. However, the AD method lacks the capability to resolve the variations in propeller performance across different installation locations. This limitation justifies the use of high-fidelity HMB3 simulations for accurate prediction and verification of propeller forces, wing loads, and the associated flow phenomena.

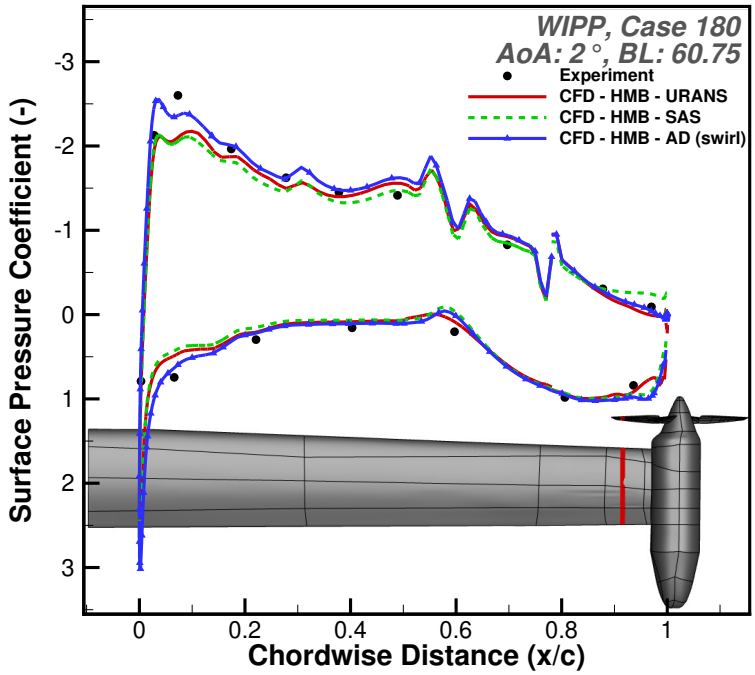

(a) BL 60.75

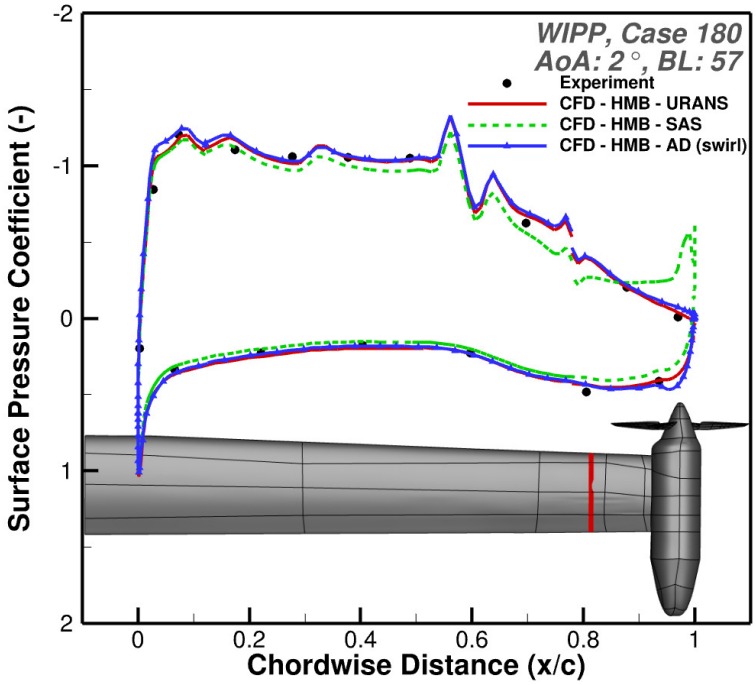

(b) BL 57

Figure 3.4: Comparison of the surface pressure results between experiments and CFD, where BL is the boundary layer position.

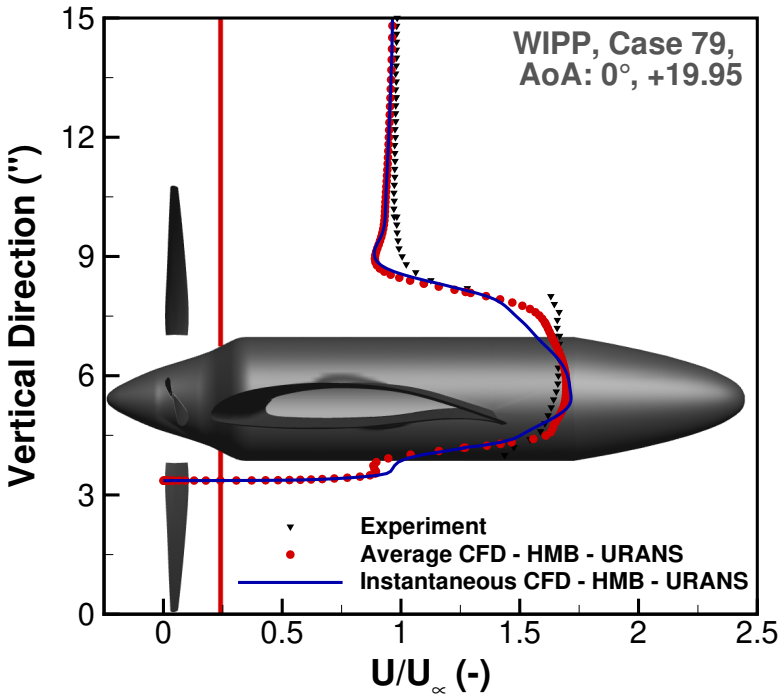

(a) Wake at 19.95 inches.

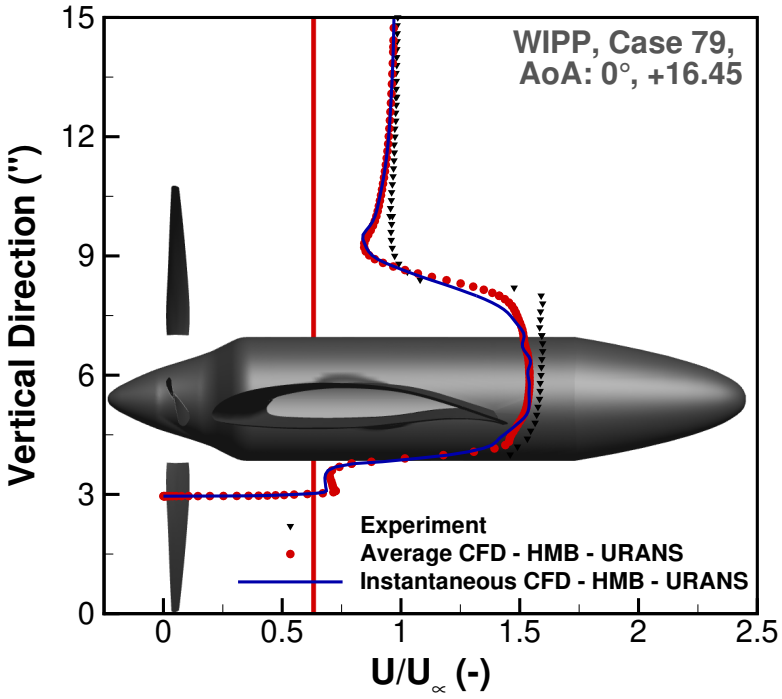

(b) Wake at 16.45 inches.

Figure 3.5: Comparison of the wake profiles between experiments and CFD, where the propeller wakes at distances of +19.95 and +16.45 inches ahead of the trailing edge of the nacelle.

3.3 GARTEUR AG26 Two Bladed Rotor

3.3.1 Test Cases Description

This section details the CFD grids, and tool validation, for isolated and tandem rotors. For isolated rotors in axial flight, Figure 3.6 illustrates the single-blade topology. A domain of 1 blade and the microphone positions used in the DLR acoustic wind tunnel are shown in Figure [73]. Figure 3.7 presents the rotor geometry and grid topology utilised for multi-rotor systems.

Table 3.6: Summary of the grid sizes utilised in tandem configurations for the GARTEUR AG26 DLR 13x7 rotor validation.

Grid Component	**Million Grid Cells**
Rotor 1	4.7
Rotor 2	4.7
Local Refinement 1	0.8
Local Refinement 2	0.8
Near-field	22.0
Far-field	0.8
Total	33.8

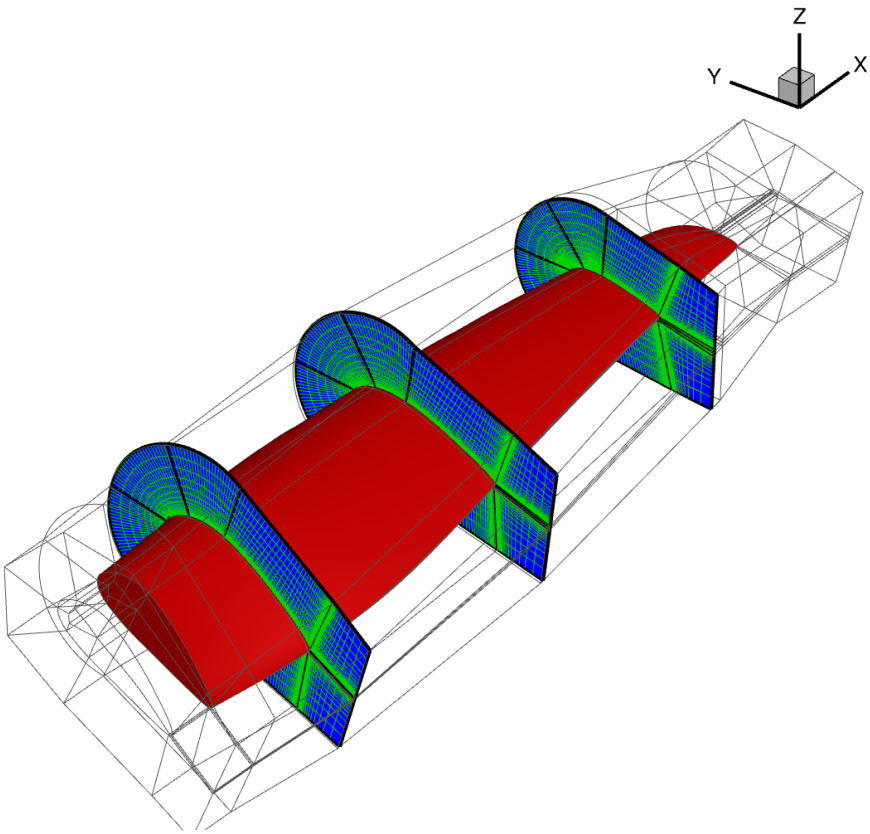

(a) Single blade mesh topology.

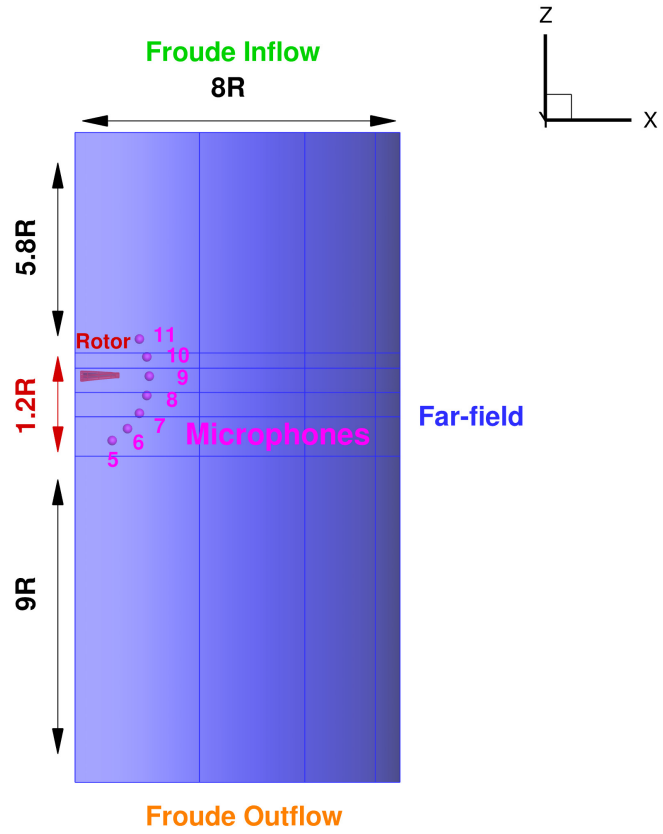

(b) Microphones positions.

Figure 3.6: Grids and microphones used for single blade steady simulations of GARTEUR AG26 DLR 13x7 rotor.

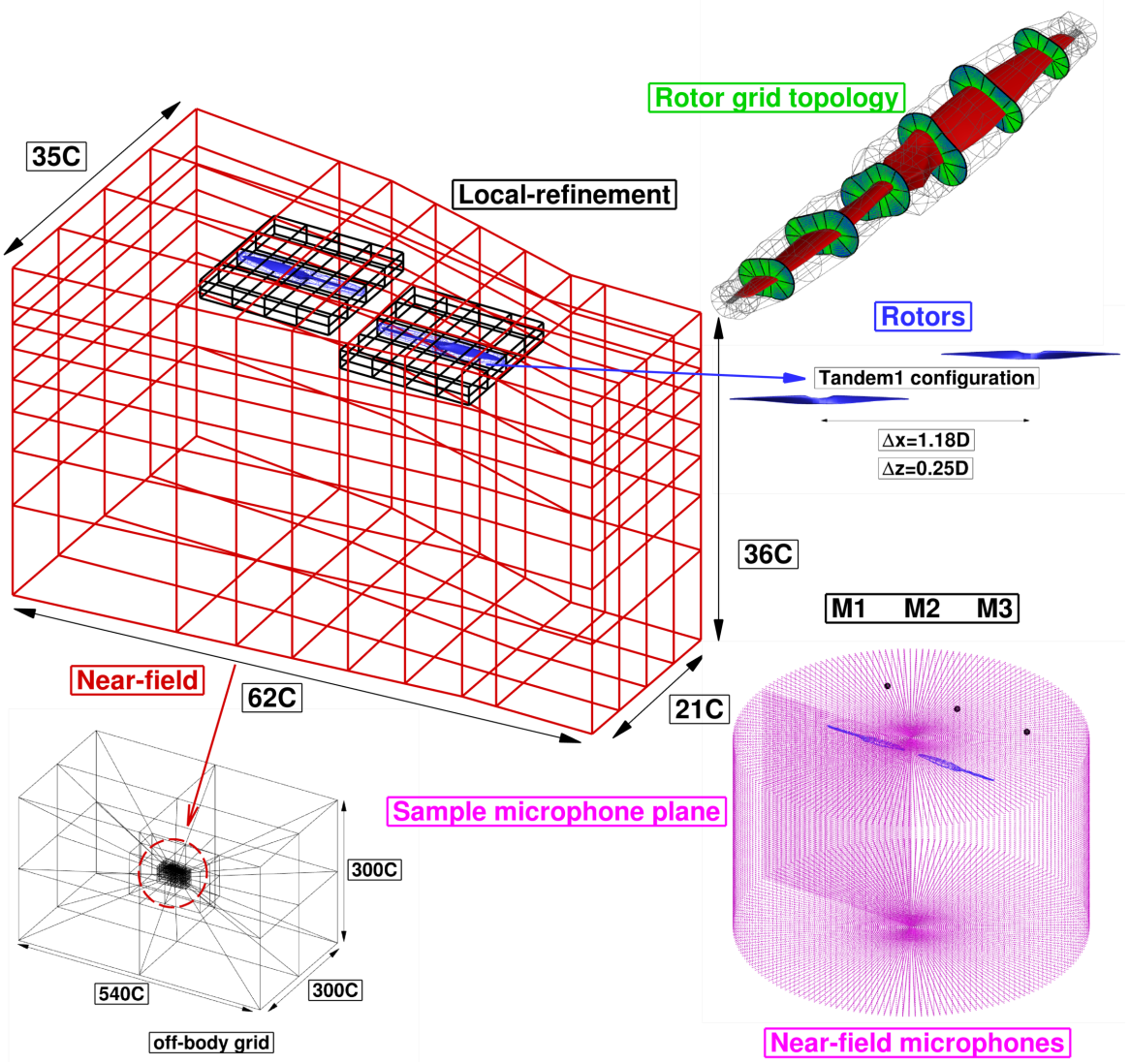

Figure 3.7: Grid topology used for HMB3 simulations of the GARTEUR AG26 multi-rotor cases. (Black dots represent upstream, interior, and downstream microphones. Pink dots represent a near-field volume containing a total of 1.8 million extracted pressure sampling points. Here, C represents the reference length used in the simulation, while D denotes the rotor diameter.)

3.3.2 Comparison with Experimental Data

First of all, the aerodynamic load results for both isolated and tandem rotor configurations, obtained using HMB3, are presented in Figure 3.8, along with earlier experimental data from the CIRA/DLR joint campaign using PIV measurements [89, 84]. The numerical and experimental results show very good agreement, validating the accuracy of the high-fidelity simulations.

To assess the sensitivity of the obtained performance and of the acoustic results to the mesh, a convergence study was conducted using axial flight simulations as shown in Figure 3.9 [89, 73, 148]. The computed overall sound pressure level (OSPL) from HMB3 compares well with the measured data from microphones at various locations, as obtained in the experiments by DLR [74, 85, 86]. The mesh convergence study indicates that the cell size utilised, is sufficient for capturing tonal noise, except for the area directly under the rotor. Refining the grid in three directions resulted in improved noise predictions, particularly in the rotor tip region. This highlights the need for adequate cell spacing, especially in high-speed and wake regions.

This study also utilised the 13x7 DLR rotor [74] tests at cruise conditions. Flow visualisation (top and side views) reveals that the wake of the isolated rotor in edge-wise flight is well-resolved, see Figure 3.10. A time step convergence study was conducted, as depicted in Figures 3.10. Noise directivity was directly extracted from the HMB3 results, and compared with the experiments. The results suggest that a time step of 1 degree per step yields a similar sound pressure level (SPL) as the 2 degree per step. The 1-degree simulation predicted a slightly higher SPL at 12,000 rpm. The time step sizes applied in this work were deemed sufficient to capture the noise directivity at different flight speeds and conditions. The agreement between simulation and experiments further confirms the reliability of the numerical approach in predicting the acoustics of these high-RPM rotors.

For the tandem configurations, the size and topology of the grids are presented in Table 5.2, and Figure 3.7, whereas Figure 3.11 shows the validation results cross-plotted with experiments [73].

The agreement between the simulations and experiments confirms the accuracy and relia-

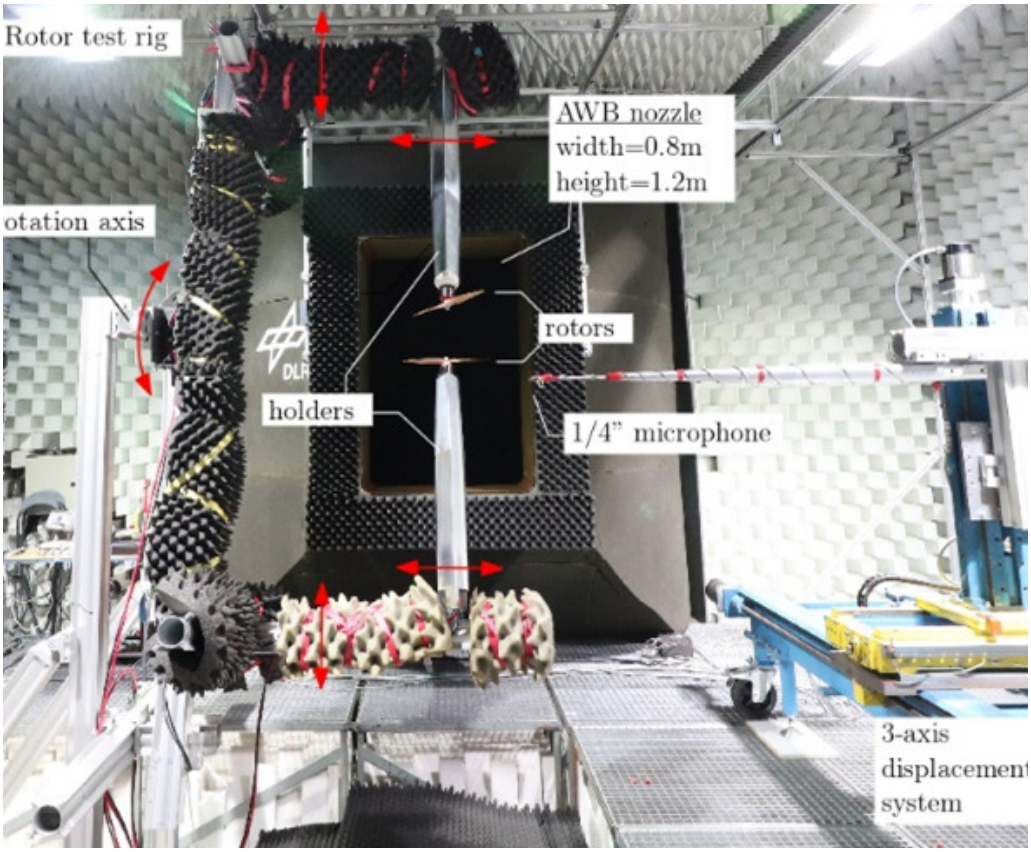

(a) Full test rig and microphone setup installed in the AWB's section.

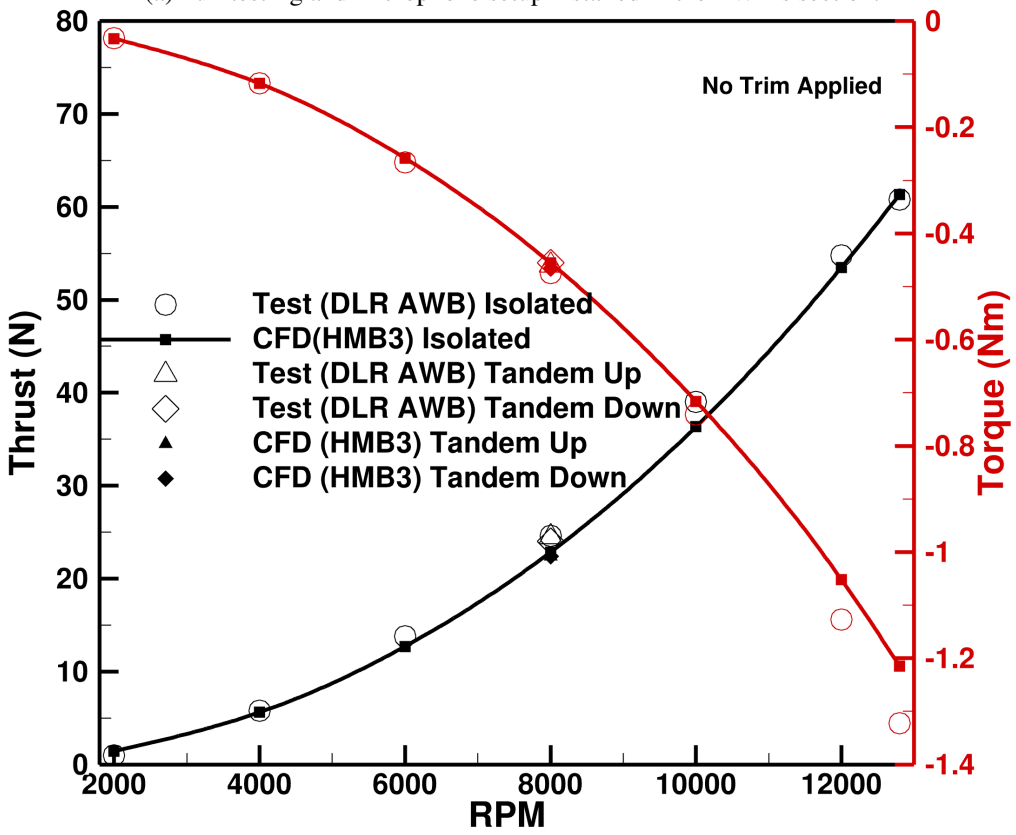

(b) Aerodynamic loads.

Figure 3.8: Comparison of the isolated and tandem vertical offset DLR 13x7 rotor performance predicted by the HMB3 solver and measured in the DLR AWB wind tunnel. [87]

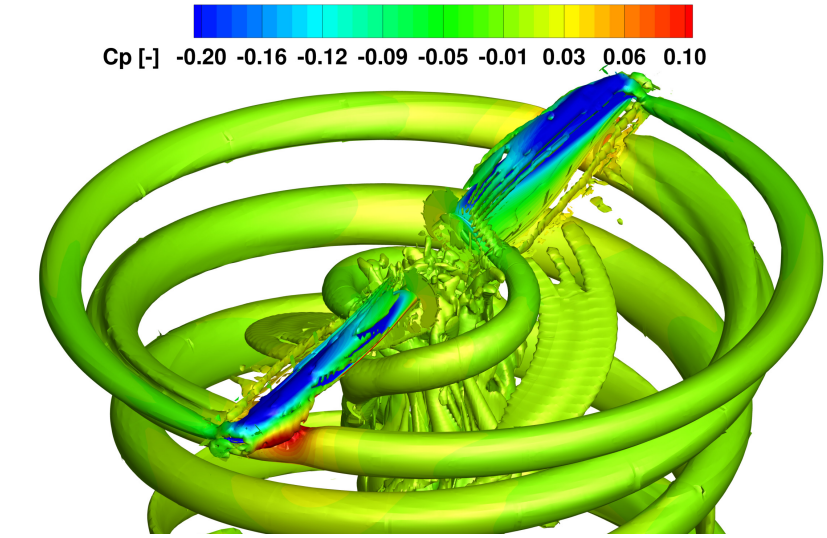

(a) Wake visualisation.

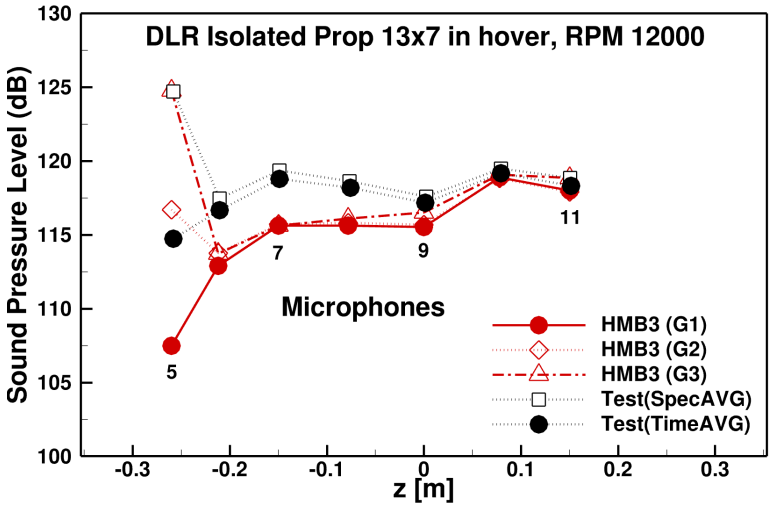

(b) OSPL comparison.

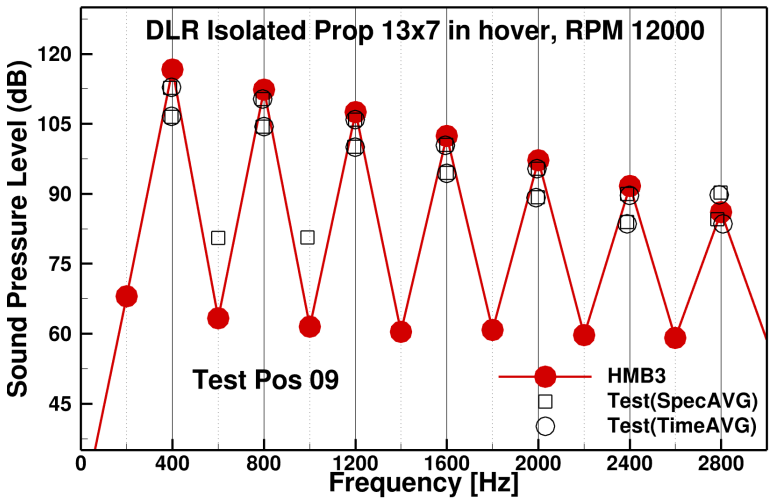

(c) Microphone 9.

Figure 3.9: Validation of DLR 13x7 isolated in hover flight. (a) Wake visualisation of isolated rotor at 12,000 RPM. (b) and (c) Acoustic validation of isolated rotor with multiple grid resolutions in hover flight at 12,000 RPM, compared with data from [87]

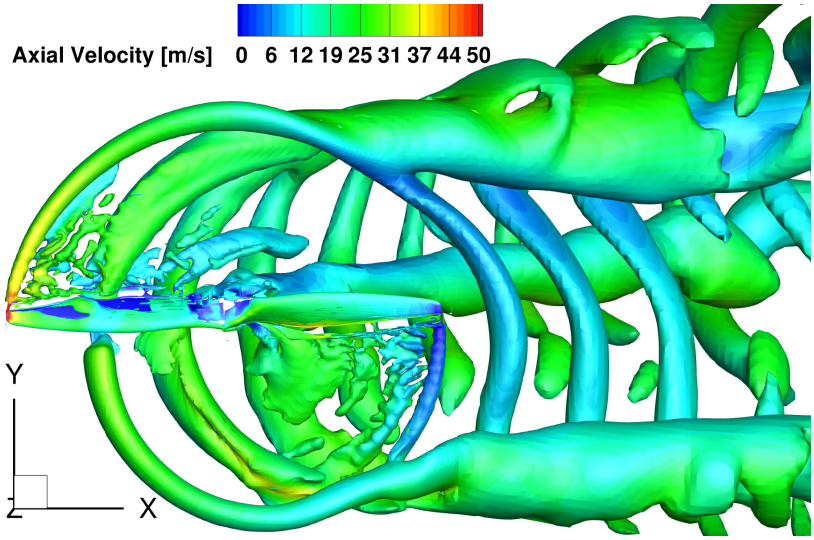

(a) Wake visualisation in edge-wise flight.

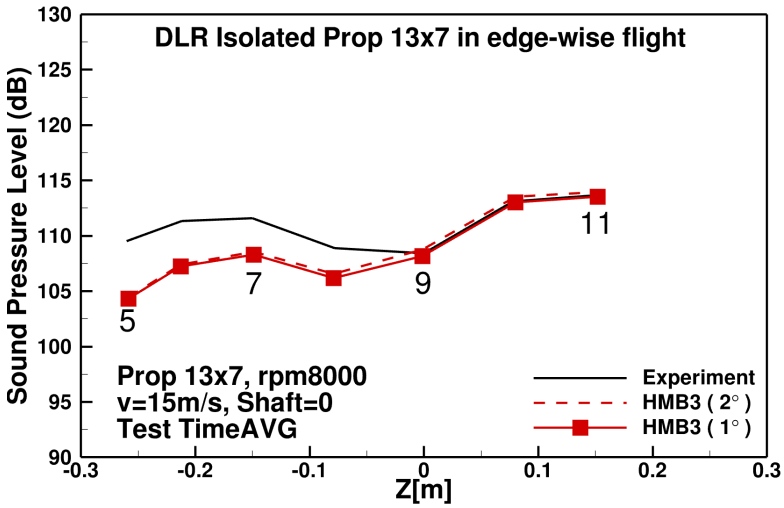

(b) OSPL in edge-wise flight, $\mu = 0.109$.

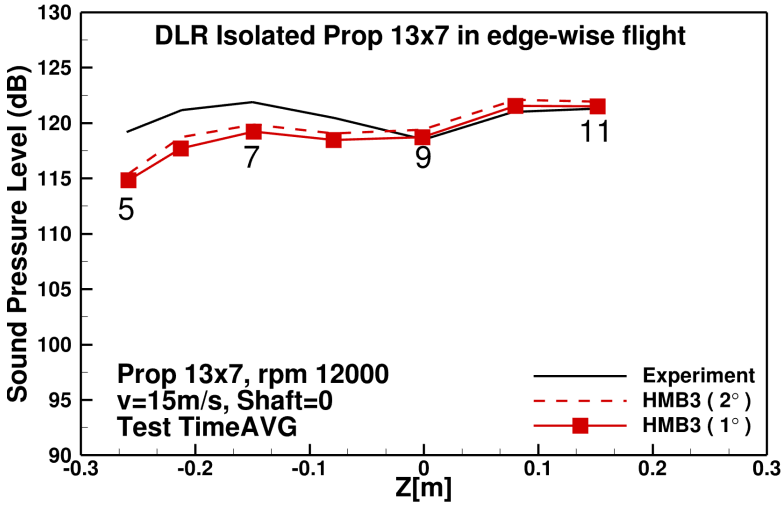

(c) OSPL in edge-wise flight, $\mu = 0.073$.

Figure 3.10: Validation of DLR 13x7 isolated in edge-wise flight. (a) Wake visualisation of isolated rotor at $\mu = 0.109$. (b) and (c) Time step refinement study in edgewise forward flight at 15 m/s and 8,000 to 12,000 RPM, compared with data from [73].

bility of the HMB3 CFD method in predicting the aerodynamic performance and acoustics of the isolated and multirotor systems. Verification results, shown in Figures 3.9 (b) and 3.10 (c), suggest that the isolated rotor, in hover and edgewise flight, at the same RPM exhibits a consistent noise directivity pattern. An increase in RPM, as illustrated by the comparison between Figures 3.10 (b) and (c), does not alter the directivity pattern, but results in a higher SPL. The spectrum shown in Figure 3.9 (c) highlights the harmonic frequencies associated with the BPF at 400 Hz, the half BPF SPL observed in the experiment is likely caused by factors such as uneven blade spacing, non-uniform inflow, unbalanced blades, nonlinear flow interactions, and even motor noise. However, in our simulations, the half BPF primarily results from the finer frequency resolution of the FFT, achieved by increasing the number of samples or extending the sampling period. This improved resolution enables us to capture nonlinear noise contributions, such as those caused by blade vortex shedding and similar effects. In conclusion, the findings suggest that neither flight condition, nor the RPM significantly affect the noise directivity pattern; instead, they primarily influence the SPL.

For the tandem rotor with a vertical offset in hover flight, an asymmetric directivity pattern from left to right is shown in Figure 3.11 (b). Additionally, the harmonic frequency matches the BPF of 267 Hz, as shown in Figure 3.11 (c), indicating that the harmonic frequency remains unaffected by the tandem offset configuration.

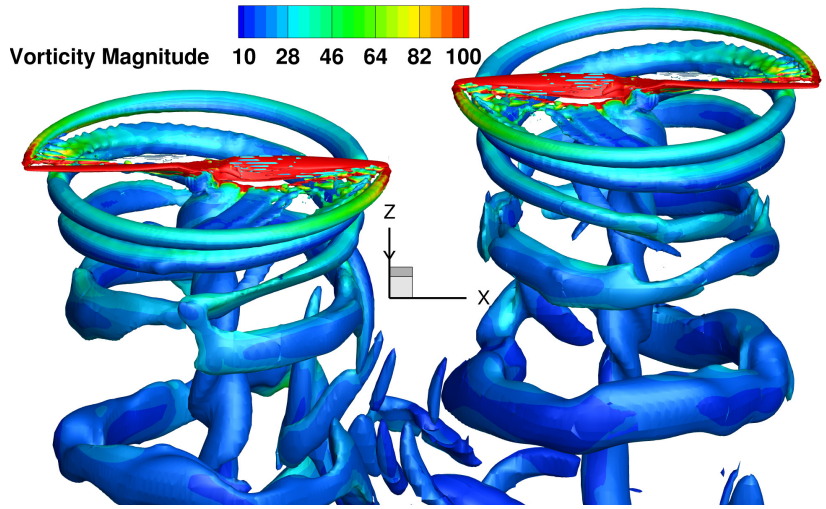

(a) Wake visualisation in hover flight.

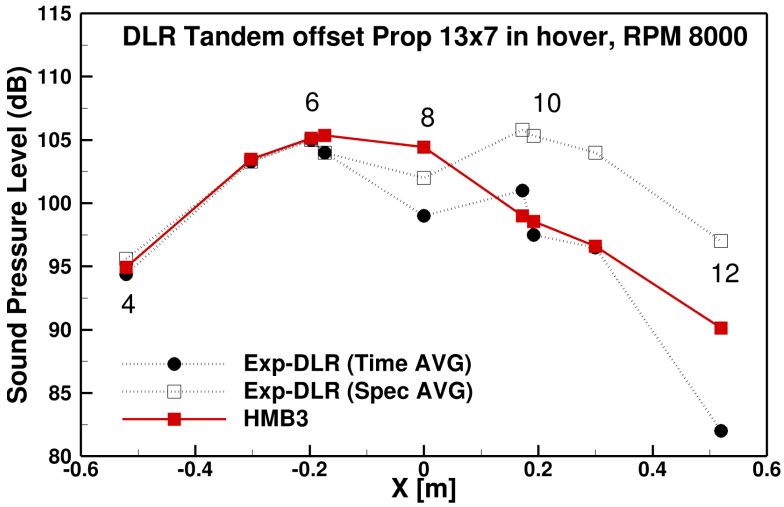

(b) OSPL comparison.

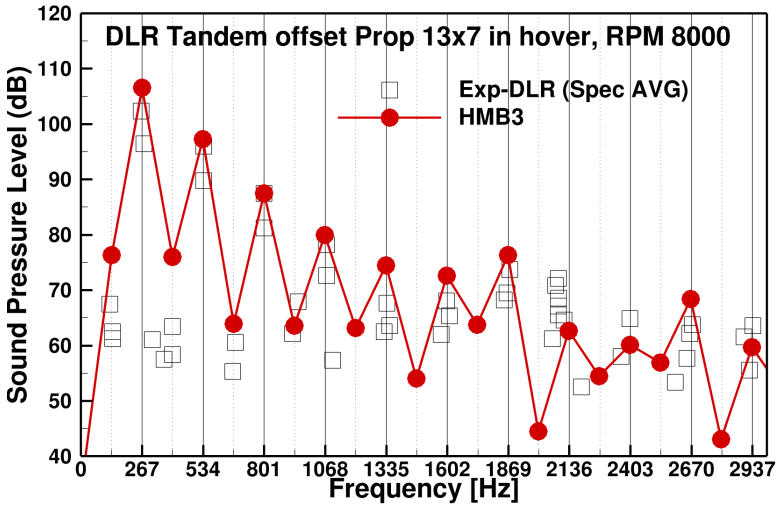

(c) Microphone 6.

Figure 3.11: Validation of DLR 13x7 tandem rotor. (a) Wake visualisation of tandem offset rotor in hover flight at 8,000 RPM. (b) and (c) Acoustic validation of tandem vertical offset configuration in hover flight at 8,000 RPM, compared with data from [87]

3.4 GARTEUR AG26 Three Bladed Propeller (synchrophasing)

As part of the GARTEUR group activities, CIRA and the University of Cusano carried out a joint experimental campaign investigating twin propellers in hover [149], while researchers from the University of Glasgow conducted corresponding numerical simulations using the same setup. This activity evaluated the effect of propeller separation distance, the phase angle, and the sense of rotation on the performance and acoustic properties. Different from the work conducted by NASA [78], this activity applied the 3-bladed propeller, which adds to the complexity of the synchrophasing study due to the increased aerodynamic/acoustic interactions. To this end, this work for the first time carried out the assessment of synchrophasing via multi-fidelity methods, including analytical methods, HMB3-FWH, and compared it with the experimental data [149].

3.4.1 Test Cases Description

The acoustic measurements were conducted in a semi-anechoic chamber as shown in Figure 3.12, and the test detail is given in Table 3.7. The microphone locations are visualised in Figure 3.13, where the red microphones in the vertical plane are representing the measurement locations used in the CIRA-CUSANO experiment campaign and the rotation plane microphones represented by the blue dots are calculated using the analytical methods. Finally, both vertical and rotation planes are examined using hybrid methods, HMB3-FWH.

3.4.2 Comparison with Experimental Data

The flow of the CIRA-CUSANO isolated propeller at hover condition with 5200 rpm is visualised in the Figure 3.14. Loads are cross-plotted between the measurement and predicted solution at a sweep of RPMs, showing that HMB3 solutions are within the error bar of the experimental measurements for both isolated and twin propeller configurations with 1.02d separation distance. The load history also shows that smaller propeller separations have stronger load fluctuations compared

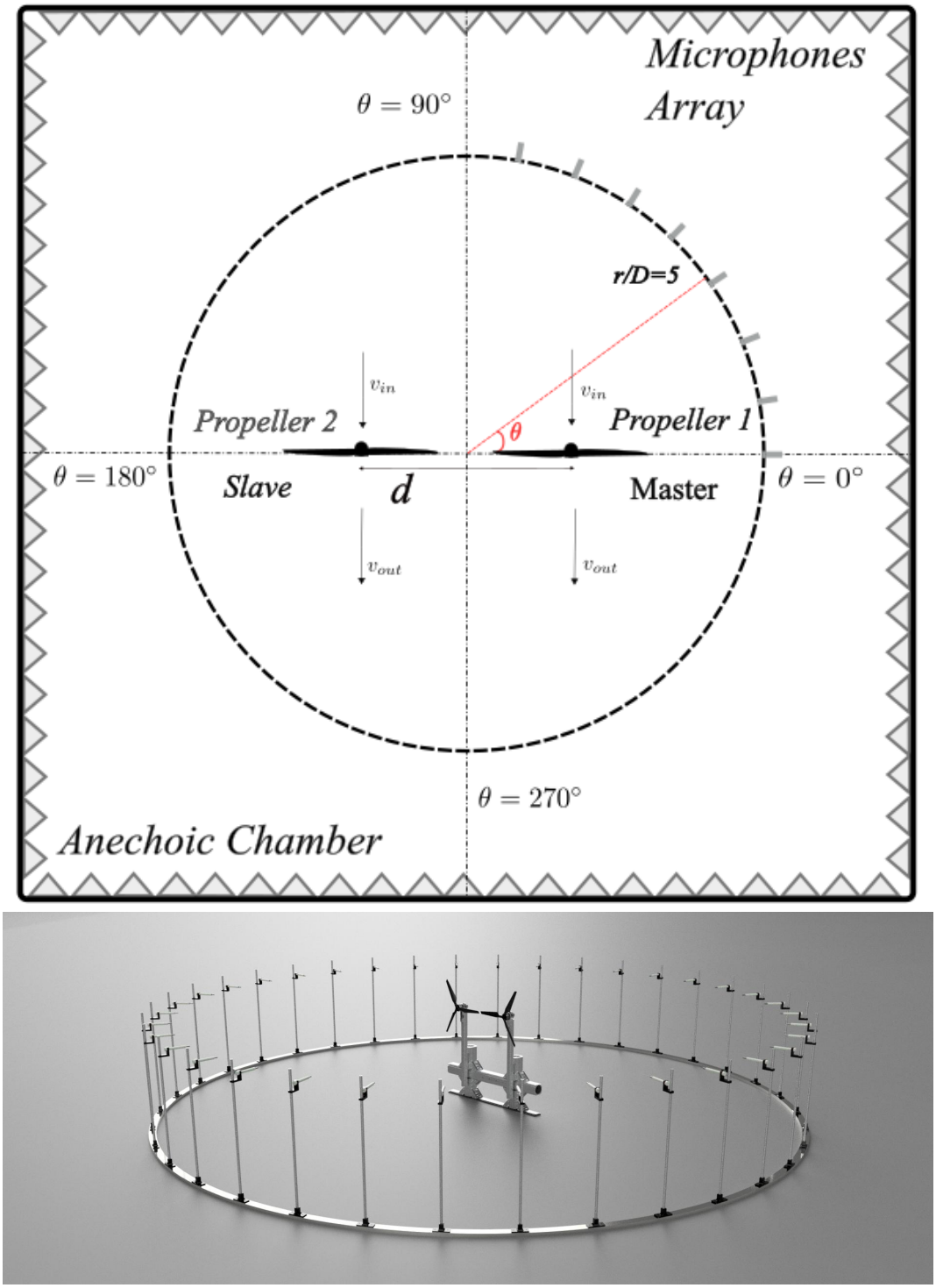

Figure 3.12: Experimental setups in the anechoic chamber of Uni Cusano.

with the larger propeller separation distances. In addition, increasing the separation distance, the fluctuation of loads history is reduced. Compared to the isolated propeller, a performance drop is seen for both twin propeller cases with different separation distances.

Table 3.7: Summary of the test condition used for GARTEUR AG26 CIRA 3-bladed rotor used in the study of far-field noise.

Condition	Hover (0m/s)
Radius	0.197 m
RPM	5200
Blade tip Mach number	0.312
Number of Microphones	36 with azimuth range $0^\circ \sim 360^\circ$
Coordinates	Vertical and rotation plane
Distance	5D
Configuration :	
Isolated	-
Twin	$\Delta x = 1.02d$, $\Delta y = 0$, $\Delta z = 0$
Twin	$\Delta x = 1.10d$, $\Delta y = 0$, $\Delta z = 0$
Rotation :	
Co-rotating	Counterclockwise
Sychrophasing :	
De-phased angles studied	0° & 60° & 90°

Table 3.8: Comparison of the experiment, HMB3 FWH, and analytical methods regarding the acoustic directivity in the rotation plane at different propeller separation distances and phase delay angles.

case	Δ Exp	Δ HMB3-FWH	Trend
Azimuth 0:			
1.02d Phase0	baseline	baseline	-
1.10d Phase0	-5.6%	-3.7%	same
Azimuth 180:			
1.02d Phase0	baseline	baseline	-
1.10d Phase0	-5.1%	-0.7%	same
1.10d Phase60	+4.9%	+4.1%	same

The effect of the noise emissions due to the change of the propeller separation distance and phase delay at different locations is reported in Table 3.8. The baseline noise levels are set as the 1.02d with phase 0 case. Results from experiments and HMB3-FWH predictions at azimuth 0 show similar trends, both with noise reduction by increasing the propeller separation distance. A similar trend from both methods is also observed at azimuth 180. Both blades are in phase in the 60 $^\circ$ phase delay case, where the increased noise level is obtained via both experiments and HMB3-FWH results.

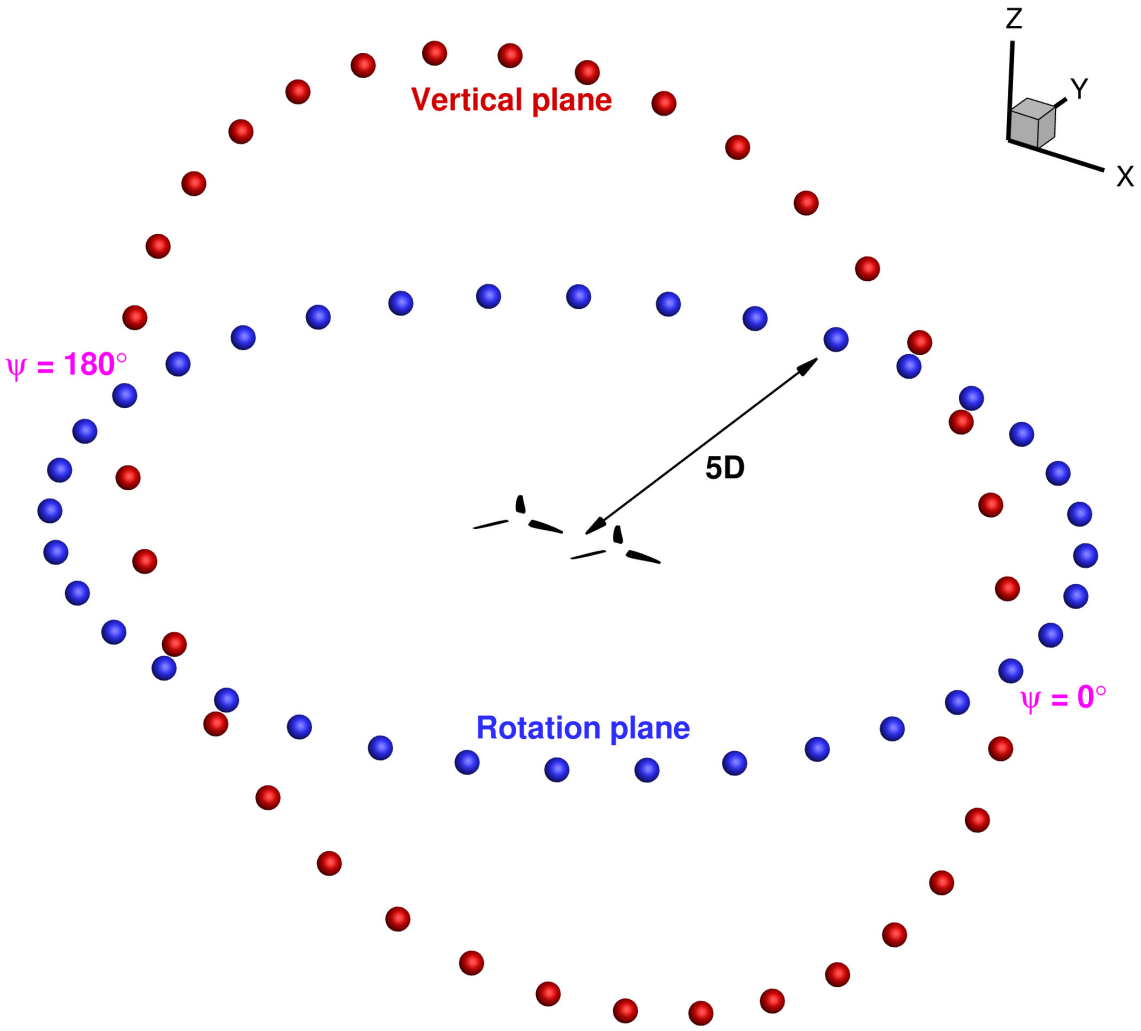

Figure 3.13: The position of microphones.

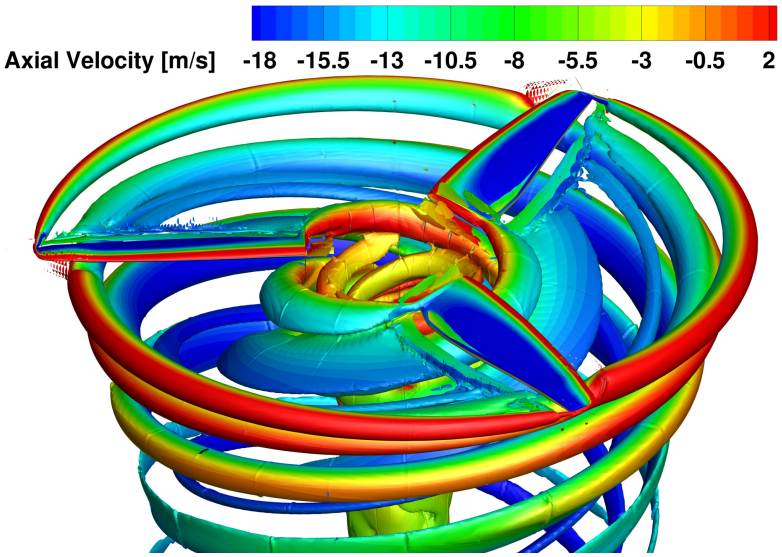

(a) Flow visualisation.

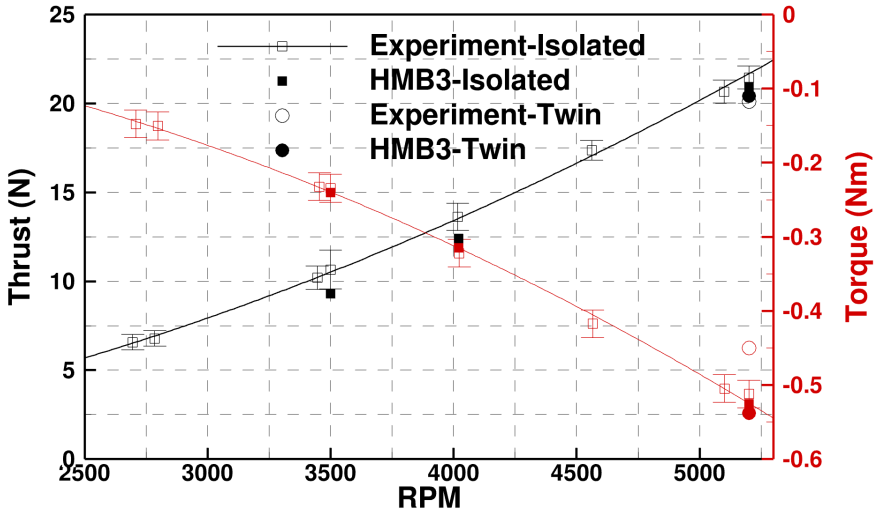

(b) loads.

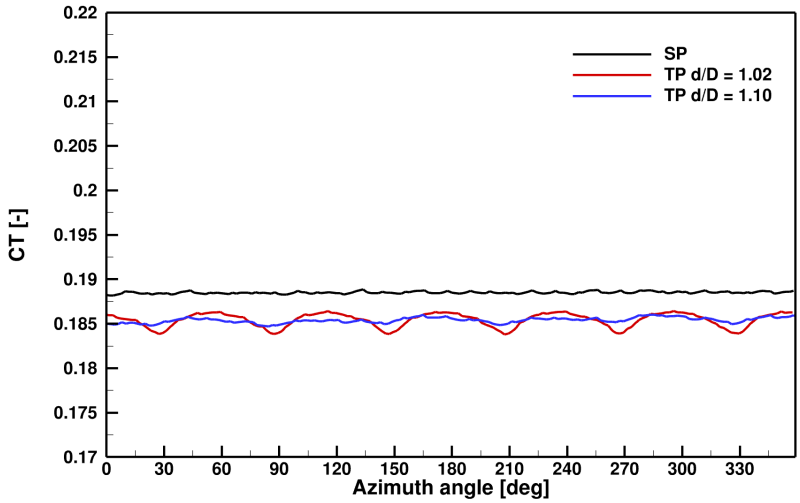

(c) CT history.

Figure 3.14: Validation of aerodynamic performance for GARTEUR AG26 CIRA three-bladed propeller.

3.5 Chapter Summary

Based on the presented results, the wingtip mounted propeller geometry from the WIPP project was simulated using CFD methods, and was compared with experimental data. A combination of resolved blade models and actuator disk models were employed in the CFD. The surface pressure coefficients, at wing stations, were found to be in good agreement between the CFD and experimental data. The resolved blade models captured better of the wake effect across the wing, while the SAS method captured more of the wake downstream. However, the actuator disk models failed to capture unsteady effects, but were able to provide the average slipstream.

In addition, this work conducted CFD simulations of propellers in isolated and tandem configurations, comparing them with the experimental database acquired during the development of the X-57 'Maxwell' electric aircraft, and from the GARTEUR AG 26 work. The results demonstrated that the simulation methods employed in this study captured the performance and associated flow phenomena, and the strong rotor-wing, rotor-rotor interactions.

Through validation studies, it was observed that neither flight conditions nor RPM, significantly changed the noise directivity pattern; instead, they primarily influenced the SPL. Spectrum analysis further revealed that the sound frequencies remained consistent with the BPF when transitioning from the isolated rotor to the tandem offset configuration.

The feasibility of the hybrid HMB3-FWH method in the acoustic prediction is further validated for the three-bladed propeller. Current work showing hybrid methods shows very good agreement at different propeller separation distances and sychrophasing angles. Increasing the propeller separation distance and moving the propeller out of phase tends to reduce the noise emissions.

Chapter 4

Distributed Propulsion

This chapter has been published as: Geng Qiao, Tao Zhang, George Barakos., "Numerical Simulation of Distributed Propulsion Systems Using CFD," Aerospace Science and Technology, (2024) doi: 2024.109011

Following the validation of the CFD method isolated (HLP), multirotor (GARTEUR AG26), and installed (WIPP) configurations. This chapter presents on investigation of the Distributed Propulsion (DP) concept, along with CFD verification, optimisation, and evaluation. This work started from examining the single and multiple installed auxiliary propellers using the actuator disk method to understand the variation of the wing performance due to the propeller installation with significant reduced complexity and cost. By approaching the optimum propeller installed location, fully resolved simulations were carried out to examine the installed propeller configurations to identify individual and overall performance differences based on their position relative to a lifting wing and compared with conventional tractor configuration. Following this, one, two, and three propellers were installed, and simulated to examine the performance of different distributed propulsion systems.

4.1 Propeller location optimisation

4.1.1 Single auxiliary propeller

An optimised DP system was studied using the actuator disk method, and a Kriging model [150], based on the WIPP geometry. The smaller propellers were scaled to match the overall size of the X-57. The initial study focused on positioning a single propeller to maximise the lift-to-drag ratio of the wing. The effectiveness of the auxiliary propeller was evaluated at nine locations along the wingspan, and above/below the wing [151].

Figure 4.1, shows the results for the lift-to-drag ratio across the examined region. The propeller positioned above the wing yields the highest lift-to-drag ratio over the nine positions analysed. This agrees with trends reported in the literature [51, 52], and is a result of the acceleration of the flow over the upper surface of the wing, which increases the suction. Placing the propeller at the highest position above the wing, reduced the drag force acting on the wing by preventing the wake from fully impacting on the wing. Relocating the propeller below the wing would also decrease the drag, but would not cause flow acceleration over the suction side, thus diminishing the lift increment. It was found that there is minimal disparity between the three span-wise locations tested across all vertical heights.

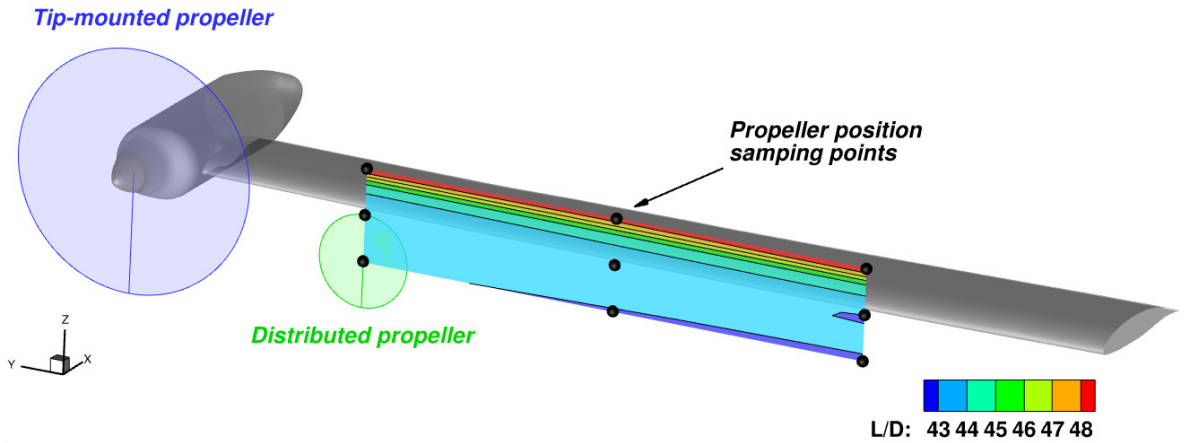

Figure 4.1: Optimisation for a single propeller.

4.1.2 Multiple auxiliary propellers

Subsequent computations concentrated on the overall performance of the complete DP setup and how the placement of propellers affected it, as illustrated in Figure 4.2(a). The propeller parameters and the operating conditions for the current study are given in Table 4.1. The six auxiliary propellers were uniformly distributed across the wingspan, and situated ahead of the wing's leading-edge at a minimum distance of 0.04 m. This corresponds to the tip chord length of the wingtip propeller, as represented by the dash-dot line in Figure 4.2(a). The distributed propellers were relocated to different positions, as illustrated by the red points in Figure 4.2(a). The corresponding performance changes were evaluated through CFD calculations. Kriging response surfaces were then constructed based on the variation of locations in wing chord-wise and vertical directions, and respective CFD results to analyse the performance alterations cased by the propeller placements.

Table 4.1: Parameters and operating conditions of the DP configuration employed in the optimisation using the actuator disk method.

Free-stream velocity	27.22 m/s
Angle of attack	2.09 degrees
Tip-mounted propeller:	
Propeller C_T, C_Q	0.038, 0.0098
Auxiliary propellers :	
R_{AP}	0.0782 m
R_{TP}	0.2058 m
R_{AP}/R_{TP}	0.38
Propeller C_T, C_Q	0.015, 0.004
Formation	Even distribution along wing span

All six propellers were relocated to different positions while maintaining their relative positions to each other. Figure 4.2(b) illustrates the range of the studied propeller positions at a wing section. The parametric investigation included alterations in position along the x- and z-directions. The longitudinal and vertical displacements, with respect to the initial configuration, were normalised using the auxiliary blade radius (R_{AP}) which is scaled based on the WIPP experimental size. A total of fifteen sampling points were examined, which included the initial baseline position. Each instance was designated by a coordinate, representing its displacement from the initial

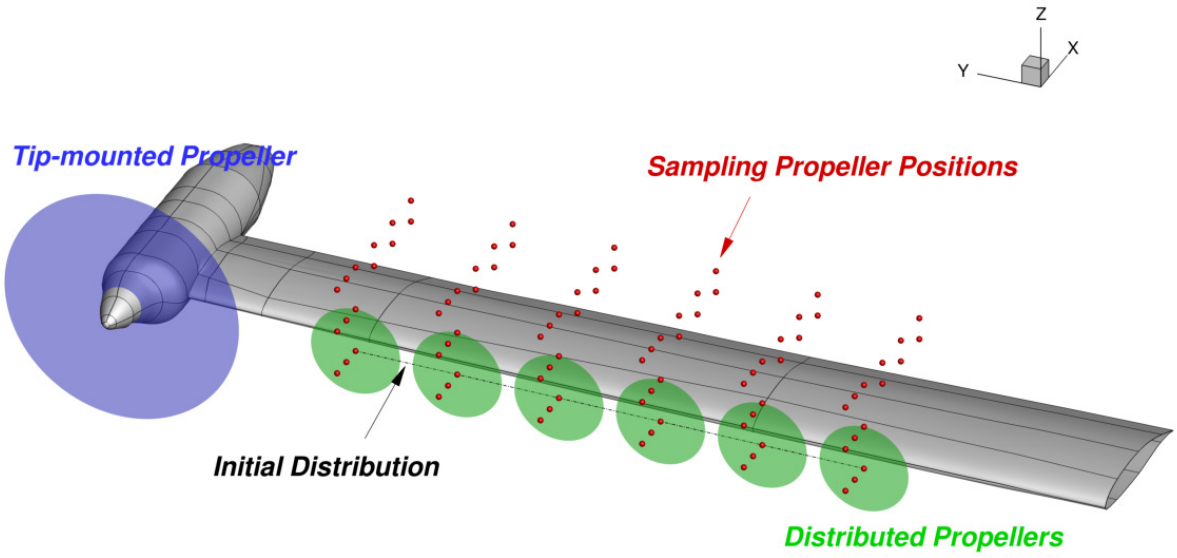

(a) Illustration of the studied DP configuration and the sampling propeller positions.

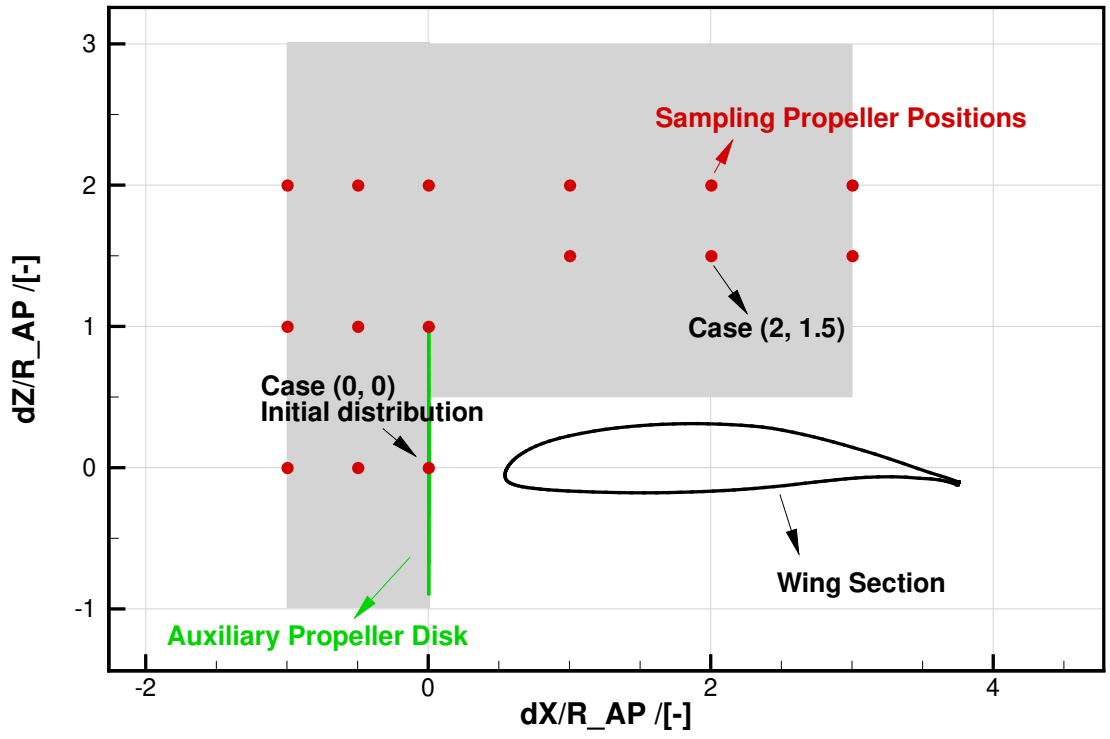

(b) Investigated range of the propeller positions at a wing section. The x and z changes were normalised using the auxiliary propeller radius R_{AP} based on the WIPP wind tunnel scale. The grey area represents the boundaries of the propeller disk.

Figure 4.2: Locations of the actuator disks around the wing.

location, as shown in Figure 4.2(b).

It is important to note that the span-wise positions of the propellers could not be changed due to geometric limitations. As shown 4.1.1, for a single propeller, positioning it below the wing would not enhance the overall performance. As a result, the current sampling sets concentrated on positions above the wing, and along the stream-wise directions.

In reduced order simulations from this section, all propellers were modeled using actuator disks. Figures 4.3(a) to 4.3(c) present the surface pressure solutions of three tested configurations, including the baseline configuration with only the tip-mounted propeller. Subsequent analyses were focused on the performance variations relative to the baseline scenario. The distributed auxiliary propellers were assigned sequential numbers ranging from 0 to 5, from the outboard to the inboard direction. It was observed that the introduction of distributed propellers, and their placements, caused differences in the flow patterns. In the baseline solution, there was a single section of high suction pressure (indicated by dark blue) downstream the tip propeller, which remained consistent in all other cases. However, the installation of the auxiliary propellers increased the suction pressure towards the leading edge of the wing, compared to the baseline. In particular, for the (2, 1.5) configuration, the amplified suction pressure on the upper surface of the wing was more pronounced, with the influence of disks 2 and 3 extending close to the mid-chord region.

The alterations in wing lift and drag due to the changes in position of the distributed propellers are presented in Figures 4.4(a) and 4.4(b). The lift and drag alterations were standardised by the corresponding values of the baseline configuration, where only the tip-mounted propeller was used. With respect to lift, the installation of distributed propellers increased the wing lift across the entire range of positions examined. The highest lift augmentation, which was approximately 15%, was achieved when the propellers were placed in front of the wing, or close to the trailing edge and above the wing. On the other hand, the lowest lift increment, which was around 3%, occurred when the propellers were located further upstream, and considerably above the wing, where the wing could barely benefit from the propeller slipstream. The wing experienced a rise in drag($D_{lifting\,surface}$ in equation 2.60) of around 35% together with the lift increase when the propellers were positioned in front of the leading edge. Conversely, when the propellers were placed

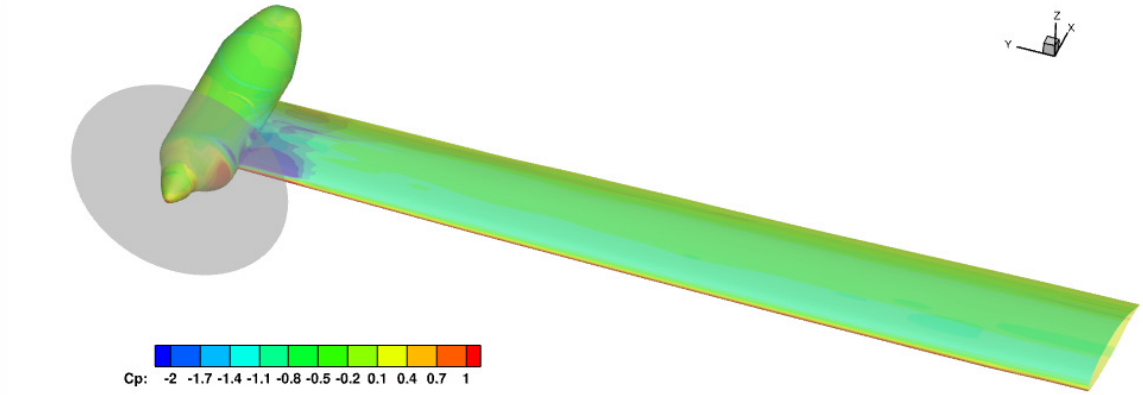

(a) Baseline configuration without auxiliary propellers.

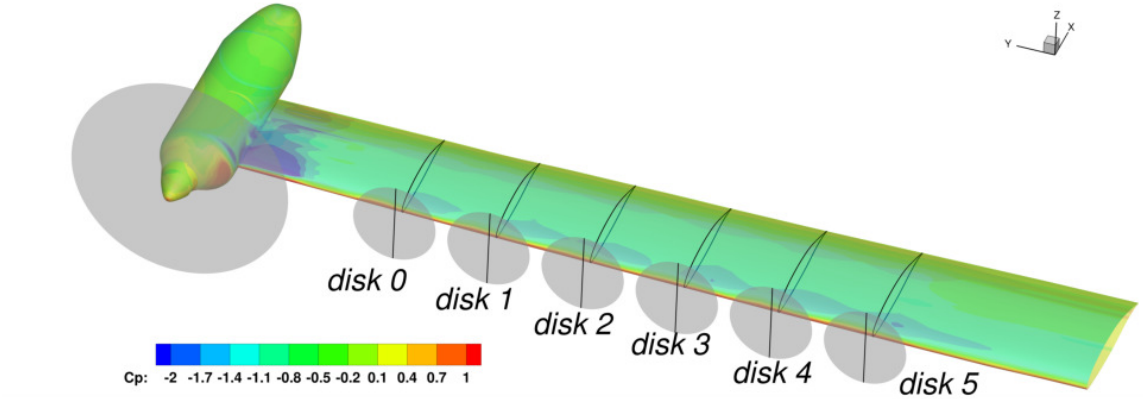

(b) Case (0, 0).

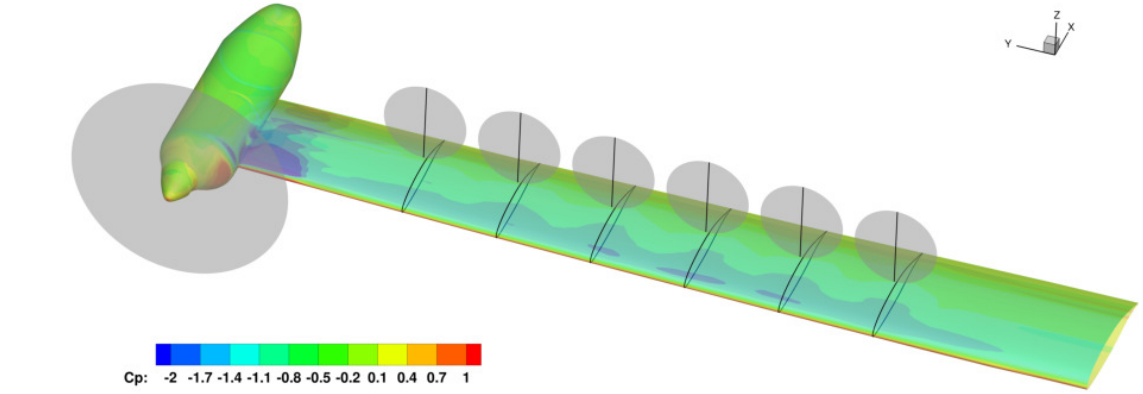

(c) Case (2, 1.5).

Figure 4.3: Surface pressure comparisons between the baseline configuration, the lowest L/D configuration case (0, 0), and the highest L/D configuration case (2, 1.5). The distributed auxiliary propellers were numbered from 0 to 5 from the wing tip to root.

above the wing near the middle chord (such as in Case (2, 1.5)), the wing drag was reduced by roughly 35%, while the lift was augmented by approximately 12%.

Figure 4.4(c) further presents variations of the wing lift-to-drag ratio brought in by the propeller position changes. As expected in Figures 4.4(a) and 4.4(b), the overall wing efficiency was reduced, when the propellers were placed upstream of the wing. Case (0, 0) (see Figure 4.2(b)) shows the largest lift-to-drag ratio reduction of about 10% compared to the baseline case. As the propellers were moved downstream, and placed above the wing, the wing efficiency was increased due to the increased lift and reduced drag as shown in Figures 4.4(a)(b). Case (2, 1.5), of Figure 4.2(b), showed the maximum lift-to-drag ratio increase of about 80% compared to the baseline case within the range studied.

Further comparisons between the baseline case, the most and least efficient configurations (Cases (0, 0) and (2, 1.5) of Figure 4.2(b)) among the tested sampling set were conducted to understand the differences. Figure 4.5 shows the sectional surface pressure distribution of the wing, at a slice passing through the innermost propeller disk (disk 5 of Figure 4.3(b)).

Compared to the baseline case, the pressure distribution of Case (0, 0) with the propellers in front of the wing leading edge showing decreased pressure on the suction side, and increased pressure on the pressure side, resulting in an overall increase in lift and drag. This effect is similar to increasing the free-stream velocity for the wing section. In contrast, for Case (2, 1.5) where the propellers were placed above the wing near the middle chord, the wing leading-edge suction was enhanced upstream of the propeller, and the pressure was slightly recovered through the propeller disk. These changes led to reductions in drag, and increases in lift, although the lift increment was less significant than that observed for Case (0, 0).

The sectional pressure force vectors presented in Figure 4.5 illustrate the surface pressure differences, and the impact on the forces for the three cases. In comparison to the baseline case without distributed propellers, both the Case (0, 0) tractor and Case (2, 1.5) OTW configurations clearly tilt the resultant pressure force vector forward, effectively increasing the angle of attack (AoA). Among these, the over-the-wing (OTW) configuration exhibits the largest increase in effec-

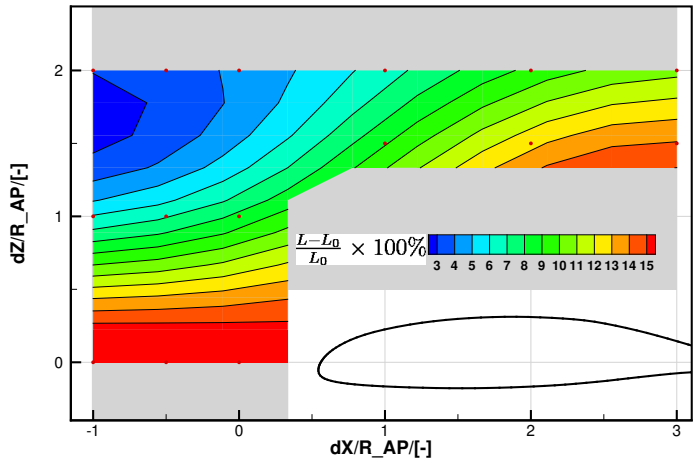

(a) Lift variations.

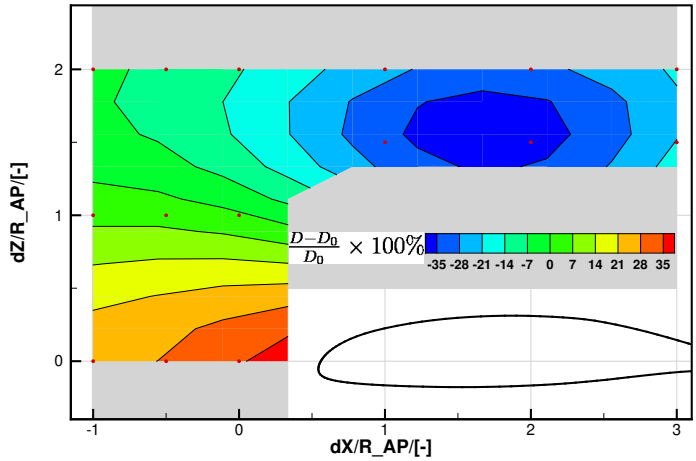

(b) Drag variations.

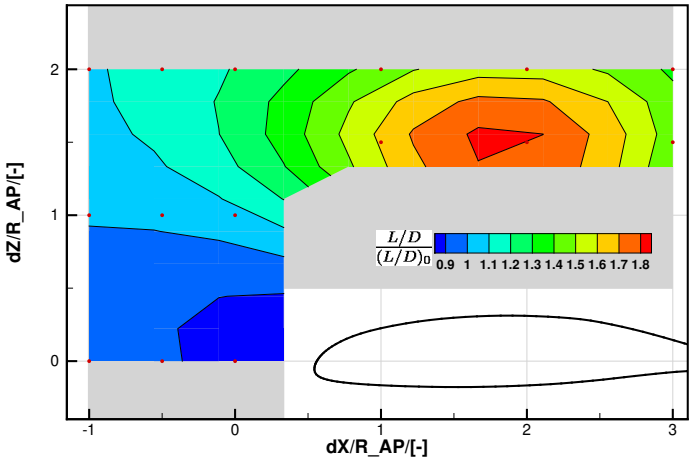

(c) Lift-to-drag ratio variations.

Figure 4.4: Wing lift, drag, and lift-to-drag ratio variations due to position changes of the distributed propellers. The x and z changes were normalised using the auxiliary propeller radius R_{AP} based on the WIPP wind tunnel scale. The lift and drag changes were normalised using the baseline values from Case (0, 0). The grey area represents the boundaries of the propeller disk.

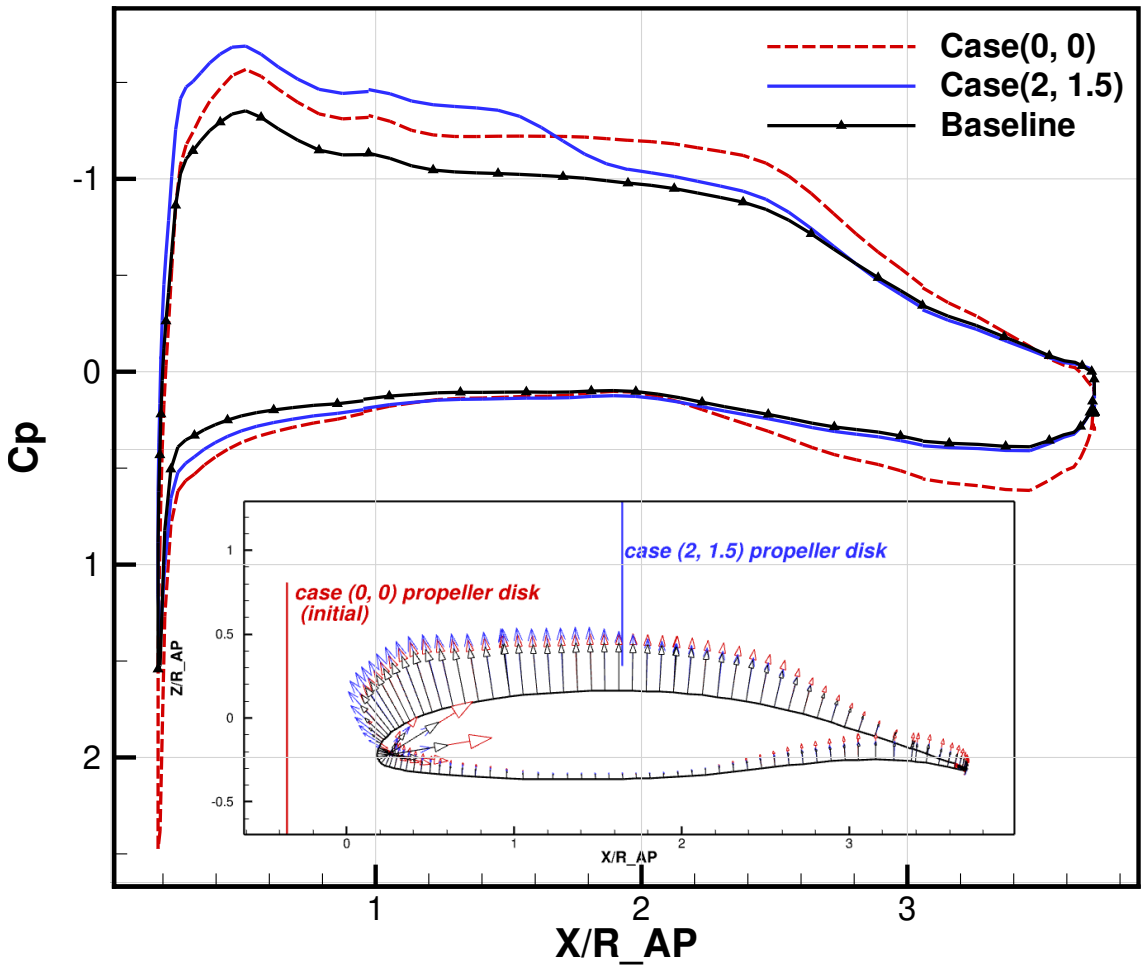

Figure 4.5: Sectional Cp distributions and pressure force vectors comparing the baseline case (clean wing), lowest L/D case (Case (0, 0), and highest L/D case (Case (2, 1.5)). The wing section through the inner-most auxiliary propeller (disk 5) is shown.

tive AoA, though this effect is primarily confined to the upper surface. Additionally, the pressure force vectors in the stagnation region, responsible for drag, are significantly amplified in the tractor configuration but substantially reduced in the OTW configuration. Overall, these findings suggest that the installed configurations enhance the effective AoA, leading to increased lift generation. However, in the OTW configuration, the reduced momentum injection near the leading edge helps to lower drag, thereby improving the lift-to-drag (L/D) ratio.

4.2 Single Propeller Installation Verification

In the preceding section on optimisation, the reduced-order method was utilised to approximately locate the optimal position of the distributed propellers. Nevertheless, the actuator disc method failed to capture the unsteadiness and swirling motion of the actual propeller wake, which impacts to the propulsion system. In addition, the performance of the propulsion system changes due to different installation effects. Furthermore, additional surfaces from nacelle and pylon structures, will also have impact on the propulsion system. Therefore, additional verification cases utilising high-fidelity methods 2.1 were carried out; see section 4.2. These investigations should include a single isolated propeller, installed tractor propeller, OTW and OTW with pylon configurations as shown in Figure 4.6. The condition investigated across all cases is shown in Table 4.2, and the employed grid topology and size are presented in Figure 4.7, and Table 4.3.

Table 4.2: Summary of the computational setup for distributed propellers

Freestream Reynolds number (-)	0.2×10^6
Freestream Mach number (-)	0.08
Rotational velocity (RPM)	4800
Pitch angle at $0.7R$ (degrees)	27.52

Verification studies using high-fidelity methods covered the baseline of the isolated HLP, installed in tractor, OTW, and pylon installed OTW configurations, as shown in Figure 4.8. All configurations were tested under identical conditions, including free-stream velocity, propeller pitch angle, angle of attack of the lifting surface, and propeller rotational speed. Installing the

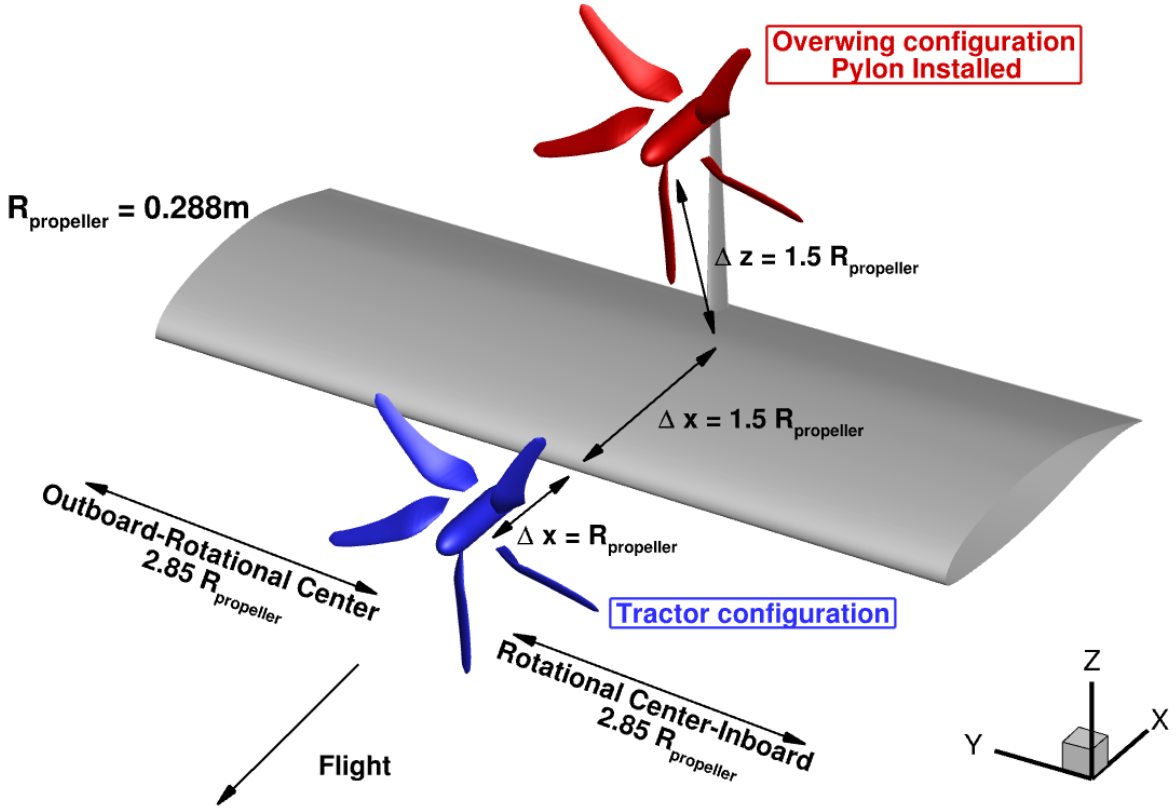

Figure 4.6: Schematic of tractor and OTW configurations, and the OTW configuration with pylon installed. A full scale of X-57 aircraft with $R_{propeller}$ equal to 0.288m and its corresponding lifting surface, are used in all verification cases.

Table 4.3: Summary of the grid size for single, installed, HLP; see Figure 4.7 for the mesh topology.

Grid Component	Volume Cells (Million)
Background	2.3
Lifting surface	44.5
Spinner	5.7
Distributed propeller	13.5
Total	66.0

propeller in front of the leading edge, a higher pressure region can be found after the propeller. The pressure recovered earlier compared to the isolated propeller and OTW configurations due to the swirl recovery from the wing and stagnation. In addition, placing the propeller OTW, further accelerates the flow along the upper surface of the lifting wing, and a higher suction region is formed. However, in the OTW configuration, the accelerated local flow increases the effective

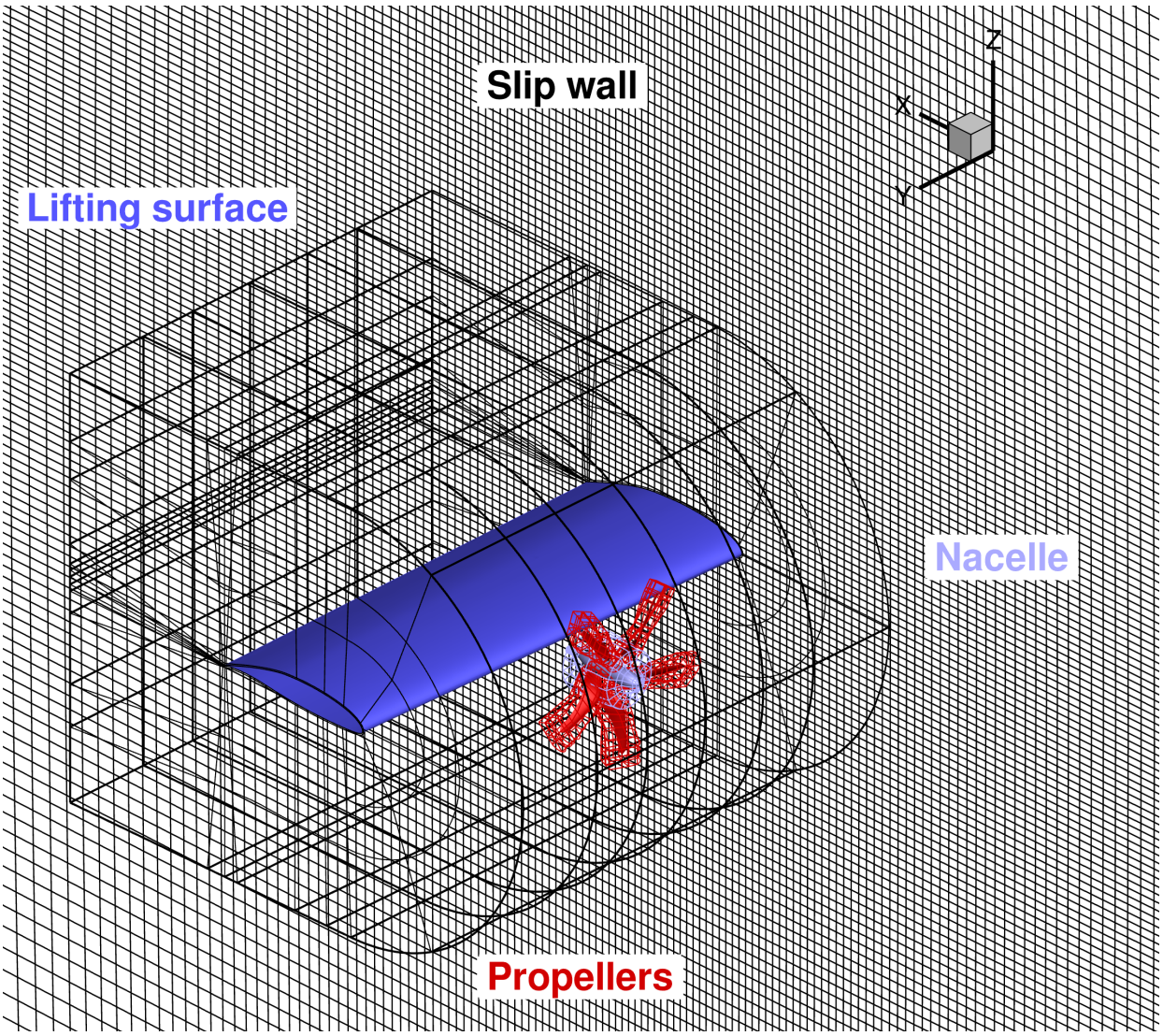

Figure 4.7: Chimera grid, and topology used for installed configurations.

advance ratio or effective angle of attack, thereby imposing additional loading on the propeller. Moreover, there is no swirl recovery effect from the lifting surface.

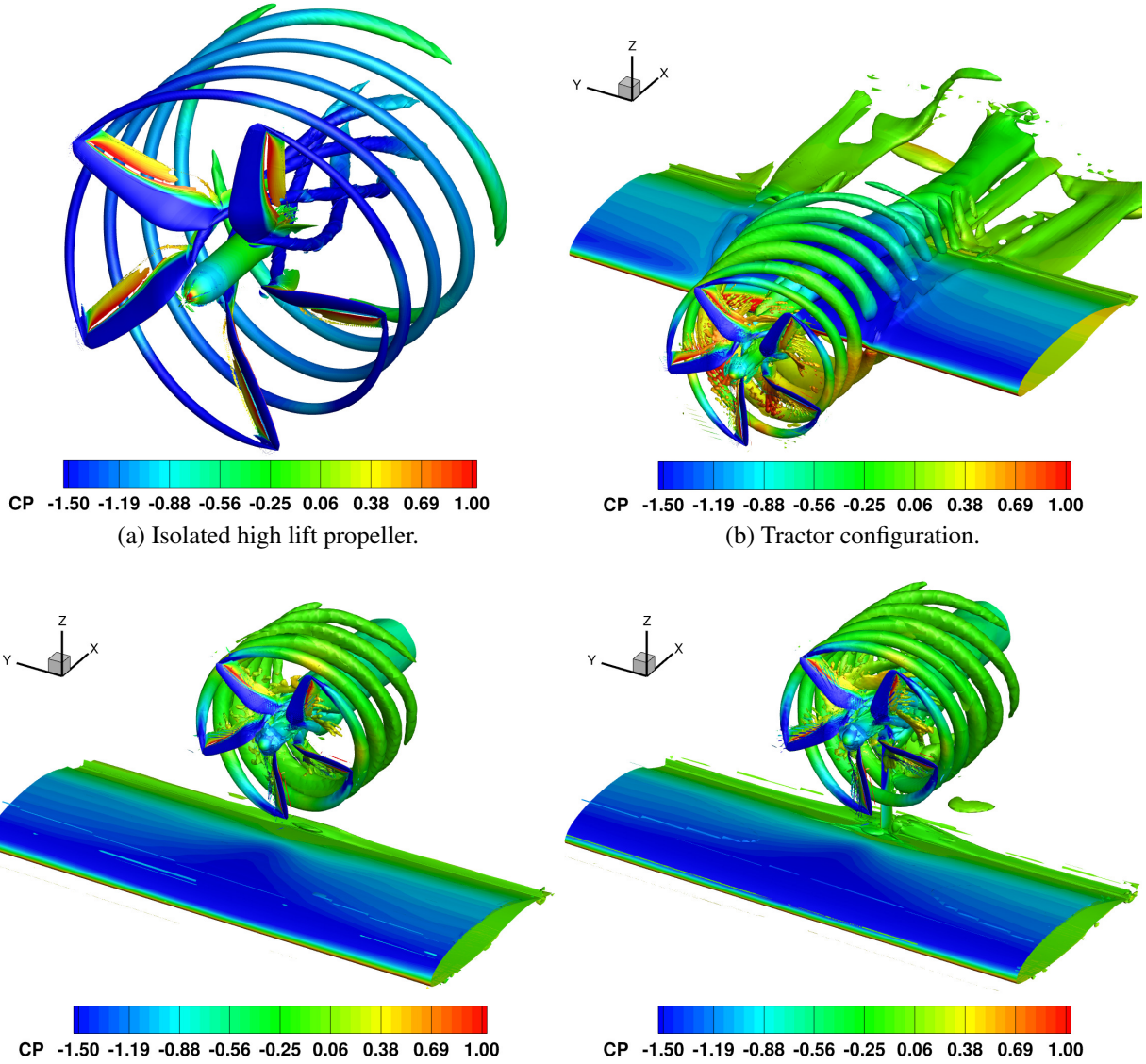

(a) Isolated high lift propeller.

(b) Tractor configuration.

(c) OTW configuration.

(d) OTW configuration with pylon installed.

Figure 4.8: Isolated and installed propeller wake visualisation using iso-surfaces of Q-criteria at a value of 0.1, colored using pressure coefficient for different configurations.

At high loading and at an advance ratio (μ) of 0.19, it was discovered that the interactions between the propeller and the lifting surface had a much greater impact on the local performance of the lifting surface. Under identical conditions, the OTW configuration experienced an increment of around 1.3% in lift, and roughly 294% in lift-to-drag ratio compared to the tractor configuration, due to the drag reduction. This decrease in drag is clearly visible in Figures 4.9 and 4.10, as the

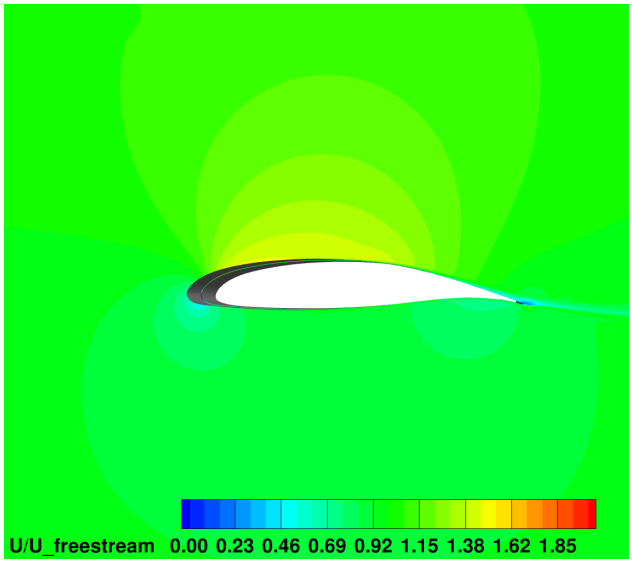

(a) Isolated wing.

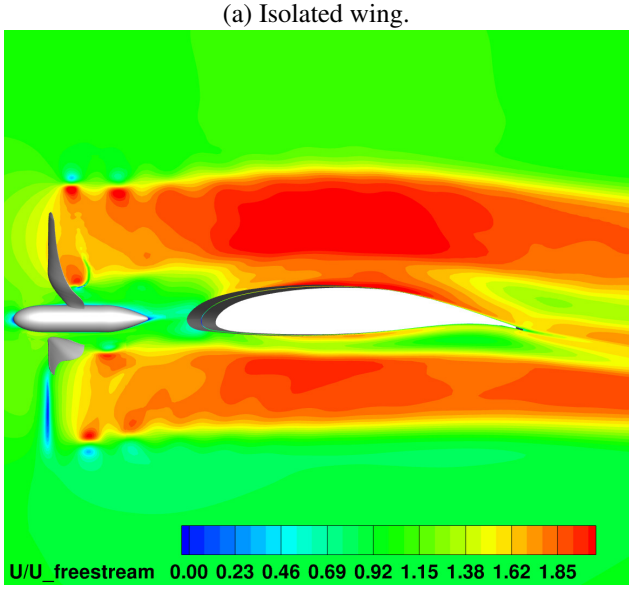

(b) Tractor configuration.

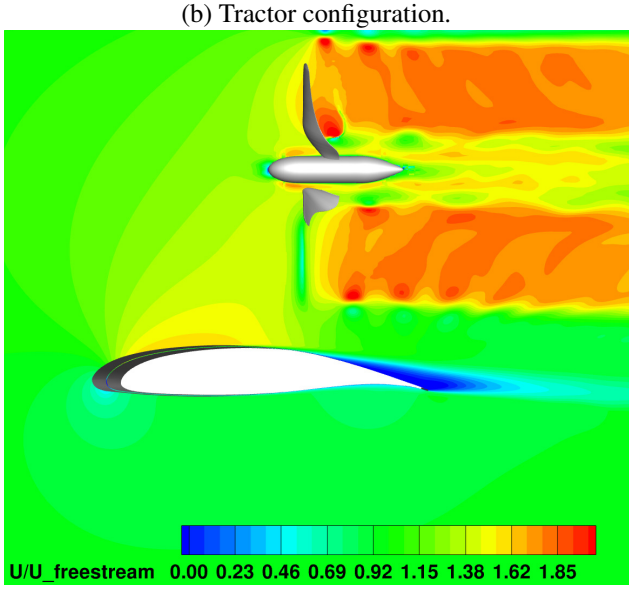

(c) OTW configuration.

Figure 4.9: Instantaneous axial flow speed (normalised using the far-field speed) for different configurations.

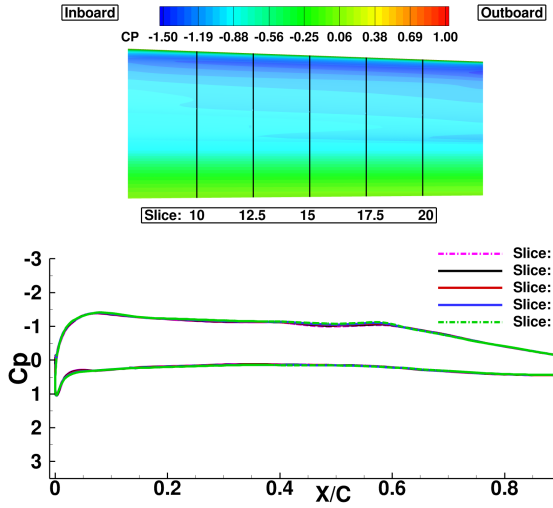

(a) Isolated Wing.

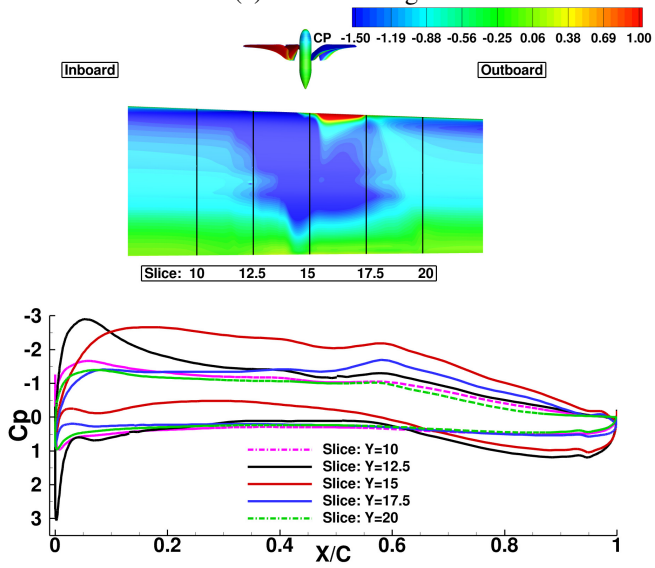

(b) Tractor configuration.

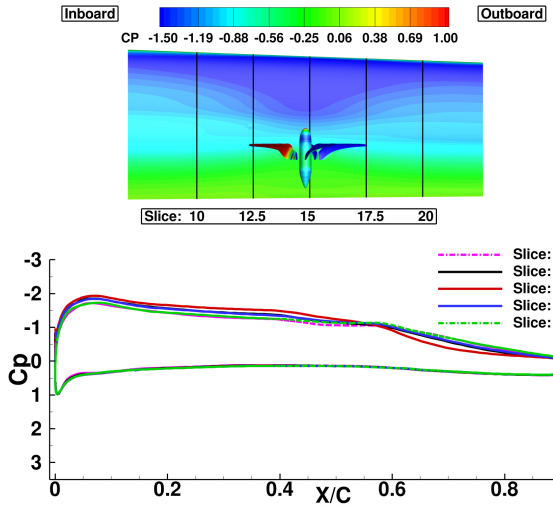

(c) OTW configuration.

Figure 4.10: Extracted pressure coefficient distributions on the wing for the baseline, tractor and OTW configurations.

Table 4.4: Performance comparison of single-propeller, installed, propulsion systems with multiple configurations. The definitions of the coefficients are given in the nomenclature and Section 2.5.2.

Performance (RPM=4800)	Clean lifting surface	Tractor	OTW	OTW+Pylon	Benefit OTW	Benefit OTW+Pylon
Lift (N)	591	582	590	605	+1.3%	+3.9%
Drag (N)	9.3	38.3	9.8	17.3	-74.4%	-54.8%
L/D (-)	63.5	15.2	60.0	35.0	+294%	+130%
Thrust (N)	-	257	238	241	-7.4%	-6.2%
Power (kW)	-	12.60	12.50	12.58	-0.8%	-0.2%
Propeller Froude efficiency (-)	-	0.56	0.52	0.53	-6.4%	-5.8%
Overall propulsive efficiency (-)	-	0.476	0.502	0.489	+5.5%	+2.7%

OTW configuration displayed a higher suction peak and pressure recovery compared to the tractor configuration. On the other hand, the tractor configuration exhibited a more significant suction peak downstream of the propeller close to the trailing edge of the wing from the Figure 4.10(b), as the velocity from the upper surface had increased significantly to over double the freestream velocity due to the propeller slipstream as shown in the Figure 4.9, and the pressure failed to recover as in the OTW configuration. Additionally, on the lower surfaces, the tractor configuration was significantly affected by the slipstream from the propeller and resulted in the formation of a high pressure gradient in the chord-wise direction. As shown in Table 4.4, the propeller performance of the OTW configuration dropped by 6.4% due to the thrust penalties. However, due to the great benefit from the lifting surface, the overall propulsive efficiency has increased by 5.5%.

Similar benefits can also be found in the OTW configuration with pylon installed. Trimmed results showed that 3.9% more lift has been generated, and the benefit of the lift-to-drag ratio was 130%, as the drag increased due to the pylon structure. In addition, propeller performance benefited slightly by the installed pylon structure in the OTW configuration which has a swirl recovery effect. Nevertheless, the overall aerodynamic performance of the OTW configuration with/with-out pylon installed was increased.

Furthermore, compared to the clean lifting surface, the tractor configuration maintains a similar level of lift; however, the lift-to-drag ratio (L/D) is significantly reduced due to increased drag. In contrast, the OTW configuration preserves both lift and L/D relative to the clean lifting surface case under the tested conditions.

Regarding the influence of the aerofoil shape, especially in the OTW configuration, it appears that the region from the leading edge to the mid-chord is primarily affected by the propeller, equivalent to an increase in the effective angle of attack. Additionally, a separation region is observed near the trailing edge, suggesting that modifications to the trailing edge shape, thickness, and length could lead to further performance improvements.

4.3 Multiple Propeller Installation Verification

This section presents further investigations into different DP systems with multiple propellers installed. The setups for these propulsion systems are given in Figure 4.11. The installed HLP was previously validated in Section 3 [151], and the lifting surface was extracted from the NASA X-57 cruise-efficient wing, which has also been used in previous WIPP studies [152]. Given the increased complexity of the aerodynamic interactions with increased number of installed propellers, this work has also investigated multi-rotor validation cases, see section 3.3 [148]. With confidence in using the same CFD tools, and grid resolution, from the validation studies, the work focused on studying the aerodynamic performance of distributed tractor and OTW propulsion systems at the optimised propeller locations in full scale.

The investigation of DP systems started with assessing the performance of the tractor and OTW configurations with two propellers installed. The setup and the corresponding flow field are depicted in Figures 4.11(a) and 4.13. Aerodynamic loads from the overall propulsion system, and their individual components are presented in Table 4.5 and Figure 4.14 (b). Both configurations were trimmed by adjusting the wing angle of attack to generate the same lift, and the results indicate a drag reduction and the lift-to-drag ratio is increased from 15.74 in the tractor configuration to 30.2 for the OTW configuration. The propeller performance drops in the OTW configuration due to the thrust reduction being higher than the power reduction. Together with considering the wing performance using the equation $\eta^{overall}_{propulsive} = \frac{T_{install} \times V_\infty}{P_{shaft}}$, also provided in the section 2.5.2, the overall propulsive efficiency has increased from 0.487 to 0.505, which is almost 4% higher than the tractor propulsion system.

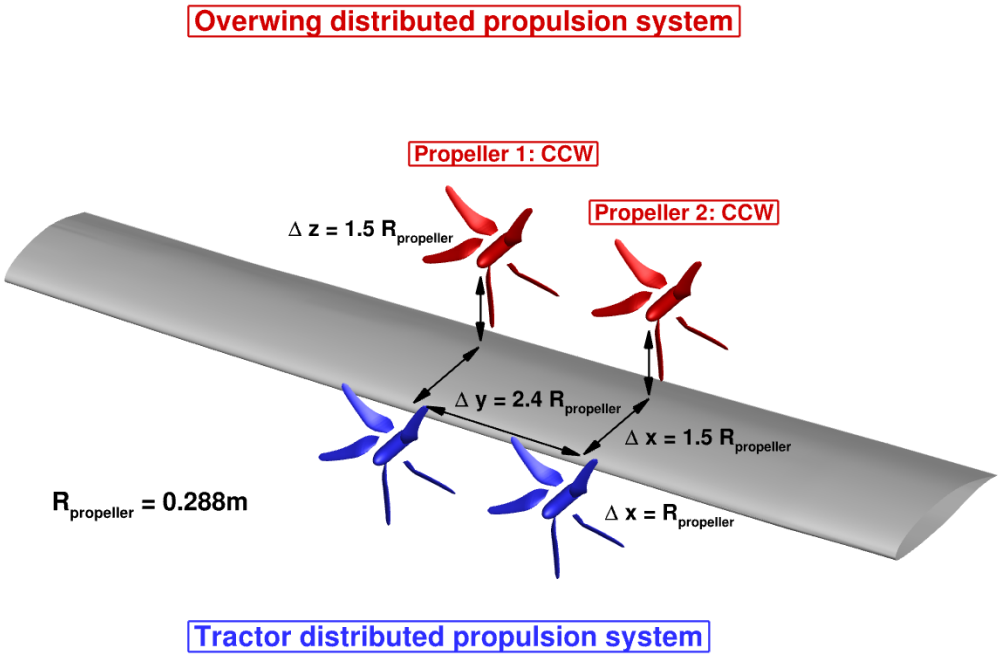

(a) Two-propeller, installed, propulsion system.

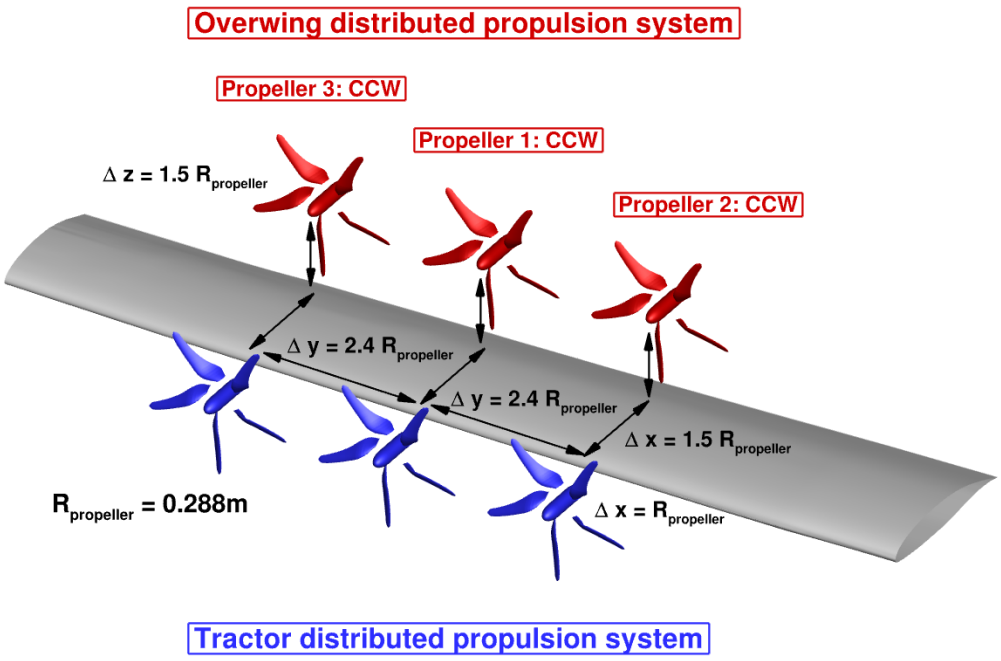

(b) Three-propeller, installed, propulsion system.

Figure 4.11: Illustration of the investigated DP systems with multiple propellers installed. A full scale of X-57 aircraft with $R_{propeller}$ equal to 0.288m and its corresponding lifting surface, are used in all verification cases.

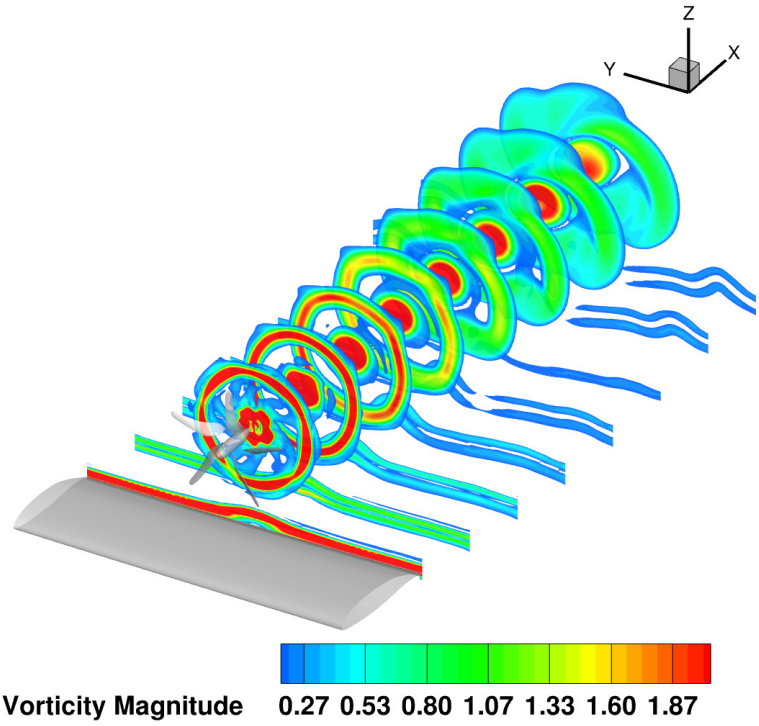

(a) Visualisation of vorticity magnitude of single propeller, installed, OTW configuration at $\mu = 0.19$.

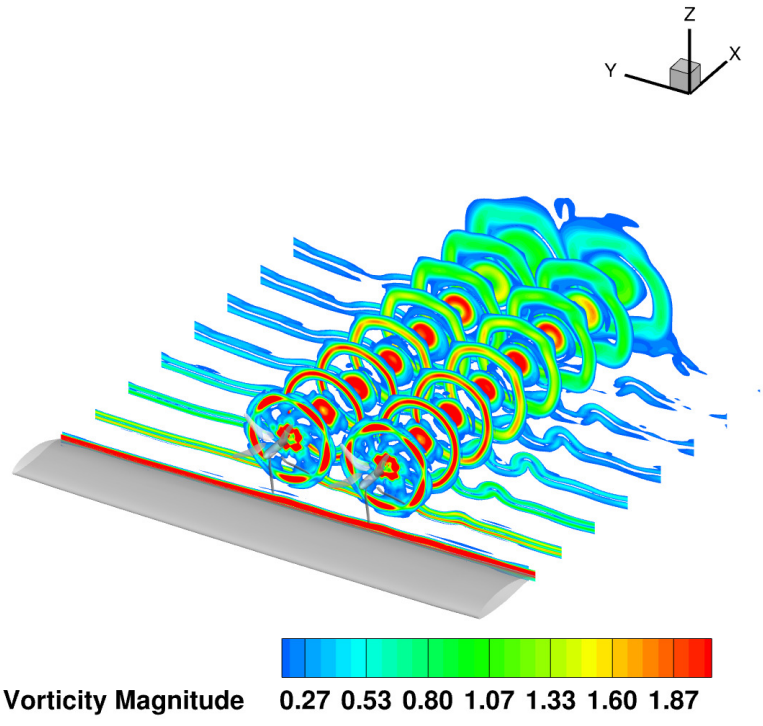

(b) Visualisation of vorticity magnitude of distributed, OTW configuration at $\mu = 0.23$.

Figure 4.12: Visualisation of vorticity magnitude of single propeller installed, and distributed OTW configurations at equivalent thrust conditions.

Furthermore, by distributing the thrust from single to two propellers, the vorticity magnitude shown in Figure 4.12 demonstrates a significant reduction in vorticity. This results in a lower tip speed for the DP system, which is important as the propeller/rotor performance and noise are highly dependent on the tip speed.

This work demonstrated that the single and two-propeller installed OTW configuration outperforms the conventional tractor configuration. However, a study conducted by Reynard et al. [49] found 1.5% drop in performance for the middle propeller when adjacent propellers were separated by 5% R. To this end, the current work carried out the investigation of three-propeller tractor and OTW configurations with a 40% R separation distance between adjacent propellers to reduce the strong aerodynamic interactions caused by adjacent propellers in close proximity. Propellers 1 and 3, visualised in Figure 4.11, exhibited identical performance. However, Propeller 2, that is located most inboard, showed almost 1% better efficiency than the other two propellers. This performance difference, under the same separation distance, RPM, and rotation direction for all three propellers, was not observed in the two-propeller OTW configuration. This discrepancy may be attributed to the tapered lifting surface, which was extracted from the X-57 cruise-efficient wing. The findings obtained suggest that the OTW configuration can be further optimised, such as the chord length from the wing design, since the installed OTW propeller accelerated flow from the upper surface, which avoids or delays the flow separation and increases the wing performance. Furthermore, the equivalent three-propeller tractor configuration with the same lift generation was also investigated; a comparison of propeller performance at different locations revealed that propellers at locations 1, 2, and 3 showed identical performance. Therefore, the propeller performance from tractor configuration does not appear to be sensitive to the tapered lifting surface. Furthermore, as shown in Figure 4.14(c), the performance benefits of the OTWDP system are maintained when compared to the equivalent tractor configuration with the same lift generation.

With the optimal OTW DP system in place, further investigation incorporated a third propeller as shown in Figure 4.11(b) and compared its performance with a one- and two-propeller OTW configuration, as presented in Table 4.6, and Figure 4.14. Flow field visualisation of two- and three-propeller, installed tractor and OTW DP systems coloured using velocity are presented in

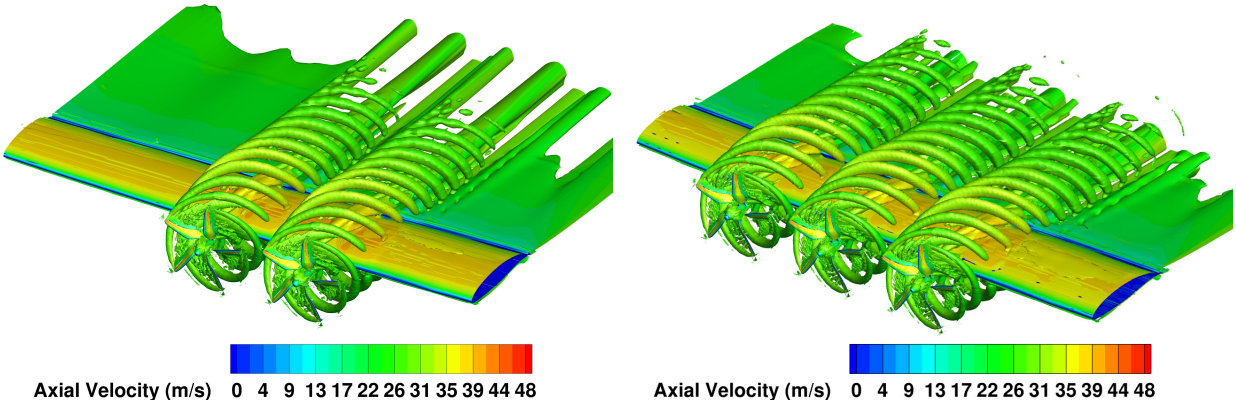

(a) Conventional tractor configuration.

(b) Tractor, DP system.

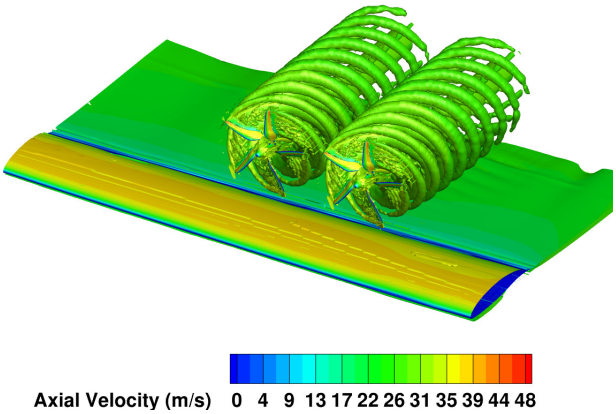

(c) OTW configuration.

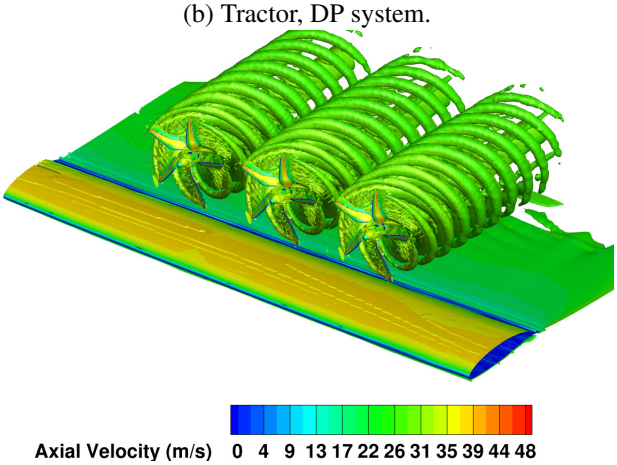

(d) OTWDP system.

Figure 4.13: Flow visualisation of distributed tractor and OTW configurations at $\mu = 0.42$ using iso-surfaces of Q-criteria at a value of 0.01, coloured using axial velocity.

Table 4.5: Performance comparison of different two-propeller, installed, DP configurations. The definitions of the coefficients are given in the nomenclature and Section 2.5.2.

Performance (RPM=3900)	Tractor	OTW	Benefit of OTW
Lift (N)	1140	1149	+0.7%
L/D (-)	15.74	30.20	+92%
Thrust (N)	308	273	-11.3%
Power (kW)	13.3	12.8	-3.8%
Propeller Froude efficiency (-)	0.64	0.59	-7.8%
Overall propulsive efficiency (-)	0.487	0.505	+3.8%

Figures 4.13. The results demonstrate distinct aerodynamic interaction mechanisms arising from different propeller installation configurations. The number of installed propellers also increases the complexity of interference effects. However, the configuration designed with a 1.2D propeller spacing yields a consistent propeller wake tube, where the resulting slipstream significantly influences the lifting surface positioned downstream or beneath the propellers.

Table 4.6: Performance comparison of different OTWDP configurations. The definitions of the coefficients are given in the nomenclature and Section 2.5.2.

Performance	One-prop	Two-prop	Three-prop	Benefit DP (2-3)	Benefit DP (1-3)
Lift (N)	1010	1083	1096	+1.2%	+8.5%
L/D (-)	24.4	35	38	+7.6%	+55.7%
Thrust (N)	240	273	353	+29.0%	+47.1%
Power (kW)	12.50	12.8	16.1	+25.8%	+28.8%
Propeller Froude efficiency (-)	0.527	0.586	0.602	+2.6%	+14.2%
Overall propulsive efficiency (-)	0.437	0.520	0.552	+6.2%	+26.3%

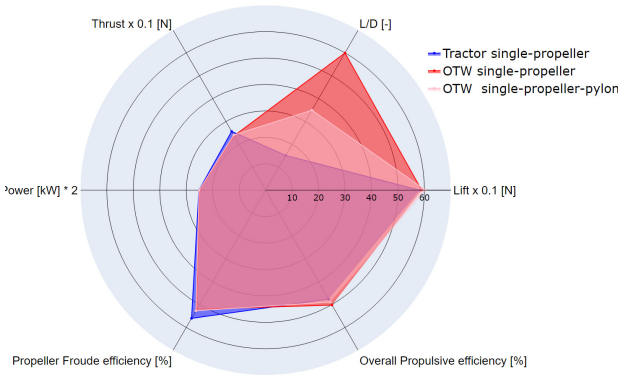

(a) Performance of single-propeller, installed, propulsion systems at $RPM = 4800$.

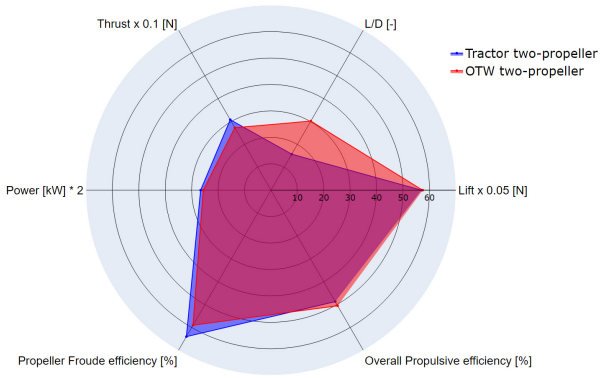

(b) Performance of two-propeller, installed, propulsion systems at $RPM = 3900$.

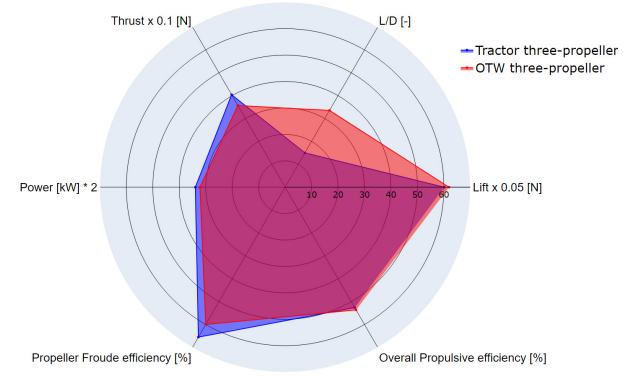

(c) Performance of three-propeller, installed, propulsion systems at $RPM = 3700$.

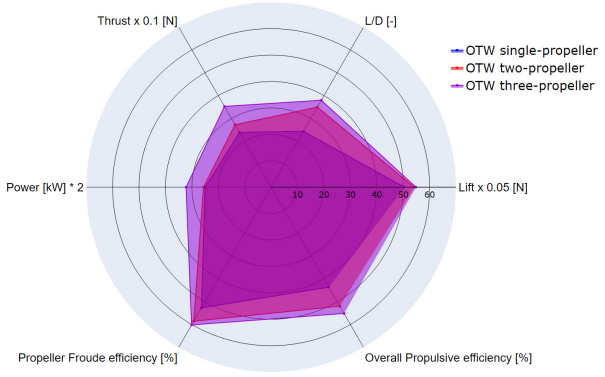

(d) Performance of OTW propulsion systems with different numbers of installed propellers.

Figure 4.14: Comparisons of tractor and OTW configurations with single, two- and three-propeller, propulsion systems.

As indicated in Figure 4.14(d), compared to the two-propeller case, the three-propeller case generates more thrust than required power, resulting in a 2.6% higher propeller efficiency. Since the larger upper lifting surface area is affected by the slipstream of the three-propeller configuration, there is 1.2% improvement in lift and a 7.6% increment in the L/D of the lifting surface. Fur-

thermore, there is an overall improvement in propulsive efficiency by 6.2% for the three-propeller configuration.

When transitioning from a single-propeller to a three-propeller, installed DP system, as shown in Figure 4.14(d), it was observed that the propellers become 14.2% more efficient. The L/D of the wing also increased by 55.7%, resulting in an additional 8.5% lift generation and 30.2% of drag reduction. In terms of overall efficiency, the three-propeller OTW configuration is 26.3% more efficient than the single-propeller installed OTW configuration, demonstrating the capability of a DP system to enhance the overall wing performance.

4.4 Chapter Summary

Based on the location optimisation study of the DP and the performance evaluation of DP systems using the high-fidelity method, the following conclusions can be drawn.

A single auxiliary propeller was evaluated to determine its optimal vertical and horizontal propeller positioning ahead of the wing. The findings revealed that an auxiliary propeller positioned above the wing, improved the overall wing lift-to-drag ratio. This was because it decreased the stagnation area at the leading edge of the wing, and increased the velocity across the upper surface, resulting in higher suction. On the other hand, the horizontal position had minimal impact on performance.

Using the same configuration as the X-57, the positioning of six auxiliary propellers was evaluated using Kriging at the optimisation stage. A variety of lateral and vertical positions were examined. A total of 15 sampling points were utilised, with the optimal position found above the wing, and close to the mid-chord. This position resulted in increased suction across the upper surface of the wing, with the increase extending to mid-chord. This suggests that the distributed propeller configuration enhanced the overall lift, and reduced the drag below the baseline case by shifting the propeller from the leading edge of the wing to a better position.

In the fully resolved verification section, the conformal HLP from the X-57 aircraft was utilised to assess the tractor and OTW configurations, under high-performance take-off conditions.

The propeller in the OTW configuration experienced a performance drop of approximately 6.4% compared to the conventional tractor configuration. However, the optimised OTW configuration exhibited superior performance, demonstrating a 1.3% improvement in lift and a 294% increment in L/D. When considering integrated performance, the optimised OTW configuration outperformed the conventional tractor configuration by 5.5%

Additional investigations included the pylon structure effect in the OTW configuration, revealing that the pylon created more drag due to the additional surfaces. Nevertheless, the pylon retained the performance benefits in overall propulsive efficiency and lift generation. Further evaluations investigated a second propeller, demonstrating that the optimised OTW configuration led to an almost 4% improvement in overall propulsive efficiency, compared to the conventional propulsion configuration at the same lift.

In the future, the findings of this work can support wing design by employing the AD method to investigate aerofoil shape effects, as the leading-edge suction induced by inflow is successfully captured and verified against high-fidelity simulations. Furthermore, incorporating weight constraints and mass distribution effects associated with multiple mounted propellers will be essential for developing an optimal distributed propulsion system for future aircraft applications.

Chapter 5

Wingtip Mounted Propulsion System and Distributed Propulsion (TMP-DP)

This chapter has been published as: Geng Qiao, George Barakos, "Aerodynamic Study of Wingtip-mounted Propeller and Distributed Propulsion System," The Aeronautical Journal, (2025) doi: 10.1017/aer.2025.36

This chapter explores the potential of employing distributed propulsion systems with multiple propellers and a full wing for advanced vehicle designs. Distributed propulsion systems create complex interactional flow effects, that remain largely unexplored and not fully understood. This chapter focuses on high-fidelity aerodynamic analyses of a tip-mounted propeller combined with over-the-wing propellers. Different configurations were tested using fully resolved simulations with the HMB3 CFD solver. Four configurations were proposed based on the design of TMP-only and TMP-DP with varying RPM, tip speed, thrust setting, and pitch angles. Following the proposed designs, a systematic analysis was conducted of individual, overall performance and their associated interactional aerodynamics.

5.1 Distributed propulsion

With the CFD method validated, the investigation of the distributed propulsion system was conducted using the Workshop for Integrated Propeller Prediction (WIPP) geometry and the HLP. The flow visualisation of the OTW-DP propulsion system is presented in Figure 5.1(a), and the performance of the OTW propulsion system with different number of installed propellers is shown in Figures 5.1(b)(c). When transitioning from single-propeller to three-propeller Distributed Propulsion (DP) system, it was observed that the propellers were 14.2% (η_{Prop}) more efficient. In terms of overall efficiency, the three-propeller OTW configuration was 26.3% ($\eta^{overall}_{propulsive}$) more efficient than the single-propeller installed OTW configuration, demonstrating the capability of a DP system to enhance the overall performance.

5.2 Test matrix

A previous study [89] in Chapter 4 on distributed propulsion systems found that the OTW configuration, with varying numbers of installed HLPs, out-performed the tractor configurations in terms of overall performance. Additionally, research on tandem hover propellers [73] has demonstrated that tip-to-tip distances and spacing significantly affect both aerodynamic performance and noise emissions. Chapter 3 further shows that the overall acoustic directivity is not strongly influenced by flight condition; however, different installation configurations alter the aerodynamic interaction mechanisms, leading to distinct acoustic signatures. Therefore, before conducting a comprehensive vehicle-level investigation, it is essential to examine the installation effects of tip-mounted and distributed propellers.

Figure 5.2 shows four configurations. Configurations C1 and C4 are compared at identical operating conditions (the TMP had the same blade pitch and rotation speed) to isolate the aerodynamic interactions introduced from the DP system. The installed HLP in configuration C2 is contrasted with the distributed HLPs in configuration C4 (HLP has the same pitch and rotation speed) to assess the impact of TMP, and the distributed OTW-installed propellers. Furthermore,

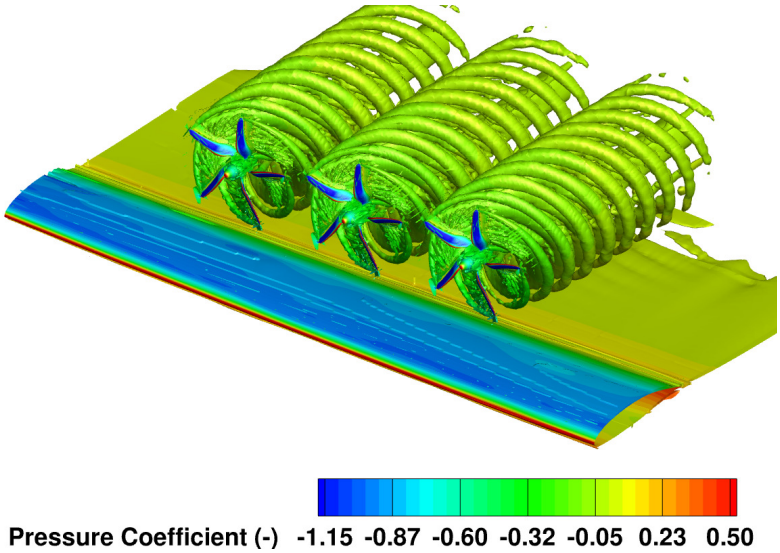

(a) Flow visualisation OTW-DP system at μ =0.42.

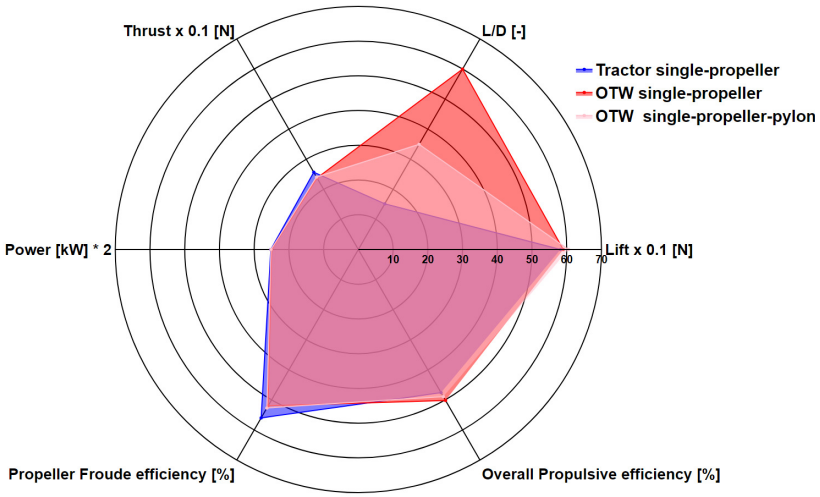

(b) Performance of single-propeller, installed, propulsion systems at propeller speed, 4800 RPM.

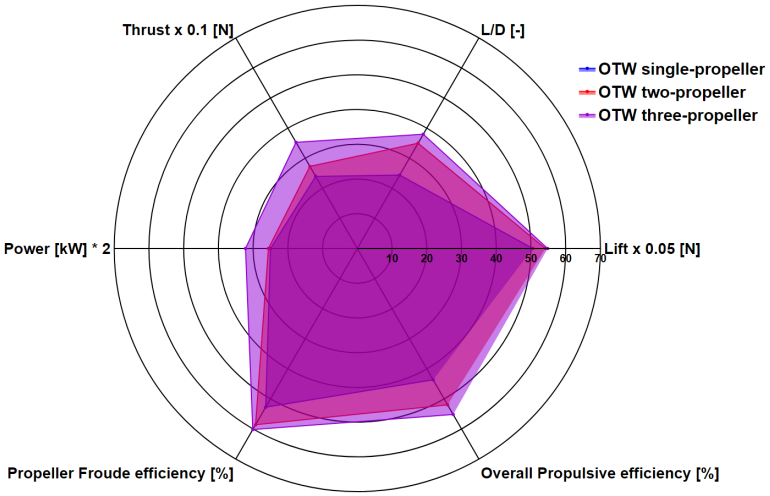

(c) Performance of propeller, OTW installed, propulsion systems.

Figure 5.1: Flow visualisation of the OTW-DP system and the performance comparisons of a single propeller-installed tractor, pylon/no-pylon OTW, and different numbers of propellers-installed OTW configurations. [89] (c) Here, the single OTW propeller is masked by both the two- and three-propeller configurations, while the two-propeller OTW setup is similarly masked by the full three-propeller arrangement.

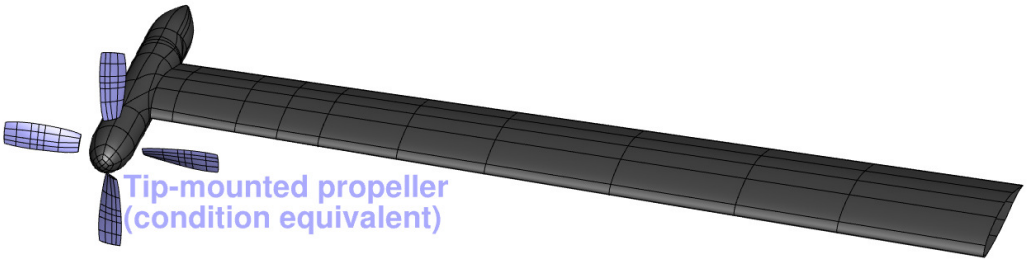

(a) C1 & C3

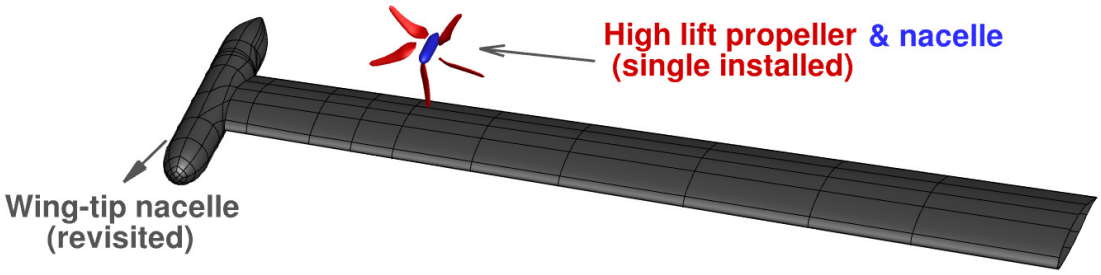

(b) C2

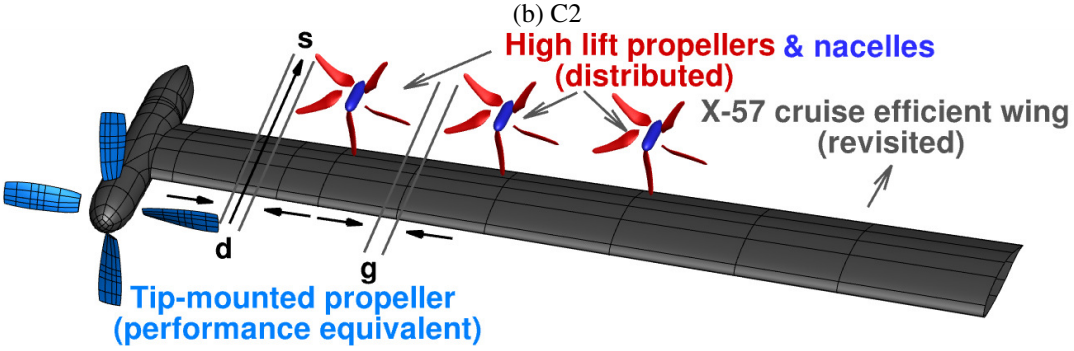

(c) C4

Figure 5.2: Schematic of investigated configurations. The TMPs in Configurations 1 and 3 operate with different blade pitch angles and rotational speeds.

a comparative analysis based on the equivalent thrust is conducted between the TMP-only configuration C3, shown in Figure 5.2(a), and the TMPDP system C4, illustrated in Figure 5.2(c), to investigate the individual component and overall propulsive performance.

The same tip speed as of the NASA WIPP experiments, corresponding to a Mach number of 0.505, is applied to the TMP in configuration C3. This is equivalent to the propeller speed of 3264 RPM in the full-scale simulation of C3, as used in the current work. In the TMP-DP system shown in Figure 5.2(c), the rotational speed and blade pitch angle at 0.75R of the TMP are precisely adjusted to generate the same thrust as propulsion system C3 in Figure 5.2(a), while the DP maintains the same configuration and operating conditions as presented in Chapter 4 [89].

Specifically, the TMP in configuration C4 operates at 1850 RPM and a pitch of 28°, while the DP operates at 3700 RPM with a pitch of 24.1°. This setup results in tip Mach number 0.286 for the TMP and 0.325 for the DP. The propeller spacing in configuration 5.2(c) as 1.2D is selected to minimise performance losses due to aerodynamic interactions and inductions based on the previous investigations. [153, 73, 149, 154] Detailed specifications for all configurations are provided in Table 5.1.

Table 5.1: Summary of the test condition used for the study of TMP and DP installed propulsion system.

Condition	Take-off and landing ($Ma_\infty = 0.08$)
Radius	
TMP	0.508 m
DP	0.288 m
propeller speed (Blade pitch at 0.75R)	
TMP	3264 (19.5°), 1850 (28°) rev/min
DP	3700 (24.1°) rev/min
Blade tip Mach number	
TMP	0.505, 0.286 -
DP	0.325 -
Configuration :	
Wing & HLP	Topout
Wing & TMP	Topout
Wing & TMP & DP	Topout
Tip-to-Tip Distance (d)	0.2 D_{TMP}
Downstream Spacing (s)	1.1 D_{TMP}
Tip-to-Tip Distance (g)	0.2 D_{DP}

5.3 CFD Grids

For an isolated rotor in axial flight, the azimuthal symmetry of the configuration can be exploited, whereby only a fraction of the grid needs to be generated. The Rotating Reference Frame (RRF) method is implemented in HMB3 [112] for simulations with rotational periodicity. The governing flow equations are solved in a non-inertial reference frame, thus transforming the unsteady problem into a steady-state one. For unsteady simulations, the entire grid is required. However, this can be obtained by copying and rotating the grids of the steady simulations. Additionally, unsteady

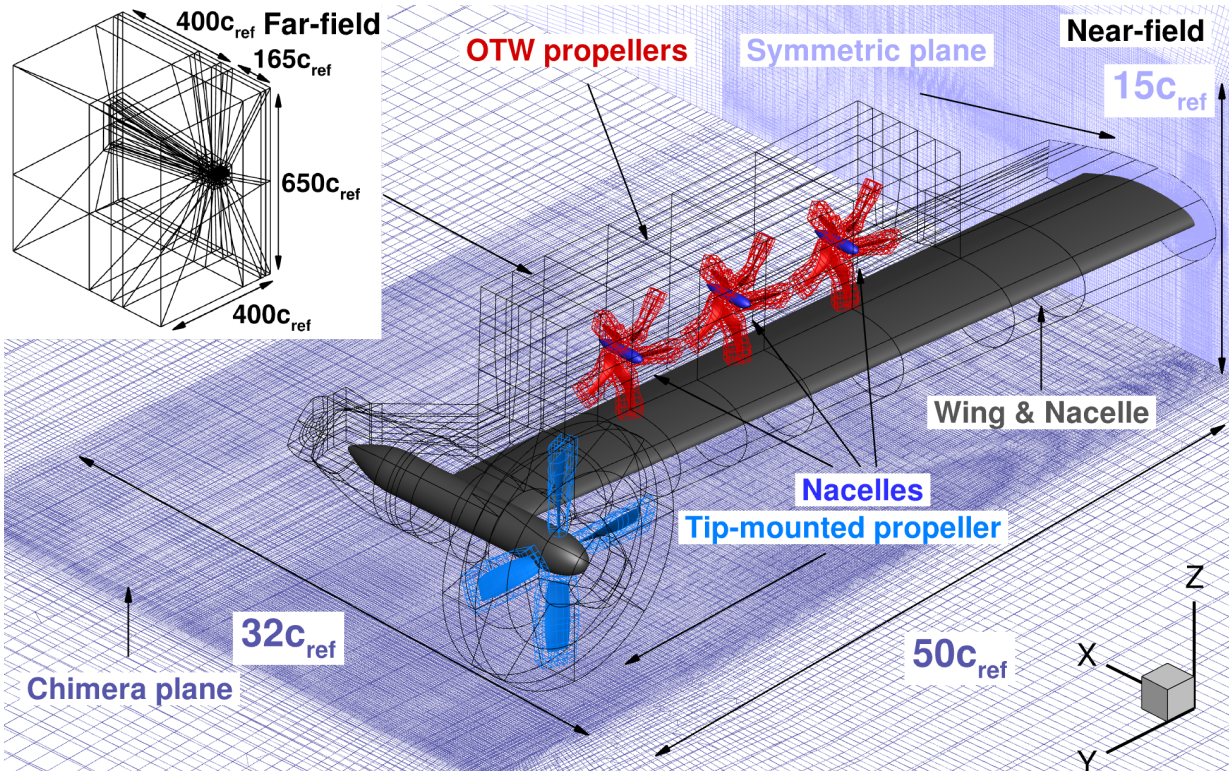

Figure 5.3: CFD grid topology used for TMP-DP configuration. The c_{ref} is the TMP tip chord length.

calculations are possible using the implicit, dual-time stepping approach. The computational grids used for propeller surfaces have a typical C-H topology. The spacing distribution has been set to the condition $\Delta y^+ < 1$, resulting in a first cell size of approximately $2.0 \times 10^{-6}c$ for all tested grids. Adiabatic wall boundary conditions are applied on the propellers, nacelles, and wing, with freestream values of pressure and velocity used elsewhere. Overset grids were employed to capture the high-pressure gradient region, and have been carefully designed for efficient load balancing. The number of near-body grid points for each TMP blade is approximately 7.6 million, or 30.3 million for all four TMP blades. The number of near-body grid points for each HLP blade is approximately 2.7 million, and for all three HLP blades with 15 blades, a total of 40.5 million grid points are used. Each propeller spinner has approximately 3 million near-body volume grid points, and all three spinners have a total of 6 million grid points. The wing, nacelle of the TMP, and additional refinement box for the OTW-DP system have an integrated design as indicated in Figure 5.3 to help capture the detailed physics of the propeller wakes, including vortices shed from the

blades, spinners, and wing with a minimum of chimera levels, and have a total of 22 million grid points. In the off-body mesh system, there is a local refinement box of approximately 2.7 million points that envelopes the overall propulsion system and its wake region, to resolve and capture the shed vortices and wake. The far-field flow has a much lower pressure gradient, to help reduce the cost for these types of expensive numerical simulations, the grid points for the far-field are approximately 4.5 million. The total number of grid points in the current simulation is 124 million for the TMP-DP configuration.

For the time-marching computations, a time step corresponding to one degree of propeller rotation was used for all TMP cases. The convergence of the implicit scheme was determined based on the reduction of the flow field residual, compared to the previous time step. In particular, either a three-order-of-magnitude reduction, or 300 inner iterations were found to be sufficient for convergence at each unsteady step.

5.4 Flow-field analysis

The interactions of the wake structures of the four configurations are presented using iso-surfaces of instantaneous Q-criterion, in Figure 5.4. In C1, the blade tip vortex, blade trailing edge vortex, root vortex, nacelle wake, and wing trailing edge vortex are all visible. The tip vortex follows a spiral path and convects downstream.

In the C2 configuration, a single OTW installed HLP shows more intense spiral structures due to its operation at higher speed. The nacelle and blade root vortices show a cylindrical shape with spirals moving downstream, and are as persistent as the tip vortices. The blade root and mid-span trailing edge vortices are mainly due to the non-uniform distribution of circulation on the propeller surface. There is no visible interference between the nacelles and the main wing wake. In addition, wingtip vortices are much weaker than the ones from the wing trailing edge and blades; hence, it is not visible in Figure 5.4 (b).

Moving to the C3 configuration, where the TMP is operating at a higher speed, and tip Mach number of 0.505, the most intense spirals are observed following a helicoidal path. Similar to the

wing trailing edge around the spirals, a much stronger vortex sheet is formed due to the interactions with the spirals from TMP. This distortion leads to the vortices deteriorating faster.

When the TMP-DP system is simulated, the tip vortex structures closely resemble those in configurations 1 and 2, as the design aims to minimise aerodynamic interactions between the propellers. Consequently, each propeller appears to operate in isolation from the others.

A more detailed flow visualisation of C3 and C4 configurations at LE and TE regions is shown in Figure 5.5. It is observed that the C3 configuration has a stronger contraction of the wake in the TMP-only configuration. The wake of the TMP expanded more in the C4 configuration, as visualised in Figure 5.5(c-d), which was caused by the TMP operating at lower speed, and the installation of the OTW-DP system. In addition, both configurations at the TE region show the vortex sheet shedding from the wing trailing edge near the TMP slipstream region. This vortex sheet is evident in Figure 5.6. It was also observed that the tip vortex at the upper side of the wing tends move to inner radii and the tip vortex at the lower side of the wing moves to outer radii.

The visualisation of the vorticity is presented in Figure 5.6 to understand the different interaction mechanics and flow environments in these two configurations. An asymmetric vortex system is observed downstream. The near-field is dominated by strong tip and trailing edge vortices due to the higher local velocity at the blade tip and blade trailing edge, where the stronger blade root vortices were shed due to a higher twist at the blade root. The nacelle vortex can also be differentiated across all cases, especially in the C3 configuration. Vortex shedding from the wing with the blunt trailing edge also interferes with the TMP. Two major differences can be identified when comparing these two configurations.

As expected, the C4 configuration has a reduced vorticity magnitude of the TMP and earlier dissipation of the blade tip, trailing edge, and root vortices, as depicted in Figure 5.6 (b). This reflects the different thrust each propeller is contributing. Slices [a] to [d] further show the paths of the wake, this suggests that the comparatively weaker wake from the TMP has a smaller impact on the wing. The vortices from the TMP in the C4 configuration indicate a higher degree of energy dissipation and tend to become more homogeneous propeller wakes than in the C3 configuration.

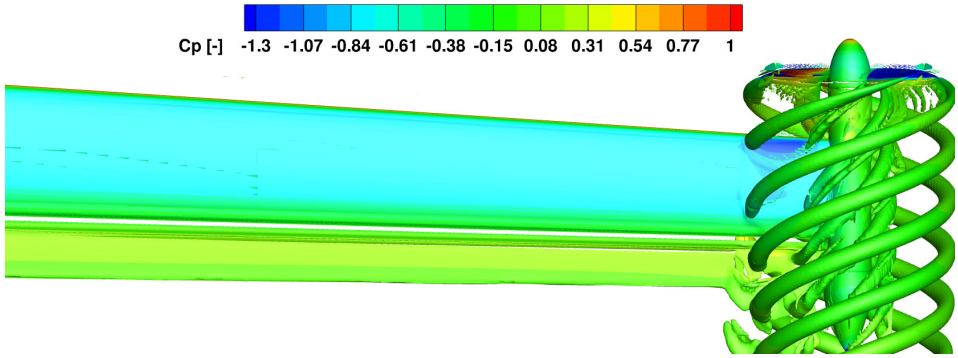

(a) C1

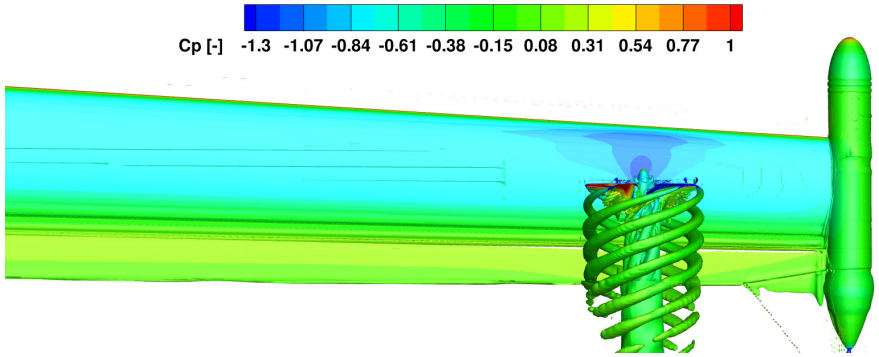

(b) C2

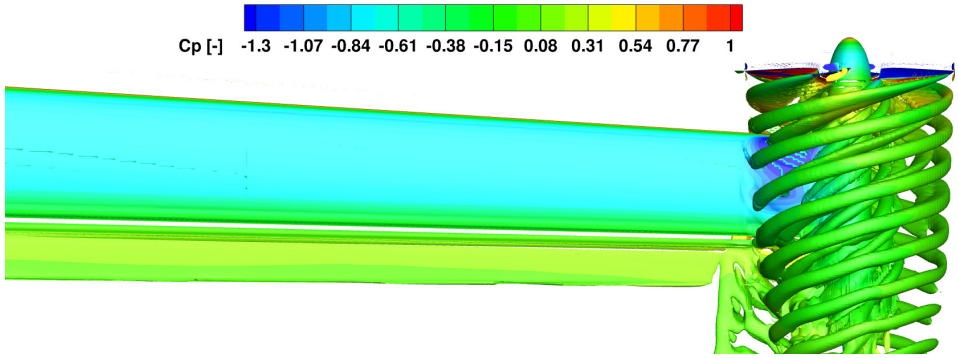

(c) C3

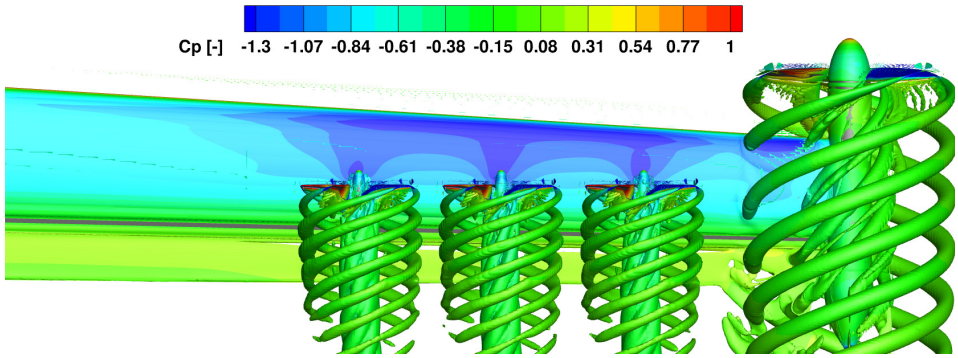

(d) C4

Figure 5.4: Flow visualisation of investigated configurations using Q-Criterion isosurfaces at $Q = 0.1$ and coloured with pressure coefficient calculated using free stream velocity. Their test conditions are given in Table 5.1.

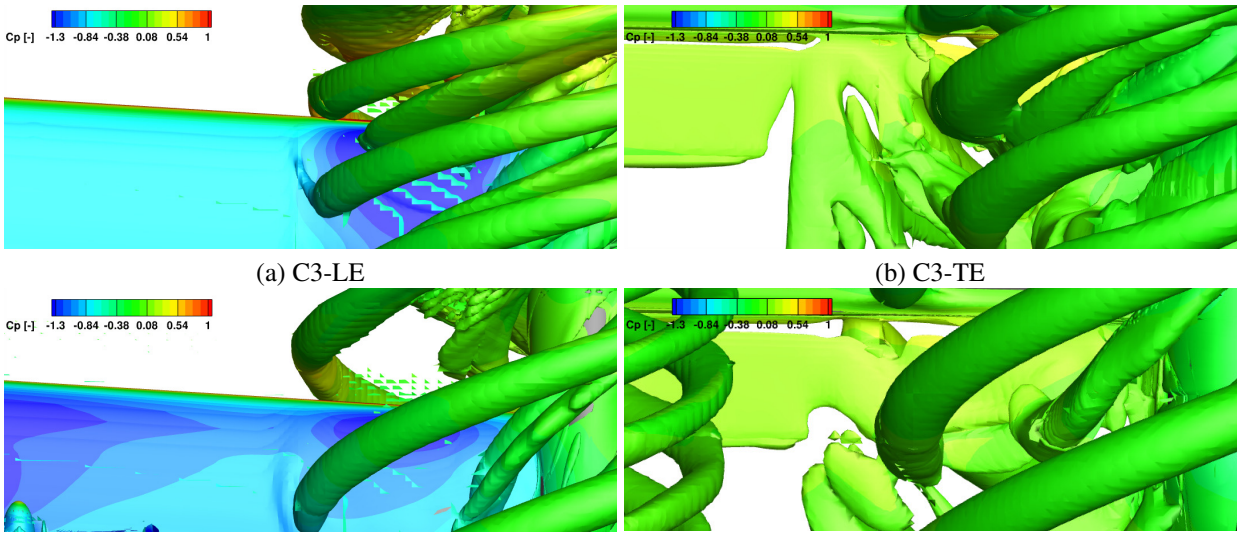

(a) C3-LE (b) C3-TE

(c) C4-LE (d) C4-TE

Figure 5.5: Flow visualisation of C3 and C4 configurations at LE and TE regions using Q-Criterion isosurfaces at $Q = 0.1$ and coloured with pressure coefficient calculated using free stream velocity. Their test conditions are given in Table 5.1

Second, the OTW installed DP system and their nacelles, introduced additional vortices. Stronger vorticity can be seen in the DP system since it has a higher tip speed compared to the TMP system. The strength of the blade tip vortices is also reduced between the adjacent propellers due to the counter-rotating vortex system.

5.5 Wing loading and interactions

Examining the averaged surface pressure coefficient across different configurations, as depicted in Figure 5.7, reveals that configurations C1 and C2 exhibit slightly lower suction pressures compared to C3 and C4. This difference is attributed to the single installed propeller operating at lower speed in C1 and C2. In contrast, configuration C3 shows the highest suction pressure among all configurations, particularly when compared to C1. This result indicates that a larger and more intense suction region is formed behind the TMP due to higher induced velocities. Consequently, the TMP in C3 significantly enhances lift generation from the wing, but may increase the bending moment.

In the C4 configuration, which includes both TMP and DP systems, a suction area similar to

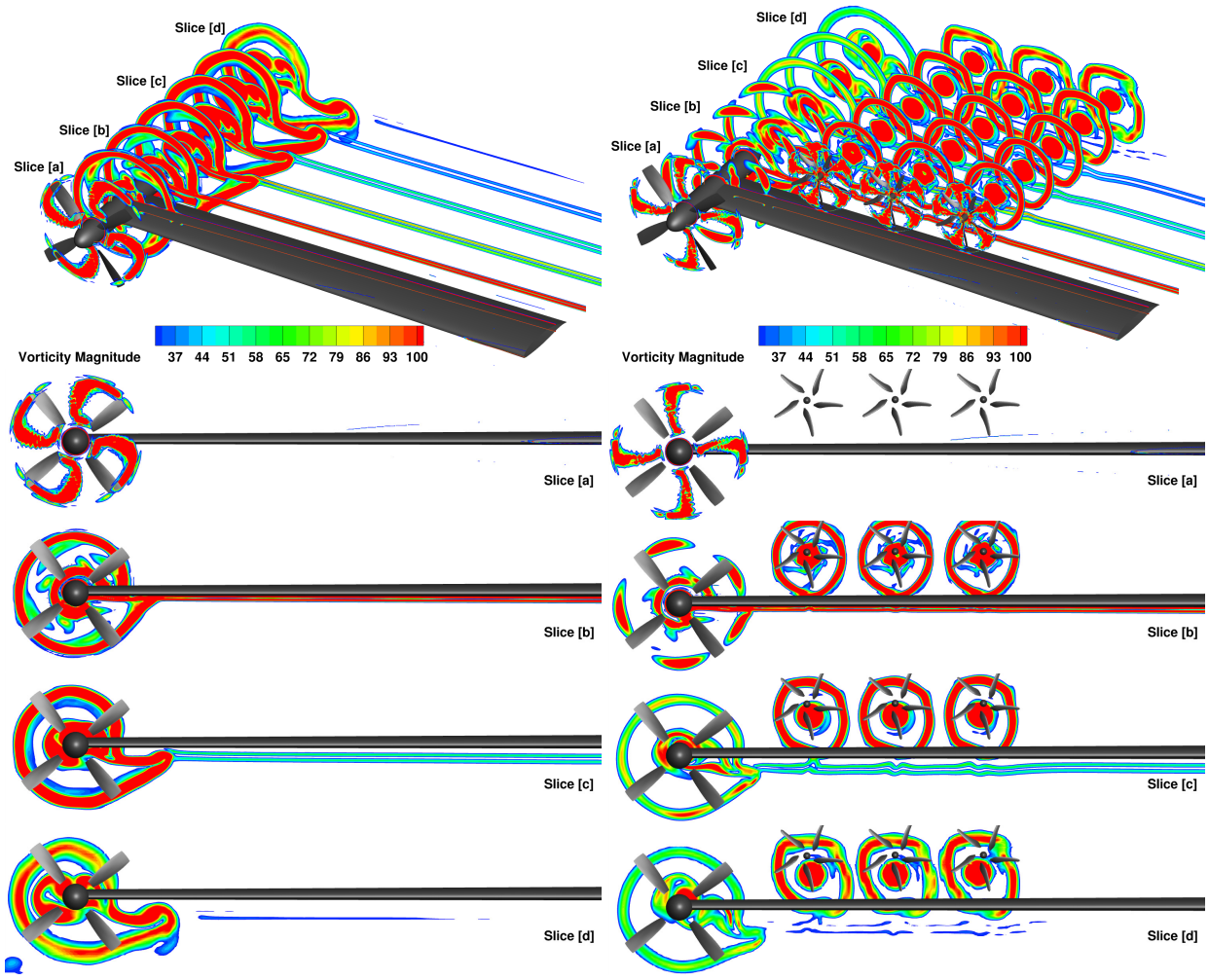

(a) C3 (b) C4

Figure 5.6: The vorticity magnitude visualisation of the thrust equivalent C3 and C4 configurations.

that in C1 is observed, as the TMP operates at the same speed. However, there are minor effects from the DP installation in the region behind the TMP. Compared to C2, the DP system in C4 exhibits an expanded suction region, highlighting favourable interactions the DP system. Within the DP system, the most significant suction region appears around the middle propeller, benefiting from the slipstream generated by the adjacent propellers. The interaction between the TMP and DP systems also results in favourable aerodynamic effects, as indicated by the suction profile from the TMP-DP system in Figure 5.7.

The effect of the pressure coefficient on the wing from different configurations alters the lift distribution along the wing span, as illustrated in Figure 5.8. In the C3 configuration, a sharp peak in lift distribution is observed behind the tip region of the TMP, caused by higher induced

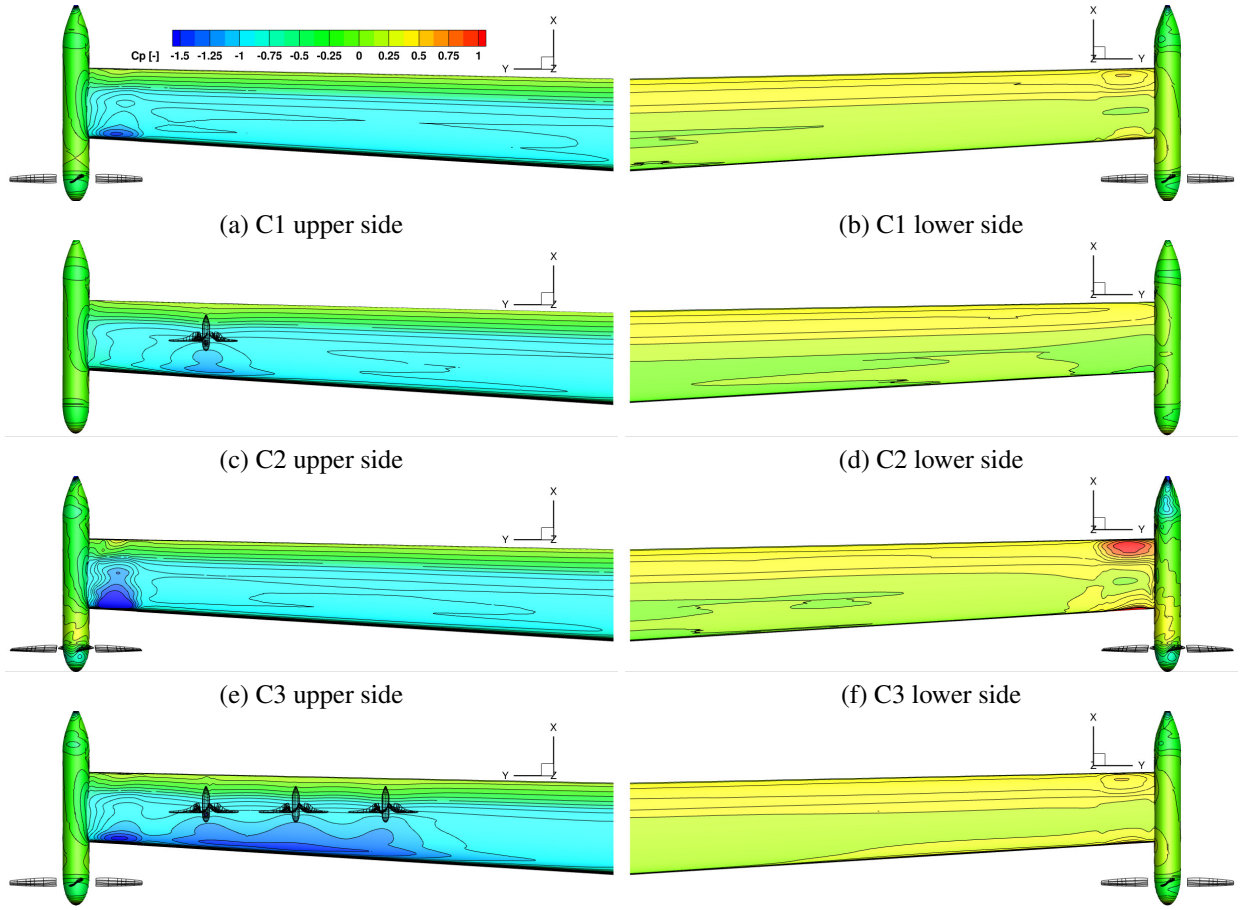

(a) C1 upper side

(b) C1 lower side

(c) C2 upper side

(d) C2 lower side

(e) C3 upper side

(f) C3 lower side

(g) C4 upper side

(h) C4 lower side

Figure 5.7: Averaged pressure coefficient of investigated configurations.

velocities. In contrast, this peak is significantly diminished in the C1 configuration, due to the lower induced velocities. In C2, an increase in wing performance is evident, particularly with a lift increase at the propeller installation point. The C4 configuration shows a marked improvement in lift generation, featuring a reduced spike behind the TMP, and there is no significant lift drop seen between OTW propellers and resulted in a more uniform lift distribution. This uniformity is attributed to the beneficial effects of the DP system, which enhances the aerodynamic performance of the wing.

The propellers in the DP system create a distinct flow environment that benefits the wing. This design results in a smooth, high-lift spike originating from the innermost propeller. Overall, the relatively smooth lift distribution observed in the C4 configuration, compared to C3, indicates a more favourable wing loading distribution achieved by the TMP-DP system. This enhancement

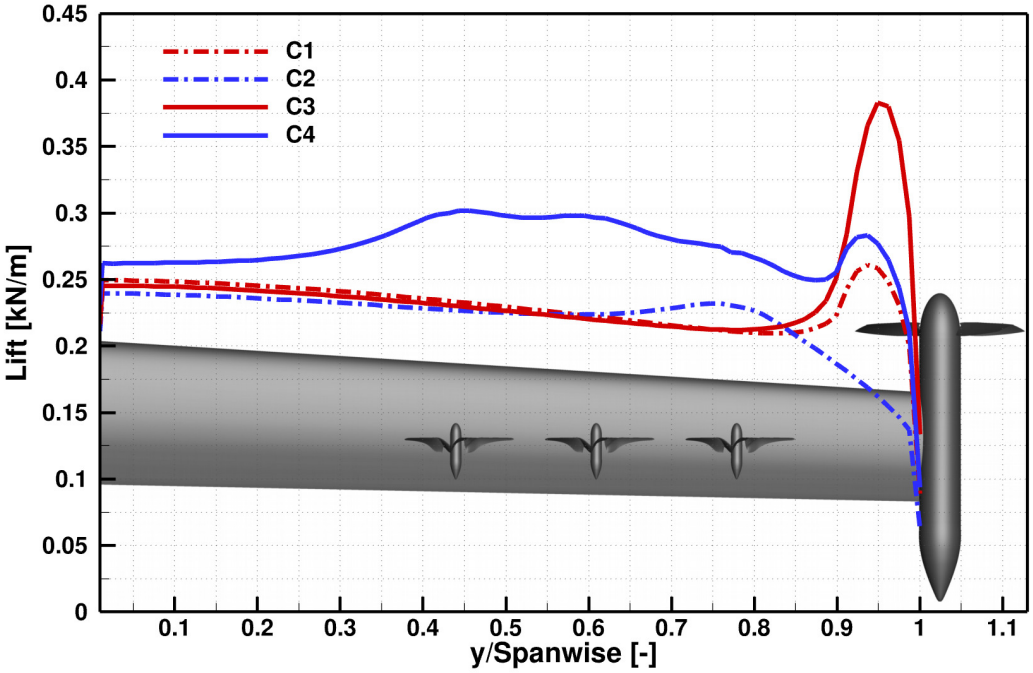

Figure 5.8: Time-averaged wing lift distributions of investigated configurations.

in wing lift has the potential to offset the additional structural weight introduced by the propellers.

5.6 Propeller blade loading and interactions

Figure 5.9 illustrates the variation in single blade thrust over the full azimuth, scaled according to the tip-mounted propeller. The data reveal a performance drop in the tip-mounted, propeller-only configurations, specifically in C1 and C3. This reduction in performance occurs as the blade passes near the wing. From configuration C1 to C3, the performance loss and the extent of the affected region increased. This trend is due to the higher tip velocity in configuration C3, which amplified unsteady loads resulting from the interaction between the propeller and the wing, as shown in Figure 5.9 with the thrust drop at azimuth angle around 120°.

Comparing the single-installed HLP with the distributed HLP, as represented by configurations C2 and C4, the setup involving distributed propellers demonstrates limited performance degradation due to the multi-propeller system. This is particularly evident with the second and

third propellers, which are positioned sufficiently far from the TMP downwash. Notably, two peaks in performance are observed, corresponding to the distributed HLPs operating at twice the speed of the TMP due to their smaller radius. Placing the distributed propeller $1.1D_{TMP}$ behind the TMP, with a tip-to-tip distance of $0.2D_{TMP}$, is effective in mitigating significant performance losses from installation effects. Furthermore, when examining the total thrust loads of the C4 configuration, the overall thrust performance is enhanced, with the two peaks preserved, thanks to the additional thrust contribution from the distributed propellers.

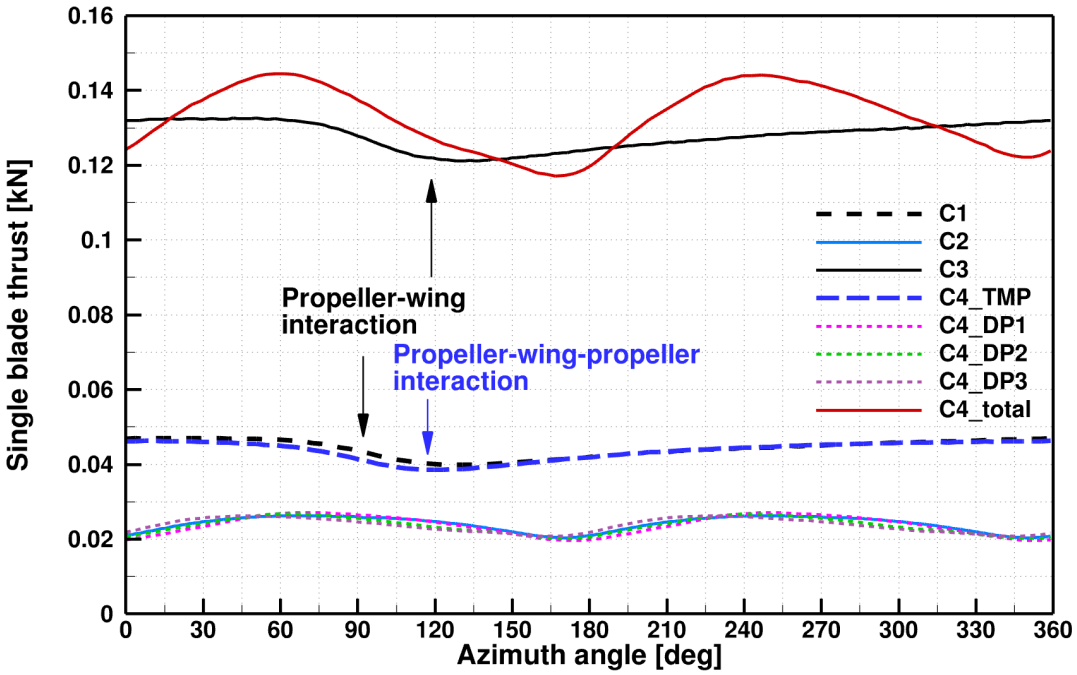

Figure 5.9: Single blade thrust variations from investigated configurations.

The thrust generated by the installed propellers varies across different configurations and conditions. Figure 5.10 presents the thrust distribution for all four configurations. The propellers exhibit asymmetric loads in all investigated cases, with variations depending on the configuration and operating conditions.

Figure 5.10(a) shows the thrust generated by the C1 propeller at different azimuth angles. It reveals that the TMP produces less thrust between azimuth angles of 0° and 90°. Similarly, Figure 5.10(c) demonstrates an expanded reduction in thrust for the TMP between azimuth angles of 0°

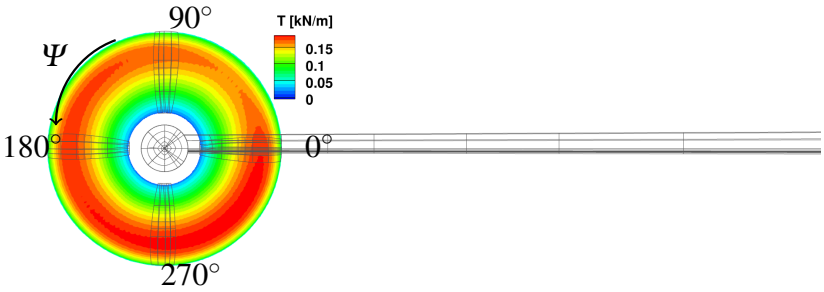

(a) C1

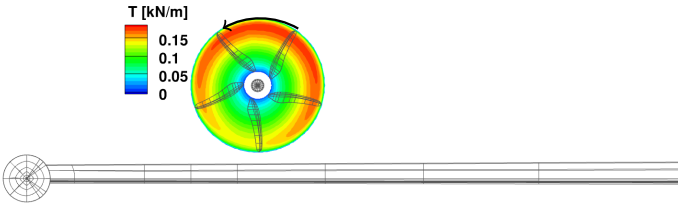

(b) C2

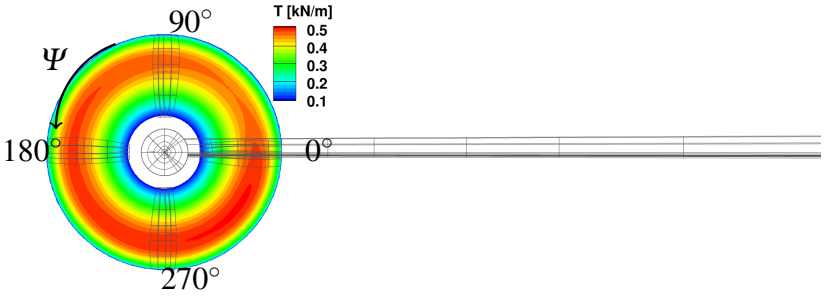

(c) C3

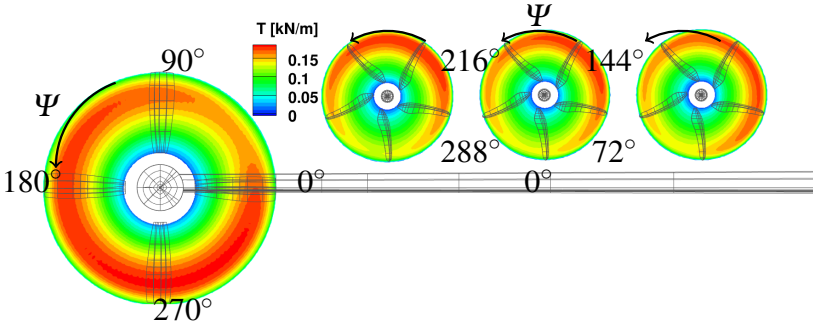

(d) C4

Figure 5.10: Propeller thrust distribution from investigated configurations. (Rotation in counter-clockwise as seen from upstream)

and 135°.

This reduction is primarily attributed to two adverse effects: the asymmetric blade/disc effect, known as the P-factor, and propeller-wing interactions. The P-factor is an aerodynamic phenomenon observed in a rotating propeller, where the center of the propeller thrust shifts off-center when the aircraft operates at a high angle of attack. This phenomenon has two primary effects, especially when the propeller disc is slightly tilted toward the horizontal plane.

First, as the propeller rotates, the descending blade moves forward, experiencing a greater forward speed, while the ascending blade moves backward, resulting in a lower forward speed. Consequently, the descending blade generates more thrust than the ascending blade.

Second, the effective angle of attack increases for the descending blade and decreases for the ascending blade due to the tilt of the propeller disc. This difference further amplifies the thrust produced by the descending blade.

The increased forward speed of the descending blade slightly reduces its effective angle of attack, but the overall tilt of the propeller disc enhances the total effective angle of attack. This leads to higher flow velocity and an increased effective angle of attack, resulting in greater thrust production by the descending blade.

In the C4 configuration, Figure 5.10(d) indicates asymmetric thrust due to installation effects. Performance loss is observed when the HLP is positioned close to the wing between azimuth angles of 288° and 72°. Comparing the single installed HLP in Figure 5.10(b) with the distributed HLPs in Figure 5.10(d), the HLP adjacent to the TMP experiences a thrust loss between azimuth angles of 72° and 216°, indicating that the combined effects increase the induced velocity in that region and slightly reduces the propeller performance at the stated azimuth angles. Around 0°, the HLPs also shows slight unloading due to interactions with the TMP, wing and the other HLPs.

Compared to the other two installed HLPs, the azimuths with higher thrust loads shift in a clockwise direction, while those experiencing performance loss tend to recover due to varying interaction mechanisms. This shift is attributed to the fact that the inboard propeller interacts primarily with the adjacent propeller and wing. Additionally, the increased wing chord length may

lead to different levels of boundary layer ingestion.

5.7 Component performance analysis

Table 5.2: Summary of the performance of TMP-only, OTW-only and TMP-DP systems. (TMP in C1 and OTW propeller in C2 have the same propeller speeds as their respective propellers in C4. C3 and C4 are thrust equivalent configurations, which matched the Tecnam P2006T aircraft at 52.6 kg thrust, from semi-wing, to achieve T/W 0.149)

Performance	**C1**	**C2**	**C3**	**C4 (TMP/DP1/DP2/DP3)**	Δ
Proplellers performance:					
Thrust (N)	177.3	120	511.56	529.7 (174.52/118.8/118.0/118.4)	+3.5%
Power (kW)	6.53	5.5	22.35	22.82 (6.416/5.47/5.46/5.48)	+2.1%
Froude efficiency (-)	0.75	0.60	0.63	0.633 (0.748/0.596/0.593/0.594)	+0.5%
Pitching moment (Nm)	6.42	-46.3	15.41	-130.43 (6.52/-45.94/-45.72/-45.29)	
Wing performance:					
Lift (N)	958	901	987	1138	+15.3%
Drag (N)	66.3	61.7	67.6	41.2	−39.1%
L/D (-)	14.45	14.6	14.6	27.6	+89.0%
Pitching moment (Nm)	-229.7	-219.7	-236.6	-248.5	
Overall efficiency (-)	46.8%	29.2%	54.6%	58.9%	+7.9%

The contribution of thrust, power, efficiency, and pitching moment is presented in Figure 5.11 for all configurations and their components. In Figure 5.11(a), shows that TMP produces slightly more thrust than the HLP in the current setting, increasing the propeller speed from 1850 RPM to 3264 RPM has more than double the thrust generation, where the C4 configuration with the TMP-DP design produces a slightly more thrust compared to the equivalent C3 (TMP-only) configuration. The contribution of each component within the C4 configuration shows that the TMP contributes about 33% of the thrust and the DP system contributes by about 66%. There is no significant performance loss within the TMP-DP system due to the aerodynamic interactions in the current design. The power distribution is seen in Figure 5.11(b), the increase of thrust generation resulting from a higher power requirement. Within the C4 (TMP-DP) configuration, the TMP required 28% of the total power, and the DP system requires the rest of the 72% of the total power. The difference in thrust and power contribution is also reflected by the propeller efficiency distribution, in Figure 5.11(c). It also indicated that the TMP is more efficient by operating at the

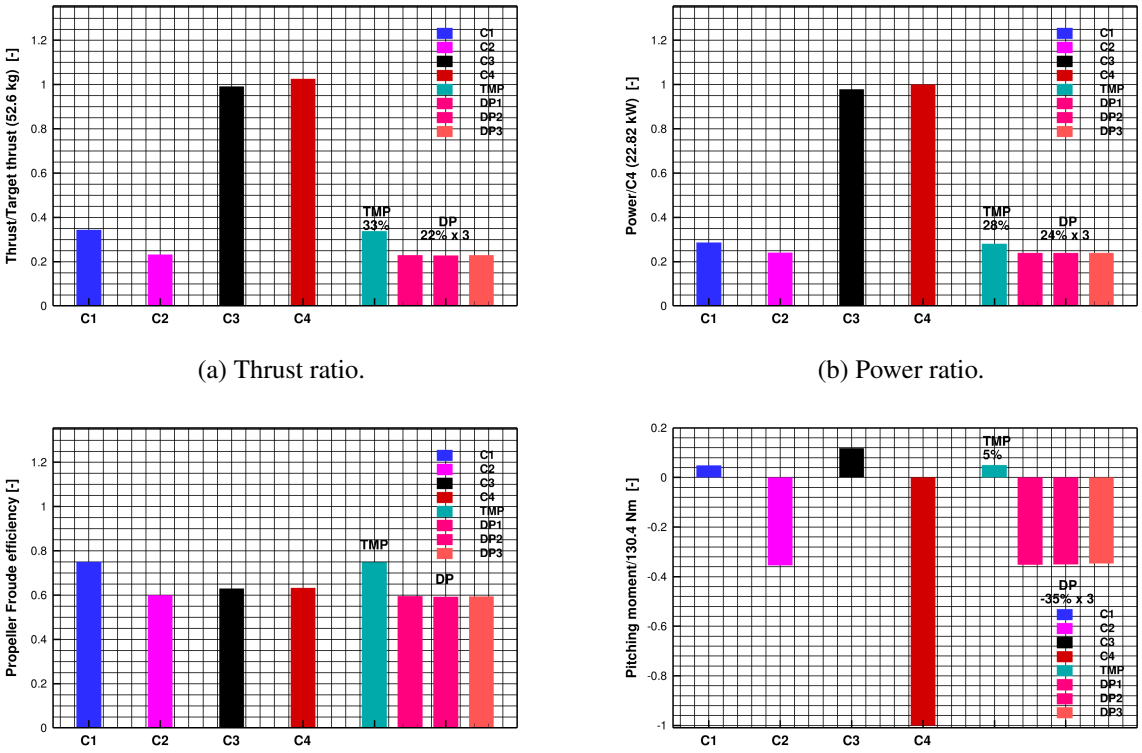

(a) Thrust ratio.

(b) Power ratio.

(c) propeller efficiency.

(d) Pitching moment ratio.

Figure 5.11: Overall and individual component performance comparisons of four configurations.

lower speed condition in C1, but C4 has a 0.5% higher propeller efficiency and also produces 3.5% of additional thrust than the C3. In the current design, with the reduced unfavourable aerodynamic interactions, there is no harm to the performance by introducing the C4 (TMP-DP system). In addition, Figure 5.11(d) shows that increasing the operating speed of the TMP would lead to an increase in nose up pitching moment (positive value), but the C4 configuration has a much larger nose down pitching moment, which is mainly contributed by the OTW installed DP system. However, this can be balanced within the propulsion system by changing the position of the DP system, increasing and reducing the thrust contribution from the TMP and DP systems, respectively, or by a net balancing at the full vehicle level.

5.8 Overall performance analysis

The performance of the overall system for equivalent configurations is presented in Figure 5.12. The TMPDP configuration exhibits the highest lift among the configurations studied. Variations in thrust for the tip-mounted propellers have a lesser impact on the lift and drag of the wing due to the smaller wetted area, resulting in only minor changes in the lift-to-drag ratio (L/D). The addition of the OTW distributed propulsion system significantly increases the nose-down pitching moment, as indicated in Table 5.2.

Comparing thrust-trimmed data between the TMP-only and TMP-DP systems in the C3 and C4 configurations, the installed propellers generate similar thrust levels. The overall propeller efficiency is comparable between these two configurations, with the exception of the C1 configuration, where the TMP demonstrates superior efficiency at lower advance ratios.

Crucially, the data indicate that increasing the thrust setting in the TMP-only configuration enhances the overall propulsive efficiency. The introduction of the OTW-DP system was further beneficial to the overall efficiency, approaching nearly 60%, with a substantial improvement in wing lift generation. As a result, the integrated TMPDP system performs better than the other configurations.

5.9 Chapter Summary

In advanced propulsion system design for flying vehicles, existing configurations must be rethought due to the increased flexibility offered by hybrid/electric powertrain systems. This suggests a need for reserve, particularly regarding aero-propulsive synergistic effects. This study presents four propulsion systems using state-of-the-art modeling approaches, each aimed at enhancing performance. Current work covers aerodynamic performance, interactional effects, and configuration design in detail. The results demonstrate that the analysed configuration can significantly improve overall propulsive efficiency and lift generation.

The study found that the placement of tip-mounted and distributed propulsion systems cre-

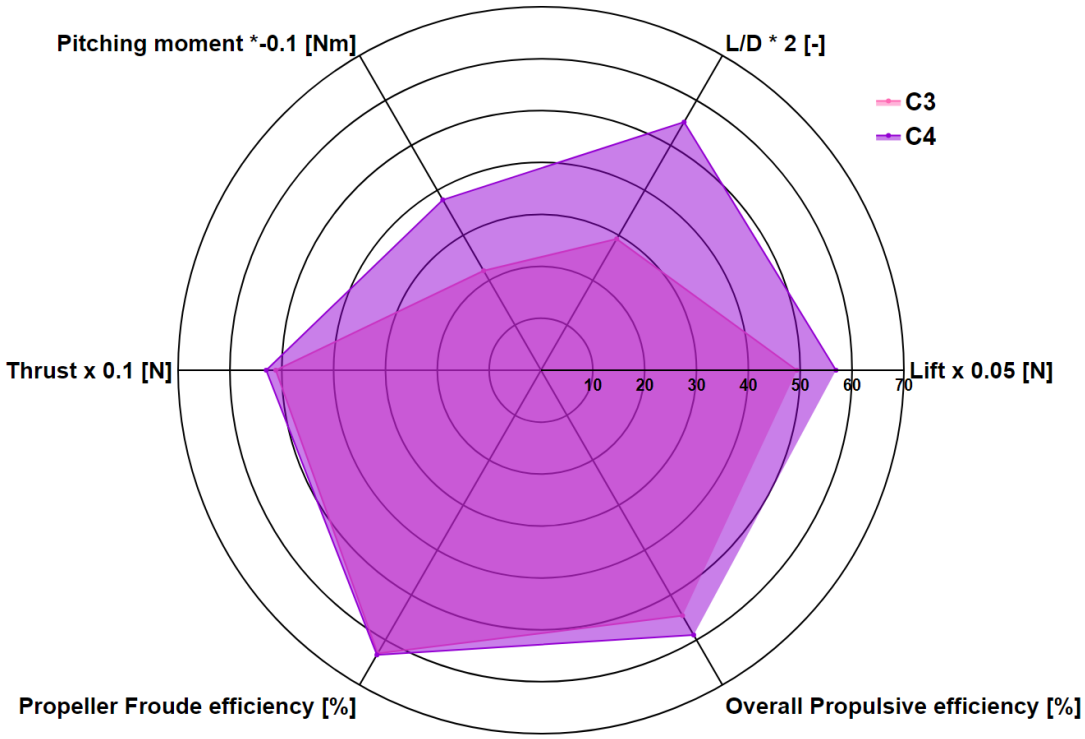

Figure 5.12: Performance comparisons of the thrust equivalent TMP-only (C3) and TMP-DP (C4) systems.

ated an aerodynamic interference region with the wing in Figure 5.7. In the higher tip-speed case of TMP compared from configuration C3 to C4, this interference becomes stronger, which reduces suction pressure near the leading edge and mid-chord region while increasing pressure at the leading and trailing edges on the pressure side due to wake-washing effects. The propeller-wing interaction caused thrust fluctuations as the propeller blades swept through the interference region, though the mean thrust was only slightly impacted, particularly in the lower tip-speed case from configuration C1.

Similar benefits, such as reduced suction pressure region, were observed in the OTW-installed HLP in configuration C2, see Figure 5.7 (c). This benefit was even more pronounced in the distributed propulsion system of configuration C4, likely due to the cooperative effect. In the proposed TMP-DP configuration, no significant thrust loss was observed when transitioning from single to distributed propellers. However, the TMP in configuration C4 exhibited thrust fluctuations similar to those in C1, indicating that TMP-DP-wing interactions have minimal impact on propeller

performance within the TMP and DP systems.

The propellers within the DP system experienced similar sinusoidal variations in thrust as shown in Figure 5.9, with the collective output of the TMP and three OTW propellers resulting in greater overall thrust fluctuations compared to the C3 configuration. The lift force distribution along the wingspan revealed a significant spike near the wingtip in the C3 configuration, which was substantially reduced in the C4 configuration. The increased lift generation near the most inboard OTW propeller may be attributed to the increased wing chord length. For the propellers, the TMP with higher speed experience expanded thrust loss due to the installation, hence a better efficiency with lower RPM case. The installation of the DP system caused a slight reduction in the thrust of the TMP while passing through the wing suction side. At the same time, the cooperative effect of the DP slightly reduces the propeller performance while the propeller passes the wing and the adjacent propellers. However, the wing performance is much improved.

The structure of the vortex system in all configurations is affected by interactional effects due to the propeller installation, resulting in an asymmetric vortex system. In the TMP-only configuration, which provides equivalent propulsion force, the vortex generated is significantly stronger. The main deformed vortex tends to rise upward and propagate downstream and inboard. In configuration C4, there is a more rapid destruction of tip vortices and faster wake dissipation observed behind the TMP. The vortex system in the DP configuration introduces additional interference with the wing system. This interference shapes the wakes from the HLPs and the wing, with the middle HLPs exhibiting enhanced wake dissipation due to the anticlockwise vortex from the adjacent propeller blades.

In terms of performance, configuration C4 generated 3.5% more thrust with improved efficiency. The enhanced wing performance resulted in nearly 15% more lift, and the overall propulsive efficiency gained 8%. Where the lift enhancement could help offset the extra weight of distributed propellers. The pitching moment was also analysed, while the wing produced a similar pitching moment between C3 and C4, the DP system in C4 contributed to a significantly higher pitching moment.

Comparing the DP system with and without the TMP propeller, as shown in Figures 5.1(b) and 5.12, the overall propulsive efficiency is further improved by incorporating the TMP propeller. This configuration also leads to enhanced lift-to-drag ratio (L/D), increased total thrust generation, and improved propeller efficiency. Moreover, the additional torque introduced into the propulsion system by the TMP or DP components is unlikely to pose a significant challenge for future electric and hybrid propulsion systems.

Given the benefits of the integrated TMP and DP system, it can operate under optimal propeller performance conditions with variable pitch and RPM, while simultaneously enhancing lift and achieving a more uniform load distribution. Moreover, the AD method is suitable for system-level optimisation when supplied with high-fidelity data that accurately represent the aerodynamic interactions between the propellers and the wing. Future work is going to focus on the configuration optimisation (e.g. pusher configuration), near-field, far-field noise investigation, and noise reduction using synchrophasing.

Chapter 6

Noise Reduction using Phase Synchronisation

This chapter has been published as: Geng Qiao, Emma San Martin, George Barakos, "Assessment of Synchrophasing for a Pair of Rotors in Close Proximity," Aerospace Science and Technology, (2024) doi:2024.109808.

This chapter investigates the aerodynamics and aeroacoustics of a pair of rotors similar to those in the distributed propulsion (DP) system, using the same propeller separation distance as defined in Chapter 5. The configuration was also studied in the "Radiation and Propagation for Multirotor Systems" project from the Group for Aeronautical Research and Technology in Europe (GARTEUR) Action Group 26. The study employs the validated, high-fidelity computational fluid dynamics (CFD), in-house Helicopter Multi-Block Solver 3 (HMB3). A pair of dual-bladed 13x7 rotors in hover and edgewise flight were studied. This study aims to reduce rotor noise by introducing a phase offset between the initial angular positions of the rotors in a tandem configuration, similar to the distributed propulsion system described in Chapter 5. The rotors maintained a constant RPM, and a tip Mach number of Mach 0.4, close to typical values for full-scale urban air mobility (UAM) rotorcraft. A comprehensive synchrophasing study based on cumulative effect of the rarefaction and compression in the acoustic wave is presented using fully resolved time-marching calculations. Following this, an analysis of aerodynamic performance and acous-

tics with accounting for human noise perception of isolated and multiple tandem configurations is presented.

6.1 Test Matrix

The text matrix involved in the synchrophasing investigation of tandem configurations is presented in Table 6.1, and the conditions were selected based on the AG26 work [73, 148]. The freestream was 15 m/s, with both rotors operating at 8,000 rpm to reach a designed tip speed of 0.4. Three configurations were tested, including isolated, coplanar, and tandem rotors, as shown in Figure 6.1 and on Table 6.1. Both configurations involve two rotors that are horizontally separated by a distance of $1.18D$, resulting in a blade tip-to-tip distance of $0.18D$. The tandem coplanar configuration, has no vertical offset, whereas the tandem offset configuration, has a vertical displacement of $0.25D$. A dataset comprising twelve unique phase offset conditions, including both low and high blade phases, was obtained for the coplanar and tandem offset, counter-rotating configurations.

Table 6.1: Summary of the test condition used for GARTEUR AG26 DLR ACCID 13x7 rotor synchrophasing studies.

Free-stream velocity	15.00 m/s
Radius	0.164 m
RPM	8000
Blade tip Mach number	0.3996
Configuration :	
Tandem coplanar	$\Delta x = 1.18D$, $\Delta y = 0$, $\Delta z = 0$
Tandem offset	$\Delta x = 1.18D$, $\Delta y = 0$, $\Delta z = 0.25D$
Synchrophasing :	
De-phased angles studied ($\times N_b$)	0° - 360° ($\Delta = 15^\circ$)
Number of computing cases	24

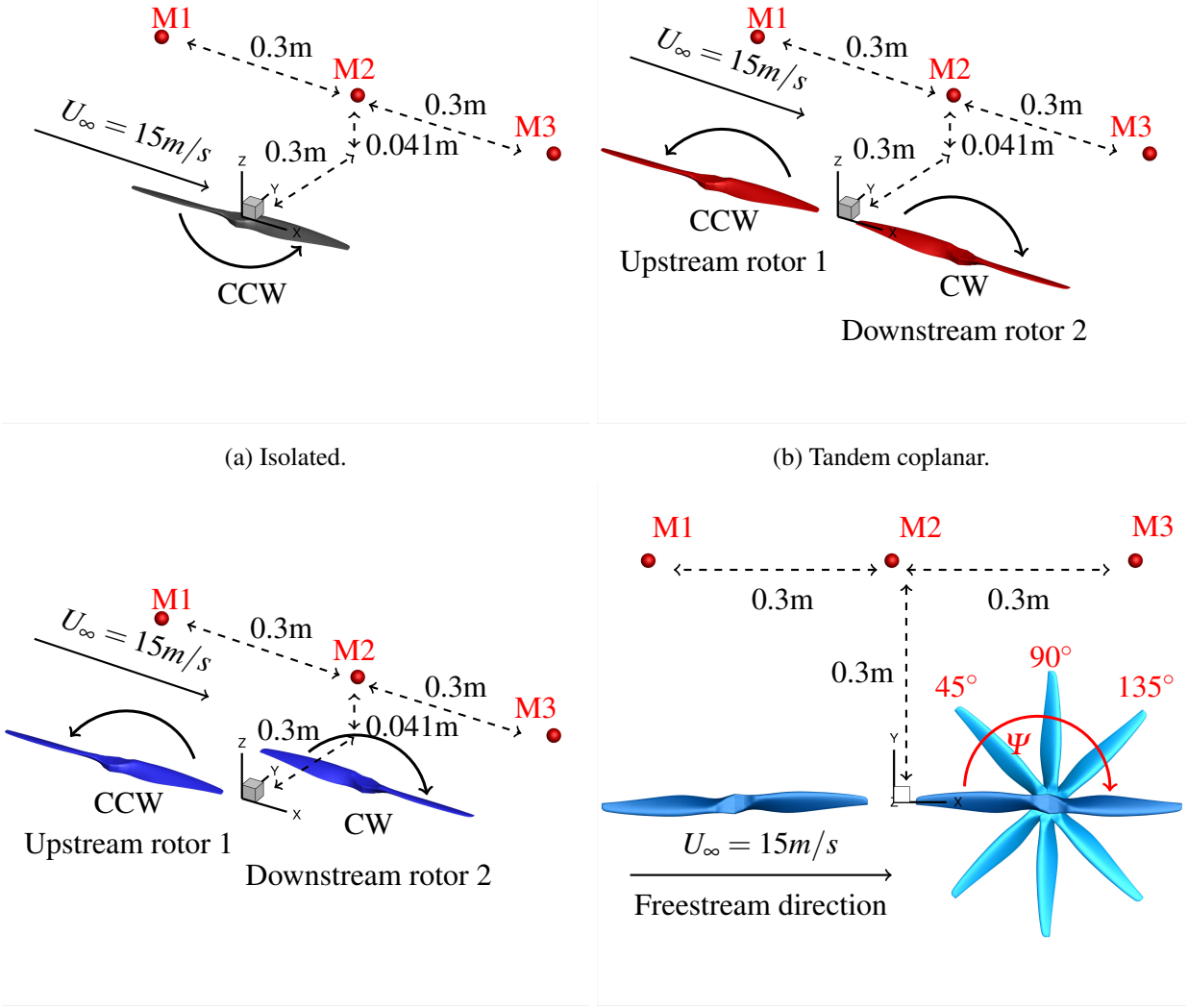

(a) Isolated.

(b) Tandem coplanar.

(c) Tandem offset.

(d) Phase offset.

Figure 6.1: Visualisation of synchrophasing and microphone positions. Microphones were chosen to study the near-field noise.

6.2 Results for Tandem Rotors

Figure 6.2 shows iso-surfaces of the Q-criterion, coloured by vorticity magnitude, for tandem rotors in different configurations. The vortex structures are well-resolved from the rotor blades to their wake region. In Figure 6.2(a), the tandem coplanar rotors exhibit clearer and stronger vortex interactions, highlighted by red circles, compared to the tandem offset rotors shown in Figure 6.2(b). The vertical offset of the downstream rotor in Figure 6.2(b) results in the first vortex spiral

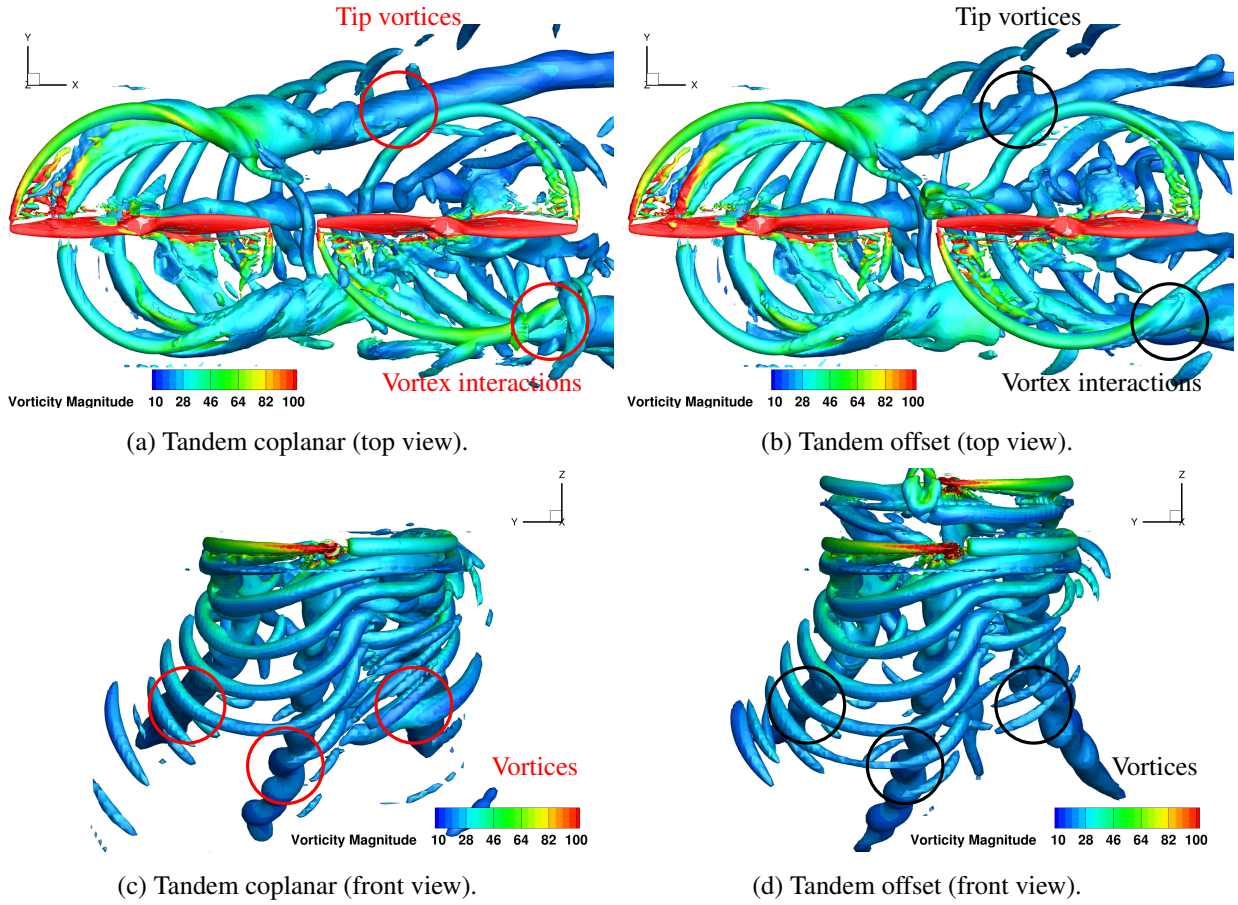

(a) Tandem coplanar (top view).

(b) Tandem offset (top view).

(c) Tandem coplanar (front view).

(d) Tandem offset (front view).

Figure 6.2: Iso-surface of the Q-criterion at $Q = 0.1$ coloured by vorticity magnitude of the tandem rotors with/without vertical offset.

being significantly deformed by the vortices from the upstream rotor.

Figures 6.2(c-d) show the wake profiles in the vertical direction for both configurations. In the front view, unsymmetrical spirals and three main vorticity streams are observed. The wake of the tandem coplanar configuration tends to propagate further back in the freestream direction, whereas in the tandem offset configuration, the wake propagates further downward. This behaviour is typically observed in low Reynolds number flows, where tip vortices break down more quickly, leading to vortex-vortex interactions [76]. It is evident that rotor interactions are more prominent in multirotor systems operating in close proximity, which distinguishes them from conventional large rotor configurations, particularly in the near field. This highlights the need for flow control techniques to mitigate aerodynamic interferences and their associated noise.

6.3 Tandem Rotors Synchrophasing Study

Using the same configuration as the wind tunnel, this section expanded the validation experiments to look into the sychrophasing impact. The CFD solver HMB3 is used to compute aerodynamic performance (thrust and torque) and acoustics (time series and spectrum analysis). Each configuration spans 12 phase offsets, for a total of 24 cases in this study.

6.3.1 Performance Results

The isolated and the tandem rotor configurations were examined under 24 different phase offset cases in edgewise flight at 15 m/s, with loads averaged over the last revolution. As anticipated, the isolated rotor outperforms tandem configurations, reflecting a performance loss in multi-rotor configurations due to interactions. Figure 6.3 illustrates the reduced performance of the downstream rotor compared to the upstream rotor in each configuration. In addition, it is noted that both rotors, in the tandem offset configuration have marginally better thrust when compared to the coplanar configuration, as a result, the overall thrust is left untrimmed in this study.

By altering the phase offsets, there is no apparent impact on the thrust of the upstream and downstream rotors. In terms of torque, the upstream rotor remains mainly unaffected by the synchrophasing. In contrast, the downstream rotor exhibits variations, with more pronounced benefits observed from 105° to 165° in the coplanar configuration. In the tandem offset configuration, the performance of the rotors is independent of the synchrophasing. However, the downstream rotor performs better than for the coplanar configuration.

The disk loadings for isolated and tandem rotors are presented in Figure 6.4(a-g). The forces are in the blade frame of reference, and M^2C_T and M^2C_Q are sectional thrust and torque coefficients about the shaft axis. The moment coefficient is represented by M^2C_M, as negative for pitch-down moments. In Figure 6.4(b) of the up stream rotor from the tandem coplanar configuration, there is a small decrease in thrust coefficient on the advancing and retreating sides at $\Psi = 65^\circ$ and $\Psi = 315^\circ$, respectively, indicative of tip vortex effects. This becomes more evident in the torque coefficient distribution on both the advancing and retreating sides, highlighting the influence of rotor-rotor

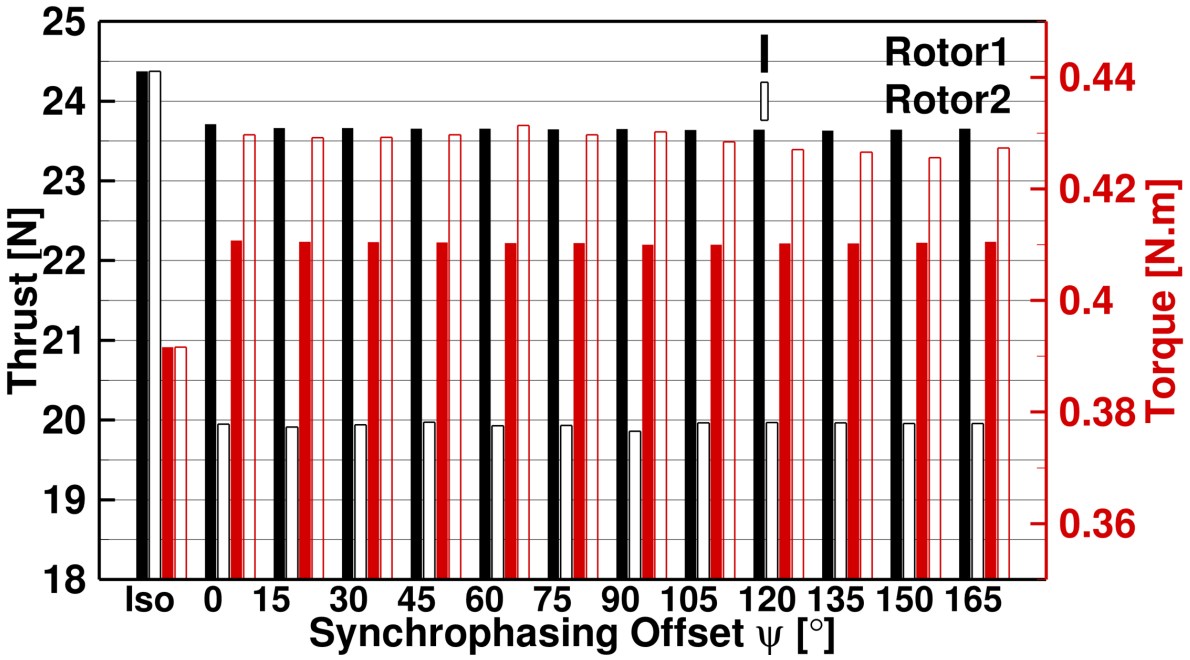

(a) Tandem coplanar.

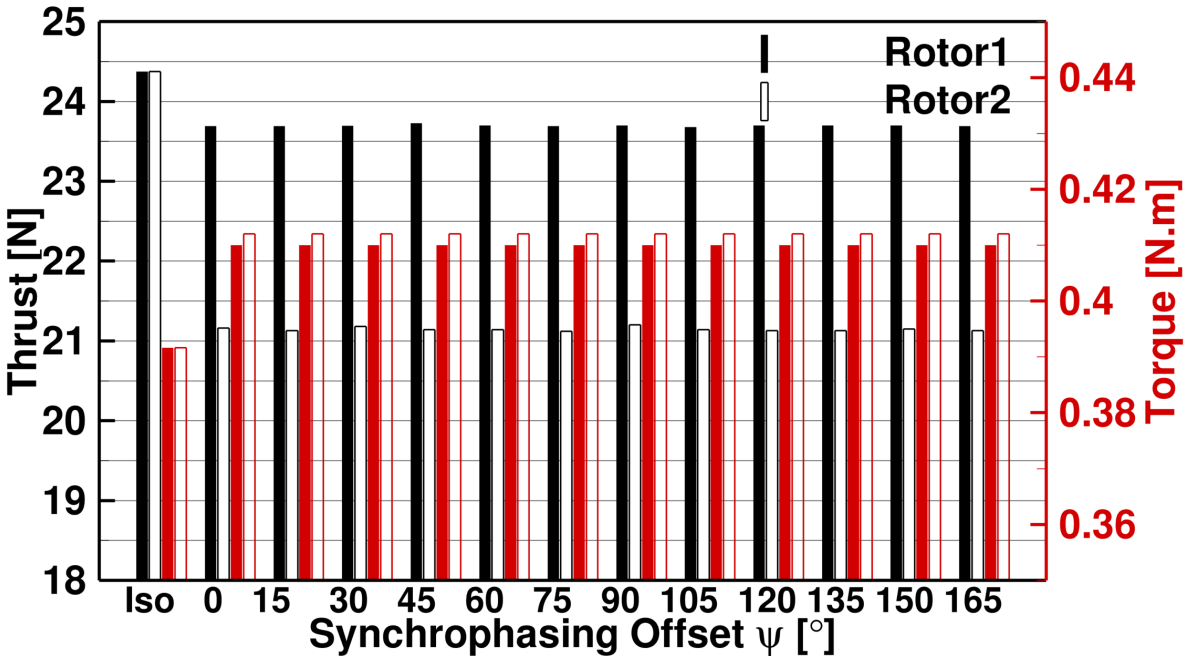

(b) Tandem offset.

Figure 6.3: Rotor performance of tandem configurations due to the synchrophasing effect. (Upstream and downstream rotors are represented by rotor 1 and 2)

interaction. The distribution of pitch moments also undergoes changes at the mentioned angles, resulting in a slight performance drop for the upstream rotor due to interference in the tandem coplanar configuration.

Comparatively, the downstream rotor in Figure 6.4(c) shows a more pronounced decrease in thrust and pitching moments. The thrust reduction is notable in the region from $\Psi = 135^\circ$ to $\Psi = 225^\circ$, attributed to rotor wake interference, contributing to a slight reduction in pitching moment in that region. In contrast, the torque coefficient increases, particularly on the retreating side, indicating a higher power requirement from the downstream rotor to counteract the wake from the front rotor.

In the tandem vertical offset configuration, as shown in Figures 6.4(d-e), the upstream rotor exhibits load distributions that are quite similar to those observed in the tandem coplanar configuration. This suggests that raising the position of the downstream rotor does not significantly impact the upstream rotor. However, when comparing the downstream rotor in the vertical offset configuration to that in the coplanar configuration, as depicted in Figures 6.4(e) and (c), a marked improvement in thrust performance is evident in the vertical offset configuration. A similar enhancement is also observed in the pitching moment distributions. Although the torque coefficient in the vertical offset configuration is higher than in the isolated configuration, it is reduced compared to the coplanar configuration.

Furthermore, by applying synchrophasing with a 90° phase offset in the tandem vertical offset configuration, as shown in Figures 6.4(f-g), the upstream rotor remains unaffected. However, the sudden loss of thrust observed in the downstream rotor is mitigated due to reduced aerodynamic interactions, as reflected in the disk loading distribution at $\Psi = 180^\circ$. This reduction suggests that the 90° phase offset effectively mitigates some of the adverse effects of rotor-rotor interactions, leading to improved performance in the downstream rotor.

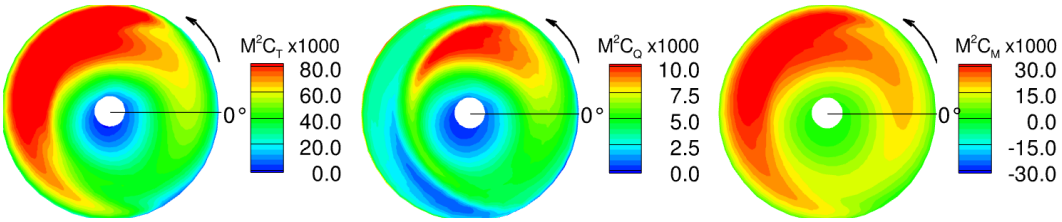

(a) Isolated rotor.

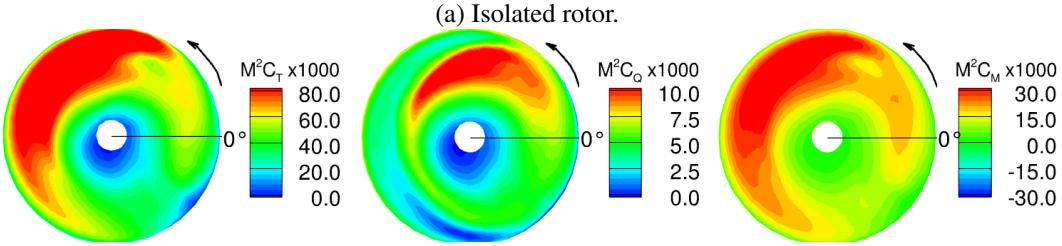

(b) Tandem coplanar upstream rotor.

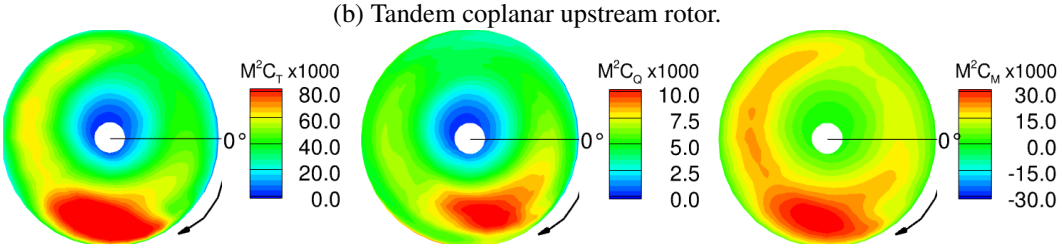

(c) Tandem coplanar downstream rotor.

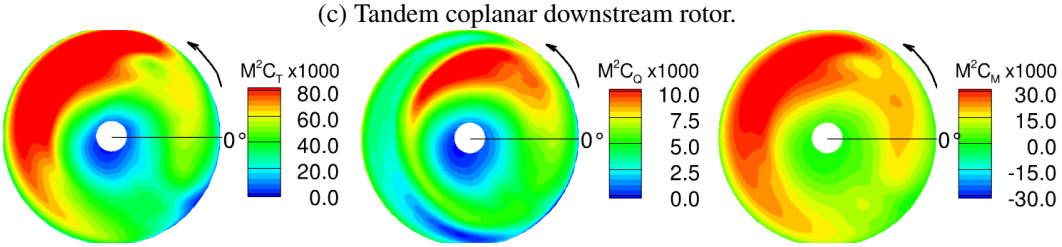

(d) Tandem vertical offset upstream rotor.

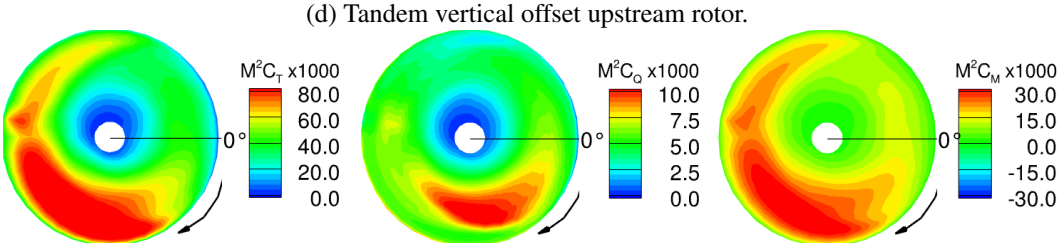

(e) Tandem vertical offset downstream rotor.

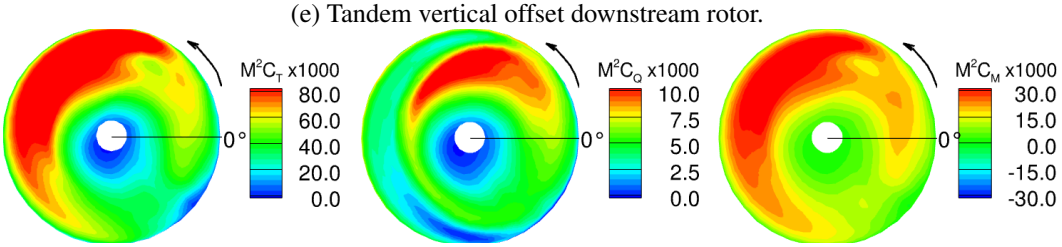

(f) Tandem vertical offset upstream rotor with 90° phase-offset.

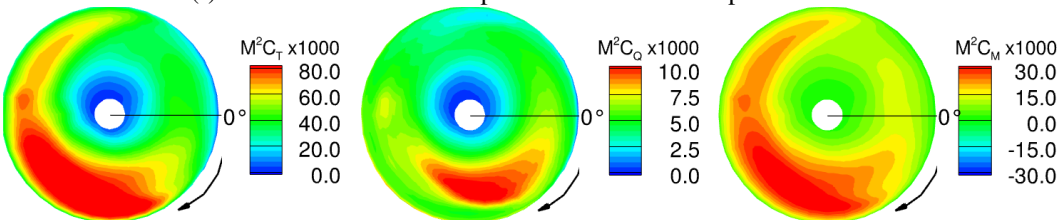

(g) Tandem vertical offset downstream rotor with 90° phase-offset.

Figure 6.4: Tandem coplanar, vertical offset, and vertical offset with 90° phase offset rotor disks contoured with thrust, torque and pitching moment coefficients in edgewise flight, $\mu = 0.109$.

6.3.2 Aeroacoustic Results

Presented in Figure 6.5 is the A-weighted OSPL of each phased case for the tandem configurations where the M1, M2, and M3 refer to the upstream, interior, and downstream microphones. The AOSPLs reveal a trend in the variation of noise at different locations due to the phasing. The effects are configuration-dependent, and a stronger phase effect is seen in the area between the two rotors. For most phase offsets, the upstream position registers the highest AOSPL, while the position between the two rotors ranks as the second highest, with the downstream microphones having the lowest noise levels.

In coplanar configuration, phase offsets 45°, 75°, 105° and 150° show reduced noise emissions in the upstream region. The benefit of the synchrophasing appears stronger in the interior region, where all phase angles show different levels of noise reduction. The downstream region is relatively less sensitive to the synchrophasing, but phases of 30°, 75°, 90°, 120° and 150° show a benefit.

In the tandem offset configuration, synchrophasing appears to benefit the upstream region from most phases, apart from the 45° and 135° offsets. Furthermore, it is advisable to steer clear of the 45° angle as it results in an approximately 1 dB greater noise level in the area between the rotors. In the interior region, where AOSPLs exhibit varying degrees of reduction, noise emission is extremely sensitive to phase offsets, much like in the coplanar design. At phase 90°, a maximum 4dB reduction of A-weighted sound pressure level is attained. The downstream noise from the tandem offset configuration was less than that from the coplanar configuration in most cases. A maximum reduction of 1 dB is seen with 120° phase offsets for the coplanar configuration. A clear benefit can be seen for cases with 75°, 90°, and 120° phase offsets for the tandem offset configuration, whereas the A-weighted sound pressure level at the case 75° is decreasing by 1.5 dB compared to its baseline case.

Figure 6.6 shows the acoustic effect of phase offsets across a wide range of BPFs for both configurations. The phase offsets have less effect in the upstream region, especially in the first three BPFs. A more visible noise reduction is seen from 4th to 10th BPFs for both configurations,

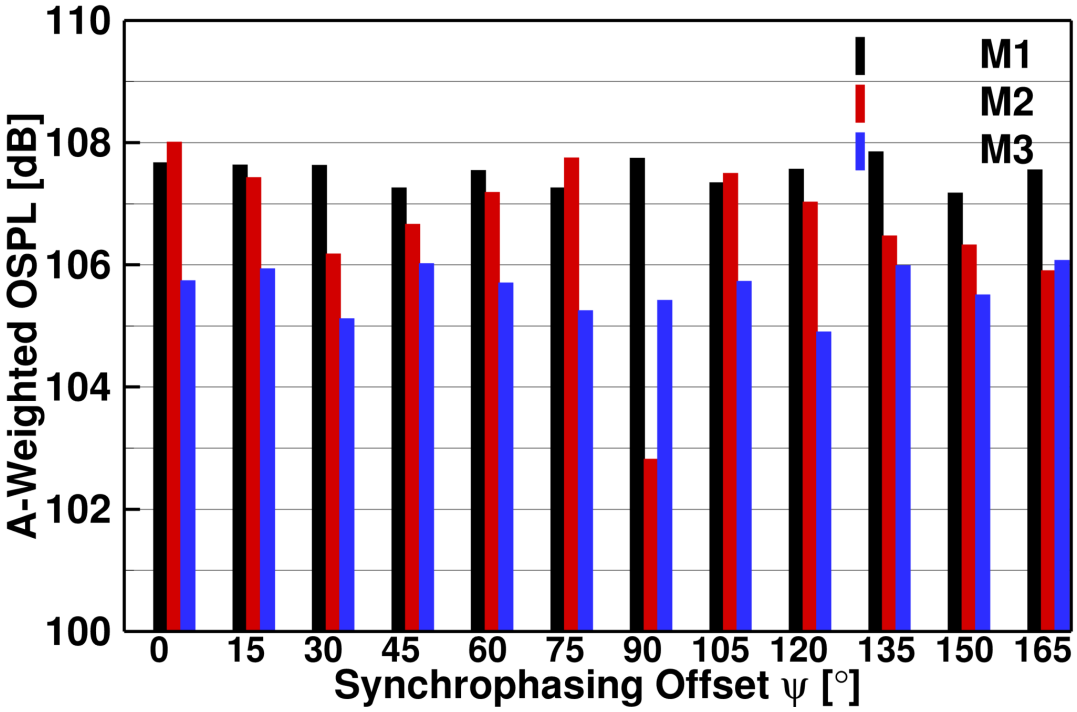

(a) Tandem coplanar.

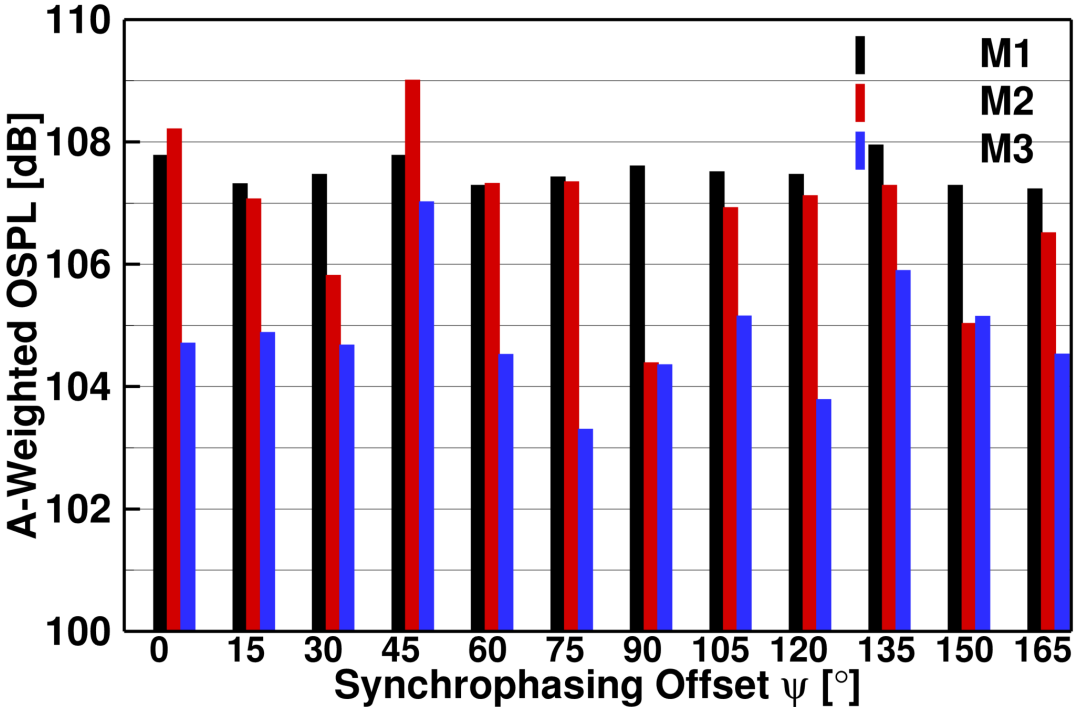

(b) Tandem offset.

Figure 6.5: AOSPL of microphones at different locations due to the synchrophasing effect of tandem configurations. (M1: upstream, M2: interior, M3: downstream microphone)

and it extends to 12th BPFs in the tandem offset configuration. In addition, a noticeable drop in ASPL is seen between the 4th and 6th BPFs in the phase offset range of 15° to 45°. Compared to the upstream region, the interior region exhibits a much greater impact from the spectrum with phase offsets. There is a noticeable decrease at the first BPF in the phase offset range of 60° to 90°. Phase angles of 45° and 135° are more prominent in terms of the 2nd BPF. Additionally, for all configurations, the benefit of synchrophasing was extended across the spectrum above 9th BPFs at phase offsets of 150° and 165°. Between the 4th and 8th BPFs in the coplanar configuration, they are primarily affected by the phasing in the downstream area. The tandem offset configuration exhibits a much more pronounced effect throughout the spectrum, while the first BPF significantly decreases between phases 120° and 150°. Overall, it is observed that the noise spectrum from the downstream region is significantly reduced by elevating the vertical position of the downstream rotor compared to the coplanar configuration. Furthermore, an improvement in noise reduction due to the sychorphasing also benefited from the elevated downstream rotor.

To better understand the impact of these distributions on a human listener, the A-weighted band-averaged SPL (ABASPL) for each of the one-third-octaves bands, as described earlier, has been analysed for each phase. Results for the tandem coplanar configurations in the phase offset angles between 15° and 165° are presented in Figures 6.7. Notably, synchrophasing exhibits more pronounced noise in the 1st and 2nd BPFs. However, slight variations are observed, with comparatively lower noise levels in the frequency bands beyond the second BPF than in the first two BPFs. Additionally, the response levels of microphones from different locations vary with the phase offset angle, emphasising the need to subtract the baseline case to discern the effect of synchrophasing on different frequency bands.

ABSPL differences are calculated by subtracting the 0° phase offset baseline from the various phase cases, are illustrated in Figure 6.8 for the tandem coplanar configuration. Across all phase offsets, the interior region has the most noise reduction, especially at the phase offsets between 30° and 90°. Noise with the A-weighted sound pressure level was reduced by more than 7 dB for phase offsets of 45° and 60°. In addition, a 90° case appears promising for noise reduction in the interior and downstream regions. In the tandem offset configurations presented in Figure

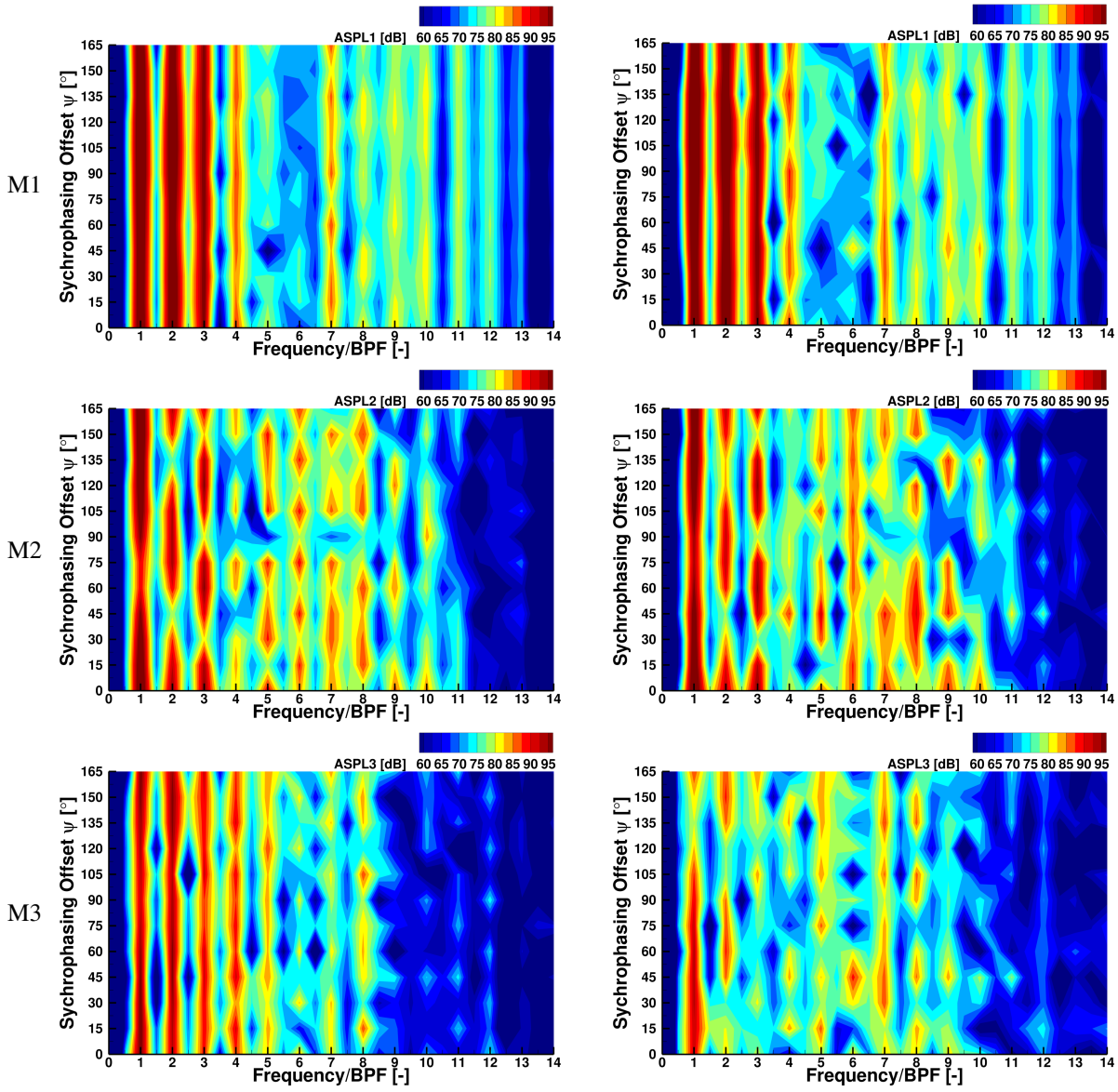

Figure 6.6: A-weighted SPL spectrum of microphones at different locations due to the synchrophasing effect at tandem configurations. (M1: upstream, M2: interior, M3: downstream microphone)

6.9, the interior region shows the most noise reduction at similar phase offsets as the coplanar configuration. Furthermore, the 120° de-phase case is much quieter in the interior and downstream regions. Almost 6 dB of reduction was achieved in the downstream region due to the acoustic benefit gained from the first two BPFs, which are located in the bands 250 and 500 Hz.

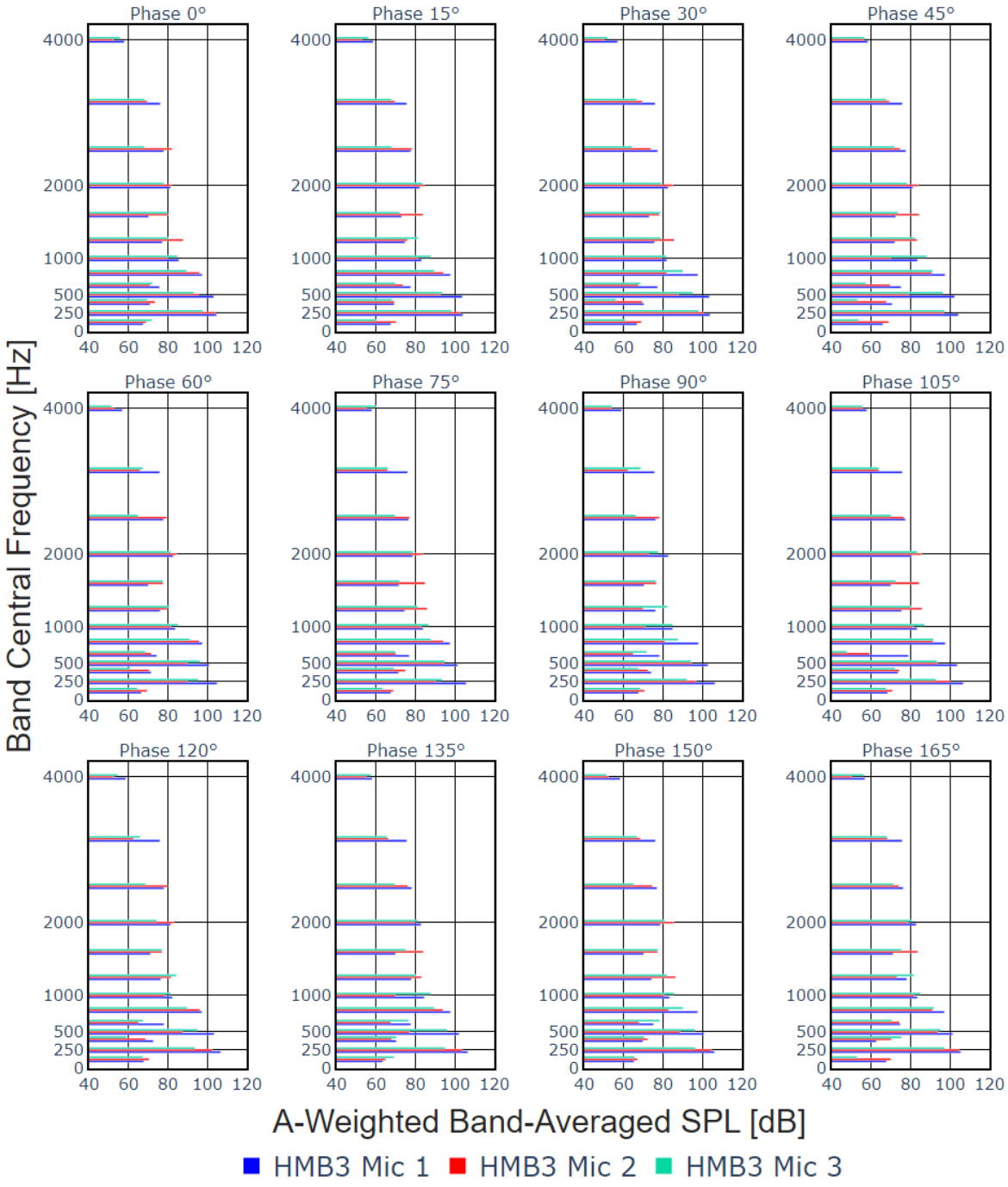

Figure 6.7: Tandem coplanar ABASPL values.

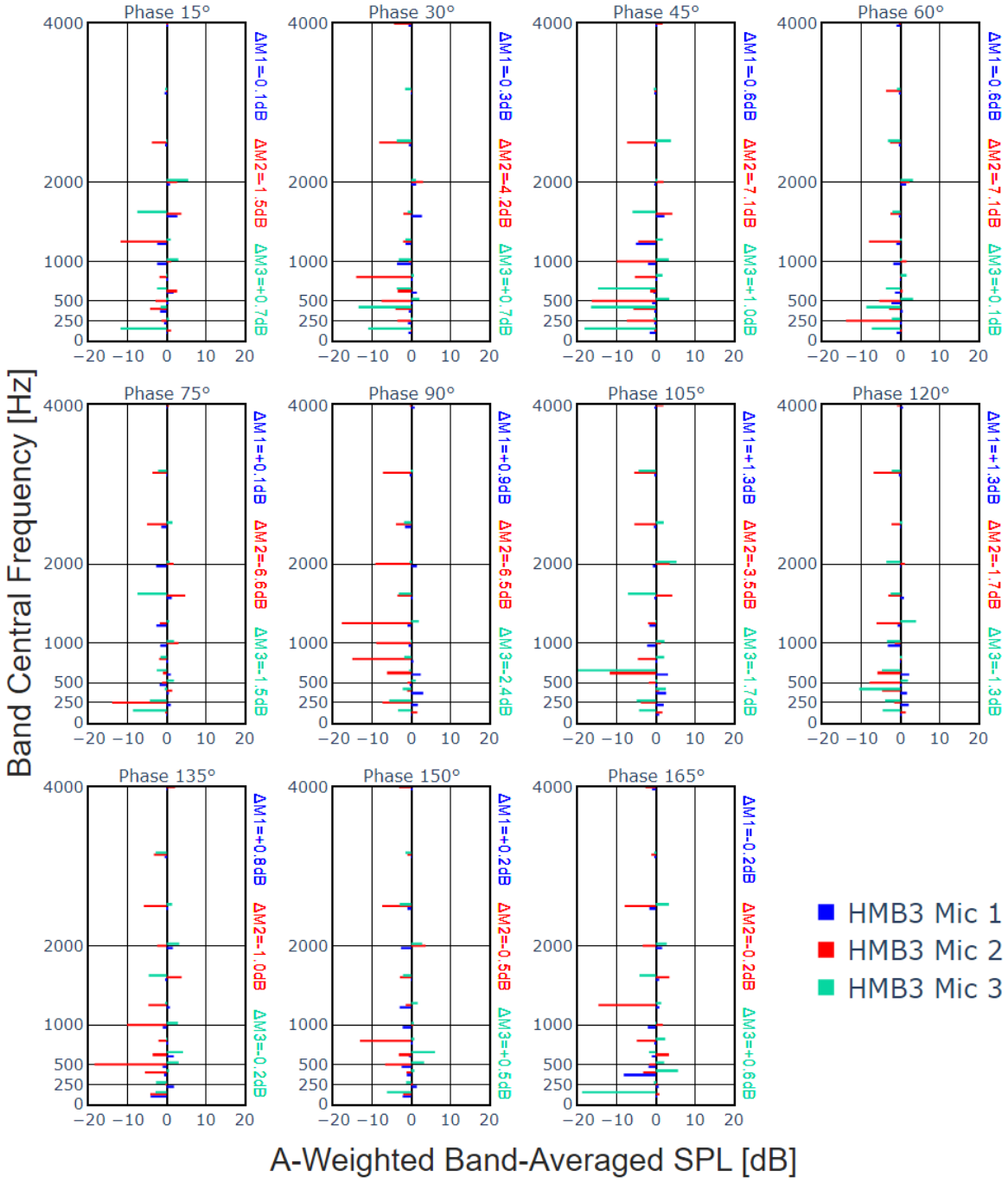

Figure 6.8: Tandem coplanar ABASPL differences from in-phase for all phase angles. The overall reduction or increase at the selected microphone locations is also shown.

6.3.3 Time Series Analysis

Acoustic pressure at different azimuths for the tandem coplanar synchrophased cases is presented in Figure 6.10, as the microphone positions are represented by black dots, and red contour colour

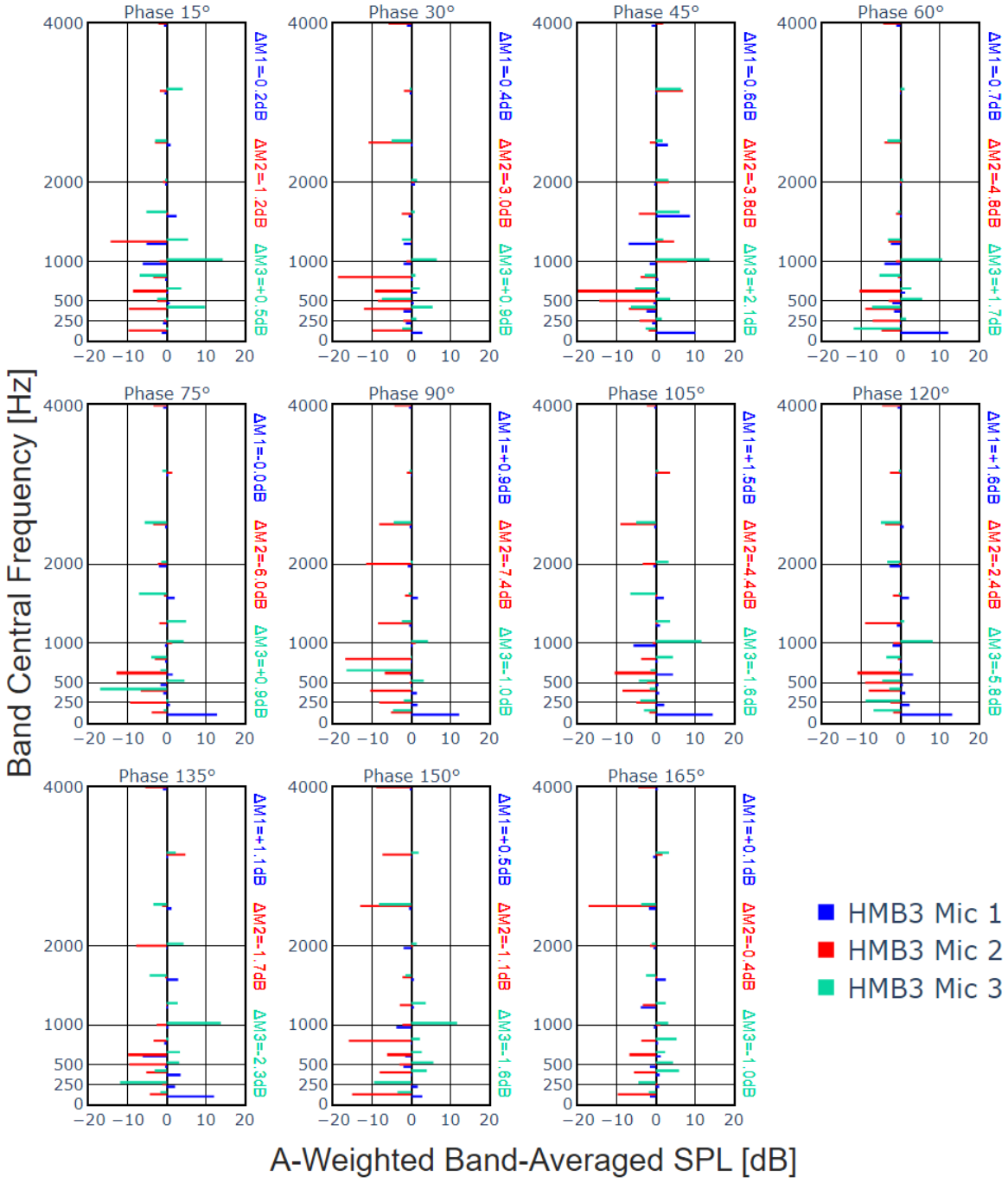

Figure 6.9: Tandem offset ABASPL differences from in-phase for all phase angles. The overall reduction or increase at the selected microphone locations is also shown.

and blue contour colour represent the positive and negative acoustic pressure. At each rotor, the directivity of the negative acoustic wave is orthogonal to the positive acoustic wave. In the baseline

in-phase case, it shows that the acoustic waves from the in-phase case arrive simultaneously at the microphones, which amplifies the strength of the original wave. Reduced acoustic pressure is seen by relatively white contour colour at microphone positions in the selected phase offset cases, such as 30°, 45°, and 90°, compared to the baseline in-phase case. On the other hand, in $\Psi = 60^\circ$ and $\Psi = 150^\circ$ from the 45° de-phased case, a solid L-shaped black line represents a smaller positive acoustic pressure zone, whereas a Z-shaped black solid line indicates a smaller homogeneous wave superposition zone and results in reduced sound pressure.

Further analyses focus on the acoustic pressure history at various locations for the tandem coplanar configuration. The time history of acoustic pressure is compared between the selected in-phase and optimal phased cases, as shown in Figure 6.11. For each microphone location, the most beneficial phase is highlighted. It is observed that the upstream and downstream regions are less sensitive to synchrophasing, suggesting that the acoustic pressure in these areas is predominantly influenced by the two-bladed rotors. In contrast, two strong peaks and valleys appear for the in-phase case, with their positions shifted in the optimal phased scenario. Additionally, greater sensitivity to noise is observed in the interior region, where the acoustic pressure history becomes more complex, likely due to dominant interactional effects. In the optimal 60° de-phase case, these strong peaks and valleys are redistributed into smaller ones, indicating that the perceived noise is significantly reduced, thanks to diminished interactions.

The time history of acoustic pressure for the tandem offset configuration is presented in Figure 6.12. Similar to the tandem coplanar cases, the upstream microphone shows a shift in acoustic pressure compared to the baseline, though the magnitude remains largely unaffected. However, unlike the coplanar configuration, the interior and downstream microphones in the tandem offset configuration display four distinct peaks and valleys within each rotor revolution. These valleys are less pronounced due to the reduced aerodynamic interactions. Additionally, with the implementation of synchrophasing, both peaks and valleys in acoustic pressure are shifted in time and exhibit reduced magnitudes compared to the in-phase scenario, leading to further acoustic attenuation.

Quantifying the noise reduction from the single to tandem offset rotor configurations with an optimal de-phased case is presented in Figure 6.13. Noise with the A-weighted sound pressure

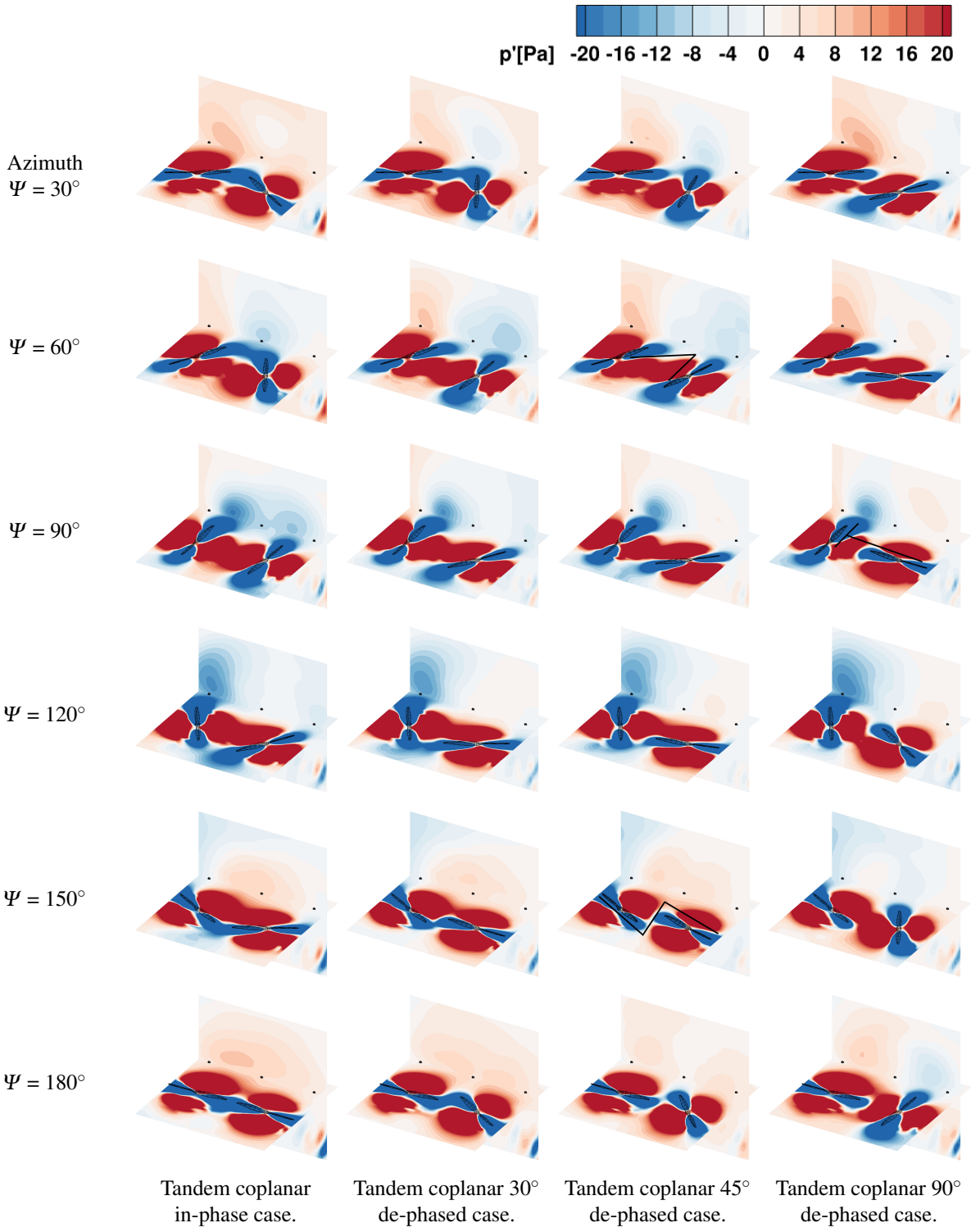

Figure 6.10: Visualisation of acoustic pressure at different azimuths for the tandem coplanar synchrophased cases. Edge-wise flight, $\mu = 0.109$. Rarefaction represented by negative acoustic pressure, whereas compression represented by positive acoustic pressure. (Black dots from left to right represent the investigated microphones from upstream to downstream.)

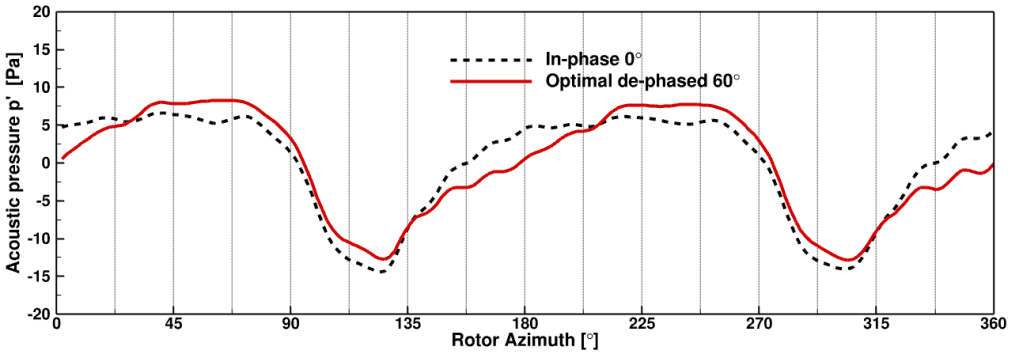

(a) Upstream microphone.

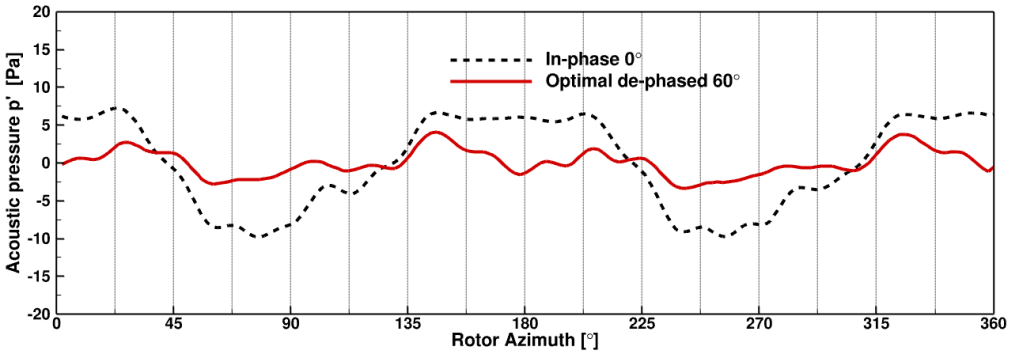

(b) Interior microphone.

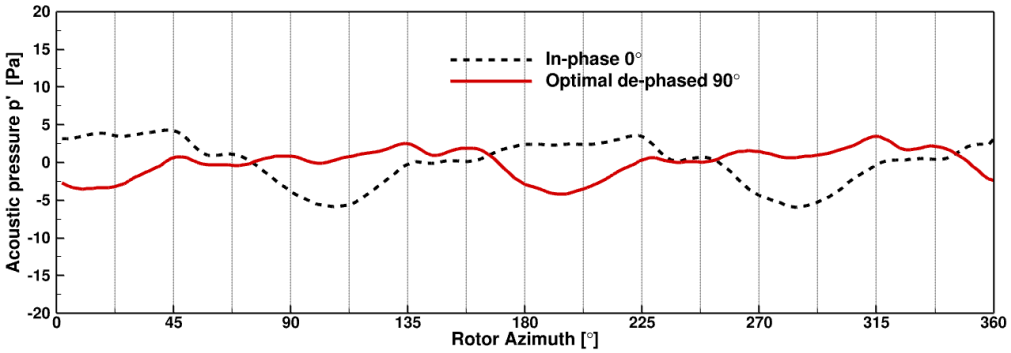

(c) Downstream microphone.

Figure 6.11: Tandem coplanar rotor in edgewise flight, $\mu = 0.109$.

level is decreased by 4 and 3 dB noise in the upstream and downstream regions by having the tandem configuration, and the overall optimal de-phased case has small effects on these regions. However, in the region between the rotors, from the single to tandem rotor configurations, there is a noise reduction of almost 6 dBA. In addition, by applying the synchrophasing with the optimal de-phased angle, the noise with the A-weighted sound pressure level is further reduced by almost 4 dB and has reached an almost 10 dB reduction compared to the thrust-trimmed equivalent single-rotor

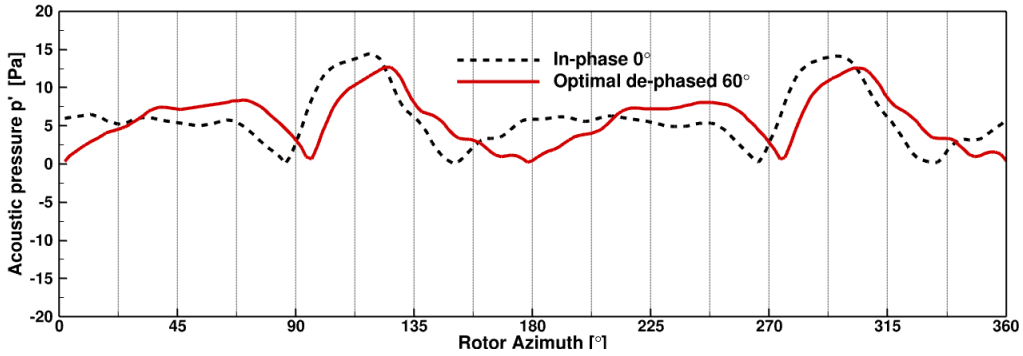

(a) Upstream microphone.

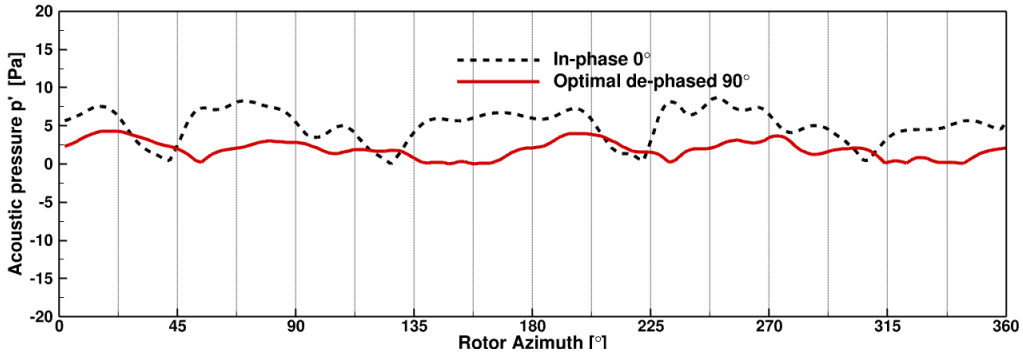

(b) Interior microphone.

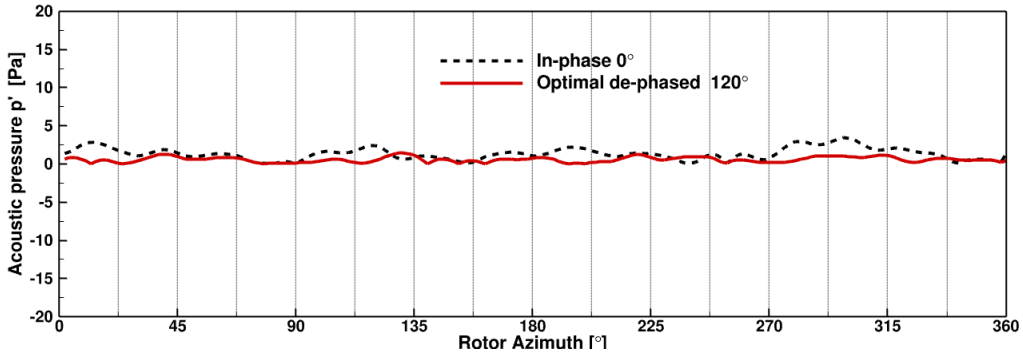

(c) Downstream microphone.

Figure 6.12: Tandem offset rotor in edgewise flight, $\mu = 0.109$.

configuration.

6.4 Chapter Summary

This work conducted a comprehensive study of two synchrophasing tandem, counter-rotating DLR 13x7 rotors in coplanar and vertical-offset configurations, operating in edgewise flight.

The performance of rotors was affected in the multirotor system, especially in the tandem

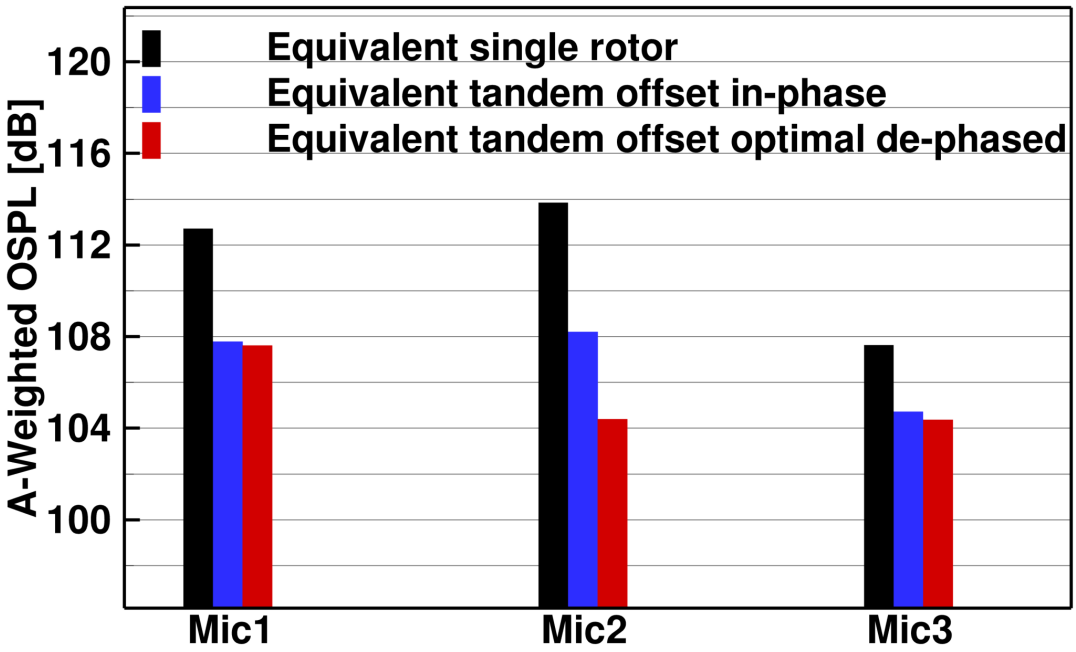

Figure 6.13: AOSPL from the tandem offset rotor. Equivalent single and tandem cases are trimmed to the same thrust. The optimal phase for the tandem offset is 90°.

coplanar configuration. Elevating the position of the downstream rotor shows better performance, suggesting tandem offset rotors are a favourable configuration.

The interference of flow and sound waves between rotors appears to play an important role in the superposition of acoustic waves, showing the need for rotor synchrophasing to achieve a quieter edgewise flight operation. Consideration of the acoustic impact of flying vehicles on humans was included by employing A-weighted SPL standards to account for the relative loudness perceived by the human ear. Higher noise appears in the upstream and interior regions between the rotors, significantly attenuated in the downstream region, and different levels of noise reduction are observed in different de-phased cases from different regions, suggesting the phase offset can be adjusted to achieve lower noise in the interested region.

Analysis using one-third octave bands to understand the contribution of different frequency components to the overall sound will aid in targeted noise control and mitigation efforts in different de-phased cases. Sychrophasing shows relatively diminutive benefits in the upstream region.

However, significant noise reduction occurs in the region between rotors in the middle phasing offsets and the downstream region at phasing 90°, suggesting a favourable resulting sound wave from synchrophasing for both tandem configurations. The best de-phased angle achieved almost 7 dB overall A-weighted sound pressure level reduction and around 20 dB reduction at several A-weighted one-third octave bands. More favourable effects of synchrophasing in the tandem offset configuration yield over 7 dB overall A-weighted sound pressure level reduction in the region between rotors. Furthermore, transforming from a single isolated rotor to the optimal de-phased tandem offset configuration while producing the same amount of lift, achieved almost 10 dB noise reduction in the A-weighted noise level.

Future work will extend the TMP-DP system investigations by incorporating synchrophasing and vertical offset to investigate its global near-field and far-field acoustic characteristics across all directions, using a combination of analytical, hybrid, and high-fidelity methods.

Chapter 7

Conclusions and Future Work

7.1 Conclusions

This work presents a series of studies on interactional aerodynamics using multiple propulsion systems. As demonstrated in Chapter 3, the actuator disk (AD) method is capable of capturing the leading-edge suction mechanism and the effective angle of attack, leading to lift enhancement and drag reduction, in agreement with high-fidelity simulations. Fully resolved simulations are essential for capturing variations in propeller performance due to installation effects, as shown in Chapter 4, where the over-the-wing (OTW) propeller exhibits reduced performance compared to the tractor configuration. However, the significant improvements in wing performance—namely lift enhancement and drag reduction—contribute to an increased lift-to-drag ratio (L/D) and overall propulsive efficiency. These findings suggest that the AD method, when informed by high-fidelity simulations, can be effectively used for system-level optimisation.

The integration of tip-mounted propellers (TMP) with distributed propulsion (DP), as studied in Chapter 5, demonstrates further improvements in lift generation, drag reduction, propeller efficiency, and overall propulsion efficiency, achieving performance levels comparable to those of practical aircraft. This configuration also introduces a nose-down pitching moment, highlighting the need for careful placement of the centre of gravity to ensure proper moment balance at the vehicle level. While the additional propulsors in the TMP-DP system may increase the overall weight,

this can potentially be offset by the aerodynamic benefits and optimised propulsive efficiency of the system.

Furthermore, the aerodynamic interaction and induction effects between propellers can be minimised with appropriate propeller separation, as shown in Chapters 3 and 6. Finally, noise reduction is achieved through the use of multi-rotor configurations and synchrophasing, paving the way for further exploration of acoustic benefits in the TMP-DP system.

The key findings that support the above conclusions of this work are summarised as follows:

CFD validations

- The actuator disk model provides an average downwash effect is capable of capturing the leading-edge suction mechanism and the effective angle of attack, leading to lift enhancement and drag reduction, in agreement with high-fidelity simulations.
- Fully resolved simulations offer a more accurate representation of wake effects across the wing and captured variations in propeller performance due to installation effects
- The SAS method captures more of the downstream wake compared to *URANS* .

Distributed Propulsion

- Optimization using an auxiliary propeller showed that horizontal positioning had minimal impact on wing performance. However, the over-the-wing configuration, particularly near the mid-chord, led to overall lift improvement and drag reduction, resulting in an increased L/D.
- Fully resolved verification found that propeller performance decreased by 6.4% compared to the conventional tractor configuration. However, wing performance improved, with a 1.3% increase in lift, a 74% reduction in drag, and a 294% increase in L/D, leading to a 5.5% improvement in overall propulsion efficiency when transitioning from the conventional tractor to the optimized OTW configuration.

- The pylon structure generated additional drag but also contributed to swirl recovery, benefiting propeller performance while retaining the overall performance advantages of the OTW configuration.

- Adding a second propeller resulted in an overall propulsive efficiency improvement of $\eta_{\text{propulsive}}^{\text{overall}} = +6.2\%$ while maintaining the same lift. Incorporating a third propeller further increased $\eta_{\text{propulsive}}^{\text{overall}} = +26.3\%$.

Tip-mounted and Distributed Propulsion

- Lowering the tip speed in the TMP configuration resulted in smaller propeller thrust and reduced wing load fluctuations, suggesting that thrust and wing load fluctuations are directly dependent on the thrust requirement.

- Distributed propulsion systems not only distribute thrust across multiple propellers but also reduce spikes in lift generation along the wing span.

- There is a $1\% - 1.5\%$ performance loss in TMP and DP due to propeller-propeller interactions in the proposed TMP-DP configuration. However, the overall performance improved with $\eta_{\text{propulsive}}^{\text{overall}} = +8\%$ and an additional $+15\%$ lift compared to the TMP-only configuration.

- A significantly higher nose-down pitching moment was produced in the C4 configuration due to the OTW-installed DP system.

- The TMP-DP system exhibits a more complex vortex structure due to interactional effects, but the overall vortex intensity is reduced compared to the TMP-only system.

Noise Reduction using Phase Sychrophasing

- Elevating the position of the downstream rotor improves performance compared to the tandem coplanar configuration.

- The upstream and interior regions experience higher noise levels than the downstream region. Among the tested cases, neither flight conditions, RPM, nor configurations significantly altered the noise directivity pattern; they primarily influenced the sound pressure level (SPL).

- Synchrophasing provides relatively minor benefits in the upstream region. A phase shift of 90° results in the most significant noise reduction in the region between the two rotors, achieving nearly 7 dB overall noise reduction and up to 20 dB reduction in specific frequency bands.

- Transitioning from a single isolated rotor to the optimal de-phased tandem offset configuration, while maintaining the same lift, achieved nearly 10 dB noise reduction.

7.2 Future Work

In the future, the findings of this work can be extended to more advanced propulsion systems, focusing on aerodynamics, aeroacoustics, and noise reduction technologies which can be developed into multiple PhD projects and research questions including:

Future A: Given the improved aerodynamic efficiency and reduced tip speed in the wingtip-mounted and distributed propulsion systems, a significant reduction in noise is expected, as propeller noise is highly dependent on tip speed. The investigation of various configurations—including tractor, over-the-wing (OTW), TMP-only, and TMP-DP systems—can be further extended to both near-field and far-field aeroacoustic analysis. Synchrophasing can also be applied to the TMP-DP configuration, building on the promising noise reduction observed in tandem propeller setups in the current work. An additional benefit of synchrophasing in the TMP-DP system could be the reduction of wing load fluctuations, which are closely associated with tonal loading noise. Minimising these fluctuations would contribute further to overall noise reduction. Moreover, future studies could explore the effects of vertical and horizontal propeller separation, as well as relative rotation directions, within distributed propulsion systems to better understand their impact on aerodynamic

performance and aeroacoustic behaviour.

Future B: In this work, we found that the actuator disk (AD) method is highly accurate in capturing the leading-edge suction mechanism and the effective angle of attack, leading to lift enhancement and drag reduction. These results are in good agreement with high-fidelity simulations, suggesting that the AD method is suitable for system-level optimisation. This optimisation framework for the TMP-DP system can be further extended to aerofoil shape optimisation by considering parameters such as maximum camber, camber position, and maximum thickness. Additionally, ensuring that all propellers operate under optimal conditions, with the optimal number of propellers, optimal wing size, and placement, will be critical to achieving the best possible overall propulsive efficiency. Furthermore, the aeroelastic and thermoeffects can be investigated for such novel propulsion systems.

Future C: Regarding the methodology, this work explored the benefits of synchrophasing using high-fidelity CFD to directly extract acoustic pressure, and also employed a hybrid CFD - Ffowcs Williams Hawkings (FWH) approach to accelerate noise prediction. Both methods demonstrated strong agreement with experimental results. A technical note drafted during my PhD, based on a coupled analytical method, also showed promising agreement with both the hybrid and high-fidelity approaches. These findings suggest that future acoustic investigations can leverage these accurate, albeit computationally expensive, methods to develop relatively accurate yet significantly more cost-effective alternatives. To illustrate the potential computational savings, tasks that currently require several months of runtime on hundreds of CPUs could potentially be reduced to minutes on a laptop. However, this approach is currently applicable only to tonal noise prediction due to the subsonic nature of the flow. For broadband noise, high-fidelity simulations using Large Eddy Simulation (LES) remain essential to capture the complex flow phenomena and acoustic wave propagation. That said, there is significant potential in applying machine learning and data-driven approaches to predict these nonlinear dynamics. Such a direction presents an exciting opportunity for future research and could form the basis of a highly compelling project.

References

[1] Dudley, M. R., Duffy, M., Hirschberg, M., Moore, M., German, B., Goodrich, K., Gunnarson, T., Petermaier, K., Stoll, A., Fredericks, B., et al., "Second Annual Transformative Vertical Flight Concepts Workshop: Enabling New Flight Concepts Through Novel Propulsion and Energy Architectures," *Annual Transformative Vertical Flight Workshop*, No. ARC-E-DAA-TN33857, 2015.

[2] Antcliff, K. R., Moore, M. D., and Goodrich, K. H., "Silicon valley as an early adopter for on-demand civil VTOL operations," *16th AIAA Aviation Technology, Integration, and Operations Conference*, 2016, p. 3466.

[3] Johnson, W. and Silva, C., "NASA concept vehicles and the engineering of advanced air mobility aircraft," *The Aeronautical Journal*, Vol. 126, No. 1295, 2022, pp. 59–91.

[4] Silva, C., Johnson, W., and Solis, E., "Multidisciplinary conceptual design for reduced-emission rotorcraft," Tech. Rep. ARC-E-DAA-TN51230, 2018.

[5] Johnson, W., Silva, C., and Solis, E., "Concept vehicles for VTOL air taxi operations," *AHS Specialists"Conference on Aeromechanics Design for Transformative Vertical Flight*, No. ARC-E-DAA-TN50731, 2018.

[6] Patterson, M. D., Antcliff, K. R., and Kohlman, L. W., "A Proposed Approach to Studying Urban Air Mobility Missions Including an Initial Exploration of Mission Requirements," 2018.

[7] Silva, C., Johnson, W. R., Solis, E., Patterson, M. D., and Antcliff, K. R., "VTOL urban air mobility concept vehicles for technology development," *2018 Aviation Technology, Integration, and Operations Conference*, 2018, p. 3847.

[8] Antcliff, K., Whiteside, S., Kohlman, L. W., and Silva, C., "Baseline assumptions and future research areas for urban air mobility vehicles," *AIAA SciTech 2019 Forum*, 2019, p. 0528.

[9] Johnson, W., "A quiet helicopter for air taxi operations," *Aeromechanics for Advanced Vertical Flight Technical Meeting*, No. ARC-E-DAA-TN76202, 2020.

[10] Whiteside, S. K., Pollard, B. P., Antcliff, K. R., Zawodny, N. S., Fei, X., Silva, C., and Medina, G. L., "Design of a Tiltwing Concept Vehicle for Urban Air Mobility," Tech. Rep. NASA/TM-20210017971, 2021.

[11] Silva, C. and Johnson, W., "Practical conceptual design of quieter urban VTOL aircraft," *Vertical Flight Society's 77th Annual Forum & Technology Display*, 2021.

[12] Nicolosi, F., Marco, A. D., and Vecchia, P. D., "Flight Tests of a Twin-Engine Aircraft: Performances, Stability and Parameter Estimation," *Proceedings of the XX Congresso AIDAA*, Politecnico di Milano, Milan, Italy, June 29 – July 3 2009, pp. 1–29, ISBN: 978-88-904668-0-9.

[13] Clarke, S., Redifer, M., Papathakis, K., Samuel, A., and Foster, T., "X-57 power and command system design," *2017 IEEE Transportation Electrification Conference and Expo (ITEC)*, IEEE, 2017, pp. 393–400.

[14] Borer, N. K., Patterson, M. D., Viken, J. K., Moore, M. D., Bevirt, J., Stoll, A. M., and Gibson, A. R., "Design and performance of the NASA SCEPTOR distributed electric propulsion flight demonstrator," *16th AIAA Aviation Technology, Integration, and Operations Conference*, 2016, p. 3920.

[15] Rizzi, S. A., Huff, D. L., Boyd, D. D., Bent, P., Henderson, B. S., Pascioni, K. A., Sargent, D. C., Josephson, D. L., Marsan, M., He, H., and Snider, R., "Urban Air Mobility Noise: Current Practice, Gaps, and Recommendations," Technical Publication NASA/TP–2020-5007433, NASA Langley Research Center, Hampton, Virginia, October 2020, Contributors from NASA Glenn Research Center, Boeing R&T, Sikorsky Aircraft, Josephson Engineering, FAA, and Bell Flight.

[16] Grunwald, K. J. and Goodson, K. W., "Aerodynamic Loads on an Isolated Shrouded-Propeller Configuration for Angles of Attack from -10 Degrees to 110 Degrees," Technical Note NASA TN D-995, National Aeronautics and Space Administration, Washington, D.C., January 1962.

[17] Grunwald, K. J. and Goodson, K. W., "Division of Aerodynamic Loads on a Semispan Tilting-Ducted-Propeller Model in Hovering and Transition Flight," Technical Note NASA TN D-1297, National Aeronautics and Space Administration, Washington, D.C., May 1962.

[18] Mort, K. W. and Gamse, B., "A wind-tunnel investigation of a 7-foot-diameter ducted propeller," 1967.

[19] Zhang, T. and Barakos, G. N., "Review on ducted fans for compound rotorcraft," *The Aeronautical Journal*, Vol. 124, No. 1277, 2020, pp. 941–974.

[20] Zhang, T. and Barakos, G. N., "High-fidelity CFD validation and assessment of ducted propellers for aircraft propulsion," *Journal of the American Helicopter Society*, Vol. 66, No. 1, 2021, pp. 1–28.

[21] Zhang, T., Qiao, G., Smith, D., Barakos, G., and Kusyumov, A., "Parametric study of aerodynamic performance of equivalent ducted/un-ducted rotors," *Aerospace Science and Technology*, Vol. 117, 2021, pp. 106984.

[22] Kim, H. D., Perry, A. T., and Ansell, P. J., "Progress in Distributed Electric Propulsion Vehicles and Technologies," Tech. rep., AIAA, 2020.

[23] Joby Aviation, "Joby Reports Record Certification Progress and Delivery of Second Aircraft to US Air Force at Edwards Air Force Base," Feb. 2025, Accessed: 2025-05-19.

[24] Rendón, M. A., Sánchez R, C. D., Gallo M, J., and Anzai, A. H., "Aircraft hybrid-electric propulsion: Development trends, challenges and opportunities," *Journal of Control, Automation and Electrical Systems*, Vol. 32, No. 5, 2021, pp. 1244–1268.

[25] Kuśmierek, A., Galiński, C., and Stalewski, W., "Review of the hybrid gas-electric aircraft propulsion systems versus alternative systems," *Progress in Aerospace Sciences*, Vol. 141, 2023, pp. 100925.

[26] Ko, A., Schetz, J., and Mason, W. H., "Assessment of the potential advantages of distributed-propulsion for aircraft," *XVI International Symposium on Air Breathing Engines (ISABE)*, 2003, pp. 2003–1094.

[27] Kim, H. D., "Distributed propulsion vehicles," *27th international congress of the aeronautical sciences*, No. E-17361, 2010.

[28] Kim, H. D., Felder, J. L., Tong, M., Armstrong, M., et al., "Revolutionary aeropropulsion concept for sustainable aviation: turboelectric distributed propulsion," Tech. rep., NASA Glenn Research Center Cleveland, OH, United States. Rolls-Royce North American Technologies, Inc. Indianapolis, IN, United States), 2013.

[29] Wick, A. T., Hooker, J. R., and Zeune, C. H., "Integrated aerodynamic benefits of distributed propulsion," *53rd AIAA Aerospace Sciences Meeting*, 2015, p. 1500.

[30] Deere, K. A., Viken, J. K., Viken, S., Carter, M. B., Wiese, M., and Farr, N., "Computational analysis of a wing designed for the X-57 distributed electric propulsion aircraft," *35th AIAA applied aerodynamics conference*, 2017, p. 3923.

[31] Pandya, M. J., Jespersen, D. C., Diskin, B., Thomas, J. L., and Frink, N. T., "Efficiency of Mixed-Element USM3D for Benchmark Three-Dimensional Flows," *AIAA Journal*, Vol. 59, No. 8, 2021, pp. 2997–3011.

[32] Allmaras, S. R. and Johnson, F. T., "Modifications and clarifications for the implementation of the Spalart-Allmaras turbulence model," *Seventh international conference on computational fluid dynamics (ICCFD7)*, Vol. 1902, Big Island, HI, 2012, pp. 1–11.

[33] Pascioni, K. A., Watts, M. E., Houston, M., Lind, A., Stephenson, J. H., and Bain, J., "Acoustic flight test of the joby aviation advanced air mobility prototype vehicle," *28th AIAA/CEAS Aeroacoustics 2022 Conference*, 2022, p. 3036.

[34] Lilium GmbH, "Official Website of Lilium GmbH," `https://www.lilium.com`, 2025, Accessed: 2025-05-20.

[35] Vertical Aerospace LTD, "Official Website of Vertical Aerospace," `https://www.vertical-aerospace.com`, 2025, Accessed: 2025-05-20.

[36] Geuther, S. C., North, D. D., and Busan, R. C., "Investigation of a Tandem Tilt-wing VTOL Aircraft in the NASA Langley 12-Foot Low-Speed Tunnel," *NASA TM-2020-5003178*.

[37] Litherland, B. L., Borer, N. K., and Zawodny, N. S., "X-57 Maxwell High-Lift Propeller Testing and Model Development," *AIAA AVIATION 2021 FORUM, Virtual*, 2-6 August 2021, p. 3193.

[38] Lee, H. and Lee, D.-J., "Rotor interactional effects on aerodynamic and noise characteristics of a small multirotor unmanned aerial vehicle," *Physics of Fluids*, Vol. 32, No. 4, 2020, pp. 047107.

[39] Alvarez, E. J. and Ning, A., "High-fidelity modeling of multirotor aerodynamic interactions for aircraft design," *AIAA Journal*, Vol. 58, No. 10, 2020, pp. 4385–4400.

[40] Alvarez, E., Schenk, A., Critchfield, T., and Ning, A., "Rotor-on-rotor aeroacoustic interactions of multirotor in hover," 2020.

[41] Stokkermans, T. C., Usai, D., Sinnige, T., and Veldhuis, L. L., "Aerodynamic interaction effects between propellers in typical eVTOL vehicle configurations," *Journal of Aircraft*, Vol. 58, No. 4, 2021, pp. 815–833.

[42] Ning, Z., *Experimental investigations on the aerodynamic and aeroacoustic characteristics of small UAS propellers*, Ph.D. thesis, Iowa State University, 2018.

[43] Pascioni, K. and Rizzi, S. A., "Tonal noise prediction of a distributed propulsion unmanned aerial vehicle," *2018 AIAA/CEAS Aeroacoustics Conference*, 2018, p. 2951.

[44] Pascioni, K. A., Rizzi, S. A., and Schiller, N., "Noise reduction potential of phase control for distributed propulsion vehicles," *AIAA Scitech 2019 Forum*, 2019, p. 1069.

[45] Tinney, C. E. and Sirohi, J., "Multirotor drone noise at static thrust," *Aiaa Journal*, Vol. 56, No. 7, 2018, pp. 2816–2826.

[46] Patterson, A., Schiller, N. H., Ackerman, K. A., Gahlawat, A., Gregory, I. M., and Hovakimyan, N., "Controller design for propeller phase synchronization with aeroacoustic performance metrics," *AIAA Scitech 2020 Forum*, 2020, p. 1494.

[47] Ehsani, M., Husain, I., Mahajan, S., and Ramani, K., "New modulation encoding techniques for indirect rotor position sensing in switched reluctance motors," *IEEE Transactions on Industry Applications*, Vol. 30, No. 1, 1994, pp. 85–91.

[48] Wang, Y., Bao, X., Hua, W., Liu, K., Wang, P., Hu, M., and Zhang, H., "Implementation of embedded magnetic encoder for rotor position detection based on arbitrary phase-shift phase-lock loop," *IEEE Transactions on Industrial Electronics*, Vol. 69, No. 2, 2021, pp. 2033–2043.

[49] de Vries, R., van Arnhem, N., Sinnige, T., Vos, R., and Veldhuis, L. L., "Aerodynamic interaction between propellers of a distributed-propulsion system in forward flight," *Aerospace Science and Technology*, Vol. 118, 2021, pp. 107009.

[50] de Vries, R. and Vos, R., "Aerodynamic performance benefits of over-the-wing distributed propulsion for hybrid-electric transport aircraft," *Journal of Aircraft*, Vol. 60, No. 4, 2023, pp. 1201–1218.

[51] Müller, L., Heinze, W., Kožulović, D., Hepperle, M., and Radespiel, R., "Aerodynamic installation effects of an over-the-wing propeller on a high-lift configuration," *Journal of Aircraft*, Vol. 51, No. 1, 2014, pp. 249–258.

[52] Marcus, E. A., de Vries, R., Raju Kulkarni, A., and Veldhuis, L. L., "Aerodynamic investigation of an over-the-wing propeller for distributed propulsion," *2018 AIAA Aerospace Sciences Meeting*, 2018, p. 2053.

[53] de Vries, R., van Arnhem, N., Avallone, F., Ragni, D., Vos, R., Eitelberg, G., and Veldhuis, L. L., "Experimental Investigation of Over-the-Wing Propeller–Boundary-Layer Interaction," *AIAA Journal*, Vol. 59, No. 6, 2021, pp. 2169–2182.

[54] De Vries, R., Brown, M., and Vos, R., "Preliminary sizing method for hybrid-electric distributed-propulsion aircraft," *Journal of Aircraft*, Vol. 56, No. 6, 2019, pp. 2172–2188.

[55] Rolls Royce, p., *The jet engine*, The Technical Publications Department, 1986.

[56] Stokkermans, T. C., Van Arnhem, N., Sinnige, T., and Veldhuis, L. L., "Validation and comparison of RANS propeller modeling methods for tip-mounted applications," *AIAA Journal*, Vol. 57, No. 2, 2019, pp. 566–580.

[57] Loth, J. and Loth, F., "Induced drag reduction with wing tip mounted propellers," *2nd Applied Aerodynamics Conference*, 1984, p. 2149.

[58] Miranda, L. and Brennan, J., "Aerodynamic effects of wingtip-mounted propellers and turbines," *4th Applied Aerodynamics Conference*, 1986, p. 1802.

[59] Patterson, Jr, J. and Bartlett, G., "Effect of a wing-tip mounted pusher turboprop on the aerodynamic characteristics of a semi-span wing," *21st Joint Propulsion Conference*, 1985, p. 1286.

[60] Janus, J. M., Chatterjee, A., and Cave, C., "Computational analysis of a wingtip-mounted pusher turboprop," *Journal of aircraft*, Vol. 33, No. 2, 1996, pp. 441–444.

[61] Hooker, J. R., Wick, A., Ginn, S. R., Walker, J., and Schiltgen, B. T., "Overview of Low Speed Wind Tunnel Testing Conducted on a Wingtip Mounted Propeller for the Workshop for Integrated Propeller Prediction," *AIAA AVIATION 2020 FORUM*, 2020, p. 2673.

[62] Baruzzi, G. S., Aliaga, C., Ozcer, I. A., Stokes, J., Svihla, K., and Saxena, S., "Numerical Simulation of an Integrated Propeller with Models of Progressively Increasing Fidelity," *AIAA AVIATION 2020 FORUM*, 2020, p. 2682.

[63] Aref, P., Ghoreyshi, M., Jirasek, A., and Seidel, J., "Application of the HPCMP CREATETM-AV Kestrel to an Integrated Propeller Prediction," *Aerospace*, Vol. 7, No. 12, 2020, pp. 177.

[64] Taniguchi, S. and Oyama, A., "Numerical Analysis of Propeller Mounting Position Effects on Aerodynamic Propeller/Wing Interaction," *AIAA SCITECH 2022 Forum*, 2022, p. 0153.

[65] Reveles, N., Seledic, K., Williams, D., Blades, E., and Shah, P. N., "Rotor/Propeller Model Fidelity Effects on Propeller-Wing Interactional Aerodynamics," *AIAA AVIATION 2020 FORUM*, 2020, p. 2676.

[66] Zhou, B. Y., Morelli, M., Gauger, N. R., and Guardone, A., "Simulation and Sensitivity Analysis of a Wing-Tip Mounted Propeller Configuration from the Workshop for Integrated Propeller Prediction (WIPP)," *AIAA AVIATION 2020 FORUM*, 2020, p. 2683.

[67] Zhou, B. Y., Morelli, M., Dehpanah, P., Gauger, N. R., and Guardone, A., "Aeroacoustic Analysis of a Wing-Tip Mounted Propeller Configuration," *AIAA Aviation 2021 Forum*, 2021, p. 2224.

[68] Heeg, J., Stanford, B. K., Kreshock, A., Shen, J., Hoover, C. B., and Truax, R., "Whirl flutter and the development of the NASA X-57 Maxwell," *International Forum on Aeroelasticity and Structural Dynamics (IFASD 2019)*, No. NF1676L-31615, 2019.

[69] EASA, N., "Study on the societal acceptance of urban air mobility in Europe," `https://www.easa.europa.eu`, 2021.

[70] Greenwood, E., Brentner, K. S., Rau, R. F., and Ted Gan, Z. F., "Challenges and opportunities for low noise electric aircraft," *International Journal of Aeroacoustics*, Vol. 21, No. 5-7, 2022, pp. 315–381.

[71] Smith, D. and Barakos, G., "Rotor Acoustics," *Lecture Notes in Rotorcraft Engineering*, Springer, 2023, pp. 141–173.

[72] Jia, Z. and Lee, S., "Acoustic analysis of a quadrotor eVTOL design via high-fidelity simulations," *25th AIAA/CEAS aeroacoustics conference*, 2019, p. 2631.

[73] Yin, J., De Gregorio, F., Rossignol, K.-S., Rottmann, L., Ceglia, G., Reboul, G., Barakos, G., Qiao, G., Muth, M., Kessler, M., Visingardi, A., Barbarino, M., Petrosino, F., Zanotti, A., Oberti, N., Galimberti, L., Bernardini, G., Poggi, C., Abergo, L., Caccia, F., Guardone, A., Testa, C., and Zaghi, S., "Acoustic and Aerodynamic Evaluation of DLR Small-Scale Rotor Configurations within GARTEUR AG26," *49th European Rotorcraft Forum (ERF), paper 80, Bückeburg, Germany*, September 5 – 7, 2023.

[74] Yin, J., Rossignol, K.-S., Rottmann, L., and Schwarz, T., "Numerical Investigations on Small-scale Rotor Configurations with Validation Using Acoustic Wind Tunnel Data," *48th European Rotorcraft Forum (ERF), 2022*, 2022, pp. 1–17.

[75] Wenwu Zhou, Zhe Ning, H. L. H. H., "An experimental investigation on rotor-to-rotor interactions of small UAV propellers," *35th AIAA applied aerodynamics conference*, 2017, p. 3744.

[76] Dhwanil Shukla, N. K., "Multirotor drone aerodynamic interaction investigation," *Drones*, Vol. 2, No. 43, 2018.

[77] Celik, A., Jamaluddin, N. S., Baskaran, K., Rezgui, D., and Azarpeyvand, M., "Aeroacoustic performance of rotors in tandem configuration," *AIAA AVIATION 2021 FORUM*, 2021, p. 2282.

[78] Schiller, N. H., Pascioni, K. A., and Zawodny, N. S., "Tonal noise control using rotor phase synchronization," *Vertical Flight Society Annual Forum and Technology Display (VFS Forum 75)*, No. NF1676L-31452, 2019.

[79] Frederic G. Pla, George Goodman, R. R. and Silcox, R., "Cabin Noise Cancellation Using Active RPM Control OV-IOA Flight Test Results." *15th AIAA Aeroacoustics Conferencei, Long Beach, CA, October 25-27, 1993*, 1993, p. 4438, 10.2514/6.1993-4438.

[80] Turhan, B., Jawahar, H. K., Gautam, A., Syed, S., Vakil, G., Rezgui, D., and Azarpeyvand, M., "Acoustic characteristics of phase-synchronized adjacent propellers," *The Journal of the Acoustical Society of America*, Vol. 155, No. 5, 2024, pp. 3242–3253.

[81] Shao, M., Lu, Y., Xu, X., Guan, S., and Lu, J., "Experimental study on noise reduction of multi-rotor by phase synchronization," *Journal of Sound and Vibration*, Vol. 539, 2022, pp. 117199.

[82] Shujun Guan, Yang Lu, T. S. X. X., "Noise attenuation of quadrotor using phase synchronization method," *Journal of Sound and Vibration*, Vol. 118, 2021, pp. 107018.

[83] Reed, N. and Cuppoletti, D. R., "Implications of Rotor-Rotor Interaction in Noise Generation of UAM Vehicles with Counter-Rotating Configurations," *AIAA SCITECH 2022 Forum*, 2022, p. 2168.

[84] De Gregorio, F., Rossignol, K.-S., Ceglia, G., and Yin, J., "Multi-rotor Wake Interaction Characterization," *49th European Rotorcraft Forum (ERF), paper 105, Bückeburg, Germany*, September 5 – 7, 2023.

[85] Yin, J., Rossignol, K.-S., Rottmann, L., and Schwarz, T., "Numerical studies on small rotor configurations with validation using acoustic wind tunnel data," *CEAS Aeronautical Journal*, 2023, pp. 1–32.

[86] Rossignol, K.-S., Yin, J., and Rottmann, L., "Investigation of Small-Scale Rotor Aeroacoustic in DLR's Acoustic Wind Tunnel Braunschweig," *28th AIAA/CEAS Aeroacoustics 2022 Conference*, 2022, p. 2838.

[87] Yin, J., Gregorio, F., Rossignol, K.-S., Rottmann, L., Ceglia, G., Reboul, G., Barakos, G., Qiao, G., Muth, M., Kessler, M., et al., "Acoustic and aerodynamic evaluation of DLR small-scale rotor configurations within GARTEUR AG26," *CEAS Aeronautical Journal*, 2024.

[88] Visingardi, A., Barbarino, M., Gregorio, F., Greco, L., Testa, C., Zaghi, S., Yin, J., Reboul, G., Abergo, L., Cavalli, A., Guardone, A., Granata, D., Zanotti, A., Bernardini, G., Poggi, C., Candeloro, P., Pagliaroli, T., Barakos, G., Qiao, G., Fausel, F., Keßler, K., and Muth, M., "Analysis of the Aeroacoustic Performance of Twin Propellers in Hover by Using the CIRA-Cusano Test Rig," *50th European Rotorcraft Forum (ERF), paper 91, Marseille, France*, September 10 – 13, 2024.

[89] Qiao, G., Zhang, T., and Barakos, G., "Numerical simulation of distributed propulsion systems using CFD," *Aerospace Science and Technology*, 2024, pp. 109011.

[90] Brandt, J. and Selig, M., "Propeller performance data at low reynolds numbers," *49th AIAA Aerospace Sciences Meeting including the New Horizons Forum and Aerospace Exposition*, 2011, p. 1255.

[91] Deters, R. W., Ananda Krishnan, G. K., and Selig, M. S., "Reynolds number effects on the performance of small-scale propellers," *32nd AIAA applied aerodynamics conference*, 2014, p. 2151.

[92] Kolaei, A., Barcelos, D., and Bramesfeld, G., "Experimental Analysis of a Small-Scale Rotor at Various Inflow Angles," *International Journal of Aerospace Engineering*, Vol. 2018, No. 1, 2018, pp. 2560370.

[93] Johnson, W., *Rotorcraft aeromechanics*, Vol. 36, Cambridge University Press, 2013.

[94] Niemiec, R. and Gandhi, F., "Effects of inflow model on simulated aeromechanics of a quadrotor helicopter," *72nd Annual Forum of the American Helicopter Society International*, 2016.

[95] Steijl, R., Barakos, G., and Badcock, K., "A framework for CFD analysis of helicopter rotors in hover and forward flight," *International journal for numerical methods in fluids*, Vol. 51, No. 8, 2006, pp. 819–847.

[96] Biava, M., Woodgate, M., and Barakos, G. N., "Fully implicit discrete-adjoint methods for rotorcraft applications," *AIAA Journal*, Vol. 54, No. 2, 2016, pp. 735–749.

[97] Antoniadis, A., Drikakis, D., Zhong, B., Barakos, G., Steijl, R., Biava, M., Vigevano, L., Brocklehurst, A., Boelens, O., Dietz, M., et al., "Assessment of CFD methods against experimental flow measurements for helicopter flows," *Aerospace Science and Technology*, Vol. 19, No. 1, 2012, pp. 86–100.

[98] Steijl, R. and Barakos, G., "CFD analysis of complete helicopter configurations–lessons learnt from the GOAHEAD project," *Aerospace Science and Technology*, Vol. 19, No. 1, 2012, pp. 58–71.

[99] Han, D., Pastrikakis, V., and Barakos, G. N., "Helicopter flight performance improvement by dynamic blade twist," *Aerospace Science and Technology*, Vol. 58, 2016, pp. 445–452.

[100] Garcia, A. J. and Barakos, G. N., "Numerical simulations on the ERICA tiltrotor," *Aerospace Science and Technology*, Vol. 64, 2017, pp. 171–191.

[101] Dehaeze, F. and Barakos, G., "Mesh deformation method for rotor flows," *Journal of Aircraft*, Vol. 49, No. 1, 2012, pp. 82–92, DOI: 10.2514/1.C031251.

[102] Chirico, G., Barakos, G., and Bown, N., "Numerical aeroacoustic analysis of propeller designs," *The Aeronautical Journal*, Vol. 122, No. 1248, 2018, pp. 283–315, DOI: 10.1017/aer.2017.123.

[103] Crozon, C., Steijl, R., and Barakos, G., "Coupled flight dynamics and CFD - demonstration for helicopters in shipborne environment," *The Aeronautical Journal*, Vol. 122, No. 1247, 2018, pp. 42–82, DOI: 10.1017/aer.2017.112.

[104] Babu, S., Loupy, G., Dehaeze, F., Barakos, G., and Taylor, N., "Aeroelastic simulations of stores in weapon bays using Detached-Eddy Simulation," *Journal of Fluids and Structures*, Vol. 66, October 2016, pp. 207–228, DOI: 10.1016/j.jfluidstructs.2016.07.014.

[105] Barakos, G. and Johnson, C., "Acoustic comparison of propellers," *International Journal of Aeroacoustics*, Vol. 15, No. 6-7, 2016, pp. 575–594, DOI: 10.1177/1475472X16659214.

[106] Higgins, R., Jimenez-Garcia, A., Barakos, G., and Bown, N., "High-Fidelity Computational Fluid Dynamics Methods for the Simulation of Propeller Stall Flutter," *AIAA Journal*, Vol. 57, No. 12, 2019, DOI: 10.2514/1.J058463.

[107] Higgins, R., Barakos, G., and Jinks, E., "Estimation of Three-Dimensional Aerodynamic Damping using CFD," *The Aeronautical Journal*, Vol. 124, No. 1271, 2020, DOI: 10.1017/aer.2019.135.

[108] Higgins, R., Zarev, A., Barakos, G., and Green, R., "Numerical Investigation of a Two-Bladed Propeller Inflow at Yaw," *Journal of Aircraft*, Vol. 57, No. 2, 2020, DOI: 10.2514/1.C035647.

[109] Higgins, R., Barakos, G., Shahpar, S., and Tristanto, I., "An Aeroacoustic Investigation of a Tiltwing eVTOL Concept Aircraft," *AIAA Aviation 2020 Forum*, AIAA, 2020, DOI: 10.2514/6.2020-2684.

[110] Qiao, G., *Parametric study of aerodynamic performance of equivalent ducted/un-ducted propellers based on high-fidelity computational fluid dynamics*, Master's thesis, University of Glasgow, 2021, http://theses.gla.ac.uk/id/eprint/82702.

[111] Menter, F. R., "Two-equation eddy-viscosity turbulence models for engineering applications," *AIAA journal*, Vol. 32, No. 8, 1994, pp. 1598–1605.

[112] Biava, M. and Barakos, G. N., "Optimisation of ducted propellers for hybrid air vehicles using high-fidelity CFD," *The Aeronautical Journal*, Vol. 120, No. 1232, 2016, pp. 1632–1657.

[113] Jarkowski, M., Woodgate, M., Barakos, G., and Rokicki, J., "Towards consistent hybrid overset mesh methods for rotorcraft CFD," *International Journal for Numerical Methods in Fluids*, Vol. 74, No. 8, 2014, pp. 543–576.

[114] Steijl, R. and Barakos, G., "Sliding mesh algorithm for CFD analysis of helicopter rotor–fuselage aerodynamics," *International journal for numerical methods in fluids*, Vol. 58, No. 5, 2008, pp. 527–549.

[115] Osher, S. and Chakravarthy, S., "Upwind schemes and boundary conditions with applications to Euler equations in general geometries," *Journal of Computational Physics*, Vol. 50, No. 3, 1983, pp. 447–481.

[116] Van Leer, B., "Towards the ultimate conservative difference scheme. V. A second-order sequel to Godunov's method," *Journal of computational Physics*, Vol. 32, No. 1, 1979, pp. 101–136.

[117] Van Albada, G. D., Van Leer, B., and Roberts, W., "A comparative study of computational methods in cosmic gas dynamics," *Upwind and high-resolution schemes*, Springer, 1997, pp. 95–103.

[118] Axelsson, O., *Iterative solution methods*, Cambridge university press, 1996.

[119] Cantariti, F., Dubuc, L., Gribben, B., Woodgate, M., Badcock, K., and Richards, B., "Approximate Jacobians for the solution of the Euler and Navier-Stokes equations," *Aerospace Engineering Report*, Vol. 5, 1997.

[120] Jameson, A., "Time dependent calculations using multigrid, with applications to unsteady flows past airfoils and wings," *10th Computational Fluid Dynamics Conference*, 1991, p. 1596.

[121] Chaderjian, N. M., "Advances in rotor performance and turbulent wake simulation using DES and adaptive mesh refinement," *7th international conference on computational fluid dynamics, Big Island, Hawaii*, 2012.

[122] Wilcox, D. C., "Formulation of the kw turbulence model revisited," *AIAA journal*, Vol. 46, No. 11, 2008, pp. 2823–2838.

[123] Rajagopalan, R. G. and Mathur, S. R., "Three dimensional analysis of a rotor in forward flight," *Journal of the American Helicopter Society*, Vol. 38, No. 3, 1993, pp. 14–25.

[124] O'Brien Jr, D. M., *Analysis of computational modeling techniques for complete rotorcraft configurations*, Ph.D. thesis, Georgia Institute of Technology, 2006.

[125] Stokkermans, T., van Arnhem, N., Sinnige, T., and Veldhuis, L., "Validation and Comparison of RANS Propeller Modeling Methods for Tip-Mounted Applications," *AIAA Journal*, Vol. 57, 12 2018, pp. 1–15, 10.2514/1.J057398.

[126] Barakos, G., Fitzgibbon, T., Kusyumov, A., Kusyumov, S., and Mikhailov, S., "CFD simulation of helicopter rotor flow based on unsteady actuator disk model," *Chinese Journal of Aeronautics*, Vol. 33, No. 9, 2020, pp. 2313–2328, DOI: 10.1016/j.cja.2020.03.021.

[127] Sacks, J., Schiller, S. B., and Welch, W. J., "Designs for Computer Experiments," *Technometrics*, Vol. 31, No. 1, 1989, pp. 41–47, DOI: 10.1080/00401706.1989.10488474.

[128] Saves, P., Lafage, R., Bartoli, N., Diouane, Y., Bussemaker, J., Lefebvre, T., Hwang, J. T., Morlier, J., and Martins, J. R. R. A., "SMT 2.0: A Surrogate Modeling Toolbox with a focus on Hierarchical and Mixed Variables Gaussian Processes," *Advances in Engineering Sofware*, Vol. 188, 2024, pp. 103571.

[129] Steger, J. L., Dougherty, F. C., and Benek, J. A., "A chimera grid scheme.[multiple overset body-conforming mesh system for finite difference adaptation to complex aircraft configurations]," 1983.

[130] Fitzgibbon, T. A., *Advanced rotor blade design based on high-fidelity computational fluid dynamics*, Ph.D. thesis, University of Glasgow, 2021.

[131] Jeong, J. and Hussain, F., "On the identification of a vortex," *Journal of fluid mechanics*, Vol. 285, 1995, pp. 69–94.

[132] Clancy, L., "Aerodynamics, Pitman Publ," *Lim., London*, 1975.

[133] Chirico, G., Barakos, G. N., and Bown, N., "Propeller installation effects on turboprop aircraft acoustics," *Journal of Sound and Vibration*, Vol. 424, 2018, pp. 238–262.

[134] Chirico, G., Barakos, G. N., and Bown, N., "Numerical aeroacoustic analysis of propeller designs," *Aeronautical Journal*, Vol. 122, No. 1248, February 2018, pp. 283–315.

[135] Zhang, T., Barakos, G. N., Foster, M., et al., "High-fidelity aerodynamic and acoustic design and analysis of a heavy-lift eVTOL," *Aerospace Science and Technology*, Vol. 137, 2023, pp. 108307.

[136] Ffowcs Williams, J. E. and Hawkings, D. L., "Sound generation by turbulence and surfaces in arbitrary motion," *Philosophical Transactions of the Royal Society of London. Series A, Mathematical and Physical Sciences*, Vol. 264, No. 1151, 1969, pp. 321–342.

[137] Farassat, F., "Derivation of Formulations 1 and 1A of Farassat," Tech. rep., 2007.

[138] Fletcher, H. and Munson, W. A., "Loudness, its definition, measurement and calculation," *Bell System Technical Journal*, Vol. 12, No. 4, 1933, pp. 377–430.

[139] "Environmental Technical Manual Volume I: Procedures for the Noise Certification of Aircraft, Doc 9501, AN/929," *International Civil Aviation Organization*, 2015.

[140] "Electroacoustics–Sound Level Meters (IEC 61672), Technical Committee TC 29 (Electroacoustics)," *International Electrotechnical Commission*, 2015.

[141] "Acoustics–Normal equal-loudness-level contours (ISO 226:2023), Technical Committee ISO/TC 43 (Acoustics)," *International Organization for Standardization*, 2023.

[142] Litherland, B. L., Patterson, M. D., Derlaga, J. M., and Borer, N. K., "A method for designing conforming folding propellers," *17th AIAA Aviation Technology, Integration, and Operations Conference*, 2017, p. 3781.

[143] Litherland, B. L. and Derlaga, J. M., "A Performance Analysis of Folding Conformal Propeller Blade Designs," *AIAA Aviation 2019 Forum, Dallas, Texas, 17-21 June 2019*, 2019, p. 3676, 10.2514/6.2019-3676.

[144] McDonald, R. A. and Gloudemans, J. R., "Open Vehicle Sketch Pad: An Open Source Parametric Geometry and Analysis Tool for Conceptual Aircraft Design," *AIAA SCITECH 2022 Forum*, 2022, p. 0004.

[145] Buning, P. G. et al., "OVERFLOW: A Structured-Grid CFD Flow Solver," *Proceedings of the AIAA CFD Conference*, 1998, NASA Langley Research Center.

[146] Barakos, G. N., Steijl, R., Badcock, K. J., and Brocklehurst, A., "Numerical Simulation of Helicopter Rotor Flow Fields Using the Helicopter Multi-Block Method," *AIAA Journal*, Vol. 43, No. 4, 2005, pp. 782–790.

[147] Helden Aerospace, L. and Empirical Systems Aerospace, I., "Wind Tunnel Tesrting of Propeller Wingtip Interactions: Final wind tunnel test and CFD report for the Low Speed Wind Tunnel test of a 40.5% scale semi-span model with a wingtip-mounted propeller in the Lockheed Martin Low Speed Wind Tunnel," Tech. rep., Helden Aerospace, LLC. and Empirical Systems Aerospace, Inc., 2019.

[148] Qiao, G. and Barakos, G., "CFD Validation for eVTOL Propeller Performance and Acoustics," *49th European Rotorcraft Forum (ERF), paper 20, Bückeburg, Germany*, September 5 – 7, 2023.

[149] Visingardi, A., Barbarino, M., De Gregorio, F., Greco, L., Testa, C., Zaghi, S., Yin, J., Reboul, G., Cavalli, A., Granata, D., et al., "Analysis of the aeroacoustic performance of twin propellers in hover by using the CIRA-CUSANO test-rig," *50th European Rotorcraft Forum (ERF 2024)*, September 10 – 12, 2024.

[150] Sacks, J., Schiller, S. B., and Welch, W. J., "Designs for computer experiments," *Technometrics*, Vol. 31, No. 1, 1989, pp. 41–47.

[151] Qiao, G., Higgins, R. J., Barakos, G. N., and Zhang, T., "CFD Study of eVTOL Distributed Propulsors," *RAeS Applied Aerodynamics Conference, No.4 Hamilton Place, London, UK*, 13-15 September 2022.

[152] Qiao, G. and Barakos, G. N., "Verification and Optimisation of Distributed Propulsion Using High-Fidelity CFD Method," *American Helicopter Society 79th Annual Forum & Technology Display, May 16-18, 2023, West Palm Beach, Florida, USA*, 2023.

[153] Qiao, G., San Martin, E., and Barakos, G., "Assessment of synchrophasing for a pair of rotors in close proximity," *Aerospace Science and Technology*, Vol. 157, 2025, pp. 109808.

[154] Qiao, G. and Barakos, G., "Aerodynamic assessment of wingtip-mounted propeller and distributed propulsion system," *Aeronautical Journal*, 2025, pp. 1–20.